Lower Hybrid Modeling and Expeiments on Alcator C-Mod

by

John E. Liptac Jr.

Submitted to the Department of Nuclear Science and Engineering
in partial fulfillment of the requirements for the degree of

Doctor of Philosophy in Applied Plasma Physics

at the

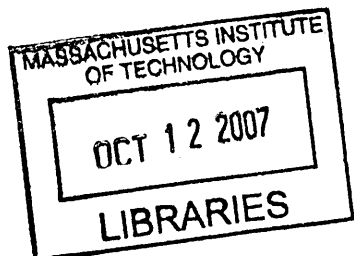MASSACHUSETTS INSTITUTE OF TECHNOLOGY

May 2006
(June 2006)

Author ....
Department of Nuclear Science and Engineering
May 16, 2006

Certified by ....
Ronald R. Parker
Professor,Departments of Electrical and Nuclear Science and Engineering
Thesis Supervisor

Certified by ....
Paul T. Bonoli
Principle Scientist, Plasma Science and Fusion Center
Thesis Reader

Accepted by ....
Jeffrey A. Coderre
Chairman, Department Committee on Graduate Students

Lower Hybrid Modeling and Experiments on Alcator C-Mod
by
John E. Liptac Jr.

Abstract

A highly flexible phase control system was developed in order to dynamically adjust the parallel wave number spectrum of driven LH waves on Alcator C-Mod. Wave coupling between the antenna and the plasma was studied using this system. A coupling code was modified to allow arbitrary phase and amplitude in each waveguide, which was required for agreement between the theory and experiment. Remarkable agreement was achieved when a small vacuum gap of 0.6 to 1.4 mm was included in the model, similar to results obtained on ASDEX. The location of the fast electron population is critical in diagnosing the performance of the lower hybrid system and can be inferred by measuring nonthermal bremsstrahlung emission. A state-of-the-art diagnostic for hard x-ray (HXR) emission was designed and used to make measurements of fast electrons bremsstrahlung during LHCD experiments on C-Mod. The HXR diagnostic consists of an array of 32 CdZnTe detectors to image energies in the 20-200 keV range. Detectors and pulse processing electronics were integrated into a compact and modular package. The system also makes use of fast digitization and software signal processing techniques allowing a maximum counting rate of 1 MHz. HXR experimental results indicate a spatially broad and centered fast electron population. HXR profiles predicted by a synthetic diagnostic in the Fokker-Planck code CQL3D are narrower than the observed profiles, suggesting the importance of spatial diffusion of fast electrons in the experiment. Lower hybrid experiments on C-Mod represent the first results obtained with density, magnetic field, plasma shape, and source frequency all near conditions expected on ITER. In initial experiments, about 400 kW of LH power was coupled for 400 ms into low density L-mode discharges. Clear evidence of current drive was seen as the loop voltage decreased by about 50%. Studies were performed by varying the phase, density, and magnetic field as well as changing the direction that the waves were launched. Analysis using CQL3D indicates that a current drive efficiency of 0.15 (10^{20} $m^{-2}A/W$) was obtained by driving 167 kA of LH current with 410 kW at a line-average density of 5.5×10^{19} m^{-3}, without an electric field. This efficiency exceeds what was observed on Alcator C, but is within the range observed on FTU for similar densities. Including the residual electric field increased the LH driven current to 308 kA, corresponding to an increased effective efficiency of 0.28. In addition to experiments, extensive modeling of current profile control through phase variation was studied, including compound spectra, using CQL3D. It was found that over 200 kA of off-axis LH current can be generated in a variety of profile shapes in an H-mode target plasma. Finally, time dependent modeling of an integrated scenario was performed using the transport code TRANSP to explore what performance can be ultimately achieved on C-Mod. Results indicate that fully non-inductive, quasi-steady-state plasmas are possible with bootstrap fractions as high as 75%.

Thesis Supervisor: Ronald R. Parker
Title: Professor, Departments of Electrical and Nuclear Science and Engineering

Thesis Reader: Paul T. Bonoli
Title: Principle Scientist, Plasma Science and Fusion Center

Acknowledgments

Contents

List of Figures

14

List of Tables

Chapter 1

Introduction

The tokamak[1] is the most developed magnetic confinement device for fusion energy. Tokamaks confine plasma through magnetic fields produced from current driven through external coils and the plasma itself.

The plasma current is driven by transformer action, and is consequently limited in time to the amount of flux available. This makes the tokamak an inherently pulsed device. This is a significant drawback as a very desirable feature for a fusion reactor is steady state operation. Steady state operation reduces energy production cost[2] and reactor engineering requirements by allowing operation at a lower plasma current and by reducing cyclic fatigue[3]. The concept of the "advanced tokamak"[4, 5, 6], or AT, has been developed to extend tokamak operation to steady state regimes.

Steady state operation with purely RF or neutral beams is not feasible because of the enormous amount of power needed to generate and sustain the current. However, it is possible to drive what is known as the bootstrap current[7] by creating the proper plasma conditions, primarily through shaping the pressure profile. Lower hybrid current drive (LHCD) provides a means to produce these conditions and also supplements the bootstrap current. LHCD may be used to manipulate the current profile and thus influence the pressure profile through the equilibrium relation of $\bar{J} \times \bar{B} = \nabla P$. Lower hybrid waves are preferred to drive the current because of their high efficiency. Bootstrap current fractions can be large, 65-80%[8][9], greatly reducing the power requirements on the current drive. If this fraction can be made large enough the cost of fusion energy may become economically competitive. LHCD can also be used to access high confinement regimes[10] further reducing the amount of current needed. The combination of driving high bootstrap fractions and high confinement is hoped to make AT operation an attractive option for fusion energy production.

In addition to addressing the steady state issue, the AT concept extends to mode control. For example the resistive wall mode (RWM) is a pressure driven external kink which limits the plasma pressure and therefore the performance of the plasma. Active stabilization of these types of modes would allow for higher pressures and a further increase in performance[11].

1.1 C-Mod

Alcator C-Mod is the only high field, high density, diverted tokamak in the world[1]and is in many areas the highest performance tokamak in the United States. C-Mod's primary heat-

ing is through RF as opposed to neutral beams meaning that no strong momentum sources are introduced. Typically hydrogen minority ion cyclotron resonance heating (ICRH) is used. C-Mod's reactor relevant density leads to high collisionality which strongly couples ions and electrons such that $T_i \sim T_e$, as expected in a reactor. C-Mod also uses high-Z, molybdenum walls opposed to most machines which use graphite or other low-Z materials. It is expected that reactors will be required to use high Z materials such as tungsten or molybdenum to reduce the rate of wall erosion. C-Mod is highly compact and is character- ized by the parameters in Table 1.1

Table 1.1: **Alcator C-Mod Machine Parameters**

Parameter	Symbol	Range or Value
Toroidal Field	B_0	3.0-8.0 T
Plasma Current	I_p	0.4-2.0 MA
Major Radius	R_0	68 cm
Minor Radius	a	22 cm
Elongation	κ	0.9-1.8
Triangularity	δ	0.1-0.85
Plasma Volume		~ 1 m^3
ICRF Source Power		8 MW
LH Source Power		3-4 MW
Central Density	n_{e0}	5×10^{19}-2×10^{21} m^{-3}
Central Temperature	T_{e0}	0.5-5.0 keV
Max pulse length		5 s

1.2   Lower Hybrid System

The system used to generate RF power and launch lower hybrid waves[12] is complex and best understood by going through a description of the major components starting at the power source and following the wave until it reaches the plasma. Figure 1-1 schematically shows the major components of the LH system and how a single source divides power into waveguides.

A master oscillator output at 4.6 GHz is divided to drive each of the 12 klystrons. A klystron is a high power, vacuum tube device capable of producing microwaves. The variable attenuator and a variable phase shifter are used to control the amplitude and phase of the klystron output. A 50 dB directional coupler, part of the transmitter protection system (TPS), monitors the output power of the klystron as well as any reflected power coming back though the circulator. The circulator protects the klystron by absorbing reflected power from the rest of the system.

The waves then go through a long section of WR-187 waveguide and the intermediate directional coupler. The forward output from the intermediate coupler is split between an I/Q detector and a diode. The I/Q detector measures amplitude and phase and is the reference for feedback control. The attenuator and low power phase shifter in the vector modulator is adjusted such that the requested amplitude and phase match what

---

[1]FTU in Frascati, Italy can reach similar fields and densities, but is circular, not diverted, and does not produce H-mode plasmas.
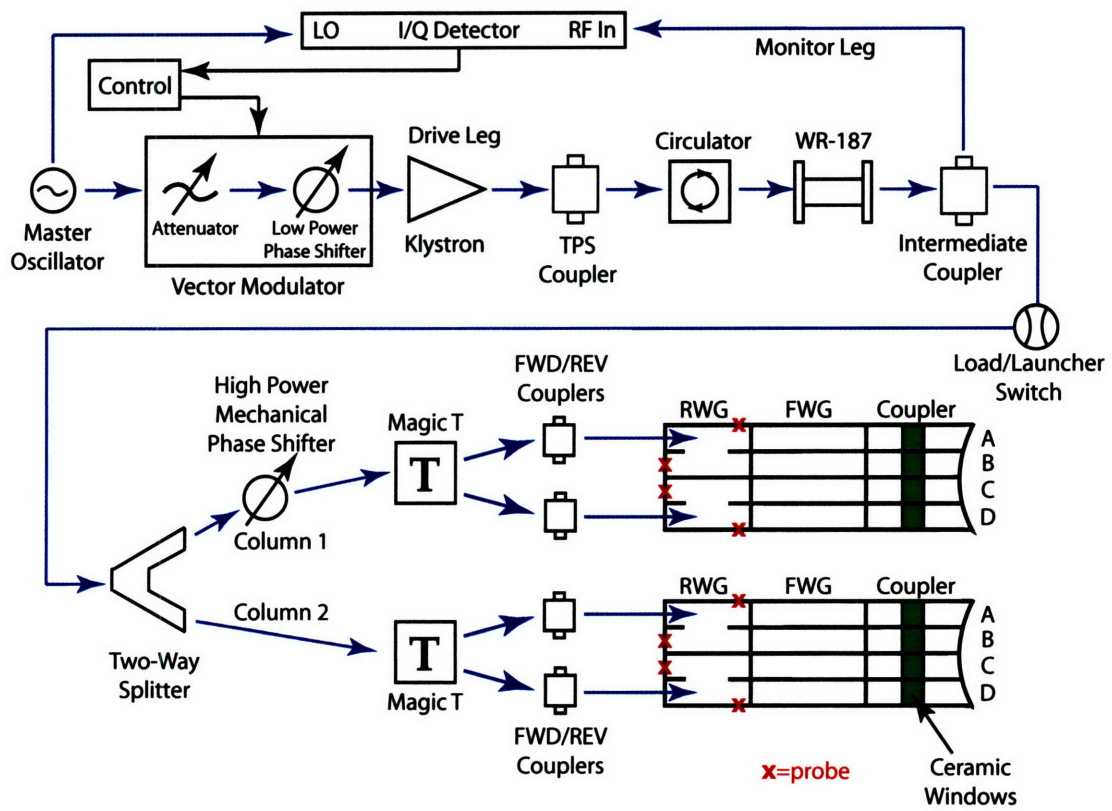
Figure 1-1: Schematic outlining major components of the lower hybrid hardware.
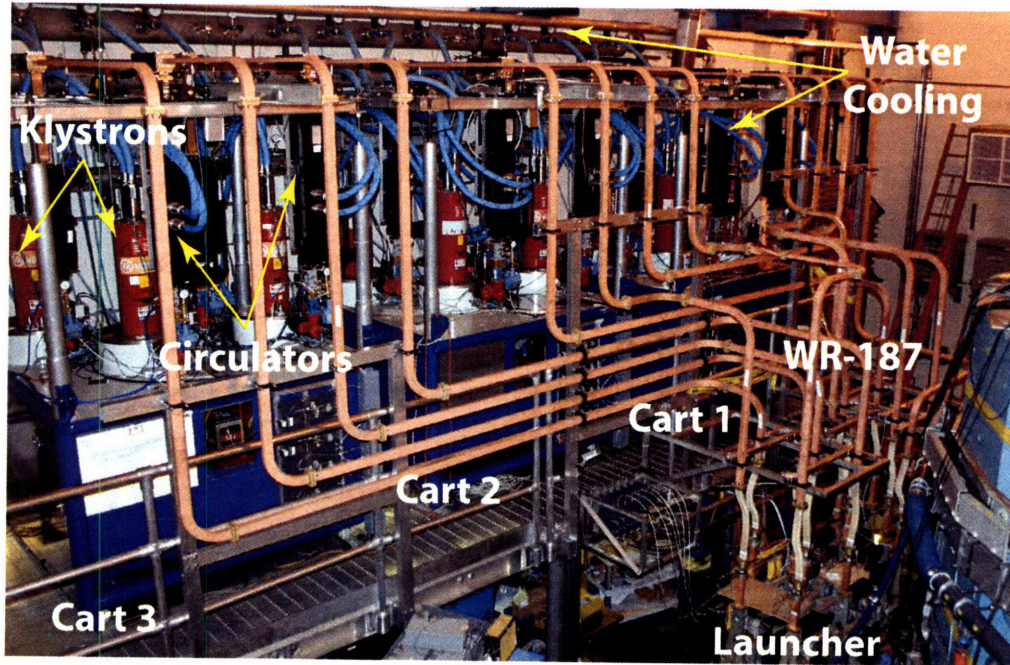
Figure 1-2: Klystron carts on mezzanine with WR-187 waveguide assembly.

is delivered at the intermediate coupler. All calibrations for phase control, covered in Appendix A, are referenced to this point. The forward and reverse diode outputs provide a direct measurement of the forward and reverse power and are also known as the "FINT" and "RINTs".

After the intermediate coupler the waves travel through a piece of flexible waveguide and into a switch that controls whether the wave is directed to the plasma or into a load. The load is used for testing purposes. If the wave is directed to the plasma, the power is then divided in two by a conventional two-way, or "pant-leg" splitter. Each leg of the splitter feeds a column of four subheight waveguides in the coupler. One leg passes through a high power phase shifter to provide control of the phasing between the columns. Then the power in each column is divided again in two by a magic T. At this point there is another set of 50 dB couplers, part of the coupler protection system, which measures the forward and reverse power. These couplers are known as the "jungle gym" or "FWD/REV" couplers. The waves now enter the rear waveguide (RWG) section of the launcher through a transformer to couple from the WR-187 to the subheight waveguides in the launcher. The primary functions of the RWG are two divide the power in two and transition from WR-187 dimension to the wide dimension of the coupler. The forward waveguide assembly (FWG) completes the transition to the size of the coupler by transforming the long dimension. The final component is the coupler where the waves transition to vacuum and are launched into the plasma.

The LH system may be further understood pictorially. Figure 1-2 shows the klystrons as they are in the experimental cell. The klystrons are each capable of producing 250 kW. Currently, 12 klystrons are used giving a total source power of 3 MW. The klystrons are

organized into groups of four and assembled into carts, which are located on a mezzanine platform on the East wall of the experimental cell.

Figure 1-2 also shows the high power circulators and the sections of WR-187 waveguide. WR-187 is the standard waveguide size of 4.75 × 2.21 cm for the C-band of frequencies, 3.95 − 5.85 GHz. The 187 number is actually the inner distance of the wider dimension of the waveguide measured in inches multiplied by 100. The sections of WR-187 from the pant-leg splitter to the RWG form a bit of a labyrinth known as the "jungle gym".

Figure 1-3 shows the visible portion of the launcher assembly in the cell. At the top of Figure 1-3 are the intermediate directional couplers, at the time of this photograph the switch and dummy load were not present. Each klystron feeds two columns of four waveguides. The first of the power divisions occurs at a two-way splitter. This divides the power in half and feeds two adjacent columns. The initial phase on both columns is set by the klystron phase. A high power, mechanical phase shifter is used to adjust the phase between adjacent columns. The phase shifters on carts one and two (2-16) are on the odd waveguides and on the even waveguides for cart three (17-23). The magic T divides the power again by two and feeds the top and bottom row of the RWG through a transformer.

An engineering drawing best depicts the internal workings of the RWG, FWG, and couplers and is shown in figure 1-4. The RWG converts the 2.2 cm dimension of the WR-187 to the 0.55 cm dimension of the coupler waveguides using an E-plane transformer. The RWG also performs the final power division to power the middle rows and contains probes to measure the forward and reverse power at the ends of the assembly. An RF gasket connects the RWG to the FWG. The FWG converts the 4.75 cm dimension of the WR-187 and RWG to the 6.00 cm dimension of the coupler using an H-plane transformer. The FWG carries the waves through the port extension and into the vacuum vessel where another RF gasket connects the coupler mounting flange.

There are four couplers, one for each row, labeled with letters from A-D, with A being the top. Each stainless steel coupler has 22 waveguides and 22 brazed, ceramic Al_2O_3, vacuum windows. A viton vacuum seal connects each coupler to the vacuum interface flange. The couplers were fabricated out of stainless steel after the original 24 waveguide titanium couplers failed and needed to be replaced. Cracks in the ceramic windows for columns 1 and 24 required the waveguides to be sealed, reducing the number of columns to 22 instead of the 24 originally planned.

The titanium couplers became embrittled by deuterium and failed, by having 10% of their weight turn to dust. Such a failure was unprecedented as titanium couplers have been used on past experiments such as Wega and Petula. Hydrogen embrittlement is sometimes used in industry to produce titanium powder, but typically under tens of atmospheres of hydrogen and at high temperatures 700 °C. The mechanism for how the deuterium was able to reach a high enough concentration inside the metal matrix to form hydrides is still unknown given the low pressure and temperature at which this process occurred.

The 0.55 × 6.00 cm dimensions of the coupler were determined by the number of waveguides needed and the space available inside the port. The septum between guides is 0.15 cm. The couplers are assembled to form the grill like structure shown in 1-5. The waveguides are numbered 1-24 with 1 starting on the D-port side. The space between couplers contains six Langmuir probes for measuring plasma density and temperature near the grill. The plasma current and field on C-Mod are both clockwise when viewing the machine from above. This makes the electron direction, and current drive direction, counterclockwise. The wave coupling is determined by the edge density and density gradient. A molybdenum limiter provides protection for the grill.
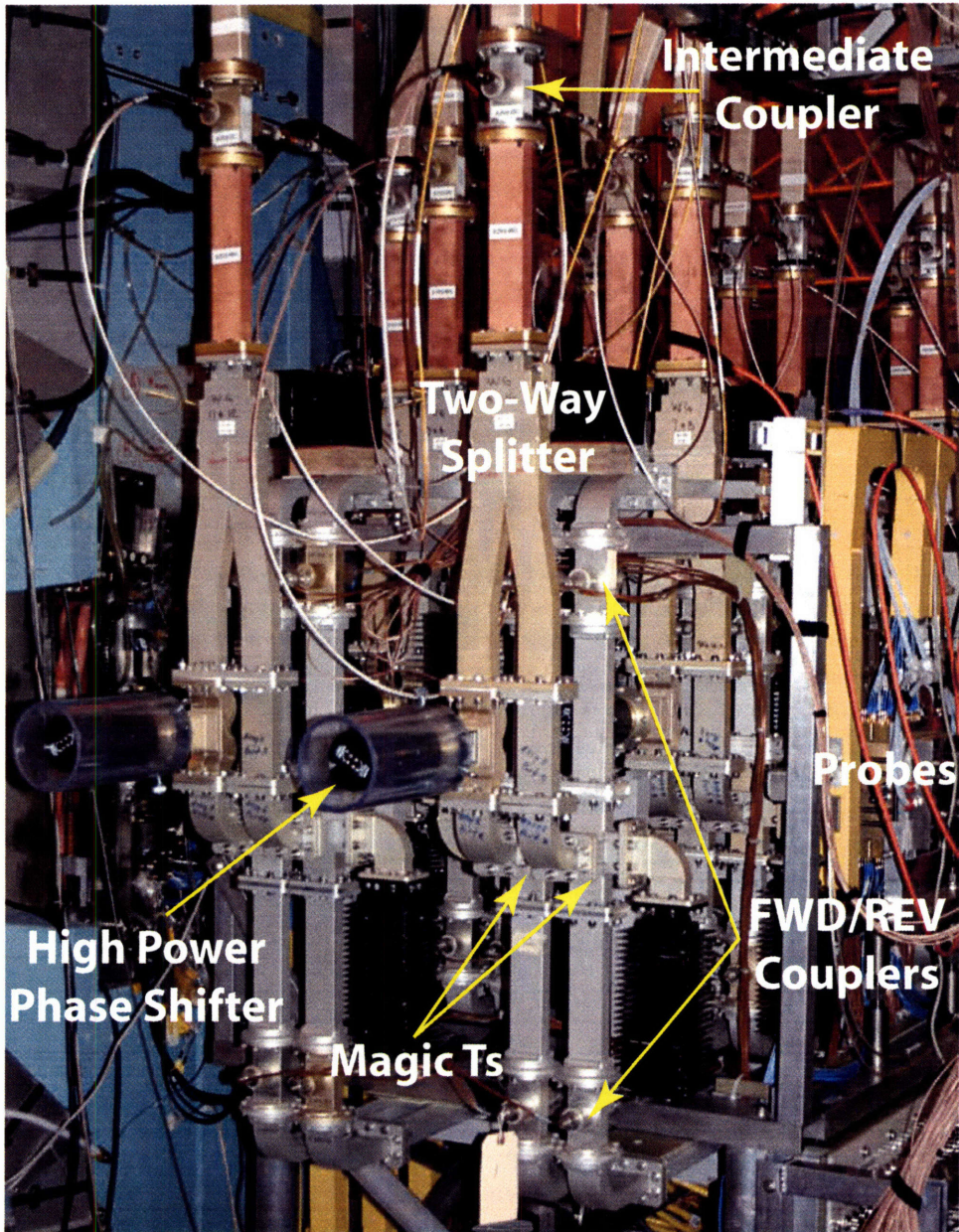
Figure 1-3: Lower hybrid launcher assembly with key components labeled.
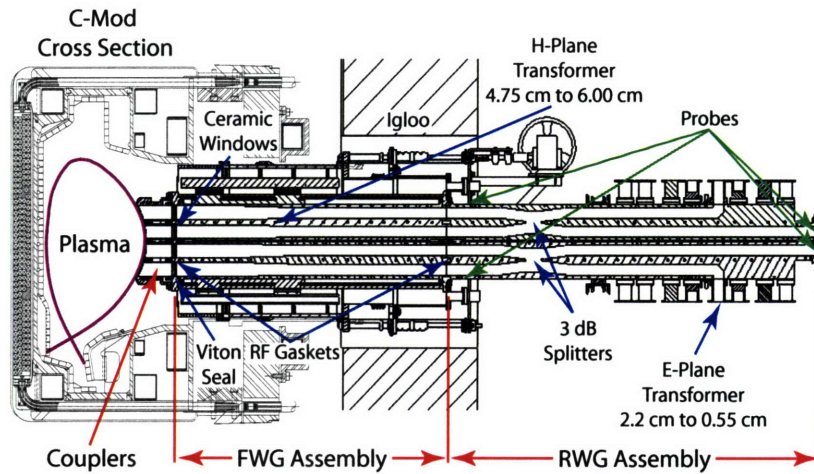
Figure 1-4: Cross sectional view of C-Mod with lower hybrid launcher. Forward and rear waveguide sections convert WR-187 dimensions to coupler dimensions.
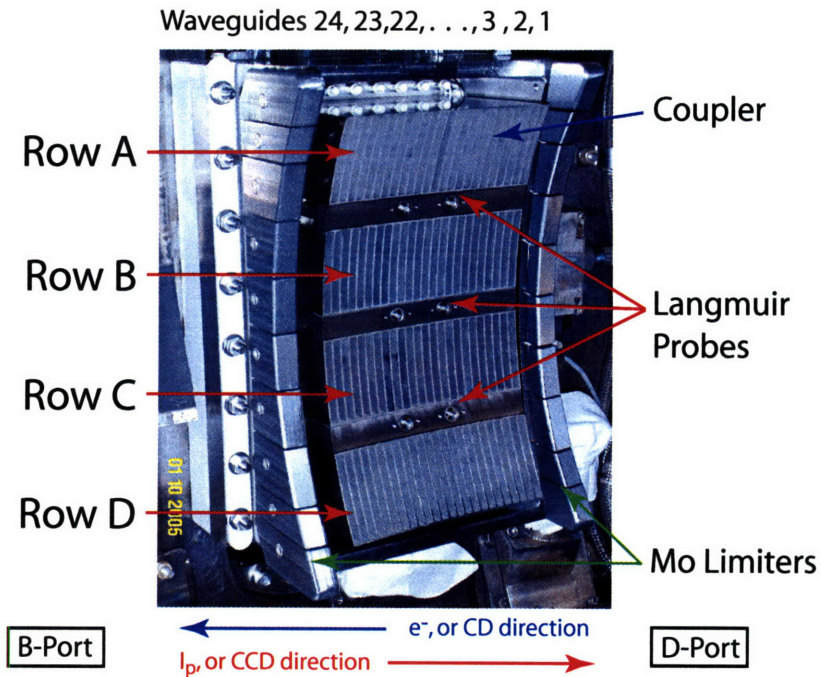
Figure 1-5: In-vessel photograph of lower hybrid antenna showing the waveguide numbering scheme, Langmuir probes, limiters, and current direction. This photo shows the titanium couplers.

A second antenna is planned, which would use a fourth cart and occupy B-port. This would bring the total source power up to 4 MW and allow compound spectra to be easily launched.

1.3 Summary of Past LH Experiments

It was initially thought that LH waves could be used to heat ions through mode conversion to the ion plasma wave[13]. Heating experiments were carried out such as on ATC[14], and Alcator A[15]. It was found that non-linear effects dominated for waves launched near the lower hybrid resonance frequency. The LH wave would undergo parametric decay[14], a three wave process, under which the LH wave decays into another wave that heats ions at the edge. The hot edge ions would not be confined and were quickly lost.

In 1978 Fisch published a ground breaking paper[16] on using LH waves for current drive. Fisch also postulated in this work that the efficiency would be high enough that only LH waves would be needed to drive the plasma current required for tokamak operation. Soon after this, the focus of lower hybrid experiments shifted from heating to current drive tried to confirm the theory. Early work on machines such as JFT-2[17] and Versator[18] were able to give very strong evidence of current drive, but were unable to do so unambiguously due to the presence of the ohmic electric field. Alcator C[19] and PLT[20] were able to disconnect the transformer and confirm the current drive without the presence of the electric field.

Many LHCD experiments have been performed in the past and are summarized in Table 1.2. The table is not meant to be exhaustive, but rather show the scope of previous work.

Table 1.2: **LH Tokamak Experiments**

Machine	Year	Location	Frequency (GHz)	Range of $n_\parallel$	Waveguides row×col.	Source Power Power (kW)
Alcator C[19, 21, 22]	1979	Cambridge, MA USA	4.6	2.5	4 Ant. 4×4	4000
ASDEX[2][23]	1980	Garching, Germany	1.3	1.0-4.0	1×8	1100
			2.45	1.0-4.4	2×24	2200
COMPASS[24]	1989	Culham, UK	1.3	2.1-6.7	1×8	400
HT-6M[25]	1985	Hefei, China	2.45	3.0	1×8	150
			2.45	2.0-3.0	2×12	150
HT-7[3][26]	1994	Hefei, China	2.45	1.0-4.0	2×12	1200
JFT-2[17]	1972	Tokai, Japan	0.75	1.0-12	1×4	125
JT-60[27, 28]	1985	Tokai, Japan	1.74-2.23	1.2-4.0	4×24	10000
			1.74-2.23	1.2-3.1	4×8	5000
PBX-M[29, 30]	1989	Princeton, NJ USA	4.6	1.0-4.2	1×32	2000
Petula[31]	1974	Grenoble, France	1.25	2.1-5.2	2 Ant. 1×4	830
PLT[20]	1975	Princeton, NJ USA	0.8	1.-3.0	1×6	500
T-7[4][32]	1981	Moscow, Russia	0.9	1.4-5.0	1×3	600
TdeV[33]	1985	Varennes, Canada	3.7	2.0-3.3	1×32	1300
Versator II[18]	1978	Cambridge, MA USA	0.8	4-11	1×6	150
Versator II[34]		Cambridge, MA USA	2.45	4-11	1×4	100
Wega[5][35]	c1978	Grenoble, France	0.8	3.0,6.3	1×4	800

[2]Operating as HL-2A in Chengdu, China, since 2002
[3]Being upgraded to the EAST tokamak
[4]Operating as HT-7 in Hefei, China, since 1994
[5]Operating as the WEGA stellarator in Greifswald, Germany, since 2001

The experiments on Alcator C are noteworthy since they were performed at high density. The work on ASDEX was also remarkable as two antennas at different frequencies were used allowing the use of compound spectra to be studied to modify the current profile.

As current drive experiments progressed it was found through theory and experiment that the current drive efficiency was too low to completely support a tokamak plasma at reactor-level densities. Attention then focused on tailoring profiles and then using the bootstrap current to carry most of the plasma current to reach steady state and control instabilities.

1.4   Current LH Experimental Programs

Tailoring the current profile remains a very active area of tokamak research with emphasis on producing AT plasmas. Table 1.3 summarizes tokamak experiments around the world that make use of and study LHCD plasmas.

Table 1.3: **Active Tokamak Experiments Using LHCD**

Machine	Frequency (GHz)	Range of $n_\parallel$	Waveguides row×col.	Source Power (MW)	Max Pulse Length (s)
Alcator C-Mod	4.6	1.0-4.7	4×22	3.0	5
FTU[36]	8.0	1.0-3.8	6 Ant. 4×12	6.0	1
JET[37]	3.7	1.4-2.3	12×32	12.0	20
JT-60U[38, 39]	1.74-2.23	1.3-3.0	4×48	10.0	10
		1.4-3.75	8×48	5.0	10
Tore Supra[40, 41]	3.7	1.7-2.3	6×34	4.0	1000
		1.6-2.2	4×34	4.0	210
TRIAM-1M[42]	2.45	1.0-4.2	1×4	0.05	CW
	8.2	1.0-2.8	2×8	0.2	CW

Many interesting and encouraging experiments have been carried out thus far to investigate AT regimes. Each machine operates within a niche of tokamak parameter space and tries to address different issues. For example FT-U experiments operate at high density while TRIAM-1M extends the limits of pulse length. Tore Supra also performs long pulse experiments, but at high power. JET and JT-60U typically try to maximize performance at moderate and low density.

AT modes may be broken down into several categories. Reverse shear (RS) plasmas are characterized by a nonmonotonic current profile giving a flat or reversed q-profile. These types of plasmas are promising since a large fraction of the plasma current may be carried by the bootstrap current. The properties of RS plasmas and their formation are discussed further in Chapter 3. Current holes are very similar to RS plasmas except that on or near the magnetic axis the plasma current is nearly zero, which makes the local value of q become large. This may slightly enhance the amount of bootstrap current due to the extended region of low poloidal field. Internal transport barriers or ITBs[43] may also enhance the bootstrap current from the increased density gradient present. When an H-mode edge is present along with an ITB a double transport barrier is formed. Completely non-inductive modes are also desirable and have been demonstrated, although mostly in plasma conditions far from what are needed in a reactor. Each machine has demonstrated some or all of these modes and are summarized in table 1.4. These modes are not completely independent as

most have significant overlap. For example, creating a RS plasma has been linked to the formation of an ITB.

Table 1.4: **Demonstrated Experimental Modes Using LHCD**

Machine	Reverse Shear	Current Hole	H-mode	ITB	Double Barrier	Non-Inductive
FTU	yes[44]	no	no	yes[44]	no	yes[45]
JET	yes[46]	yes[47]	yes	yes[48]	yes[48]	yes[49]
JT-60U	yes[50]	yes[51]	yes	yes[50]	yes[50]	yes[50]
Tore Supra	yes[52]	no	no	yes[52]	no	yes[52]
TRIAM-1M	yes[53]	no	no	yes[53]	no	yes[54]

1.5 Unique Aspects of LH Experiments on Alcator C-Mod

Alcator C-Mod is a diverted and high density tokamak which allows experiments to uniquely contribute understanding of AT physics in this operational space. FTU also shares this space, but is not diverted and cannot produce H-mode plasmas; however, FTU has been able to produce RS and ITB plasmas as well as study current drive efficiency[55]. C-Mod experiments will provide a comparison of these results and also extend them by using H-mode edge conditions and longer time scales, characteristic of what is expected during steady state operation. C-Mod has the capability to produce plasmas with a pulse length several times the current diffusion time. Tore Supra and TRIAM-1M are the only other machines that can produce plasmas with these time scales, but operate at lower density and can not produce H-modes. C-Mod's LH system also has the ability to dynamically change phase and the $n_\parallel$ spectrum during a pulse to study how the current profile may be modified in time.

1.6 The Author's Original Contributions

Alcator C-Mod is a large experiment, which requires the contributions of many people working together to produce high quality scientific results. Even within C-Mod, the LH experiment is composed of a group of scientists, engineers and technicians making much of the work collaborative. This section is to highlight the Author's original contributions.

A highly flexible phase control system was developed in order to dynamically adjust the parallel wave number spectrum of driven LH waves on Alcator C-Mod. The basic design and hardware for the system was done by Alcator engineers. The Author developed and implemented software to realize this capability. Wave coupling between the antenna and the plasma was studied using this system. This allowed multiple data points to be taken during a single shot, greatly increasing the amount of data gathered and minimizing the time required to obtain the data. The coupling data was analyzed using a coupling code that was modified to allow arbitrary phase and amplitude inputs as well as greatly improved I/O. This modification was required for agreement between the theory and experiment. Remarkable agreement was achieved when a small vacuum gap of 0.6 to 1.4 mm was included in the model, which was similar to results obtained on ASDEX. A significant amount of software was also developed to evaluate LH system performance.

The location of the fast electron population is critical in diagnosing the performance of the lower hybrid system and can be inferred by measuring nonthermal bremsstrahlung emission in the HXR region of the spectrum. A state-of-the-art diagnostic for HXR emission was designed, built, and used to make measurements of fast electron bremsstrahlung during LHCD experiments on C-Mod. The HXR diagnostic consists of an array of 32 CdZnTe detectors to image energies in the 20-200 keV range. Detectors and pulse processing electronics were integrated into a compact and modular package. This integration required a number of custom electronic components, which were designed and fabricated by the Author. The system also makes use of fast digitization and software signal processing techniques allowing a maximum counting rate of 1 MHz.

HXR experimental results indicate a spatially broad and centered fast electron population. HXR profiles predicted by a synthetic diagnostic in the Fokker-Planck code CQL3D are narrower than the observed profiles, suggesting the importance of spatial diffusion of fast electrons in the experiment. CQL3D was an existing code that the Author helped to implement for C-Mod on the parallel computing cluster. The Author also implemented the HXR synthetic diagnostic in CQL3D and contributed to the proper implementation of the DC electric field.

Lower hybrid experiments on C-Mod represent the first results obtained with density, magnetic field, plasma shape, and source frequency all near conditions expected on ITER. The Author was responsible for directing the coupling and current drive experiments while being the C-Mod Session Leader on six occasions. In initial experiments, about 400 kW of LH power was coupled for 400 ms into low density L-mode discharges. Clear evidence of current drive was seen as the loop voltage decreased by about 50%. Studies were performed by varying the phase, density, and magnetic field as well as changing the direction that the waves were launched. Analysis using CQL3D indicates that a current drive efficiency of 0.15 (10^{20} $m^{-2}A/W$) was obtained by driving 167 kA of LH current with 410 kW at a line-average density of 5.5×10^{19} m^{-3}, without an electric field. This efficiency exceeds what was observed on Alcator C, but is within the range observed on FTU for similar densities. Including the residual electric field increased the LH driven current to 308 kA, corresponding to an increased effective efficiency of 0.28.

In addition to experiments, extensive modeling of current profile control through phase variation was studied, including compound spectra, using CQL3D. It was found that over 200 kA of off-axis LH current can be generated in a variety of profile shapes in an H-mode target plasma. In total over 50 CQL3D runs were made. Finally, time dependent modeling of an integrated scenario was performed using the transport code TRANSP to explore what performance can be ultimately achieved on C-Mod. Over 100 runs were made while the sensitivity of plasma parameters were studied. Results indicate that fully non-inductive, quasi-steady-state plasmas are possible with bootstrap fractions as high as 75%.

1.7 Thesis Outline

The thesis is organized as follows. Chapter 2 presents the LH background physics needed to understand the modeling and experimental results of later chapters. Chapter 3 discusses time dependent modeling of AT scenarios, while Chapter 4 covers detailed Fokker-Planck simulations. The design of a hard x-ray (HXR) camera for diagnosing LHCD experiments is presented in Chapter 5 with initial results and analysis shown in Chapter 6. Chapter 7 discusses coupling results and comparison to theory. The thesis summary and possible

directions for future work are covered in chapter 8. The appendices present useful information on the phase calibration and control of the LH system in addition to analysis tools that were developed to process and view LH data.

Chapter 2

Lower Hybrid Background Physics

The lower hybrid frequency exists in the regime $\omega_{ce}^2 \gg \omega_{lh}^2 \gg \omega_{ci}^2$, well separated from both the electron and ion cyclotron frequencies. To get a quantitative sense for this range, C-Mod has a typical magnetic field on axis of about 5 T and uses deuterium, so $f_{ce} = 140$ GHz and $f_{ci} = 40$ MHz. This puts f_{lh} in the range of a few GHz. As will be discussed in more detail in the following sections, the lower hybrid wave is normally cutoff, meaning that it cannot propagate in the plasma.

A solution to this problem is to excite the wave with a non-zero component of the index of refraction parallel to the magnetic field, $n_{\parallel}$. The parallel refractive index is an important parameter in LHCD since it is responsible for the wave accessibility, where the current will be driven within the plasma, and the current drive efficiency. The wave is coupled with finite $n_{\parallel}$ using an antenna launching structure. A phased array of many waveguides is used as the antenna and sets $n_{\parallel}$, determined by the phase difference between the guides and the geometry of the structure. Because of their appearance, the antennas are also known as "grills". The grill phasing also gives the wave directivity, meaning that most of the power is directed in the desired direction, which is critical for current drive.

Once the wave is in the plasma it propagates until it reaches a region where the wave's phase velocity is about three times the thermal velocity. Once this condition is met the wave will Landau damp, giving its energy to electrons which have the appropriate velocity. Since the waves are launched mostly in one direction, this causes the distribution function to develop an asymmetric tail, and thus drive current. By controlling $n_{\parallel}$, the location of the driven current may also be controlled, which can influence the pressure profile and consequently the location and magnitude of the bootstrap current. The driven current per unit input power is higher for lower hybrid waves than for any other RF current drive method. These factors make LHCD a desirable tool to study advanced tokamak plasmas.

Current profile control with LHCD is not straight-forward since $n_{\parallel}$ changes as the wave propagates. Ray tracing and detailed modeling in addition to experimental data from diagnostics such as the hard x-ray camera become important to know where the waves are damping and where the current is ultimately driven.

This section includes the necessary background physics of lower hybrid waves to understand LHCD. The cold plasma dispersion relation, covered in Section 2.1, provides a good starting point by defining the lower hybrid wave's characteristics and leads to the accessibility condition in Section 2.2. Once the accessibility condition is known, it is necessary to couple the wave with the appropriate $n_{\parallel}$ spectrum, which is covered in Section 2.3. Section 2.4 discusses wave propagation and ray tracing. The damping of the LH wave is a thermal

effect which is analyzed using the hot plasma dispersion relation in 2.5. Current drive and efficiency are discussed in Sections 2.6 and 2.7.

2.1 Cold Magnetized Plasma Dispersion Relation

Information about the accessibility and propagation of lower hybrid waves may be obtained by modeling the plasma as a cold and therefore pressureless system. The lower hybrid frequency, a resonance condition, and the lower cutoff frequency may also be found through this simple description of the plasma. Derivation of the cold magnetized plasma dispersion relation begins with Ampere's and Faraday's laws:

$$\nabla \times \overline{B} = \mu_0 \overline{J} + \frac{1}{c^2} \frac{\partial \overline{E}}{\partial t} \tag{2.1}$$

$$\nabla \times \overline{E} = -\frac{\partial \overline{B}}{\partial t}. \tag{2.2}$$

Taking the curl of Faraday's law and substituting in Ampere's law gives

$$\nabla \times \nabla \times \overline{E} = -\frac{\partial}{\partial t} \left(\mu_0 \overline{J} + \frac{1}{c^2} \frac{\partial \overline{E}}{\partial t} \right).$$

The next step is to use the tensor form of Ohm's law, which includes anisotropies, $\overline{J} = \overline{\overline{\sigma}} \cdot \overline{E}$ and perform a Fourier analysis by assuming quantities vary like $e^{i(\overline{k} \cdot \overline{r} - \omega t)}$. This makes $\nabla \rightarrow i\overline{k}$ and $\frac{\partial}{\partial t} \rightarrow -i\omega$. Using Ohm's law to replace $\overline{J}$, and a little algebra gives an eigenvalue equation with the electric field,

$$\left\{ \frac{ic^2 \mu_0}{\omega} \overline{\overline{\sigma}} + \overline{\overline{I}} + \frac{c^2}{\omega^2} \left(\overline{kk} - k^2 \overline{\overline{I}} \right) \right\} \cdot \overline{E} = 0, \tag{2.3}$$

where $\overline{\overline{I}}$ is the identity matrix, and the relative dielectric tensor is defined in terms of $\overline{\overline{\sigma}}$ as,

$$\overline{\overline{\epsilon}} = \frac{ic^2 \mu_0}{\omega} \overline{\overline{\sigma}} + \overline{\overline{I}}.$$

All plasma phenomena affecting wave propagation are contained within this term. Also noting that the index of refraction is $n = ck/\omega$, the equation may be rewritten as

$$\left\{ n^2 \left(\frac{\overline{kk}}{k^2} - \overline{\overline{I}} \right) + \overline{\overline{\epsilon}} \right\} \cdot \overline{E} = 0. \tag{2.4}$$

Setting the determinant of $\left\{ n^2 \left(\frac{\overline{kk}}{k^2} - \overline{\overline{I}} \right) + \overline{\overline{\epsilon}} \right\}$ to zero gives non-trivial solutions to the eigenvalue problem. This is the dispersion relation, $D(\omega, \overline{k})$. At this point it is best to proceed by choosing a coordinate system to perform the analysis. It is chosen such that $\overline{B}$ is along the z-axis and such that $\overline{k} = k_x \hat{x} + k_z \hat{z}$, and φ is the angle measured from the magnetic field. In relation to the field $k_x = k_\perp = k \sin \varphi$ and $k_z = k_\parallel = k \cos \varphi$. This is done without loss of generality since the choice of coordinate system is arbitrary. The φ representation is useful in examining O and X-mode polarizations. So

$$\overline{kk} = \begin{pmatrix} k_x k_x & k_x k_y & k_x k_z \\ k_y k_x & k_y k_y & k_y k_z \\ k_z k_x & k_z k_y & k_z k_z \end{pmatrix} = \begin{pmatrix} k_\perp^2 & 0 & k_\perp k_\parallel \\ 0 & 0 & 0 \\ k_\parallel k_\perp & 0 & k_\parallel^2 \end{pmatrix} = \begin{pmatrix} k^2 \sin^2 \varphi & 0 & k^2 \sin \varphi \cos \varphi \\ 0 & 0 & 0 \\ k^2 \cos \varphi \sin \varphi & 0 & k^2 \cos^2 \varphi \end{pmatrix}.$$
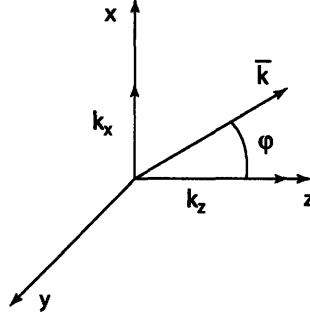
Figure 2-1: Geometry for wave propagation with the magnetic field along the z-axis.

The $n^2\left(\frac{\overline{kk}}{k^2} - \overline{\overline{I}}\right)$ term can be rewritten by introducing $n_\perp^2 = \frac{c^2}{\omega^2}k_\perp^2$, $n_\parallel^2 = \frac{c^2}{\omega^2}k_\parallel^2$ and noting that $n^2 = \frac{c^2}{\omega^2}\overline{k}\cdot\overline{k} = n_\perp^2 + n_\parallel^2$. This gives the index of refraction, or n matrix as

$$
n^2\left(\frac{\overline{kk}}{k^2} - \overline{\overline{I}}\right) = \begin{pmatrix} -n_\parallel^2 & 0 & n_\perp n_\parallel \\ 0 & -n_\parallel^2 - n_\perp^2 & 0 \\ n_\parallel n_\perp & 0 & -n_\perp^2 \end{pmatrix} = \begin{pmatrix} -n^2\cos^2\varphi & 0 & n^2\sin\varphi\cos\varphi \\ 0 & -n^2 & 0 \\ n^2\cos\varphi\sin\varphi & 0 & -n^2\sin^2\varphi \end{pmatrix}.
$$

The n matrix is primarily wave geometry, and all the plasma effects are included in the dielectric tensor, $\overline{\overline{\epsilon}}$. Finding this quantity means solving for the plasma's conductivity, $\overline{\overline{\sigma}}$, which is related to velocity through Ohm's law,

$$
\overline{J} = \sum_\alpha q_\alpha n_\alpha \overline{u}_\alpha = \overline{\overline{\sigma}}\cdot\overline{E}. \tag{2.5}
$$

Where the sum over α is the sum over all particle species. The velocity, $\overline{u}_\alpha$, is a vector quantity that may be represented as a tensor dotted into the electric field to yield $\overline{\overline{\sigma}}$, the conductivity, directly by multiplying the constant $q_\alpha n_\alpha$. This tensor is known as the mobility tensor and is defined as $\overline{u}_\alpha = \overline{\overline{\mu}}_\alpha \cdot \overline{E}$, so

$$
\overline{\overline{\sigma}} = \sum_\alpha q_\alpha n_\alpha \overline{\overline{\mu}}_\alpha.
$$

The velocity components needed to build $\overline{\overline{\mu}}_\alpha$ are taken from the linearized momentum equation. For a cold plasma the equation of motion is

$$
m_\alpha \frac{d\overline{u}_\alpha}{dt} = q_\alpha(\overline{E} + \overline{u}_\alpha \times \overline{B}). \tag{2.6}
$$

The equation of motion is linearized assuming the magnetic field is given by $\overline{B} = \overline{B}_0 + \overline{B}_1$, with the conditions $\overline{u}_{\alpha 0} = 0$ and $\overline{E}_0 = 0$, no zero-order flow or electric field, to give

$$
m_\alpha \frac{\partial \overline{u}_\alpha}{\partial t} = q_\alpha \overline{E}_1 + q_\alpha \overline{u}_{\alpha 1} \times \overline{B}_0.
$$

Transforming again to Fourier space and writing out the components, letting $\overline{B}_0 = \overline{B}$, $\overline{u}_{\alpha 1} = \overline{u}_\alpha$, and $\overline{E}_1 = \overline{E}$ gives

$$
\begin{aligned}
\hat{x} : -i\omega m_\alpha u_x &= q_\alpha(E_x + u_y B) \\
\hat{y} : -i\omega m_\alpha u_y &= q_\alpha(E_y - u_x B) \\
\hat{z} : -i\omega m_\alpha u_z &= q_\alpha E_z.
\end{aligned}
$$

33

Solving for perturbed velocities in terms of electric field gives

$$u_x = \frac{q_\alpha(i\omega \mathrm{E}_x - \omega_{c\alpha}\mathrm{E}_y)}{m_\alpha(\omega^2 - \omega_{c\alpha}^2)}, \tag{2.7}$$

$$u_y = \frac{q_\alpha(i\omega \mathrm{E}_y + \omega_{c\alpha}\mathrm{E}_x)}{m_\alpha(\omega^2 - \omega_{c\alpha}^2)}, \tag{2.8}$$

$$u_z = \frac{iq_\alpha \mathrm{E}_z}{\omega m_\alpha}, \tag{2.9}$$

where

$$\omega_{c\alpha} = \frac{q_\alpha \mathrm{B}}{m_\alpha}$$

is the signed cyclotron frequency, which is positive for ions and negative for electrons. Since u_x and u_y are coupled, $\overline{\overline{\mu}}_\alpha$ will be a non-diagonal matrix. Examining the velocity components, $\overline{\overline{\mu}}_\alpha$ can be constructed as,

$$\overline{\overline{\mu}}_\alpha = \frac{q_\alpha}{m_\alpha}
\begin{pmatrix}
\dfrac{i\omega}{\omega^2 - \omega_{c\alpha}^2} & \dfrac{-\omega_{c\alpha}}{\omega^2 - \omega_{c\alpha}^2} & 0 \\[2ex]
\dfrac{\omega_{c\alpha}}{\omega^2 - \omega_{c\alpha}^2} & \dfrac{i\omega}{\omega^2 - \omega_{c\alpha}^2} & 0 \\[2ex]
0 & 0 & \dfrac{i}{\omega}
\end{pmatrix}.$$

Multiplying and taking the sum of $q_\alpha n_\alpha \overline{\overline{\mu}}_\alpha$ over all the species gives the conductivity, so the dielectric tensor is

$$\overline{\overline{\epsilon}} = \frac{ic^2}{\omega}\mu_0\overline{\overline{\sigma}} + \overline{\overline{\mathrm{I}}} =
\begin{pmatrix}
1 - \displaystyle\sum_\alpha \dfrac{\omega_{p\alpha}^2}{\omega^2 - \omega_{c\alpha}^2} & -\displaystyle\sum_\alpha \dfrac{i\omega_{c\alpha}\omega_{p\alpha}^2}{\omega(\omega^2 - \omega_{c\alpha}^2)} & 0 \\[3ex]
\displaystyle\sum_\alpha \dfrac{i\omega_{c\alpha}\omega_{p\alpha}^2}{\omega(\omega^2 - \omega_{c\alpha}^2)} & 1 - \displaystyle\sum_\alpha \dfrac{\omega_{p\alpha}^2}{\omega^2 - \omega_{c\alpha}^2} & 0 \\[3ex]
0 & 0 & 1 - \displaystyle\sum_\alpha \dfrac{\omega_{p\alpha}^2}{\omega^2}
\end{pmatrix}, \tag{2.10}$$

where

$$\omega_{p\alpha}^2 = \frac{q_\alpha^2 n_\alpha}{\epsilon_0 m_\alpha}$$

is the plasma frequency. The perpendicular, cross, and parallel components of the dielectric tensor can be defined as

$$\epsilon_\perp = 1 - \sum_\alpha \frac{\omega_{p\alpha}^2}{\omega^2 - \omega_{c\alpha}^2}, \tag{2.11}$$

$$\epsilon_\times = \sum_\alpha \frac{\omega_{c\alpha}\omega_{p\alpha}^2}{\omega(\omega^2 - \omega_{c\alpha}^2)}, \tag{2.12}$$

$$\epsilon_\parallel = 1 - \sum_\alpha \frac{\omega_{p\alpha}^2}{\omega^2}. \tag{2.13}$$

Adding the n and dielectric matrices together gives the matrix whose determinant is the dispersion relation,

$$D(\omega, \overline{k}) =
\begin{vmatrix}
\epsilon_\perp - n_\parallel^2 & -i\epsilon_\times & n_\perp n_\parallel \\
i\epsilon_\times & \epsilon_\perp - n_\parallel^2 - n_\perp^2 & 0 \\
n_\parallel n_\perp & 0 & \epsilon_\parallel - n_\perp^2
\end{vmatrix}
=
\begin{vmatrix}
\epsilon_\perp - n^2\cos^2\varphi & -i\epsilon_\times & n^2\sin\varphi\cos\varphi \\
i\epsilon_\times & \epsilon_\perp - n^2 & 0 \\
n^2\cos\varphi\sin\varphi & 0 & \epsilon_\parallel - n^2\sin^2\varphi
\end{vmatrix},$$

and

$$det(D(\omega,\overline{k})) = (\epsilon_\perp - n_\parallel^2)(\epsilon_\perp - n_\parallel^2 - n_\perp^2)(\epsilon_\parallel - n_\perp^2) - \epsilon_\times^2(\epsilon_\parallel - n_\perp^2) - n_\perp^2 n_\parallel^2(\epsilon_\perp - n_\parallel^2 - n_\perp^2).$$

Collecting terms in powers of $n_\perp$ gives

$$\epsilon_\perp n_\perp^4 + (-\epsilon_\perp^2 + \epsilon_\times^2 - \epsilon_\parallel \epsilon_\perp + \epsilon_\perp n_\parallel^2 + \epsilon_\parallel n_\parallel^2)n_\perp^2 + (-\epsilon_\times^2 \epsilon_\parallel + \epsilon_\perp^2 \epsilon_\parallel - 2n_\parallel^2 \epsilon_\parallel \epsilon_\perp + n_\parallel^4 \epsilon_\parallel).$$

So the dispersion relation has the form $D(\omega,\overline{k}) = C_4 n_\perp^4 + C_2 n_\perp^2 + C_0$. Simplifying the coefficients yields

$$C_4 = \epsilon_\perp, \tag{2.14}$$

$$C_2 = (n_\parallel^2 - \epsilon_\perp)(\epsilon_\parallel + \epsilon_\perp) + \epsilon_\times^2, \tag{2.15}$$

$$C_0 = \epsilon_\parallel((n_\parallel^2 - \epsilon_\perp)^2 - \epsilon_\times^2). \tag{2.16}$$

This is a form of the cold plasma dispersion relation that may be used to determine the ray trajectories of LH waves in a plasma. Ray tracing is discussed in Section 2.4.

In taking certain limits of the dispersion relation, the lower hybrid frequency and a cutoff may be found. The lower hybrid frequency corresponds to a resonance, and the cutoff corresponds to a point where lower hybrid waves are reflected.

Writing the relation in terms of φ gives

$$D(\omega,\overline{k}) = (\epsilon_\perp \sin^2\varphi + \epsilon_\parallel \cos^2\varphi)n^4 - ((\epsilon_\perp^2 - \epsilon_\times^2)\sin^2\varphi + \epsilon_\perp \epsilon_\parallel \cos^2\varphi + \epsilon_\perp \epsilon_\parallel)n^2 + \epsilon_\parallel(\epsilon_\perp^2 - \epsilon_\times^2) = 0.$$

This can be written in terms of $\tan^2\varphi$ by using $\sin^2\varphi + \cos^2\varphi = 1$, and dividing through by $\cos^2\varphi$,

$$\tan^2\varphi = -\frac{\epsilon_\parallel\{(n^2 - (\epsilon_\perp - \epsilon_\times))(n^2 - (\epsilon_\perp + \epsilon_\times))\}}{(\epsilon_\perp n^2 - (\epsilon_\perp^2 - \epsilon_\times^2))(n^2 - \epsilon_\parallel)}. \tag{2.17}$$

The poles and zeros of $\tan^2\varphi$ give rise to resonances and cutoffs. Note that by setting $n_\perp = 0$ or $\varphi = 0$ gives waves traveling only along the magnetic field. Similarly setting $n_\parallel = 0$ or $\varphi = \frac{\pi}{2}$, the dispersion relation reduces to propagation only perpendicular to the magnetic field and recovers ordinary (O-mode) and extraordinary (X-mode) polarizations. This is most clearly seen using the φ representation, $\tan^2\frac{\pi}{2} = \infty$ so the denominator must equal zero giving

$$n^2 = \epsilon_\parallel \text{ (O-mode) or } n^2 = \frac{\epsilon_\perp^2 - \epsilon_\times^2}{\epsilon_\perp} \text{ (X-mode)}.$$

The X-mode polarization is the root containing the lower hybrid wave. Resonances occur when $n \to \infty$ and cutoffs when $n \to 0$. The frequency of the lower hybrid resonance is found by setting $\epsilon_\perp = 0$ For a single ion species the resonance condition is

$$1 = \frac{\omega_{pe}^2}{\omega^2 - \omega_{ce}^2} + \frac{\omega_{pi}^2}{\omega^2 - \omega_{ci}^2}, \text{ or}$$

$$\epsilon_\perp = \omega^4 - (\omega_{ce}^2 + \omega_{ci}^2 + \omega_{pe}^2 + \omega_{pi}^2)\omega^2 + \omega_{ci}^2\omega_{ce}^2 + \omega_{pe}^2\omega_{ci}^2 + \omega_{pi}^2\omega_{ce}^2 = 0.$$

This is bi-quadratic in ω. Some subtle algebra is helpful in determining the roots and finding the lower hybrid frequency. Any quadratic may be written as

$$x^2 + bx + c = 0 \text{ and factored into } (x + r_1)(x + r_2) \text{ so } b = r_1 + r_2, c = r_1 r_2.$$

If the roots are well separated, that is $r_1 \gg r_2$, then

$$r_1 \approx b \text{ and } r_2 \approx \frac{c}{b}.$$

The discriminant will show if the roots are well separated or not. The frequencies can easily be evaluated for a given density and magnetic field. Choosing n $= 10^{20}$ m^{-3} and B = 5 T gives the following ordering $\omega_{ce}^2 > \omega_{pe}^2 \gg \omega_{pi}^2 \gg \omega_{ci}^2$ with frequencies of 140, 90, 1.4, and 0.04 GHz respectively. So

$$b = \omega_{ce}^2 + \omega_{ci}^2 + \omega_{pe}^2 + \omega_{pi}^2 \approx 2\omega_{pe}^2$$

$$c = \omega_{ci}^2\omega_{ce}^2 + \omega_{pe}^2\omega_{ci}^2 + \omega_{pi}^2\omega_{ce}^2 \approx \omega_{pi}^2\omega_{ce}^2$$

$$\frac{b^2}{4c} = \frac{4\omega_{pe}^4}{4\omega_{pi}^2\omega_{ce}^2} \approx \frac{\omega_{pe}^2}{\omega_{pi}^2} \approx \frac{m_i}{m_e} \gg 1$$

The roots are well separated and so

$$\omega^2 \approx r_1 \quad \approx \quad b \approx \omega_{ce}^2 + \omega_{pe}^2, \text{ the upper hybrid frequency}$$

$$\omega^2 \approx r_2 \quad \approx \quad \frac{c}{b} \approx \frac{\omega_{pi}^2\omega_{ce}^2}{\omega_{ce}^2 + \omega_{pe}^2}, \text{ the lower hybrid frequency.}$$

Or if the frequency range is known a priori as $\omega_{ce}^2 \gg \omega^2 \gg \omega_{ci}^2$, then $\epsilon_\perp = 0$ may be written as

$$\epsilon_\perp \simeq 1 - \frac{\omega_{pi}^2}{\omega^2} + \frac{\omega_{pe}^2}{\omega_{ce}^2}.$$

Solving for ω^2 gives

$$\omega^2 = \omega_{lh}^2 = \frac{\omega_{pi}^2}{1 + \omega_{pe}^2/\omega_{ce}^2}, \quad (2.18)$$

which is the definition of the lower hybrid frequency.

The possible cutoffs for X-mode propagation are given by $\epsilon_\times^2 = \epsilon_\perp^2$, which can be written as $\epsilon_\perp \pm \epsilon_\times = 0$. The cutoff of interest for lower hybrid waves is the lower or left-hand cutoff. This occurs from the $\epsilon_\perp - \epsilon_\times = 0$ Using partial fractions and noting that $\frac{\omega_{pi}^2}{\omega_{ci}} = -\frac{\omega_{pe}^2}{\omega_{ce}}$, $\epsilon_\times$ may be rewritten as

$$\frac{\omega_{pi}^2}{\omega_{ci}}\left(\frac{\omega}{\omega^2 - \omega_{ci}^2} - \frac{\omega}{\omega^2 - \omega_{ce}^2}\right).$$

The cutoff can be written as

$$\epsilon_\perp - \epsilon_\times = 1 + \frac{\omega_{pe}^2}{\omega_{ce}^2 - \omega^2}\left(1 + \frac{\omega}{\omega_{ce}}\right) + \frac{\omega_{pi}^2}{\omega_{ci}^2 - \omega^2}\left(1 + \frac{\omega}{\omega_{ci}}\right)$$

$$= 1 + \frac{\omega_{pi}^2}{\omega_{ci}^2}\left(\frac{1}{\omega_{ci} - \omega} - \frac{1}{\omega_{ce} - \omega}\right)$$

$$= \omega^2 - (\omega_{ce} + \omega_{ci})\omega + \omega_{ce}\omega_{ci} + \frac{\omega_{pi}^2}{\omega_{ci}}(\omega_{ce} - \omega_{ci}).$$

Using $\omega_{ce}^2 \gg \omega_{ci}^2$ with the quadratic formula gives the left-hand cutoff

$$\omega_{lco} = \frac{1}{2}\left(\omega_{ce} + \sqrt{\omega_{ce}^2 + 4\omega_{pe}^2}\right), \quad (2.19)$$

while keeping in mind that ω_{ce} is a negative quantity because of the electron charge. If $\omega_{pe}^2/\omega_{ce}^2 > 1$ then $\omega_{lco} \approx \omega_{pe}^2/\omega_{ce}$. The cutoff determines the wave accessibility, that is if and how far the wave is able to propagate in the plasma. This is discussed in detail in the next section.

There is a certain body of terminology that is commonly used in plasma waves. The terms "parallel" and "perpendicular" refer to the direction of $\overline{k}$ relative to $\overline{B}$. "Longitudinal" and "transverse" refer to to the polarization of the wave, that is the direction of $\overline{k}$ relative to $\overline{E}$. "Electrostatic" waves are longitudinal with $\overline{B}_1 = 0$, "electromagnetic" waves have a transverse component of $\overline{E}$ with $\overline{B}_1 \neq 0$.

2.2 Accessibility

To use the lower hybrid wave for heating or current drive the wave must be accessible, meaning that it will not be cutoff and reflected before reaching the desired plasma region. First, the frequency of the wave must be above the plasma frequency, determined by the density at the grill, otherwise there will be a region of evanescence before propagation. Assuming that the wave frequency is high enough, the lower cutoff determines where the wave can propagate in the plasma. Figure 2-2 shows the lower hybrid resonance frequency in red, the lower cutoff in black and C-Mod's LHCD operating frequency in blue. The density
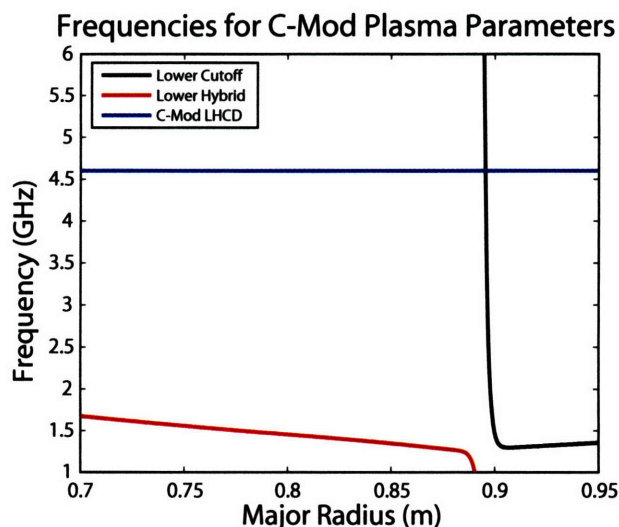
Figure 2-2: Lower hybrid resonance, left-hand cutoff, and C-Mod's LHCD frequencies versus major radius for an AT, H-mode target plasma.

and field are taken from an AT target plasma, shot 1030530014, with 5.4 T field on axis and a low density H-mode density profile. C-Mod is a high field and high density machine and these parameters give an the electron cyclotron frequency of order the plasma frequency in the core region with ω_{ce} dominating at the edge, outside of the pedestal region, as the density falls rapidly. In fact, as the density is quite low and ω_{ce} is becoming less negative, the lower cutoff frequency actually increases slightly near the edge. An important point from Figure 2-2 is that C-Mod's LHCD system operates well above the lower hybrid resonance

frequency. The current drive wave damps on fast electrons through Landau damping once electron thermal effects are included into the plasma model. The LH resonance is a cold plasma effect where the denominator of the dispersion relation goes to zero causing $n_\perp^2$ to go to infinity. Once ion temperature effects are included in the model the resonance is replaced by linear mode conversion to the ion-plasma wave which mostly heats ions and does not drive current. In practice, however, this does not occur as the wave will undergo a parametric decay instability before reaching the density required for mode conversion[56].

In any event, the left hand cutoff blocks access to both the resonance and the current drive wave. For all practical purposes there isn't a way to couple to the wave by using pure X-mode. The solution to this problem is to use the full nature of the dispersion relation by adding a small component of the wave number in the parallel direction, that is $n_\parallel$.

The dispersion relation is solved for values of $n_\perp^2$. The wave $n_\perp$ can be either positive or negative, with the sign just giving the direction of the propagation. This means that $n_\perp^2$ must be positive for propagation. If $n_\perp^2$ is negative, there is an imaginary component of $\overline{k}$, the wave number. Writing $\overline{k} = \overline{k}_r + \overline{k}_i$, in terms of real and imaginary components, the electric field of a traveling wave would have the form of

$$\overline{E} \sim e^{i\overline{k}\cdot\overline{r}} = e^{i\overline{k}_r\cdot\overline{r}}e^{-\overline{k}_i\cdot\overline{r}}.$$

For $\overline{k}_i \neq 0$ there is a decaying (or growing) wave.

Returning to the cold plasma dispersion relation, $D(\omega, \overline{k})$ is bi-quadratic so the quadratic formula may be used to examine the roots and determine when there is an imaginary part of $\overline{k}$.

$$n_\perp^2 = \frac{-C_2 \pm \sqrt{C_2^2 - 4C_4C_0}}{2C_4} \tag{2.20}$$

$$n_\perp = \pm\sqrt{\frac{-C_2 \pm \sqrt{C_2^2 - 4C_4C_0}}{2C_4}} \tag{2.21}$$

For propagating waves the condition of the coefficients is $C_2 \leq -2\sqrt{C_4C_0}$. This is seen graphically in Figure 2-3. The dispersion relation is solved for values of $n_\perp^2$ for a given density and constant magnetic field of 5.4 T. In this case the frequency used is 1.5 GHz to illustrate what happens when the LH resonance exists inside the plasma. Two roots of the dispersion relation exist, a slow and a fast wave, and are characterized by small and large values of perpendicular phase velocity, $\omega/k_\perp$. The slow wave is electrostatic and the fast wave is electromagnetic. Both waves require plasma to propagate. The slow wave is plotted in green and is the root with the lower hybrid resonance while the fast wave is plotted in blue. The imaginary components of the roots are plotted in red. When the magnitude of the imaginary part is non-zero the wave is cutoff and reflects. Negative solutions are also evanescent. The three panels show what happens to the roots as $n_\parallel$ is varied. In the top panel the wave is cutoff in the region where the imaginary part of the dispersion relation is non-zero. A wave launched from low density as a slow wave will hit the cutoff and be reflected back as a fast wave, the fast wave will then be reflected off a $n_\perp = 0$ surface and travel back inside and again be mode converted back into the slow wave and this process will continue. In the middle panel the two roots barely touch and the slow wave becomes accessible to all densities. In the bottom panel, above the critical $n_\parallel$, the roots are well separated and accessible. The density profile of a real plasma peaks near the center and

CPDR Roots vs Density
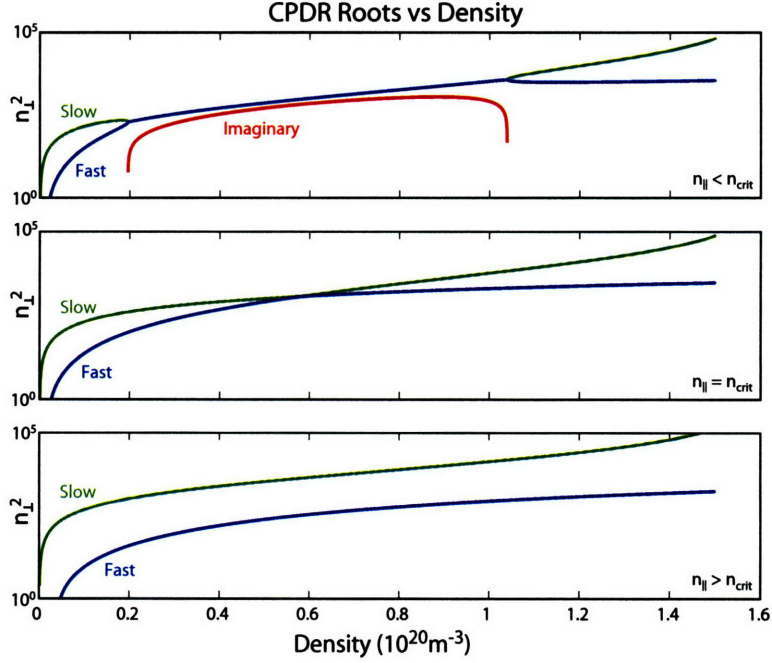
Figure 2-3: Plots of $n_\perp^2$ vs density with varying $n_\parallel$. Top panel, $n_\parallel = 1.2$, middle panel $n_\parallel = 1.25$, and bottom panel $n_\parallel = 1.5$. Other parameters of interest are linear density and constant magnetic field of 5.4 T, with a launch frequency of 1.5 GHz.

decreases on both the high and low field sides, this produces a LH resonance on both sides which is slightly asymmetric from the $1/R$ dependance of the magnetic field.

As pointed out earlier the current drive mechanism is not related to the lower hybrid resonance. In fact it has been experimentally observed that efficient LHCD occurs for $\omega/\omega_{lh} > 2$[57]. If this condition is not met the wave energy is absorbed nonlinearly by the ions rather than the electrons[14]. Figure 2-4 plots the accessibility against major radius for an AT target plasma developed for current drive. The plasma conditions are the same as in Figure 2-2, and include the field and density variations. The results are similar in nature to Figure 2-3, with waves propagating from the low field side. Accessibility to either the LH resonance, or simply the plasma center, as in the current drive case, clearly depends on the value of $n_\parallel$. This is known as the accessibility condition, which is $C_2 \leq -2\sqrt{C_4 C_0}$, and can be written in a more useful form by considering the ordering of the dielectric terms.

$\epsilon_\perp$, $\epsilon_\parallel$, and $\epsilon_\times$ can be written in terms of n/n_0, where n_0 is the resonant density(where $\epsilon_\perp \to 0$). Again using the lower hybrid limit

$$\epsilon_\perp \approx 1 - \frac{\omega_{pi}^2}{\omega^2} + \frac{\omega_{pe}^2}{\omega_{ce}^2}$$

and taking $\epsilon_\perp = 0$ and $\frac{n}{n_0} = 1$ the above expression may be rewritten as

$$1 = \frac{n}{n_0} = \frac{\omega_{pi}^2}{\omega}(1 - \frac{\omega^2}{\omega_{ce}\omega_{ci}}).$$

39
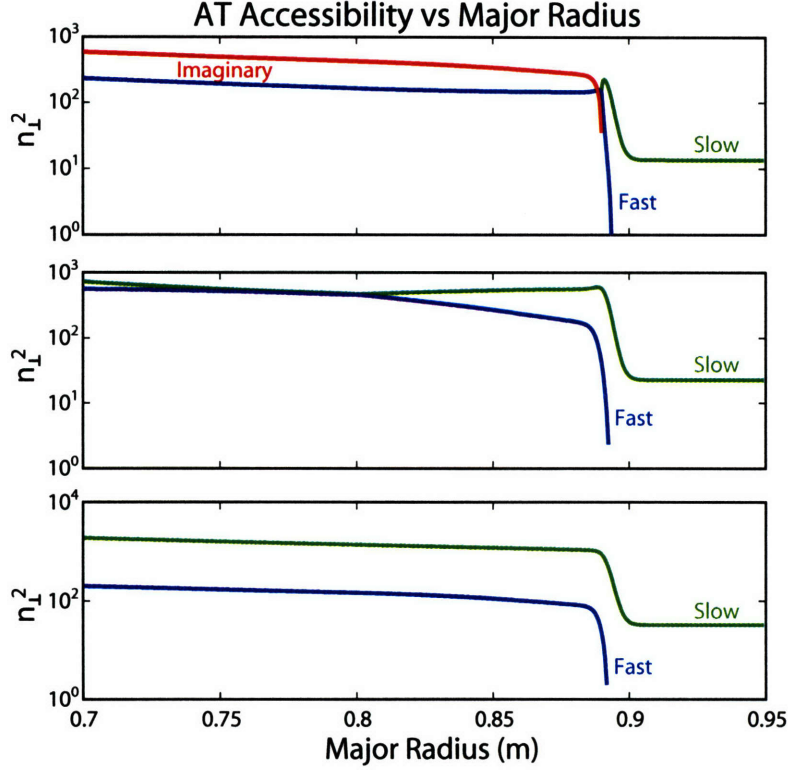
Figure 2-4: Cold plasma roots showing the accessibility of lower hybrid waves with varying $n_\parallel$ as a function of major radius. Plots include actual density profile and magnetic field from AT target plasma.

The result is

$$\epsilon_\perp = 1 - \frac{n}{n_0} \sim O(1).$$

From equation 2.12

$$\epsilon_\times = \frac{\omega_{pi}^2}{\omega_{ci}} \left(\frac{\omega}{\omega^2 - \omega_{ci}^2} - \frac{\omega}{\omega^2 - \omega_{ce}^2} \right) \approx \frac{\omega_{pi}^2}{\omega_{ci}} \left(\frac{1}{\omega} + \frac{\omega}{\omega_{ce}^2} \right) \approx \frac{\omega_{pi}^2}{\omega_{ci}} \frac{1}{\omega}.$$

Substituting in

$$\omega_{pi}^2 = \frac{n}{n_0} \left(\frac{\omega^2}{1 - \frac{\omega^2}{\omega_{ce}\omega_{ci}}} \right) \text{ and multiplying by } \sqrt{\frac{m_e}{m_i}} \text{ gives}$$

$$\epsilon_\times = \sqrt{\frac{m_i}{m_e}} \frac{n}{n_0} \left(\frac{\frac{\omega}{\sqrt{\omega_{ce}\omega_{ci}}}}{1 - \frac{\omega^2}{\omega_{ce}\omega_{ci}}} \right) \sim O\left(\sqrt{\frac{m_i}{m_e}} \right).$$

$$\epsilon_\parallel = 1 - \frac{\omega_{pi}^2}{\omega^2} - \frac{\omega_{pe}^2}{\omega^2} \approx -\frac{\omega_{pe}^2}{\omega^2} = -\frac{m_i}{m_e} \frac{n}{n_0} \left(\frac{1}{1 - \frac{\omega^2}{\omega_{ce}\omega_{ci}}} \right) \sim O\left(\frac{m_i}{m_e} \right)$$

40

Given the ordering of these coefficients, $D(\omega, \bar{k})$ may be written as

$$
\begin{aligned}
C_4 &= \epsilon_\perp \\
C_2 &= \epsilon_\parallel(n_\parallel^2 - \epsilon_\perp) + \epsilon_x^2 \\
C_0 &= -\epsilon_\parallel \epsilon_x^2.
\end{aligned}
$$

Noting that $\epsilon_\parallel$ is a negative quantity, the access condition can be written as

$$
\begin{aligned}
C_2 \le -2\sqrt{C_4 C_0} = \quad & \epsilon_\parallel(n_\parallel^2 - \epsilon_\perp) + \epsilon_x^2 \le -2\sqrt{\epsilon_\perp |\epsilon_\parallel| \epsilon_x^2} \\
= \quad & n_\parallel^2 \ge \epsilon_\perp + \frac{\epsilon_x^2}{|\epsilon_\parallel|} + 2\sqrt{\frac{\epsilon_\perp \epsilon_x^2}{|\epsilon_\parallel|}} \\
= \quad & n_\parallel \ge \sqrt{\epsilon_\perp} + \sqrt{\frac{\epsilon_x^2}{|\epsilon_\parallel|}}.
\end{aligned}
$$

This condition may be written in terms of frequencies by using the dielectric elements evaluated in the lower hybrid range of frequencies.

$$
n_\parallel \ge \sqrt{1 - \frac{\omega_{pi}^2}{\omega^2} + \frac{\omega_{pe}^2}{\omega_{ce}^2}} + \frac{\omega_{pe}}{|\omega_{ce}|} \tag{2.22}
$$

This is a local condition, since the quantities above depend on values of density and magnetic field. An upper bound is given by evaluating at the maximum density and the field at the maximum density. This expression can be used to find the edge density needed to launch a given value of $n_\parallel$, or to ensure that the wave is accessible throughout the plasma. Figure 2-5 plots the contours of the critical value of $n_\parallel$, that is the minimum accessible value, given the local density and magnetic field. Examining Figure 2-5 it is clear that an $n_\parallel$ above 2 is needed to reach the magnetic axis of a typical high density C-Mod discharge.

2.3   LH Wave Launching

The local value of $n_\parallel$ is the most important parameter for LH waves as it determines the accessibility and the damping location. Even though the wave may evolve in $n_\parallel$ as it propagates, it is largely determined by the initial value as set by the launching structure. The lower hybrid launcher, or "grill", is actually a phased array antenna. By controlling the phase difference between a number of adjacent structures, waveguides in the case of lower hybrid, the wave power may be directed in a given direction. The geometry of the antenna as well as the phasing between waveguides fixes the $n_\parallel$ spectrum. Only a simple picture is needed to calculate the primary peek in the spectrum. Begin by assuming that the $n_\parallel$ peak has the form of

$$
n_{\parallel peak}(\Delta\phi) = n_{\parallel max}\frac{\Delta\phi}{180^\circ},
$$

where $\Delta\phi$ is the change in phase from waveguide to waveguide in degrees and $n_{\parallel max}$ is the maximum $n_\parallel$ capable of being produced by the antenna structure. $n_{\parallel max}$ is given by the shortest parallel wavelength, λ_{min}, possible which occurs for 180°; at 180° it takes two waveguides to complete one wavelength. So the wavelength may be written in terms of
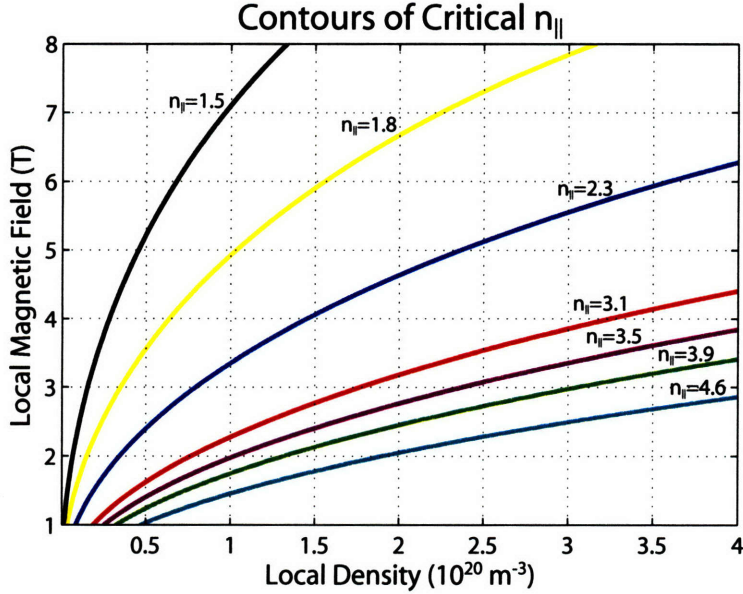
Figure 2-5: Contours of critical $n_\parallel$ for f=4.6 GHz against the local density and local magnetic field. Values of $n_\parallel$ plotted correspond to spectral peaks produced by C-Mod's grill for different phase progressions.

the system geometry, the waveguide channel width, L and the septum thickness, Δ, giving $\lambda_{min} = 2L + 2\Delta$. This allows the spectral peak location to be written as

$$n_{\parallel peak}(\Delta\phi) = \frac{c}{2f(L+\Delta)}\frac{\Delta\phi}{180°}. \tag{2.23}$$

with c being the speed of light and f the frequency. For C-Mod $L = 5.5$ mm and $\Delta = 1.5$ mm, which gives

$$n_{\parallel peak}(\Delta\phi) = 4.66\frac{\Delta\phi}{180°}.$$

The simple picture above is useful for quick estimations, but insufficient for detailed analysis. There are two more levels of complexity that are useful, the first takes into account the complete grill structure and allows the calculation of higher order modes. This is done through Fourier analysis, the second includes the plasma which is useful for determining the correct power fractions of the spectral peaks and the reflection coefficients, this model is presented in Chapter 7.

A simple Fourier analysis of the electric field in the grill gives the relation between $k_\parallel$ and the phase of the waveguides as well as the power spectrum. Figure 2-6 graphically represents the problem. The electric field is modeled simplistically as N box functions, $E_n(z)$, with amplitude E_0 and phase ϕ_n.

$$E_n(z) = \begin{cases} E_0 e^{i\phi_n} & \text{if } (n-1)L + n\Delta < z < n(L+\Delta); \ n = 1, 2\ldots, N \\ 0 & \text{otherwise.} \end{cases}$$

L is the width of the electric field, or which is the waveguide opening width. A septum of width Δ separates the electric fields. ϕ_n represents an arbitrary phase on the nth waveguide.

42
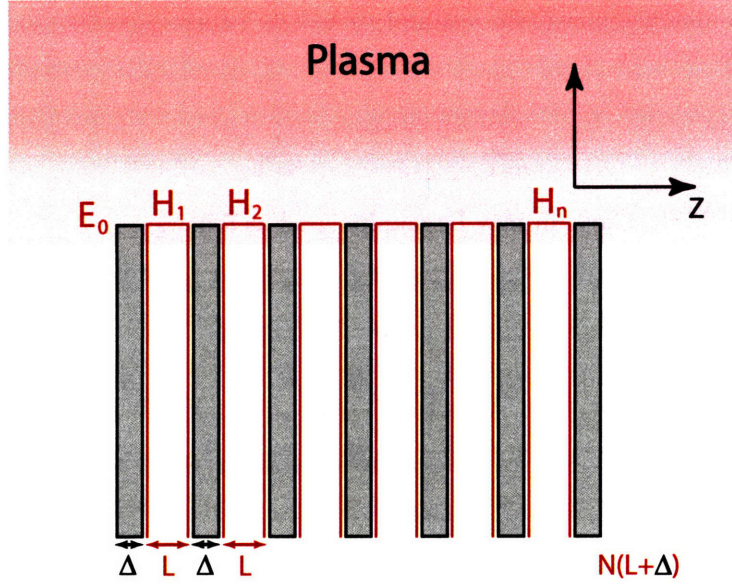
Figure 2-6: A simple model of the launch structure for N waveguides

The C-Mod antenna has 22 waveguides of width 5.5 mm and a septum of 1.5 mm. In real space the total antenna electric field is just the sum of the box functions,

$$E_z(z) = \sum_{n=1}^{N} E_n(z).$$

In k-space the electric field becomes

$$E_z(k) = \sum_{n=1}^{N} \int_{(n-1)L+n\Delta}^{n(L+\Delta)} E_0 e^{i\phi_n} e^{ikz} dz.$$

Performing the integration gives

$$E_z(k) = \frac{E_0}{ik} \sum_{n=1}^{N} e^{i(kz+\phi_n)} \Big|_{(n-1)L+n\Delta}^{n(L+\Delta)},$$

which can be rewritten as

$$E_z(k) = \frac{E_0}{ik} \sum_{n=1}^{N} e^{i(knL+kn\Delta+\phi_n)} \left(1 - e^{-ikL}\right).$$

$1 - e^{-ikL}$ is a sine function with argument $kL/2$ multiplied by a phase factor, $2ie^{-ikL/2}$. Putting this back into $E_z(k)$ gives an expression for the electric field with an arbitrary phase that can be quickly evaluated numerically to get the spectrum,

$$E_z(k) = \frac{2E_0}{k} \sin\left(\frac{kL}{2}\right) e^{-i\frac{kL}{2}} \sum_{n=1}^{N} e^{i(knL+kn\Delta+\phi_n)}. \tag{2.24}$$

43

To continue to get an analytic expression, assume that the phase varies as $n\phi$, where ϕ is the initial and difference phase. For example if $\phi = 90°$, then $\phi_n = 90, 180, 270, 0, etc.$ The sum may now be written as

$$\sum_{n=1}^{N} e^{in(kL+k\Delta+\phi)} = \sum_{n=1}^{N} x^n,$$

where $x = e^{i(kL+k\Delta+\phi)}$. The sum may be manipulated as follows:

$$
\begin{aligned}
\left(x + x^2 + \ldots + x^N\right) &= x(1 + x + x^2 + \ldots + x^{N-1} + x^N + x^{N+1} + \ldots + x^\infty \\
&\quad - x^N - x^{N+1} - \ldots - x^\infty) \\
&= x\left(\frac{1}{1-x} - x^N - x^{N+1} - \ldots - x^\infty\right) \\
&= x\left(\frac{1}{1-x} - x^N\left(1 + x + x^2 + \ldots + x^\infty\right)\right) \\
&= \frac{x(1 - x^N)}{1-x}.
\end{aligned}
$$

Substituting back in for x and letting $\psi = kl + k\Delta + \phi$ gives

$$e^{i\psi}\frac{1 - e^{iN\psi}}{1 - e^{i\psi}} = e^{i(N+1)\frac{\psi}{2}}\frac{\sin\left(N\frac{\psi}{2}\right)}{\sin\left(\frac{\psi}{2}\right)}$$

Using this result to write the electric field now becomes

$$E_z(k) = \frac{2E_0}{k}\sin\left(\frac{kL}{2}\right)\frac{\sin\left(N\frac{kL+k\Delta+\phi}{2}\right)}{\sin\left(\frac{kL+k\Delta+\phi}{2}\right)}e^{i\frac{1}{2}(NkL+(N+1)k\Delta+(N+1)\phi)}.$$

The radiated power from the grill is proportional to $E \cdot E^*$, which is

$$P_z(k) = \frac{4E_0^2}{k^2}\sin^2\left(\frac{kL}{2}\right)\frac{\sin^2\left(N\frac{kL+k\Delta+\phi}{2}\right)}{\sin^2\left(\frac{kL+k\Delta+\phi}{2}\right)}. \tag{2.25}$$

This gives the power spectrum in terms of $n_\parallel$ by multiplying by a constant. Figure 2-7 plots power in arbitrary units against $n_\parallel$ for a given phase between the waveguides. The power has been normalized to the amplitude of the largest peak, which corresponds to 60° phasing. Not all the power is launched in the forward direction. Negative lobes of the spectrum exist at a higher value of $n_\parallel$ and will drive some current, albeit small and inefficient, in the opposite direction as the main current drive. For a phasing of 60° about 70% of the power is in one direction. The negative spectrum is shown in Figure 2-8. As the phase angle is increased the directionality goes down until there is equal power in each direction; this occurs at 180°. No net current is driven with 180° phasing since equal current is driven in both directions. 180° phasing can be used for heating the plasma for experiments where no current is desired. Higher harmonics also exist, but contain little power since the power goes as $1/k^2$. The spectrum is quite robust to changes in phase from waveguide to waveguide. A random variation of 10° does not significantly impact the spectrum. Using less than 24 waveguides broadens the spectral peaks. Going from 16 to 24 waveguides the FWHM of the primary lobe decreases the width from 0.53 to 0.35.
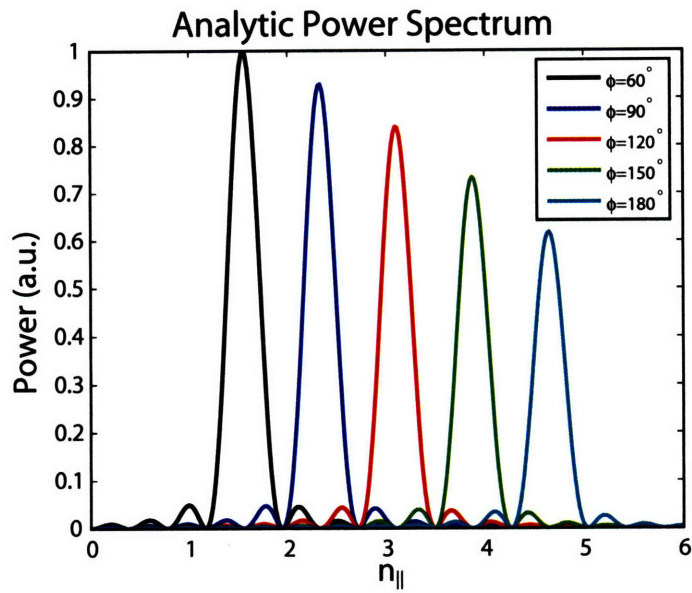
Figure 2-7: Analytic $n_\parallel$ power spectrum for C-Mod's antenna parameters with varying phase. The parallel index of refraction is $n_\parallel = ck_\parallel/\omega$.
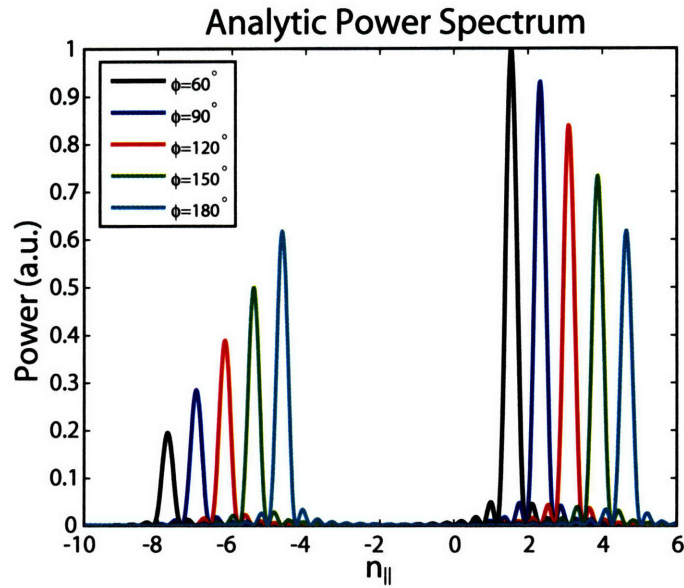
Figure 2-8: The presence of counter current drive lobes in the $n_\parallel$ spectrum decrease overall power available for current drive.

2.4 Ray Tracing

The $n_\parallel$ spectrum from the grill provides initial conditions necessary to follow the wave trajectory in the plasma. The goal is to find how the group velocity and wave number change as the wave propagates given the initial conditions. These relationships are known as the ray equations. A ray is a curve which is tangent to the direction of wave propagation at every point. The ray neglects the wave properties of the wave and is basically the $\lambda \to 0$ limit of the wave. This limit is valid on scales where the wavelength is much smaller than the typical scale length variations in the plasma. That is

$$\lambda \left(\frac{1}{\overline{\overline{\mathbf{B}}}} \nabla \overline{\mathbf{B}} \right) \ll 1, \text{ and } \lambda \left(\frac{1}{n} \nabla n \right) \ll 1.$$

Now that the range of validity for using ray approximations has been established, the ray equations can be derived as follows. In general the phase dependence of the wave electric field goes as $e^{i\phi}$, where $\phi = \overline{k} \cdot \overline{r} - \omega t + \phi_0$ is the total phase, and ϕ is also known as the eikonal. In general $\overline{k} = \overline{k}(\overline{r}, t)$ and $\omega = \omega(\overline{r}, t)$ A relationship between $\overline{k}$ and ω may be found by examining the derivatives of ϕ.

$$\left. \frac{\partial \phi}{\partial \overline{r}} \right|_{\omega,\overline{k}} = \nabla \phi = \overline{k}, \text{ and } \left. \frac{\partial \phi}{\partial t} \right|_{\omega,\overline{k}} = -\omega$$

An important note is that $\overline{k}$ can be written as the gradient of the phase. This means that $\nabla \times \overline{k} = 0$, that is $\overline{k}$ is irrotational. This will later become important in writing the ray equations in toroidal geometry. As long as ϕ is continuous then

$$\frac{\partial^2 \phi}{\partial \overline{r} \partial t} = \frac{\partial^2 \phi}{\partial t \partial \overline{r}}$$

and so

$$\left. \frac{\partial \overline{k}}{\partial t} \right|_{\overline{r}} = - \left. \frac{\partial \omega}{\partial \overline{r}} \right|_t . \tag{2.26}$$

So far nothing has been mentioned about how the plasma changes the phase, these effects are included by using the local dispersion relation.

$$D \left(\omega, \overline{k}, \overline{r}, t \right) = 0 \tag{2.27}$$

The dispersion relation is in general a function of frequency, wavenumber, position, time, and must have the right hand side equal to zero to satisfy the eigenvalue problem for the electric field. Since $D \left(\omega, \overline{k}, \overline{r}, t \right)$ must be zero the incremental change in D must also be zero[58], so

$$dD = \frac{\partial D}{\partial \omega} d\omega + \frac{\partial D}{\partial \overline{k}} \cdot d\overline{k} + \frac{\partial D}{\partial \overline{r}} \cdot d\overline{r} + \frac{\partial D}{\partial t} dt = 0. \tag{2.28}$$

Using $dD = 0$ while holding certain variables constant gives rise to the following relationships:

$$dD|_{\overline{k},\overline{r}} = \frac{\partial D}{\partial \omega} d\omega + \frac{\partial D}{\partial t} dt = 0 \quad \to \quad \left. \frac{\partial \omega}{\partial t} \right|_{\overline{k},\overline{r}} = \frac{-\partial D/\partial t}{\partial D/\partial \omega} \tag{2.29}$$

$$dD|_{\overline{k},t} = \frac{\partial D}{\partial \omega} d\omega + \frac{\partial D}{\partial \overline{r}} \cdot d\overline{r} = 0 \quad \to \quad \left. \frac{\partial \omega}{\partial \overline{r}} \right|_{\overline{k},\overline{r}} = \frac{-\partial D/\partial \overline{r}}{\partial D/\partial \omega} \tag{2.30}$$

$$dD|_{\overline{r},t} = \frac{\partial D}{\partial \omega} d\omega + \frac{\partial D}{\partial \overline{k}} \cdot d\overline{k} = 0 \quad \to \quad \left. \frac{\partial \omega}{\partial \overline{k}} \right|_{\overline{r},t} = v_g = \frac{-\partial D/\partial \overline{k}}{\partial D/\partial \omega} \equiv \frac{d\overline{r}}{dt}. \tag{2.31}$$

The last equation above is known as the group velocity equation and is the first ray equation. $D\left(\omega, \overline{k}, \overline{r}, t\right) = 0$ may be solved in terms of ω to give

$$\omega\left(\overline{k}\left(\overline{r}, t\right), \overline{r}, t\right) = 0.$$

Using the multivariable chain rule yields

$$\frac{\partial \omega}{\partial \overline{r}}\bigg|_t = \frac{\partial \omega}{\partial \overline{k}} \cdot \frac{\partial \overline{k}}{\partial \overline{r}}\bigg|_t + \frac{\partial \omega}{\partial \overline{r}}\bigg|_{\overline{k},t} = v_g \cdot \frac{\partial \overline{k}}{\partial \overline{r}}\bigg|_t + \frac{\partial \omega}{\partial \overline{r}}\bigg|_{\overline{k},t} \tag{2.32}$$

$$\frac{\partial \omega}{\partial t}\bigg|_{\overline{r}} = \frac{\partial \omega}{\partial \overline{k}} \cdot \frac{\partial \overline{k}}{\partial t}\bigg|_{\overline{r}} + \frac{\partial \omega}{\partial t}\bigg|_{\overline{k},\overline{r}} = v_g \cdot \frac{\partial \overline{k}}{\partial t}\bigg|_t + \frac{\partial \omega}{\partial t}\bigg|_{\overline{k},\overline{r}}. \tag{2.33}$$

Note that $\partial \overline{k}/\partial \overline{r}$ is a tensor quantity. The derivatives on the LHS can be substituted using the derivatives of the phase to give

$$-\frac{\partial \overline{k}}{\partial t}\bigg|_{\overline{r}} = v_g \cdot \frac{\partial \overline{k}}{\partial \overline{r}}\bigg|_t + \frac{\partial \omega}{\partial \overline{r}}\bigg|_{\overline{k},t} \tag{2.34}$$

$$\frac{\partial \omega}{\partial t}\bigg|_{\overline{r}} = -v_g \cdot \frac{\partial \omega}{\partial \overline{r}}\bigg|_t + \frac{\partial \omega}{\partial t}\bigg|_{\overline{k},\overline{r}}. \tag{2.35}$$

The last term on the RHS is given by the $dD = 0$ relations, so plugging in gives

$$\frac{\partial \overline{k}}{\partial t}\bigg|_{\overline{r}} + v_g \cdot \frac{\partial \overline{k}}{\partial \overline{r}}\bigg|_t = \frac{\partial D/\partial \overline{r}}{\partial D/\partial \omega} \tag{2.36}$$

$$\frac{\partial \omega}{\partial t}\bigg|_{\overline{r}} + v_g \cdot \frac{\partial \omega}{\partial \overline{r}}\bigg|_t = \frac{-\partial D/\partial t}{\partial D/\partial \omega}. \tag{2.37}$$

By inspection the LHS of the equations are just the total derivatives for $\overline{k}$ and ω, so finally the three ray equations are

$$\frac{d\overline{r}}{dt} = \frac{-\partial D/\partial \overline{k}}{\partial D/\partial \omega} \tag{2.38}$$

$$\frac{d\overline{k}}{dt} = \frac{\partial D/\partial \overline{r}}{\partial D/\partial \omega} \tag{2.39}$$

$$\frac{d\omega}{dt} = \frac{-\partial D/\partial t}{\partial D/\partial \omega}. \tag{2.40}$$

In most cases ω is fixed by the frequency source, meaning $\partial D/\partial t = 0$, and so the ray equations reduce to a total of six equations that can then be written into geometry specific forms. The conventional coordinate system for tokamaks is toroidal coordinates. $\nabla \times \overline{k} = 0$ can be used to express $\overline{k}$ in a natural way[59]. Figure 2-9 below shows the toroidal coordinate system. The general method for coordinate transformation proceeds as follows[60]. Express the new coordinate system in terms of the old:

$$\begin{aligned}
x &= x\left(u_1, u_2, u_3\right) = x\left(r, \theta, \phi\right) = R\sin\phi = R_0\sin\phi + r\cos\theta\sin\phi, \\
y &= y\left(u_1, u_2, u_3\right) = y\left(r, \theta, \phi\right) = r\sin\theta, \\
z &= z\left(u_1, u_2, u_3\right) = z\left(r, \theta, \phi\right) = R\cos\phi = R_0\cos\phi + r\cos\theta\cos\phi,
\end{aligned}$$
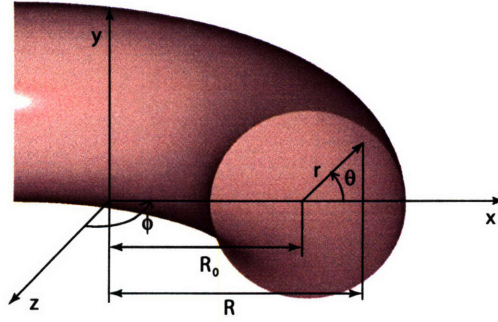
Figure 2-9: Toroidal Geometry

where u_1, u_2, u_3 are the new coordinates. A position vector $\bar{p}$ is given by

$$\bar{p} = x\hat{x} + y\hat{y} + z\hat{z} = (R_0 \sin\phi + r\cos\theta\sin\phi)\,\hat{x} + r\sin\theta\hat{y} + (R_0\cos\phi + r\cos\theta\cos\phi)\,\hat{z}.$$

The key lies in constructing tangent vectors in the new coordinate system to that of the old, giving

$$\frac{\partial\bar{p}}{\partial u_1} = h_1\hat{e}_1 \quad\rightarrow\quad \frac{\partial\bar{p}}{\partial r} = h_1\hat{r}$$

$$\frac{\partial\bar{p}}{\partial u_2} = h_2\hat{e}_2 \quad\rightarrow\quad \frac{\partial\bar{p}}{\partial\theta} = h_2\hat{\theta}$$

$$\frac{\partial\bar{p}}{\partial u_3} = h_3\hat{e}_3 \quad\rightarrow\quad \frac{\partial\bar{p}}{\partial\phi} = h_3\hat{\phi}.$$

Here $\hat{e}_1, \hat{e}_2, \hat{e}_3$ are unit vectors and h_1, h_2, h_3 are the scale factors of the transformation.

$$\frac{\partial\bar{p}}{\partial r} = \cos\theta\sin\phi\hat{x} + \sin\theta\hat{y} + \cos\theta\cos\phi\hat{z} \rightarrow h_1 = 1, \hat{r} = \cos\theta\sin\phi\hat{x} + \sin\theta\hat{y} + \cos\theta\cos\phi\hat{z}$$

$$\frac{\partial\bar{p}}{\partial\theta} = r\left(-\sin\theta\sin\phi\hat{x} + \cos\theta\hat{y} - \sin\theta\cos\phi\hat{z}\right)$$

$$\rightarrow \quad h_2 = r, \hat{\theta} = -\sin\theta\sin\phi\hat{x} + \cos\theta\hat{y} - \sin\theta\cos\phi\hat{z}$$

$$\frac{\partial\bar{p}}{\partial\phi} = R\left(\cos\phi\hat{x} - \sin\phi\hat{z}\right) \rightarrow h_3 = R, \hat{\theta} = \cos\phi\hat{x} - \sin\phi\hat{z}$$

The unit vectors may be checked for magnitude and orthogonality by taking $\hat{u}_i \cdot \hat{u}_i = 1$ and $\hat{u}_i \cdot \hat{u}_j = 0$. Now the curl of $\bar{k} = 0$ may be constructed. In general

$$\nabla \times \bar{k} = \frac{1}{h_1 h_2 h_3} \begin{vmatrix} h_1\hat{e}_1 & h_2\hat{e}_2 & h3\hat{e}_3 \\ \dfrac{\partial}{\partial u_1} & \dfrac{\partial}{\partial u_2} & \dfrac{\partial}{\partial u_3} \\ h_1 k_1 & h_2 k_2 & h_3 k_3 \end{vmatrix} = \frac{1}{rR} \begin{vmatrix} \hat{r} & r\hat{\theta} & R\hat{\phi} \\ \dfrac{\partial}{\partial k_r} & \dfrac{\partial}{\partial k_\theta} & \dfrac{\partial}{\partial k_\phi} \\ k_r & r k_\theta & R k_\phi \end{vmatrix}. \tag{2.41}$$

Looking component by component

$$\hat{r}: \quad = \frac{1}{rR}\left\{\frac{\partial}{\partial\theta}\left(Rk_\phi\right) - \frac{\partial}{\partial\phi}\left(rk_\theta\right)\right\} = 0 \tag{2.42}$$

48

$$\hat{\theta}: \quad = \frac{1}{R}\left\{ \frac{\partial}{\partial\phi}\left(k_r\right) - \frac{\partial}{\partial r}\left(Rk_\phi\right)\right\} = 0 \tag{2.43}$$

$$\hat{\phi}: \quad = \frac{1}{r}\left\{ \frac{\partial}{\partial r}\left(rk_\theta\right) - \frac{\partial}{\partial\theta}\left(k_r\right)\right\} = 0 \tag{2.44}$$

and using toroidal, ϕ, symmetry the quantity Rk_ϕ is constant in both $\hat{r}$ and $\hat{\theta}$. Rk_ϕ is known as the toroidal mode number, n. The quantity rk_θ also appears naturally and is defined as the poloidal mode number, m. This quantity varies due to poloidal asymmetry. The ray equations may be written in toroidal geometry by letting the generic position vector $\bar{r} = (r, \theta, \phi)$ and the generic wave number, $\bar{k} = (k_r, m, n)$. The result is

$$\frac{dr}{dt} = \frac{-\partial D/\partial k_r}{\partial D/\partial\omega}, \quad \frac{dk_r}{dt} = \frac{\partial D/\partial r}{\partial D/\partial\omega}$$

$$\frac{d\theta}{dt} = \frac{-\partial D/\partial m}{\partial D/\partial\omega}, \quad \frac{dm}{dt} = \frac{\partial D/\partial\theta}{\partial D/\partial\omega}$$

$$\frac{d\phi}{dt} = \frac{-\partial D/\partial n}{\partial D/\partial\omega}, \quad \frac{dn}{dt} = \frac{\partial D/\partial\phi}{\partial D/\partial\omega} = 0.$$

The parameter that determines the location of damping and accessibility is $n_\parallel$, that is $k_\parallel$. The magnetic field within a tokamak can be described by

$$\bar{B} = B_r(r,\theta)\hat{r} + B_\theta(r,\theta)\hat{\theta} + B_\phi(r,\theta)\hat{\phi}.$$

The parallel wave number is then

$$k_\parallel = \bar{k} \cdot \bar{B}/|B| = \left(k_r B_r + \frac{m}{r}B_\theta + \frac{n}{R}B_\phi\right)/|B|. \tag{2.45}$$

This means that as m and B_θ vary the parallel wave number will change! This makes the location of cutoff and resonance layers impossible to predict without the use of ray tracing. For current drive, which modifies the poloidal field the calculation of ray propagation, absorption, and current needs to be done self consistently. A number of codes have been developed over the years to model this such as ACCOME[61], CQL3D[62], DKE/CRONOS[63], and LSC[64]. Figure 2-10 shows the ray trajectories given for different poloidal launch points from ACCOME.

2.5 Hot Plasma Dispersion Relation

Introducing temperature effects into the dispersion relation is critical for calculating any damping that may be present. Landau damping is a finite temperature effect in which cold plasma models are not applicable for study. The inclusion of temperature manifests itself as an imaginary part of the dispersion relation which gives the damping. The imaginary part arises from a pole at $\omega = k_\parallel v_\parallel$, that is when the electron thermal speed matches the phase velocity of the wave. This is to be distinguished from the imaginary parts of the roots which lead to evanescence and reflection plotted in Figures 2-3 and 2-11. The hot plasma dispersion relation derivation is similar to the cold plasma case, but now requires the current to be the first moment of the distribution function, that is

$$\bar{J} = ne\left(\int \bar{v}f_i(v)d\bar{v} - \int \bar{v}f_e(v)d\bar{v}\right). \tag{2.46}$$
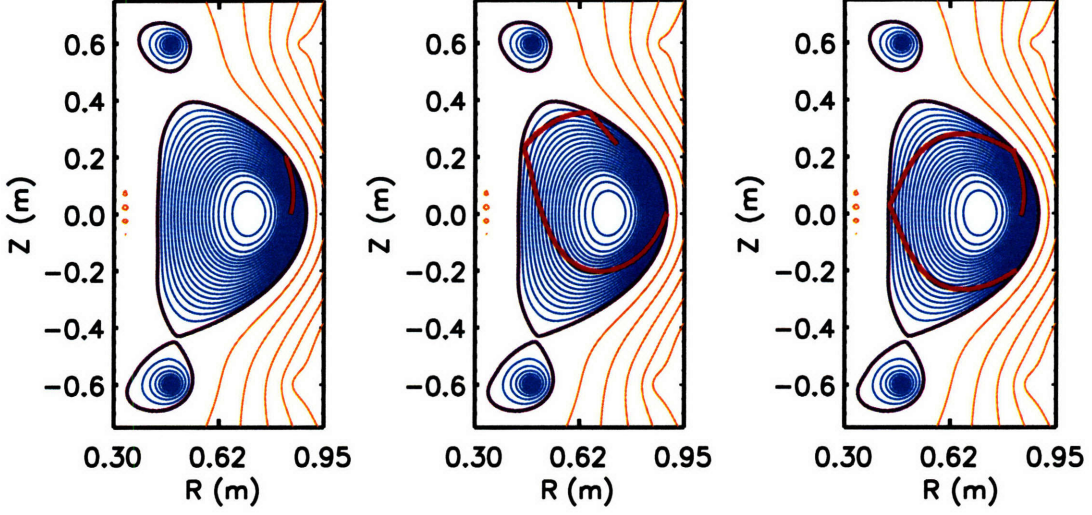
Figure 2-10: C-Mod poloidal cross section with ray trajectories from different poloidal launch points using ACCOME. Plots courtesy of P. Bonoli.

The key is to find a representation of the distribution function that is modified by the current drive. The simplest starting point is to take the linearized Vlasov equation and look for first order corrections to a Maxwellian distribution, $f = f_0 + f_1$,

$$\frac{\partial}{\partial t} f_{1\alpha} + \overline{v} \cdot \nabla f_{1\alpha} + \frac{q_\alpha}{m_\alpha} \overline{v} \times \overline{\mathrm{B}}_0 \cdot \nabla_v f_{1\alpha} = \frac{q_\alpha}{m_\alpha} \left(\mathrm{E}_1 + \overline{v} \times \overline{\mathrm{B}}_1 \right) \cdot \nabla_v f_{0\alpha}, \qquad (2.47)$$

where α is again the particle species. More specifically $f_{0\alpha}$ is

$$\frac{1}{(2\pi)^{3/2} v_\alpha^3} \exp\left(-\frac{v_\perp^2 + v_\parallel^2}{2v_\alpha^2} \right),$$

with $v_\alpha = (T_\alpha/m_\alpha)^{1/2}$. This partial differential equation can be solved by the method of characteristics, or by integrating particle orbits along $\overline{\mathrm{B}}_0$[65]. This is then used to derive the full dispersion matrix. For lower hybrid waves, there exists a simple limit[66], where the dispersion relation may be broken into real and imaginary parts, $D(\omega, \overline{k}) = D_r + iD_i$. Here, $D_i = D_i^e + D_i^i$, with contributions from the electrons and ions. The real part may be written as a polynomial similar to the cold plasma expression,

$$D_r(\omega, \overline{k}) = C_6 n_\perp^6 + C_4 n_\perp^4 + C_2 n_\perp^2 + C_0, \qquad (2.48)$$

where all the hot plasma effects are included in the sixth order term in $n_\perp$.

$$C_6 = -3 \frac{\omega_{pi}^2 v_{thi}}{\omega^2 c^2} - \frac{3\omega_{pe}^2 \omega^2 v_{the}}{4\omega_{ce}^4 c^2}, \qquad (2.49)$$

and C_4, C_2, and C_0 are the coefficients given by the cold plasma dispersion relation. v_{the} and v_{thi} are the electron and ion thermal velocities. The imaginary parts are

$$D_i^{(e)} = 2\sqrt{\pi} \frac{\omega_{pe}^2}{\omega^2} n_\perp^2 n_\parallel^2 x_{oe}^3 e^{-x_{oe}^2} \qquad (2.50)$$

$$D_i^{(i)} = 2\sqrt{\pi} \frac{\omega_{pi}^2}{\omega} n_\perp^4 x_{oi}^3 e^{-x_{oi}^2}. \qquad (2.51)$$

50

Here x_{oe} and x_{oi} are the dimensionless parallel phase velocities given by $\omega/(\sqrt{2}k_{\parallel}v_{the})$ and $\omega/(\sqrt{2}k_{\parallel}v_{thi})$.

In a similar manner as in Figure 2-3, the roots may be plotted against density, with the only change being the temperature set to $T_e = T_i = 1$ keV. The slow and fast waves are again present, with the same accessibility condition. This time however, the lower hybrid resonance is gone and is replaced by mode conversion to an ion plasma wave. The mode conversion location depends on $n_{\parallel}$ as can be seen by examining the top through bottom panels. The ion plasma wave is not desirable for current drive since the wave energy goes to the ions, which are too heavy, and therefore immobile, to carry current. In fact near the mode conversion point it is possible to have Landau damping on the ions.
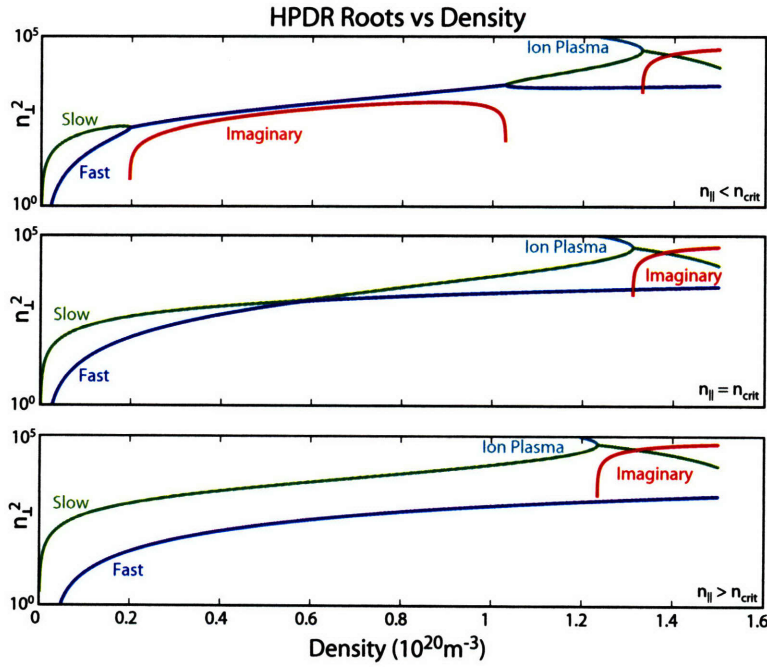
Figure 2-11: Plots of $n_{\perp}^2$ vs density with varying $n_{\parallel}$ by 1.2, top panel, 1.25, middle panel, and 1.5 bottom panel. Other parameters of interest are linear density and constant magnetic field of 5.4 T, with a launch frequency of 1.5 GHz.

Solving for x_{oe} gives the critical particle velocity for Landau damping of LH waves for current drive. The first step is to examine the power in a propagating wave[67]. Power is proportional to $E \cdot E^*$, and the spatially dependent part of the phase of E goes like $e^{i\bar{k}\cdot\bar{r}}$. Writing $\bar{k}$ as $(k_{\perp r} + ik_{\perp i})\hat{x} + k_{\parallel}\hat{z}$ results in the wave power varying like $\exp(-2k_{\perp i}(x)x)$. The integral form of this expression,

$$P(x) = P_0 \exp\left(-\int 2k_{\perp i}(x)dx\right) \tag{2.52}$$

can be used in ray tracing to compute the power absorbed along a ray path.

Examining the power loss over a small, characteristic distance, Δx; the power loss becomes large for $2k_{\perp i}\Delta x \sim 1$. The next step is to find an expression for $k_{\perp i}$ by Taylor

expanding the dispersion relation around $k_{\perp r}$,

$$D(\omega, \overline{k}) = D(\omega, k_{\perp r}) + (k_\perp - k_{\perp r})\frac{\partial D}{\partial k_{\perp r}} + \cdots = 0$$

but $D(\omega, \overline{k}) = D_r + iD_i$, and $k_\perp = k_{\perp r} + ik_{\perp i}$ with $k_{\perp r} \gg k_{\perp i}$ so

$$D_r(\omega, k_{\perp r}) + iD_i(\omega, k_{\perp r}) + ik_{\perp i}\frac{\partial D_r}{\partial k_{\perp r}} = 0.$$

Setting real and imaginary parts equal to zero and solving for $k_{\perp i}$ gives

$$k_{\perp i} = -\frac{D_i}{\partial D_r/\partial k_{\perp r}}. \tag{2.53}$$

For simplicity the electrostatic limit,$(n^2 = n_\perp^2 + n_\parallel^2 \gg 1)$, of the cold plasma relation is used to develop an expression that is easy to evaluate,

$$D_r = 4C_4 n_\perp^3 + 2C_2 n_\perp.$$

Taking the largest order terms for the coefficients gives $C_4 = \epsilon_\perp$, and $C_2 = \epsilon_\parallel n_\parallel^2$. Rewriting the denominator as

$$n_\perp \frac{c}{\omega}\left(2\epsilon_\perp n_\perp^2 + 2\epsilon_\perp n_\perp^2 + 2\epsilon_\parallel n_\parallel^2\right),$$

and using the electrostatic dispersion relation,

$$D(\omega, \overline{k}) = \epsilon_\parallel n_\parallel^2 + \epsilon_\perp n_\perp^2 = 0, \tag{2.54}$$

the last two terms cancel to leave

$$2\frac{c}{\omega}\epsilon_\perp n_\perp^3.$$

Then

$$k_{\perp i} = \sqrt{\pi}\frac{-\omega}{c}\frac{\omega_{pe}^2}{\omega^2}\frac{n_\parallel^2}{\epsilon_\perp n_\perp}x_{oe}^3 e^{-x_{oe}^2}. \tag{2.55}$$

Further simplification comes through writing the dispersion relation as $n_\perp = n_\parallel\sqrt{-\epsilon_\parallel/\epsilon_\perp}$ and estimating the order of the dielectric constants to be $\epsilon_\perp \sim 1$ and $\epsilon_\parallel \sim -\frac{\omega_{pe}^2}{\omega^2}$. The final result is

$$k_{\perp i} = \sqrt{\pi}\frac{-\omega_{pe}}{c}n_\parallel x_{oe}^3 e^{-x_{oe}^2}. \tag{2.56}$$

Using this result the simple expression for significant electron Landau damping becomes

$$2\sqrt{\pi}\frac{-\omega_{pe}}{c}\Delta x n_\parallel x_{oe}^3 e^{-x_{oe}^2} \sim 1. \tag{2.57}$$

This is a transcendental equation for x_{oe} which can be solved numerically. The damping velocity is plotted as $w = \sqrt{2}x_{oe}$ as a function of $n_\parallel$ in Figure 2-12. The simple linear theory limit is plotted along with the results using the hot and cold dispersion relations in the denominator for $k_{\perp i}$. The hot and cold dispersion relations give almost identical results. The simple limit works well at higher $n_\parallel$, where the wave is more electrostatic. An estimate from quasi-linear theory is also plotted which reduces the linear velocity by about a factor of 1.3. Quasi-linear theory will be covered in detail in section 2.6.

52
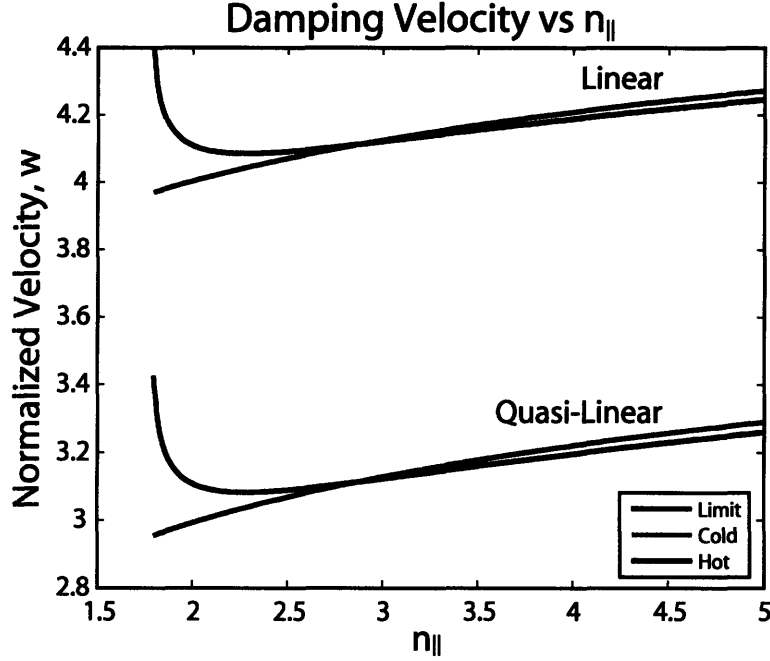
Figure 2-12: Damping velocity as a function of $n_\parallel$ for linear and quasi-linear theory. $n = 1 \times 10^{20} m^{-3}$, B=5 T, and $\Delta x \sim$ 1cm. The damping velocity is nearly identical for the hot and cold dispersion relations.

2.6 Current Drive

Lower hybrid waves drive current through electron Landau damping. Landau damping is a collisionless process where a wave can give energy to a particle. Calculation of the wave-driven current begins with a description of the electron distribution function[16, 68]. Landau damping tends to locally flatten the distribution. This flattening occurs because wave energy is being deposited on electrons, moving them to a higher velocity, and reducing the number of resonant velocity particles. Another process that must be considered is collisions. Coulomb collisions tend to restore the distribution to a Maxwellian. It is the interaction of these two processes that describe the time evolution of the distribution function. Mathematically the time evolution of the distribution function may be described by a Fokker-Planck equation consisting of a RF term and a collision term

$$\frac{\partial f}{\partial t} = RF + \left.\frac{\partial f}{\partial t}\right|_c. \tag{2.58}$$

The question is what to use for the RF term? Since the damping is a collisionless process the Vlasov equation may be used. Consider an unmagnetized plasma, $\overline{B}_0 = 0$, with no zero order electric field, $\overline{E}_0 = 0$, resulting from charge neutrality. The primary force felt by the electrons is due to a first order electric field, $\overline{E}_1$ set up by the alteration of the electron distribution from the RF wave,

$$\frac{\partial f}{\partial t} + \overline{v} \cdot \nabla f - \frac{e}{m_e}\overline{E}_1 \cdot \nabla_v f = 0. \tag{2.59}$$

Let $f = f_0(v_\parallel, t) + f_1(v_\parallel, z, t)$, consisting of a zero order, spatially independent term and a perturbed quantity that has a spatial dependence. A key point in the derivation of this term is the idea of spatial averaging. The spatial average of any quantity varying like $e^{i\vec{k}\cdot\vec{r}}$ is zero. This is shown below. The spatial average of a function g is given by

$$\langle g \rangle = \lim_{L_x, L_y, L_z \to \infty} \frac{1}{8L_xL_yL_z} \int_{-L_x}^{L_x} \int_{-L_y}^{L_y} \int_{-L_z}^{L_z} g(\overline{v}, \overline{r}, t) d^3r.$$

This average has the property that any space independent function is its own spatial average, that is $\langle h(\overline{v}, t, etc) \rangle = h$. In perturbation analysis all perturbed or first order quantities are assumed to go like $e^{i\vec{k}\cdot\vec{x}}$. For example consider $\langle f_1(\overline{v}, \overline{r}, t) \rangle$. In Fourier space

$$f_1(\overline{v}, \overline{r}, t) = \frac{1}{(2\pi)^3} \int_{-\infty}^{\infty} e^{i\overline{k}\cdot\overline{x}} f(\overline{v}, \overline{k}, t) d^3k.$$

Now take the spatial average considering the x-coordinate

$$\langle f_1(\overline{v}, x, t) \rangle = \frac{1}{2\pi} \int_{-\infty}^{\infty} f(\overline{v}, k_x, t) dk_x \lim_{L_x \to \infty} \frac{1}{2L_x} \int_{-L_x}^{L_x} e^{ik_x x} dx, \text{ and}$$

$$\lim_{L_x \to \infty} \frac{1}{2L_x} \int_{-L_x}^{L_x} e^{ik_x x} dx = \lim_{L_x \to \infty} \frac{\sin(k_x L_x)}{k_x L_x} = 0, \text{ so } \langle f_1(\overline{v}, x, t) \rangle = 0.$$

This result is the same in the other spatial coordinates yielding $\langle f_1(\overline{v}, \overline{r}, t) \rangle = 0$. This means that in linear theory the spatial average of any perturbed quantity is zero. This is very useful in kinetics for simplifying equations.

Next, apply a spatial average to the Vlasov equation,

$$\frac{\partial}{\partial t} \left(\langle f_0 \rangle + \langle f_1 \rangle \right) + \overline{v} \cdot \left(\langle \nabla f_0 \rangle + \langle \nabla f_1 \rangle \right) - \frac{e}{m_e} \nabla_v \cdot \left(\langle f_0 \overline{E}_1 \rangle + \langle f_1 \overline{E}_1 \rangle \right) = 0.$$

The properties of the spatial average simplify this expression to

$$\frac{\partial}{\partial t} f_0 + \overline{v} \cdot \langle \nabla f_1 \rangle - \frac{e}{m_e} \nabla_v \cdot \left(\langle f_0 \overline{E}_1 \rangle + \langle f_1 \overline{E}_1 \rangle \right) = 0.$$

The term $\overline{v} \cdot \langle \nabla f_1 \rangle$ is zero since the spatial average of the derivative of f_1 is zero. The derivative simply brings down a factor of $i\overline{k}$ so the limit still goes to zero. The $\langle f_0 E_1 \rangle$ term is zero since f_0 is spatially independent and $\langle \overline{E}_1 \rangle = 0$, so

$$\frac{\partial}{\partial t} f_0 = \frac{e}{m_e} \nabla_v \cdot \langle f_1 \overline{E}_1 \rangle. \tag{2.60}$$

Note that the evolution of the distribution function depends on a second order quantity, something that would not result using pure linear theory.

Returning to the unaveraged Vlasov equation,

$$\frac{\partial}{\partial t} (f_0 + f_1) + \overline{v} \cdot \nabla f_1 - \frac{e}{m_e} \nabla_v \cdot \left(f_0 \overline{E}_1 + f_1 \overline{E}_1 \right) = 0.$$

Substituting in the second order expression for $\partial f_0 / \partial t$ gives

$$\frac{\partial}{\partial t} f_1 + \overline{v} \cdot \nabla f_1 = \frac{e}{m_e} \nabla_v \cdot \left(f_0 \overline{E}_1 + f_1 \overline{E}_1 - \langle f_1 \overline{E}_1 \rangle \right)$$

54

Retaining only the linear terms and solving for f_1 in Fourier space yields

$$f_1 = \frac{ie}{m_e} \frac{\nabla_v \cdot \overline{E}_1 f_0}{(\omega - \overline{v} \cdot \overline{k})}.$$ (2.61)

Finally substituting this linear expression for f_1 into the spatially averaged equation for $\partial/\partial t f_0$ gives

$$\frac{\partial}{\partial t} f_0 = \frac{e}{m_e} \nabla_v \cdot \langle \frac{ie}{m_e} \frac{\nabla_v \cdot \overline{E}_1 f_0}{(\omega - \overline{v} \cdot \overline{k})} \overline{E}_1 \rangle = \nabla_v \cdot \langle \frac{ie^2}{m_e^2} \frac{\overline{E}_1^2}{(\omega - \overline{v} \cdot \overline{k})} \rangle \cdot \nabla_v f_0.$$

Define

$$\overline{\overline{D}}_{ql} \equiv \langle \frac{ie^2}{m_e^2} \frac{\overline{E}_1^2}{(\omega - \overline{v} \cdot \overline{k})} \rangle$$ (2.62)

as the quasi-linear diffusion coefficient. This coefficient describes the "diffusion" in velocity space of electrons due to the presence of the RF waves. This term is called quasi-linear since both linear and nonlinear theory have been used in its derivation. For lower hybrid waves the "parallel-parallel" component of $\overline{\overline{D}}_{ql}$ is the most significant. The RF term may be written in one dimensional form

$$RF = \frac{\partial}{\partial v_\parallel} D_{ql}(v_\parallel) \frac{\partial}{\partial v_\parallel} f_0.$$ (2.63)

Now that the RF term is known a collision operator is needed to complete the description for the time evolution of f_0. The correct choice of collision operator must describe the scattering of fast electrons from a fixed background of ions and electrons[69, 70] and is given by

$$\left. \frac{\partial f_0}{\partial t} \right|_c = \frac{2 + Z_{eff}}{2} \frac{\partial}{\partial v_\parallel} \left\{ \nu(v_\parallel) \left(v_{the}^2 \frac{\partial}{\partial v_\parallel} + v_\parallel \right) f_0 \right\}$$ (2.64)

where

$$\nu(v_\parallel) = \nu_0 \frac{v_{the}^3}{v_\parallel^3}, \text{ and } \nu_0 = \frac{\omega_{pe}^4 \ln \Lambda}{2\pi n_e v_{the}^3}.$$

Combining the two terms gives

$$\frac{\partial f_0}{\partial t} = \frac{\partial}{\partial v_\parallel} D_{ql}(v_\parallel) \frac{\partial}{\partial v_\parallel} f_0 + \frac{2 + Z_{eff}}{2} \frac{\partial}{\partial v_\parallel} \left\{ \nu(v_\parallel) \left(v_{the}^2 \frac{\partial}{\partial v_\parallel} + v_\parallel \right) f_0 \right\}.$$ (2.65)

For a steady state solution the RF term must balance the collision term. Integrating over $v_\parallel$ gives

$$D_{ql}(v_\parallel) \frac{\partial}{\partial v_\parallel} f_0 = \frac{2 + Z_{eff}}{2} \nu(v_\parallel) \left(v_{the}^2 \frac{\partial}{\partial v_\parallel} + v_\parallel \right) f_0.$$

Solving for $\partial/\partial v_\parallel f_0$

$$\frac{\partial}{\partial v_\parallel} f_0 = \frac{-v_\parallel f_0 / v_{the}^2}{1 + 2D_{ql}(v_\parallel)/((2 + Z_{eff})\nu(v_\parallel)v_{the}^2)}.$$

This is a separable equation for f_0 so

$$f_0 = A_0 \exp \left(\int \frac{-v_\parallel / v_{the}^2 dv_\parallel}{1 + D v_\parallel^3 / v_{the}^3} \right), \text{ where } D = \left(\frac{2}{2 + Z_{eff}} \right) \frac{D_{ql}(v_\parallel)}{\nu_0 v_{the}^2}$$

and A_0 is a constant to be determined through particle conservation. Note that this function is Maxwellian everywhere except for the region where the lower hybrid waves modify or "flatten" the distribution. It is convenient to write the expression for f_0 in terms of the parallel velocity normalized to the thermal velocity, let $w = v_\parallel / v_{the}$, so

$$f_0 = K_0 \exp\left(\int \frac{-w \, dw}{1 + D_0 w^3}\right).$$

D_{ql} vanishes everywhere except in the resonant region where the response is very large. This behavior is modeled as

$$D(w) = \begin{cases} D_0(w) & \text{if } w_1 < w < w_2; \\ 0 & \text{otherwise.} \end{cases}$$

where w_1 and w_2 are the resonant velocities for a given $n_\parallel$ spectrum, determined by the critical damping velocity and the accessibility condition. D_0 is the normalized quasi-linear coefficient, which is very large in magnitude, such that $D_0 \gg 1/w_{res}^3$, where w_{res} is the normalized velocity in the resonant region. The distribution function may be written by performing integrals over three regions

$$f_0(w) = \begin{cases} K_0 \exp\left(\frac{-w^2}{2}\right) & \text{if } w_1 < w; \\ K_1 \exp\left(\frac{1}{D_0 w}\right) & \text{if } w_1 \le w \le w_2; \\ K_2 \exp\left(\frac{-w^2}{2}\right) & \text{if } w_2 < w. \end{cases}$$

K_1 and K_2 are determined by matching conditions at w_1 and w_2,

$$K_1 = K_0 \exp\left(\frac{-w_1^2}{2} - \frac{1}{D_0 w}\right)$$

$$K_2 = K_0 \exp\left(\frac{w_2^2 - w_1^2}{2} + \frac{w_1 - w_2}{D_0 w_1 w_2}\right).$$

K_0 is determined by normalization from particle conservation

$$\int_{-\infty}^{\infty} f_0(w) \, dw = 1.$$

Figure 2-13 shows the initial and steady state distribution functions for $w_1 = 2.3$, and $w_2 = 5$. The value of w_1 was chosen to be 2.3, less than the typical value of 3, for illustrative purposes. Larger values of w_1 reduce the height of the quasi-linear plateau. The integrals for the normalization are performed numerically. The higher the value of D_0, the flatter the plateau is. The asymmetric plateau gives a net current when integrated over all velocities.

Once the distribution function is known the driven current may be calculated by taking the velocity moment of the distribution,

$$J = e n_e \int_{-\infty}^{\infty} f_0(v_\parallel) v_\parallel \, dv_\parallel,$$

or in terms of normalized quantities

$$J|_{norm} = \frac{J}{e n_e v_{the}} = \int_{-\infty}^{\infty} f_0(w) w \, dw.$$

In the limit of large D_0 the current is

$$J|_{norm} = \frac{K_0}{2} \left\{ \exp\left(\frac{-w_1^2}{2}\right) + K_1 \left(w_2^2 - w_1^2\right) - K_2 \exp\left(\frac{-w_2^2}{2}\right) \right\}.$$

LHCD Modified Distribution Function
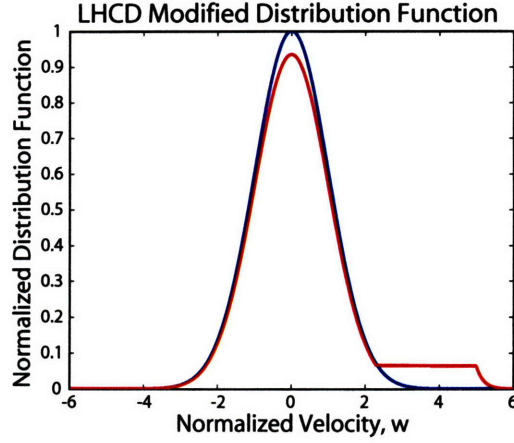
Figure 2-13: Alteration of the electron distribution function in the presence of lower hybrid waves with $w_1 = 2.3$ and $w_2 = 5$.

2.7 Efficiency

The current drive efficiency is defined as the amount of current driven per unit power dissipated, J/P_d. This efficiency is surprisingly high for LHCD. This is due to two counter-intuitive points:

1. It is more efficient to accelerate high energy electrons to form the current than low energy electrons.

2. An asymmetric resistivity may be formed, implying that no net momentum injection is needed to drive current.

Examining point one first[57]:

Consider a magnetized plasma with Maxwellian ion and electron distributions such that there is no net current. Now add an incremental velocity, $\Delta v_\parallel$, to a number of electrons, δf. This velocity is small when compared to the initial electron velocity, that is $v_\parallel \gg \Delta v_\parallel$. This could be done for example by wave damping on a certain velocity class of particles. This gives rise to a current

$$J = e\Delta v_\parallel \delta f$$

while requiring a change in energy of

$$
\begin{aligned}
\Delta E &= \frac{1}{2}m_e \left(v_\parallel + \Delta v_\parallel\right)^2 \delta f - \frac{1}{2}m_e v_\parallel^2 \delta f \\
&\approx m_e v_\parallel \Delta v_\parallel \delta f
\end{aligned}
$$

giving rise to a current to energy ratio of

$$\frac{J}{\Delta E} = \frac{e}{m_e v_\parallel}.$$

57
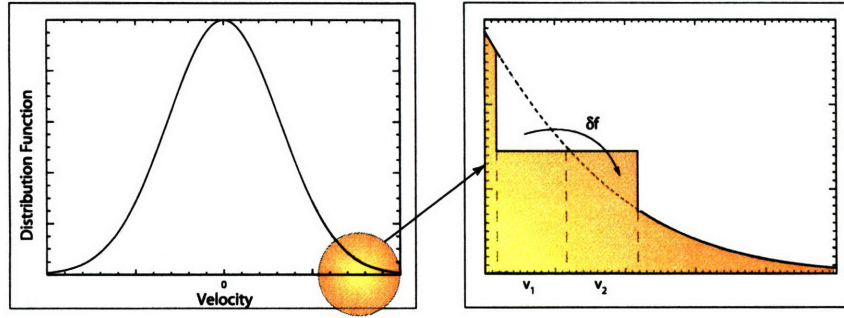
Figure 2-14: Modification of the Distribution Function by Localized Energy Input.

Looking at this quantity alone it appears that it is better to accelerate low energy electrons, but this does not take into account how long the current will last once it is created. Remember that the effective rate at which the current decays is related to $\nu(v)$, the ion-electron momentum exchange frequency. Electron-electron collisions do not contribute since like particle collisions simply swap guiding centers from momentum conservation. Here $\nu(v)$ is deliberately left somewhat ambiguous, as energy loss will need to be considered later. The collision frequency can be used to write the power dissipated, $P_d = \nu(v)\Delta E$. The efficiency is

$$\frac{J}{P_d} = \frac{e}{m_e v_\parallel \nu(v)}. \tag{2.66}$$

So for high efficiency $v_\parallel \nu(v)$ must be small. This can be accomplished for two limits of the collision frequency. If $v_\parallel$ is small and $v_\perp \sim v_{th}$ then the collision frequency is essentially constant using the temperature of the distribution. In this case J/P_d gets large, and this motivated early current drive efforts using Alfvén waves. The principle drawback for using these type of waves is that the current drive suffers from a lack of charge carriers since most of the electrons in this region of velocity space are trapped. The second limit has $v_\parallel \gg v_{th}$, in this case the distribution is like a beam with $\nu(v) \sim v_\parallel^{-3}$ and $J/P_d \sim v_\parallel^2$. In this case J/P_d is also large and supports the use of lower hybrid waves to drive current. Electrons in this region are not trapped and free to carry current, thus it is more efficient to accelerate high energy electrons to form the current than low energy electrons.

Next examine point two[71]:

The goal is to calculate J/P_d for a plasma current generated by energy input from lower hybrid waves. Begin the analysis by again considering a magnetized plasma with Maxwellian ion and electron distributions such that there is no net current. The initial electron distribution is perturbed at time t by moving δf electrons from parallel velocity v_1 to v_2. This requires an energy

$$\Delta E = (E_2 - E_1)\,\delta f.$$

Figure 2-14 schematically shows the change in the distribution function.

The two velocity classes of electrons will lose their momentum at different rates, v_1 at rate $\nu_1 = \nu(v_1)$ and v_2 at rate $\nu_2 = \nu(v_2)$. The generic momentum loss rate relation is

$$\frac{dp}{dt} = -p\nu(v).$$

This implies that

$$v_1(t) = v_{1_0}e^{-\nu_1 t} \text{ and } v_2(t) = v_{2_0}e^{-\nu_2 t}.$$

The differing momentum decay rates give rise to a time dependent current

$$J(t) = e\delta f\left(v_{1_0}e^{-\nu_1 t} - v_{2_0}e^{-\nu_2 t}\right).$$

This is the current at time t as a result of the initial energy input. If ΔE is continually added then the current at any time is the cumulative result of the total amount of energy. However, only ΔE added within a time Δt, such that $\Delta t \gg 1/\nu_1, 1/\nu_2$, will contribute significantly to the steady state current. This allows the steady state current to be found as the time average of $J(t)$,

$$J = \frac{1}{\Delta t}\int_0^{\Delta t} J(t)dt = \frac{e\delta f}{\Delta t}\left(-\frac{v_{1_0}}{\nu_1}e^{-\nu_1 \Delta t} + \frac{v_{1_0}}{\nu_1} + \frac{v_{2_0}}{\nu_2}e^{-\nu_2 \Delta t} - \frac{v_{2_0}}{\nu_2}\right).$$

Since $\Delta t \gg 1/\nu_1, 1/\nu_2$, the exponential terms are small and so

$$J \approx \frac{e\delta f}{\Delta t}\left(\frac{v_{1_0}}{\nu_1} - \frac{v_{2_0}}{\nu_2}\right).$$

Dividing by the energy gives the ratio of the driven current to the dissipated power as

$$\frac{J}{P_d} = -e\frac{v_{1_0}/\nu_1 - v_{2_0}/\nu_2}{E_1 - E_2}.$$

This expression can be written in differential form by taking the limit where $v_{2_0} \to v_{1_0}$. As v_{2_0} approaches v_{1_0} let

$$v_{1_0} = v_\| \text{ and } v_{2_0} = v_\| + \Delta v_\|$$

so

$$\nu_1 = \nu(v) \text{ and } \nu_2 = \nu(v + \Delta v_\|).$$

Similarly

$$E_1 = E(v) \text{ and } E_2 = E(v + \Delta v_\|).$$

ν_2 and E_2 can be Taylor expanded as

$$\nu_2 \approx \nu(v) + \Delta v_\|\frac{\partial}{\partial v}\nu \text{ and } E_2 \approx E(v) + \Delta v_\|\frac{\partial}{\partial v}E.$$

Substituting into the expression for J/P_d gives

$$\frac{J}{P_d} = -e\frac{v_\|\left(\nu + \Delta v_\|\frac{\partial}{\partial v}\nu\right) - \nu\left(v_\| + \Delta v_\|\right)}{-\nu\left(\nu + \Delta v_\|\frac{\partial}{\partial v}\nu\right)\Delta v_\|\frac{\partial}{\partial v}E} = -e\frac{v_\|\frac{\partial}{\partial v}\nu - \nu}{\left(-\nu^2 - \nu\Delta v_\|\frac{\partial}{\partial v}\nu\right)\frac{\partial}{\partial v}E}.$$

The limit of $v_{2_0} \to v_{1_0}$ is equivalent to letting $\Delta v_\| \to 0$, resulting in

$$\frac{J}{P_d} = -e\frac{\nu - v_\|\frac{\partial}{\partial v}\nu}{\nu^2\frac{\partial}{\partial v}E},$$

59

Notice that the numerator and the ν^2 in the denominator is just the rule for the derivative of a fraction. Using this fact and defining the velocity displacement unit vector as $\hat{s}$ the efficiency can be cast in the form of

$$\frac{J}{P_d} = -e\frac{\hat{s} \cdot \nabla_v(v_\parallel/\nu)}{\hat{s} \cdot \nabla_v E}. \tag{2.67}$$

If $\nu \propto v^{-3}$ with $v = v_\parallel + v_\perp$ and $\hat{s} \parallel \overline{B}$, as is the case for lower hybrid waves, then J/P_d may be evaluated,

$$\frac{J}{P_d} \propto \frac{\frac{\partial}{\partial v_\parallel}\left\{v_\parallel\left(v_\parallel + v_\perp\right)^3\right\}}{\frac{\partial}{\partial v_\parallel}\left\{\frac{1}{2}m\left(v_\parallel + v_\perp\right)^2\right\}} \propto \frac{1}{v_\parallel}\frac{\partial}{\partial v_\parallel}\left\{v_\parallel\left(v_\parallel^2 + v_\perp^2\right)^{3/2}\right\}.$$

Before proceeding further it is important to examine the physical interpretation of the two terms that will arise from the derivative. The first term is the derivative of $v_\parallel$, and is the expected contribution to the current from input of momentum. The second term is the derivative of $1/\nu$ and is contribution to the current from the fact that slow electrons lose their momentum faster than fast electrons. This is associated with the addition of energy to the distribution function,

$$\frac{J}{P_d} \propto \underbrace{\frac{\left(v_\parallel^2 + v_\perp^2\right)^{3/2}}{v_\parallel}}_{momentum} + \underbrace{3v_\parallel\left(v_\parallel^2 + v_\perp^2\right)^{1/2}}_{energy}. \tag{2.68}$$

Typically $v_\parallel \gg v_\perp$ and so the dominant term in determining the efficiency is actually the energy input, being about three times larger than the momentum term. This has the important implication that no net momentum addition is needed to drive current and that LHCD efficiency is primarily due to the energy input. This is called asymmetric resistivity since there are more electrons of a higher velocity class on one side of the distribution function losing their momentum at a slower rate. This counter-intuitive point means that it is possible to drive current using no parallel momentum waves such as electron cyclotron waves.

The only thing needed to complete the analysis is the correct form for ν. The correct frequency to use comes from analysis of the Fokker-Planck[71] equation and is given by

$$\nu = \frac{\nu_0(5 + Z_i)}{2u^3}, \text{ and } \nu_0 = \frac{\omega_{pe}^4 \ln\Lambda}{2\pi n_e v_{the}^3}$$

where Z_i is the ion charge state, $u = v/v_{the}$ the normalized velocity. Substituting this into the expression for J/P_d gives

$$\frac{J}{P_d} = -e\frac{\hat{s} \cdot \nabla_v(v_\parallel/\nu_0)}{\hat{s} \cdot \nabla_v(m_e v^2)}\frac{4}{5 + Z_i}. \tag{2.69}$$

It is convenient to normalize this expression as the following dimensionless form

$$\frac{J}{P_d}\bigg|_{norm} = \frac{J}{P_d}\frac{(m_e v_{the}^2 \nu_0 n_e)}{(-e n_e v_{the})} = \frac{4}{5 + Z_i}\frac{\hat{s} \cdot \nabla_v(wu^3)}{\hat{s} \cdot \nabla_v(u^2)}.$$

60

This gives an accurate analytic result for calculating the efficiency. Note that this expression goes like w^2.

Current drive experiments are also characterized in terms of a figure of merit defined as "nIR/P". This can be evaluated from a single particle picture. The current of a single electron driven by a wave is $J = ev_\parallel$. The energy of the particle is $\frac{1}{2}m_e v_\parallel^2$, and $P_d = m_e v_\parallel dv_\parallel/dt$ is the power dissipated as the particle slows down. Taking $d/dt \sim \nu(v_\parallel)$, the power can be written as $m_e v_\parallel^2 \nu(v_\parallel)$. Using $\nu(v_\parallel) = \nu_0 v_{the}^3/v_\parallel^3$, the expression for the efficiency is

$$\frac{J}{P_d} = \frac{ev_\parallel^2}{m_e \nu_0 v_{the}^3}. \tag{2.70}$$

Normalizing to dimensionless form yields

$$\frac{J}{P_d}\bigg|_{norm} = \frac{J}{P_d}\frac{(m_e v_{the}^2 \nu_0 n_e)}{(e n_e v_{the})} = w^2 \propto \frac{1}{n_\parallel^2 T_e}.$$

This dependence on w^2 is the same as in the more complex form for J/P_d. The w^2 may be related to $n_\parallel$, and so the efficiency is another performance characteristic that depends on $n_\parallel$. The inverse square dependency means that to be as efficient as possible the wave must have a small value of $n_\parallel$, this minimum value is determined by accessibility conditions. This efficiency can be related to tokamak parameters by taking

$$I_p \simeq \pi a^2 J, \ P \simeq \pi a^2 2\pi R P_d, \text{ and } \frac{J}{P_d} = \frac{2\pi IR}{P}.$$

Using this result and the definition of ν_0 gives

$$\begin{aligned}\frac{J}{P_d}\bigg|_{norm} &= \frac{2\pi IR}{P}\frac{(m_e v_{the}\nu_0)}{e} \\ &= \left(\frac{n_e IR}{P}\right)\frac{e^3 \ln \Lambda}{\epsilon_0^2 T_e}.\end{aligned}$$

If $\omega, n_\parallel, B_0, R_0$ are fixed and T_e is assumed constant then the efficiency is constant. This means that for a given experimental setup to maintain the same current at a higher density requires more power. Similarly for a fixed density increasing the current requires increasing the power.

Chapter 3

Time Dependent Modeling of Integrated Scenarios

In preparation for lower hybrid experiments, time dependent modeling of integrated scenarios was carried out using TRANSP. TRANSP was chosen because of its ability to model a number of different aspects of tokamak plasmas including ion cyclotron heating, heat transport, and lower hybrid current drive. TRANSP is a large and complex code that may be used to analyze tokamak transport, or predict performance for a set of input data and parameters. TRANSP has about 180,000 lines and is maintained by Princeton Plasma Physics Laboratory. The code is run remotely from MIT at Princeton. This ensures that MIT has access to running the code, but without the heavy burden of maintaining it. The scenarios studied were based upon an experimentally demonstrated reverse shear plasma, and most of the work included a simulated internal transport barrier. The goals of the study were to examine the use of LHCD to control the current profile in time. Specifically, cases were run to test the following:
1. Sensitivity to LH power level
2. Sensitivity to density profile
3. Current holes
4. Spectral control of the shear reversal point.

Dynamic simulations help to provide a basis for C-Mod experiments and point out possible areas of interest. These simulations coupled with detailed Fokker-Planck modeling of single time slices and modeling for lower hybrid wave coupling provide a complete theoretical framework for both designing experiments and understanding results.

Section 3.1 briefly describes TRANSP, introduces the base shot for the study, presents initial results, and describes the setup used for studying the integrated scenario. Sections 3.2 through 3.5 cover study results from the four points listed above. Finally, section 3.6 goes over experimental recommendations based upon the results of previous sections.

3.1 Using TRANSP to Model Integrated Scenarios

As mentioned earlier TRANSP may be used in either "analysis" mode or "predictive" mode, both of which are very useful. Analysis mode takes experimental data such as the kinetic profiles, and magnetics as inputs. Other inputs that are required, but not measured must use a relevant model to derive the needed quantity. For example, ion temperature is

required, but not measured and the neutron rate, however, is known and along with some assumptions may be used to estimate the ion temperature. Once all of the inputs have been entered, TRANSP solves the transport equations for the profile of the thermal diffusivity, χ.

Predictive mode uses prescribed information, such as χ, to solve for the resulting temperature profile. In this mode LHCD may be added, or the ICRF power increased to study changes in the current and temperature profiles. Using the predictive mode is fundamentally not self-consistent with the original data, but provides one of the only means of obtaining insight into what the behavior of the plasma will be in time. That said, the results should be viewed more from a standpoint of trying to illustrate general trends in behavior than to say that a specific amount of bootstrap current will be driven for a specific set of parameters on the actual experiment.

For more specific details of how the code works, the TRANSP web site, http://w3.pppl.gov/transp/, is an excellent resource. A great overview of the equations used, including the poloidal field diffusion and heat transport equations, is found in reference [72]. TRANSP contains modules for each aspect of a tokamak plasma, such as magnetic equilibrium, LHCD, ICRF, and neutral beams. The LSC[73] module simulates LHCD in TRANSP and is based on the adjoint calculation, making it 1.5D in velocity. Limitations of the adjoint calculation are discussed when full, 2D, Fokker-Planck (FP) modeling is covered in Chapter 4. LSC is also limited in having a single lobe in the $n_\parallel$ spectrum, a single poloidal launch point for ray tracing, and does not include particle trapping. LSC appears to have many drawbacks when compared to state of the art FP codes, and it does; however, the results should not be as poor as one would expect. First, not accounting for the secondary lobe in the $n_\parallel$ spectrum means that all the power is going in the current drive direction, in actual experiments about 20% or so of the power is actually in the counter current drive direction. The adjoint method underestimates the current driven by about 30 to 50%[74], so these two limitations partly compensate for each other. Having only one launch point for the rays could lead to inaccuracies in shape and location of the LH driven current profile. These inaccuracies are minimized since there is a significant amount of diffusion which broadens the current profile. Plans have been made to incorporate a full 2D solver such as CQL3D into TRANSP, but have not yet been implemented. Other modules of note that were used are TORIC[75] for ICRF heating, and the Hinton and Hazeltine[76] model for calculating the bootstrap current.

TRANSP requires and produces a tremendous amount of information at every time point in the simulation. It was found that the best way to examine the results was to look at animations of the profiles most critical to the performance of the plasma. A web based archive with a java script animator was used to display the results of each simulation. The web archive also has copies of the namelist parameters used and may be viewed using a web browser in the following directory: /home/jliptac/public_html/research/modsim/transp/.

Four panels are used in the animations. The top left plots the ohmic, bootstrap, and LHCD current profiles. The top right panel is the electron density profile. The bottom left panel is the q-profile and the bottom right is the ion and electron temperature profiles. Snapshots from the animations compose the bulk of the figures in this chapter and are used to illustrate key times or characteristics of the results. It should be noted that over 120 TRANSP runs were done to produce the following results. A significant amount of time was spent to determine the correct way to use different modules and then explore parameter space.

3.1.1 Base Shot Parameters

Reverse or optimized shear plasmas have good confinement properties and high bootstrap fractions[4], and have been demonstrated on most of the world's major tokamaks including JET[77] and JT60U[78, 79]. More recently these types of plasmas have been demonstrated with the goal of producing similar discharges on ITER[48, 80]

Reverse shear plasmas have been observed on C-Mod[81], but without the major improvement in confinement. The experimental recipe to form such a plasma without any form of off axis current drive consisted of a fast current ramp and early ICRF heating. The fast current ramp was used to quickly reach the total current value and the early heating was used to slow the current penetration by increasing the temperature. This resulted in a reversed shear q-profile with q on axis above one for a little over 220 ms, on discharge 960223047. After 220 ms the hollow current profile was lost as the ohmic current diffused into the core of the plasma as evidenced by the onset of the sawtooth instability. Time traces of plasma properties of shot 960223047 are shown in Figure 3-1.
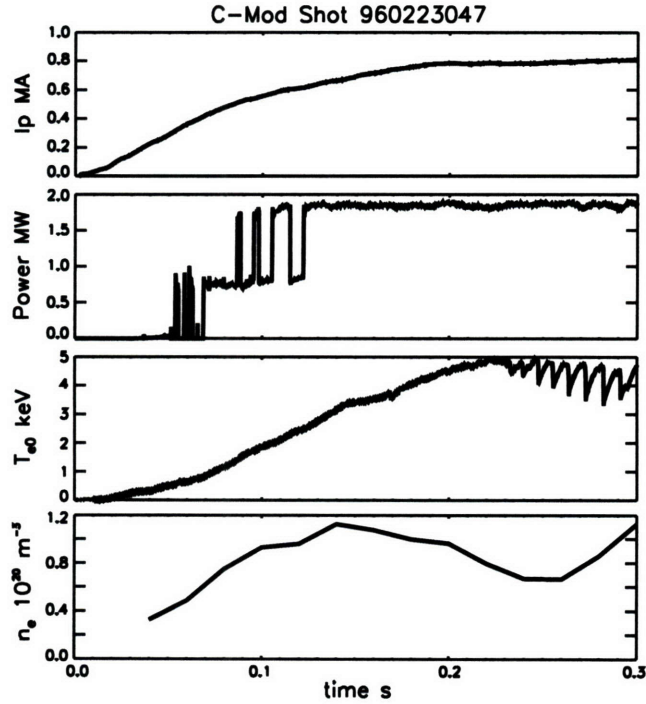
Figure 3-1: Traces of plasma parameters for shot 960223047, a current ramp shot, which forms the bases for all scenarios studied. The current, ICRF power, central electron temperature, and average density, are plotted out to 300 ms.

Current ramp discharges provide an interesting target for LHCD as a means to explore advanced tokamak physics. The idea is to replace most of the off axis ohmic current with

lower hybrid driven current and extend the length of the pulse and the overall performance of the discharge. If the the magnitude of the current and the current profile shape are well matched in going from ohmic to LHCD, inductive losses are minimized.

3.1.2 Initial Results on Sawtooth Stabilization

One of the first things studied using TRANSP was how long the period of shear reversal could be maintained by applying LHCD to shot 960223047. First results were obtained by Bonoli[82] who completed TRANSP runs showing that the shear reversal could be maintained to 0.28 s by 2.7 MW of LH power using an $n_\parallel$ of 2.7 and 3 MW of ICRF power. At 0.28 s the simulation was terminated. The simulation time was extended to 1.0 s to observe changes in the current profile as the plasma further evolved in TRANSP run 2282. The experimental density profile for shot 960223047 was used in these simulations. The profile of χ_e was frozen at 0.15 s to allow T_e prediction. Figure 3-2 shows the time histories of the input powers and currents.
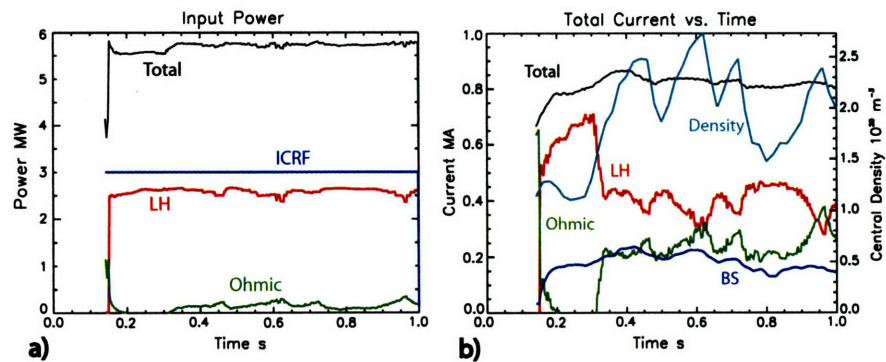
Figure 3-2: TRANSP run 2282 showing, a), the distribution of power between ohmic, ICRF, and LH, and, b), the distribution of current between ohmic, LH, and bootstrap. The central density is also shown on the current plot. As the density rose the amount of LH current being driven decreased which changed the character of the simulation from the current being primarily LH supported to ohmic supported.

The most notable event occurred at 300 ms when the density began to rise, in fact the central density more than doubled over about a 100 ms period. This drastically changed the current profiles and the character of the discharge. Figure 3-3 shows the current density, q, density, and electron temperature profiles at 215 ms. The plasma current was primarily supported by lower hybrid current and the q profile is reversed with a minimum near r/a of 0.5. As the density rose the amount of lower hybrid current decreased, which corresponded to an increase in the ohmic current. The ohmic current quickly diffused to the core and the reverse shear is lost. Looking again at the integrated currents as a function of time in Figure 3-2, panel b), shows that there were several times in the simulation where the density decreased after 300 ms, which corresponded to an increase in the amount of LH driven current, but the discharge did not return to a shear reversed q profile since the ohmic current remained on-axis and brought q back down to one. The characteristic profiles are shown again at 1.0 s in Figure 3-4, which are fairly similar to all times after the density increase at 300 ms.

The next test performed was to see if the reverse shear could be maintained if the
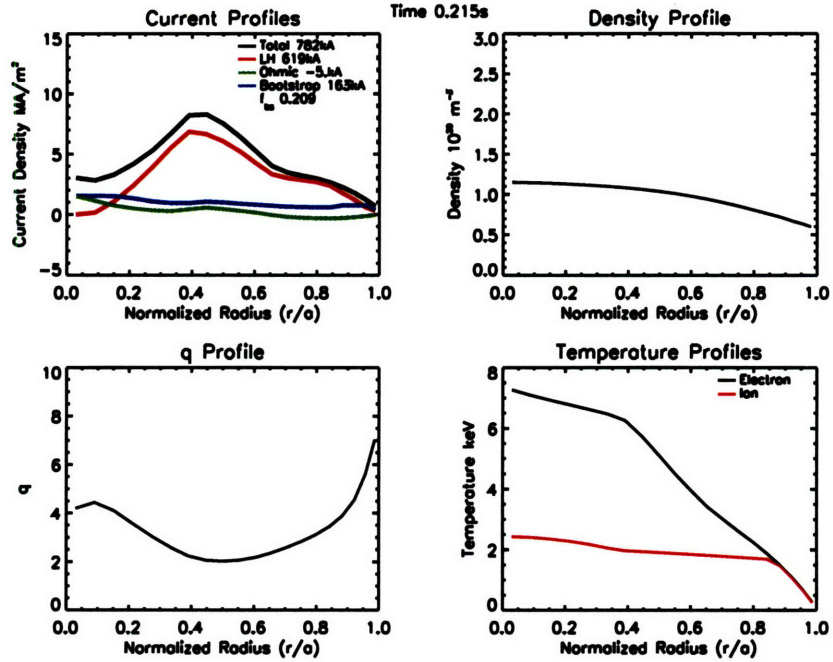
Figure 3-3: TRANSP run 2282 profiles at t=0.215 s, showing reverse shear and a primarily LH supported plasma current.
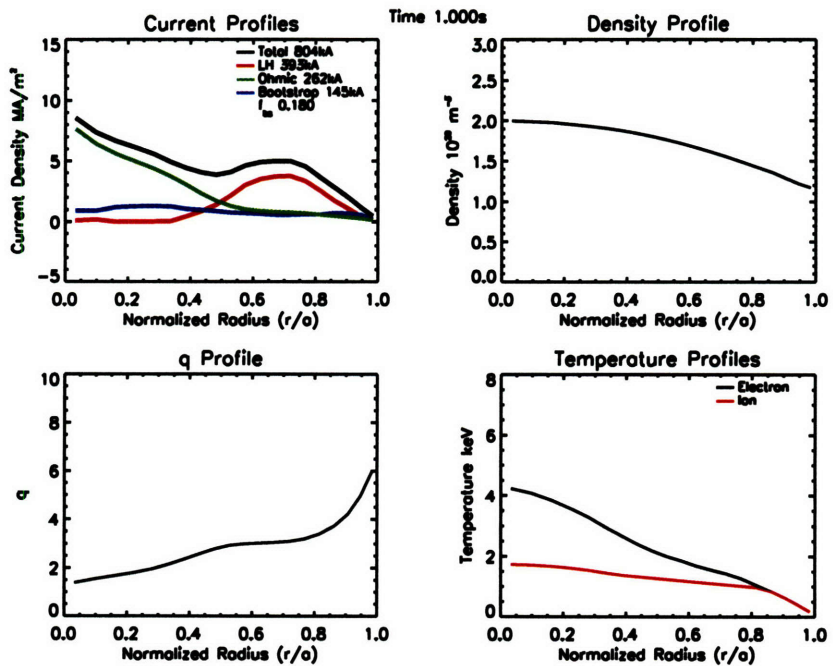
Figure 3-4: TRANSP run 2282 profiles at t=1.0 s. The shear reversal has been lost due to the density rise which lowered the amount of LH current driven. The location of the LH current was also pushed out since the waves are less accessible. However, q_0 was still maintained above one.
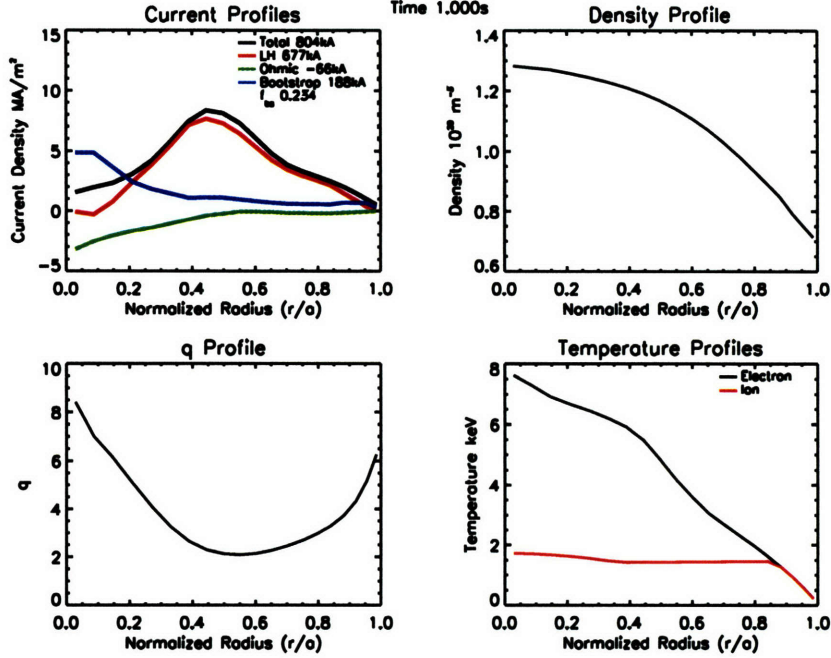
Figure 3-5: TRANSP run 2283 profiles at t=1.0 s. The plasma current remained LH supported throughout the run as the density was fixed at t=0.2 s. As a result of the strong LH current centered at r/a=0.5, the q-profile was strongly reversed.

density profile could be better controlled. TRANSP run 2283 was identical to 2282 except that the density profile was fixed at 200 ms. In this case the q-profile remained strongly reversed all the way to 1.0 s when the simulation was ended. The plasma current was primarily supported by LH throughout the run. Results from runs 2282 and 2283 indicate that density control is critical in maintaining the reverse shear q-profile.

3.1.3 Setup for Integrated Scenario Studies

Internal transport barriers (ITB) have also been shown to exist on C-Mod[83, 84]. Combining reverse shear and ITB discharges may lead to high performance plasmas which have good confinement properties along with high bootstrap fractions. TRANSP was used to study the integration of these two types of plasmas and simulate overall performance. The integrated scenario also uses the current ramp shot, 960223047 as its base. The principle change comes from simulating the formation of a transport barrier. To do this the density and χ profiles were prescribed. The profiles chosen were based upon shot 1002210016, a double barrier case. Only an internal barrier was used as LHCD is very sensitive to the edge density. Simulations using the actual density profile showed the density was far too high and that the LH current was small in magnitude and driven far in the periphery. For this reason a profile was chosen to roughly match the ITB gradient, but have an overall lower density. Figure 3-6 shows the experimental density in panel a), the χ profile produced using analysis mode in TRANSP in panel b), and the χ profile used in the integrated scenario simulations in panel c). The density profile was varied as part of the study. In most cases the barrier was grown over a period of about 60 ms and was fully formed 200 ms into the

run. Lower hybrid power was applied early in the simulations, typically at 150 ms.
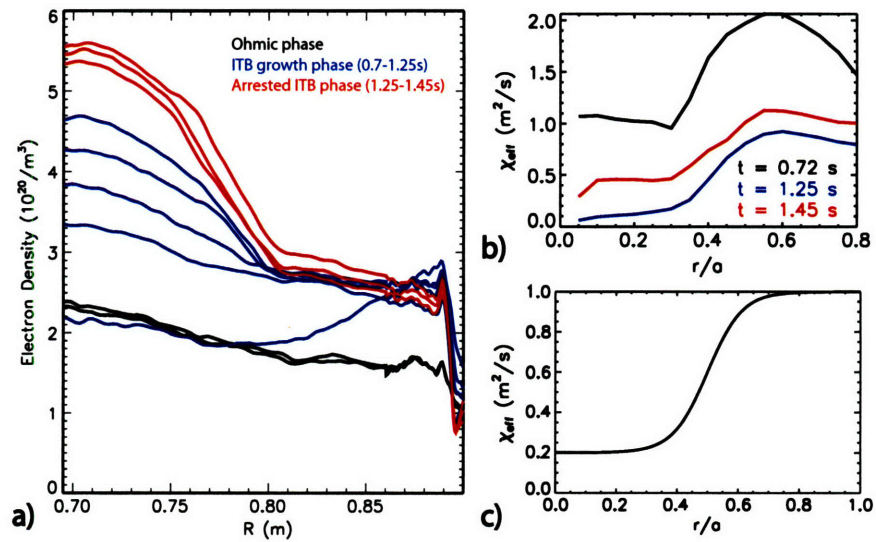
Figure 3-6: a)Density profile in time of internal transport barrier showing three stages of development, ohmic, ITB growth, and arrested for shot number 1002210016. b) Resulting χ profiles from TRANSP analysis mode. c) Analytical model of χ profile used as an input for integrated scenario runs using predictive TRANSP.

Current Profiles

Time 1.000s

Density Profile

Total 804kA
LH 315kA
Ohmic 89.4kA
Bootstrap 391kA
f_{bs} 0.486

Current Density MA/m²

Density 10¹⁹ m⁻³

Normalized Radius (r/a)

q Profile

Temperature Profiles

Electron
Ion

q

Temperature keV

Normalized Radius (r/a)
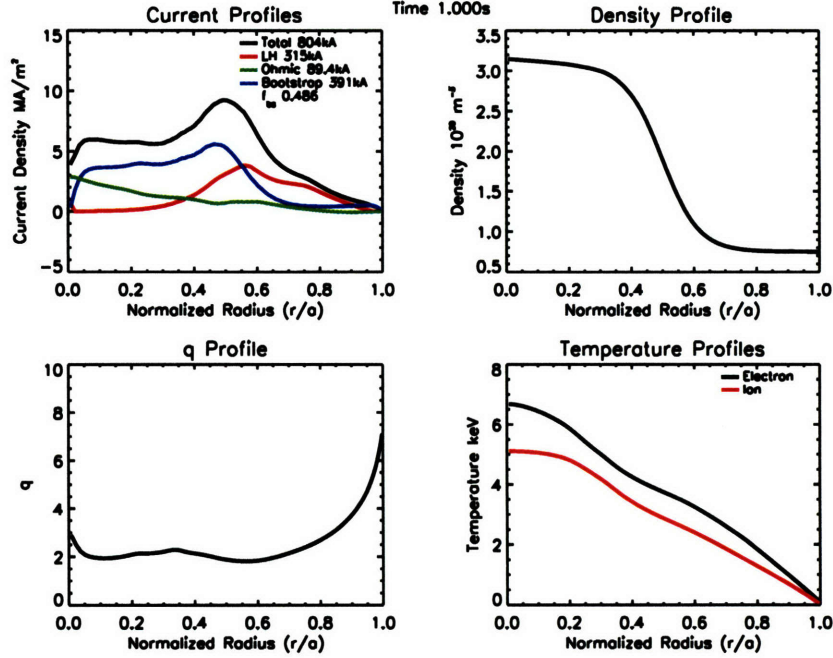
Figure 3-7: TRANSP run 2439 with 1.35 MW of LH power. Profiles at t=1.0 s indicate that not enough LH power was being supplied to make the scenario non-inductive, and in this respect the run was underdriven.

3.2   Power Sensitivity Study

The integrated scenario's response to different levels of lower hybrid power may be seen by examining three TRANSP runs. Run 2439 had 1.35 MW, 2418 had 1.65 MW, and 2440 had 1.95 MW. A time of 1.0 s was chosen to display the profiles of J, q, n_e, and T in Figures 3-7, 3-8, and 3-9, since by this time all the transients have died away and the profiles shown could exist indefinitely. Changing the power by 300 kW from case to case had the most pronounced effect on the current profile. The temperature profiles were very similar in all cases as were the bootstrap fractions, which were near 50%. The distribution of the current between ohmic, LH, and bootstrap in these cases distinguishes three modes of operation, underdrive, quiescent, and overdrive.

The underdriven case, 2439, had too little LH power to make the run non-inductive with 89 kA of ohmic current mostly distributed within a normalized radius of 0.5. This current tended to flatten the q-profile, but it was maintained above 1.5 everywhere. This case also interesting in that it showed the effect of a little central current drive.

The quiescent case, 2418, had just enough current from LH and bootstrap such that the run was non-inductive and the ohmic current profile was flat and near zero everywhere. The minimum q was near two and was located at r/a of 0.6.

Run 2440 with 1.95 MW of LH power produced a tremendous amount of LH current. So much so that the ohmic current was driven negative to keep the total current constant. Driving too much LH current leads to inefficiency and transformer recharge. The q-profile showed evidence of the formation of a current hole, that is where the current on axis goes to zero and as a result q goes to infinity. There regimes are interesting in their own right
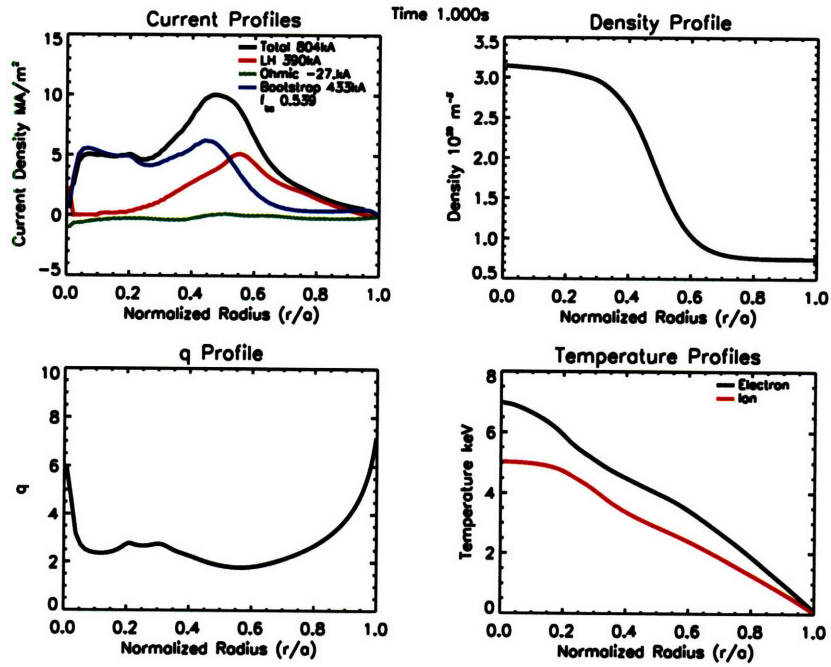
Figure 3-8: TRANSP run 2418 with 1.65 MW of LH power was just enough to make the run non-inductive and bring the ohmic current near zero everywhere.
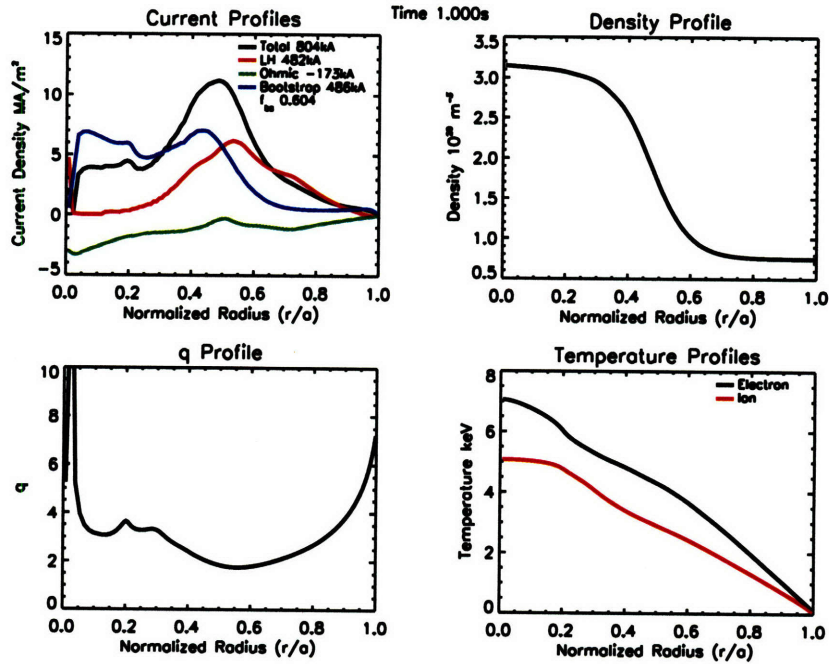
Figure 3-9: TRANSP run 2440 with 1.95 MW of LH power produced a large, negative, ohmic current to respond to the combination of LH and bootstrap current in order to maintain a constant total current. In this respect the system was overdriven.

and will be examined further in section 3.4.

3.3 Density Barrier Magnitude Scan

As mentioned above the role of the density profile is of great importance to the overall performance of plasmas using LHCD. To study this role the density profile in the integrated scenario was scanned in magnitude from a central density of 3 to 5×10^{20} m^{-3}. As the density was raised the temperature decreased, so different levels of ICRF power were also compared. Table 3.1 shows the parameters used and the temperatures and bootstrap fractions obtained. $\langle \rangle$ denotes a time averaged quantity over the length of the simulation. Figure 3-8 shows the

Table 3.1: **Plasma Conditions for Density Scan Runs**

	2418	2432	2433	2438	2442
n_{e0} $(10^{20}m^{-3})$	3.1	4.1	5.0	5.0	5.0
$\langle T_{e0} \rangle$ (keV)	6.7	5.5	4.5	5.6	6.4
P_{ICRF} (MW)	3.0	3.0	3.0	4.0	5.0
P_{LH} (MW)	1.65	1.75	1.85	1.65	1.85
$Max f_{bs}$ (%)	55	62	61	58	75
$\langle f_{bs} \rangle$ (%)	48	54	55	53	67

profiles for run 2418 and Figures 3-10 through 3-13 for runs 2432 through 2442.

Run 2418 was described above as an example of a fully non-inductive scenario. It also has a high bootstrap fraction, with a maximum value of 55%. The maximum value of the bootstrap current is a better figure of merit than the time average, as the maximum typically represents values in steady conditions. The time average includes the startup, which have lower bootstrap fractions and lower the average from what is typical during steady conditions.

Increasing the density from 3 to 4 $\times 10^{20}$ m^{-3} in run 2432 increased the bootstrap fraction by 7%, but the average central temperature was reduced by about 20%. Figure 3-10 plots the profiles at the quiescent point in this simulation. At times the plasma was overdriven, as the combination of the bootstrap and LH current required a negative ohmic current to maintain the constant total plasma current. Lowering the LH power slightly would bring the ohmic current near zero.

Increasing the density from 4 to 5 $\times 10^{20}$ m^{-3} in run 2433 did not further increase the bootstrap fraction. This was a result of the drop in temperature. Figure 3-11 plots the profiles at the quiescent point in the simulation. As was the case in 2432, the plasma was at times overdriven. The q-profiles are very similar, which indicated that the changes in bootstrap fraction were due to temperature effects and not changes in B_θ.

Since 2433 was overdriven, and the bootstrap fraction was slightly reduced from 2432, the LH power was decreased, by 200 kW, and the ICRF power was increased to 4 MW. Figure 3-12 shows typical profiles of the simulation results. Increasing the ICRF power increased the temperature as expected, but reducing the LH power made the run underdriven and reduced the amount of bootstrap current despite the temperature increase. This indicates using the optimum LH power is a very important when trying to maximize plasma performance.

The final run in the scan, 2442, increased the LH power back to 1.85 MW and the ICRF to 5 MW. The result was the highest performance run conducted with a maximum
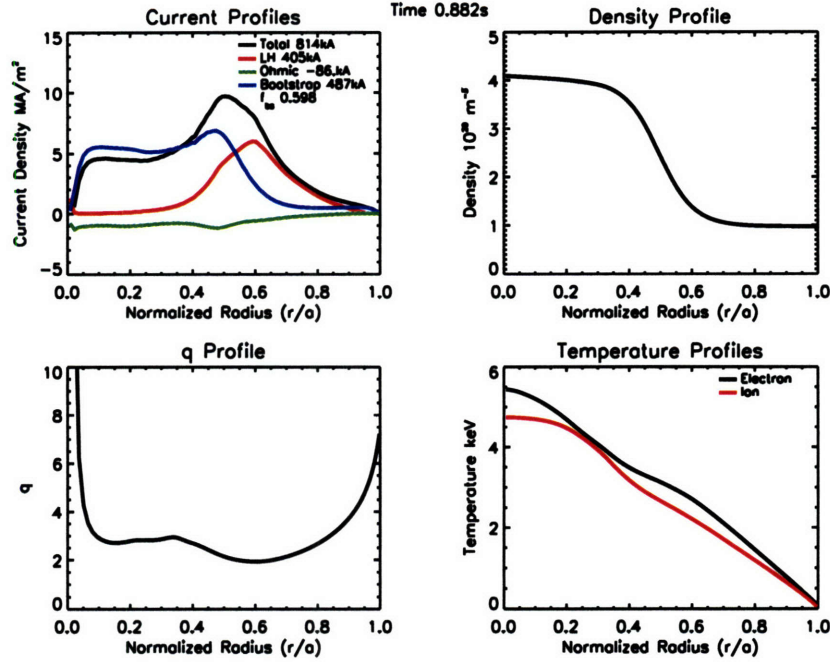
Figure 3-10: TRANSP run 2432 at 0.882 s with a central density of 4.1×10^{20} m^{-3}, 1.75 MW of LH power and 3.0 MW of ICRF. This run showed a 7% increase in bootstrap fraction when compared to run 2418.
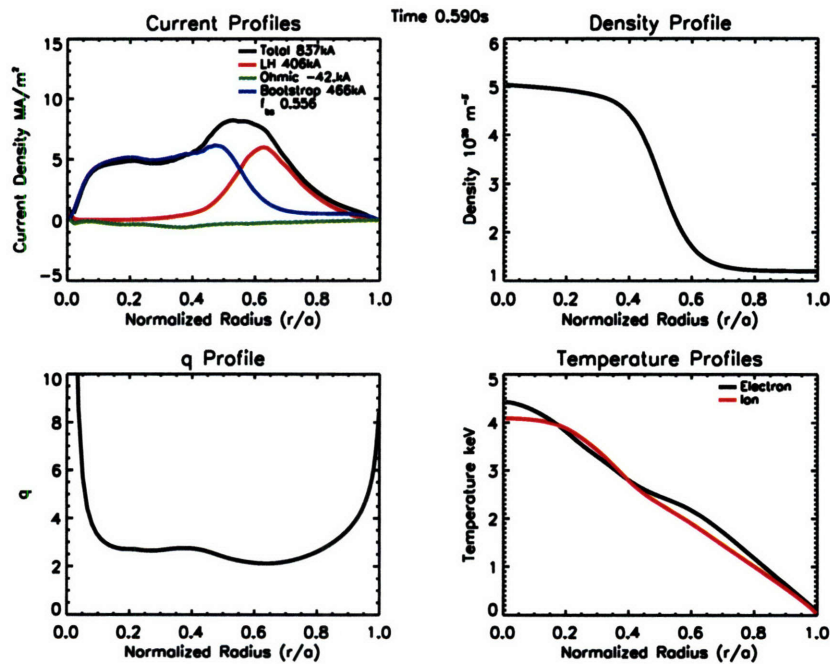
Figure 3-11: TRANSP run 2433 at 0.590 s with a central density of 5.0×10^{20} m^{-3}, 1.85 MW of LH power and 3.0 MW of ICRF. The bootstrap fraction decreased slightly when compared to run 2432 as the increased density lowered the temperature.
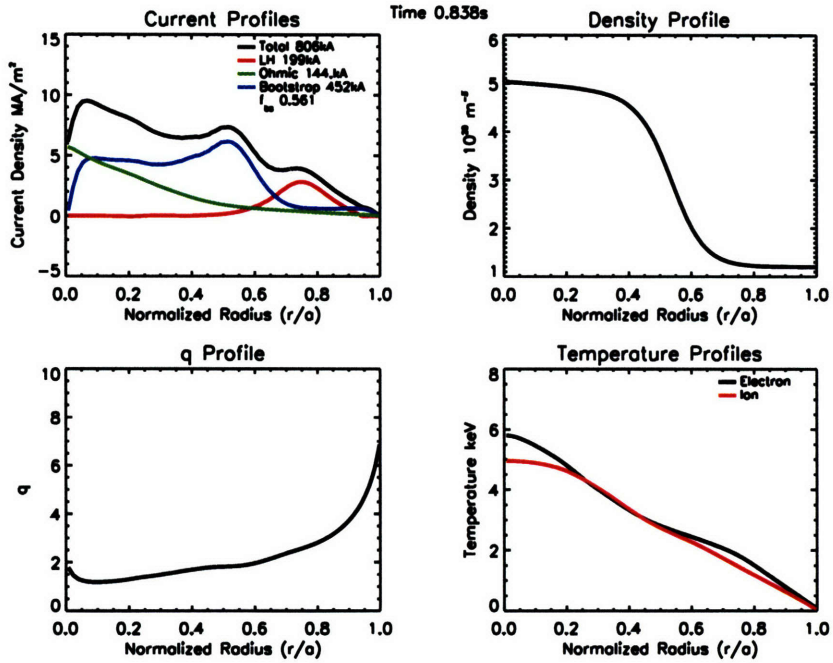
Figure 3-12: TRANSP run 2438 at 0.838 s with a central density of 5.0×10^{20} m^{-3}, 1.65 MW of LH power and 4.0 MW of ICRF. This run exhibited lower bootstrap fractions from the presence of ohmic current on-axis.
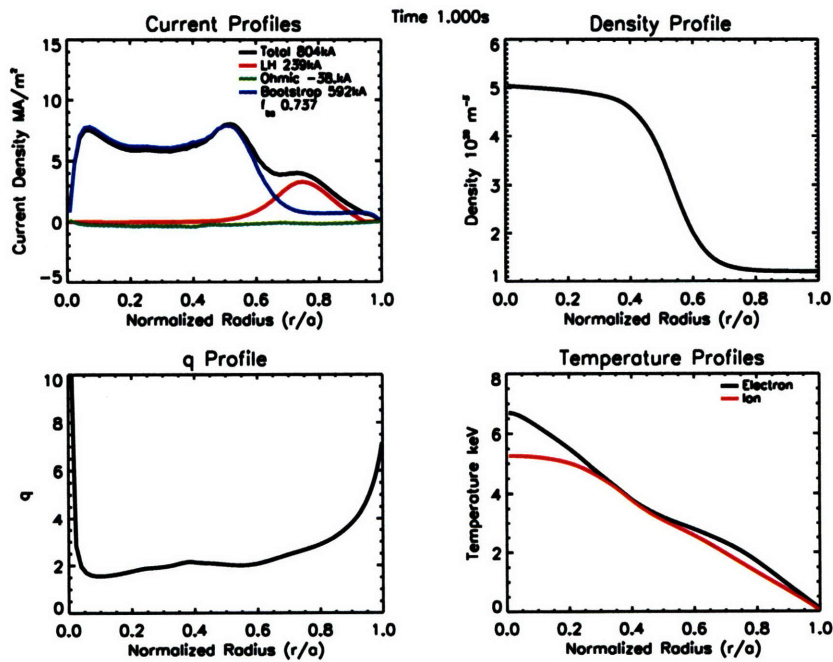
Figure 3-13: TRANSP run 2442 at 1.0 s with a central density of 5.0×10^{20} m^{-3}, 1.85 MW of LH power and 5.0 MW of ICRF. This run had the highest bootstrap fraction of all TRANSP runs and exhibited quiescent behavior throughout after the startup.

bootstrap fraction of 75%. This run exhibited quiescent operation throughout and high levels of bootstrap current due to both the high temperature and low B_θ.

3.4 Current Hole Study

JT-60U has extensively explored current hole experiments at low density[51], and JET has also observed them[47]. Current holes form when there is zero or very little current in the central region of the plasma. This makes the local value of the poloidal field, B_θ, small and the safety factor in this region become very large. The well known, but approximate, expression for the bootstrap current is

$$J_B = -\frac{1}{B_\theta}\frac{dP}{dr}, \tag{3.1}$$

where P is the pressure, This expression is valid for $\epsilon \to 1$, when most of the particles are trapped. The inverse dependence of the bootstrap current on the poloidal field means that for current hole-like plasmas the bootstrap fraction may be increased. The simple expression for the bootstrap current above is not realistic for an actual plasma, in fact the aspect ratio dependence makes the full form quite cumbersome. Another illustrative limiting case was derived by Wesson[1],

$$J_B = -\frac{\epsilon^{1/2}n}{B_\theta}\left(2.44(T_e + T_i)\frac{1}{n}\frac{dn}{dr} + 0.69\frac{dT_e}{dr} - 0.42\frac{dT_i}{dr}\right). \tag{3.2}$$

Here the dependence on density and temperature is seen more explicitly. TRANSP was used to explore the sensitivity of the bootstrap current with low poloidal field in order to take advantage of this dependence to maximize the bootstrap current. Current holes were produced in quiescent or overdriven simulations. Three power switching schemes were used to isolate the poloidal field effect from the dependance on the temperature and temperature gradient for the integrated scenario. The first run, 2418, has a constant LH and ICRF power throughout. 2430 was identical to 2418 until 0.5 s, when the LH power was turned off. 2441 was identical to 2418 except that when the LH power is switched off the ICRF power is increased to over 4 MW. The power switching and integrated currents are plotted in panels a) and b) of Figures, 3-14, 3-15, and 3-16, for runs 2418, 2430, and 2441, respectively. Table 3.2 displays the temperature, bootstrap current, and fraction for the three runs at a time of 1.0 s.

Table 3.2: Current Hole Performance Evaluated at 1.0 s

	2418	2430	2441
T_{e0} (keV)	7.0	6.7	9.0
I_{BS} (kA)	434	219	322
f_{BS} (%)	54	27	40

2418 had the highest bootstrap fraction. Switching off LHCD significantly reduces the amount of bootstrap current driven due to the changes in the current profiles. Run 2430 had 26% less bootstrap current than 2418, even though the the two runs had similar temperatures. Run 2441 had much higher temperatures than 2418, but still 14% less bootstrap fraction. Runs 2430 and 2441 are both ohmic supported plasmas by 1.0 s. The profiles are shown in figures 3-17 and 3-18 for runs 2430 and 2441. The profiles in 2418 profiles were shown previously in Figure 3-8. Low poloidal field operation, as is created during current hole plasmas, significantly increases the bootstrap current.
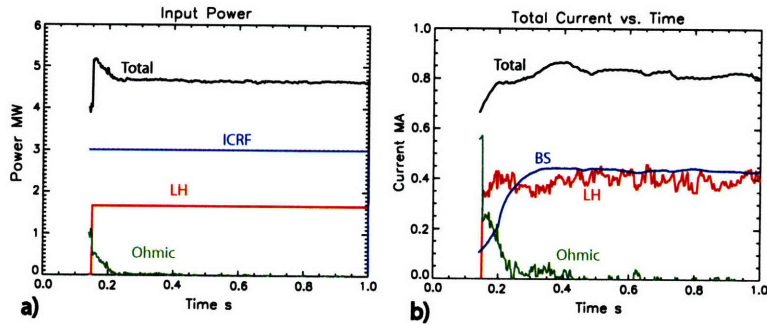
Figure 3-14: TRANSP run 2418 with a central density of 3.0×10^{20} m^{-3}, 1.65 MW of LH power and 3.0 MW of ICRF. Panel a) shows the LH and ICRF power levels are maintained at constant levels throughout the simulation. Panel b) shows the steady behavior of the currents after the initial startup.
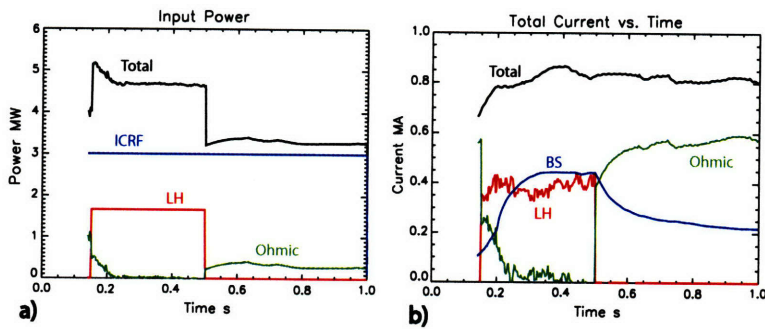
Figure 3-15: TRANSP run 2430 was identical to 2418, except the LH power was switched off at 0.5 s as shown in panel a). Panel b) shows the decay of the bootstrap current and the corresponding increase in ohmic current.
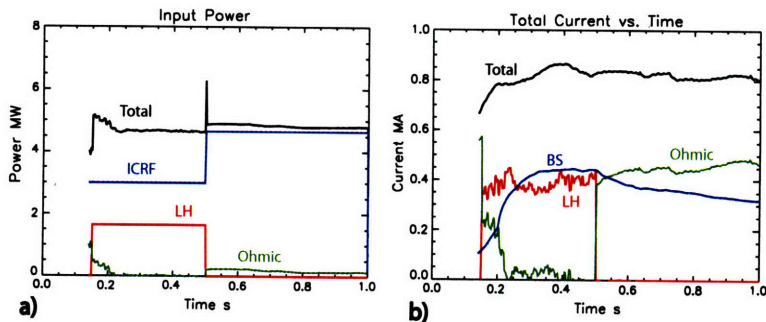
Figure 3-16: TRANSP run 2441 was also identical to 2418 except that the LH power was switched off at 0.5 s and the ICRF power was simultaneously increased to increase the temperature as shown in panel a). In panel b) the bootstrap current decayed at a slower rate and ends at a higher value than run 2430.

77
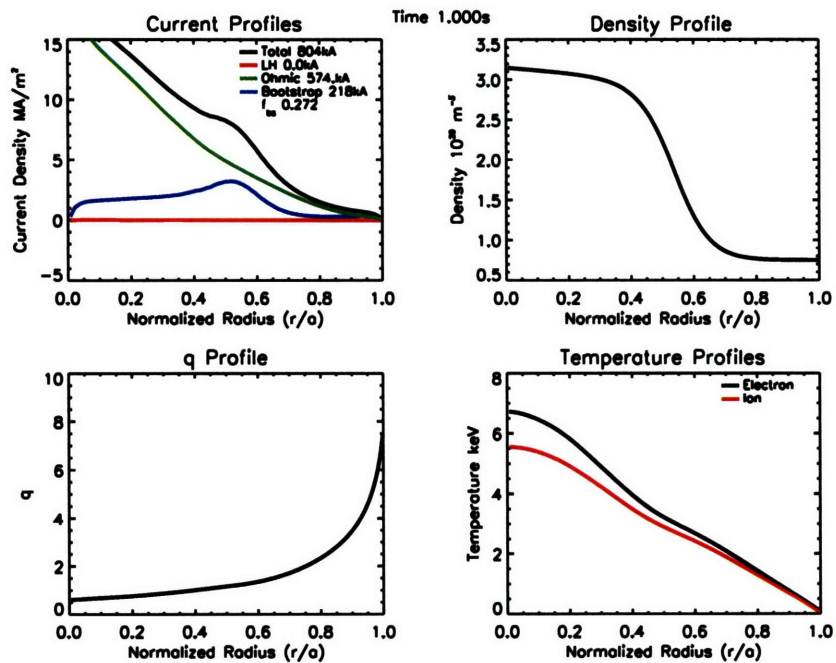
Figure 3-17: Profiles for TRANSP 2430 at 1.0 s showing a primarily ohmic driven current with q on-axis of about 1.
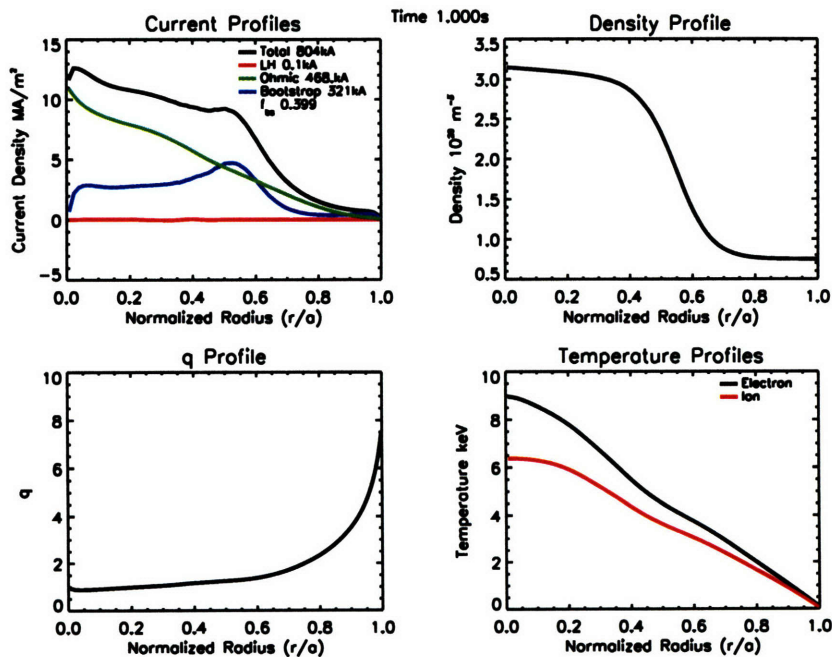
Figure 3-18: Profiles for TRANSP run 2441 at 1.0 s, which is similar in character to 2430, except a larger fraction of the current is carried by the bootstrap due to the higher temperature.
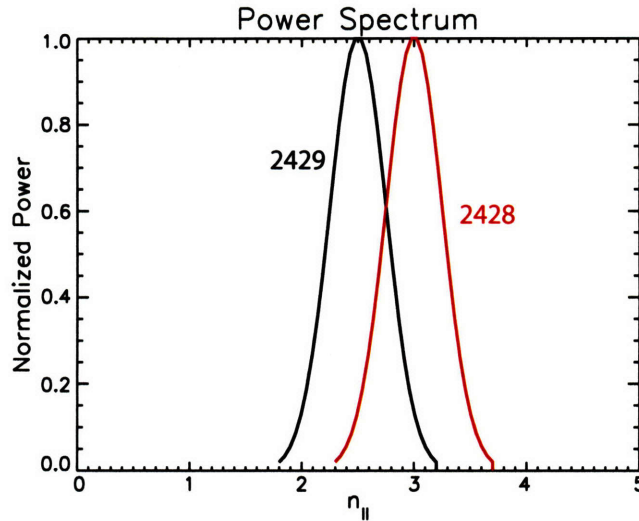
Figure 3-19: Gaussian spectra used for runs 2428 and 2429 centered at $n_\parallel$ of 3.0 and 2.5 respectively.

3.5 Spectral Control of the Shear Reversal Point

One of the major features of C-Mod's lower hybrid system is the ability to change the $n_\parallel$ spectrum dynamically, with the goal of modifying the lower hybrid current profile and the resulting q and pressure profiles. The effect of changing $n_\parallel$ was modeled simply by running two cases with different values of central $n_\parallel$. Run 2428 used an $n_\parallel$ of 3.0 and 2.0 MW, while run 2429 used an $n_\parallel$ of 2.5 and 1.4 MW of power. A higher power was used for the $n_\parallel$ of 3.0 in order to try and drive the same amount of lower hybrid current, since the efficiency decreases as $n_\parallel$ increases. Figure 3-19 shows the input spectra for the two cases. Typical current profiles for 2428 and 2429 are shown in panels a) and b) of Figure 3-20. Panel c) plots the q-profiles from each run on the same axis. As can be seen from this figure there was very little difference between the two cases. The q-profiles were nearly identical with the difference in shear reversal points being less than 1 cm apart. 2428 had a slightly broader current profile and has slightly more current density inside the barrier region. This seems reasonable as the higher $n_\parallel$ gave better LH wave accessibility. Perhaps a greater difference in initial values of $n_\parallel$ would yield more dramatic results.

The lack of significant differences between these two cases underscores the importance of other factors when trying to control the current and q-profile using LHCD. In addition to the important role of the density profile, spatial diffusion of the hot electrons may also play a significant role in the overall control of the profile. If the diffusion is high, changing the value of $n_\parallel$ may have little effect on the current profile as the differences would be smeared out. For these simulations a fast electron diffusivity of 0.35 m^2/s was used. This corresponds to a region of good confinement in the bulk plasma as shown in Figure 3-6.

Current Profiles

a)

Current Profiles

b)

q Profile

c)
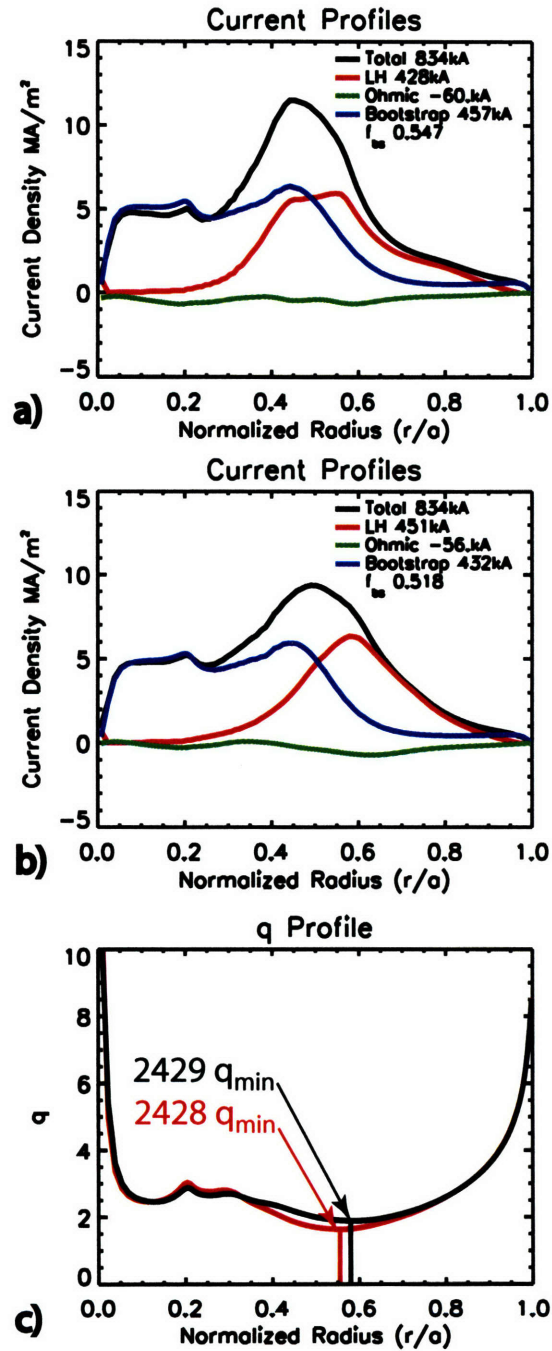
Figure 3-20: Comparison of current and q-profiles for runs 2428 and 2429 where the $n_\parallel$ was decreased from 3.0 to 2.5. Panel a) shows current profiles for $n_\parallel$ of 3.0 on run 2428. Panel b) shows current profiles for 2429 and $n_\parallel$ of 2.5. Panel c) shows the resulting q-profiles to be nearly identical.

3.6 Experimental Recommendations

First experiments with the LH system on C-Mod will focus on studying wave plasma coupling, conditioning, and protection system testing. These experiments will be done at low power and short duration. Another additional experiment that could be done under these conditions is to combine ICRF heating with small amounts of LH power to produce a mode converted IBW wave to stabilize sawteeth over the duration of the lower hybrid power. This has recently been demonstrated on HT-7, and further IBW synergy experiments may be performed at higher powers[85].

Once a significant amount of LH power becomes available, a simple experiment would be to demonstrate the ability to control the current profile enough to prevent the onset of sawteeth. While 2.7 MW was used to drive 600 kA and strongly reverse the q-profile in the simulation, such conditions may not be realistic for the experiment. However, using a lower value of $n_{\parallel}$ increases the efficiency of the current drive and reducing the total amount of current in the discharge would allow for a greater fraction to be driven by LHCD and give greater control of the q-profile. Use of a cryopump to regulate the density may also be extremely helpful to keep the density profile steady and avoid sudden increases, which would change the character of the discharge.

Current ramp discharges provide an attractive target for LHCD to produce low or reverse shear plasmas. On other tokamaks ITBs may be formed under these conditions. The details and confinement properties of this type of barrier could then be compared to the typical ITB produced on C-Mod through off-axis ICRF heating. ICRF heating has also been used to control the density of the ITB, the compatibility and interplay of these two techniques could then be studied. This type of scenario could possibly by optimized for maximum bootstrap fractions thus leading to the development of a high current non-inductive discharge.

Chapter 4

Fokker-Planck and HXR Emission Models

The Fokker-Planck (FP) equation was introduced in chapter 2. Despite of its complexity, numerical techniques have been developed to solve for the distribution function, while incorporating the physics aspects to be modeled. For example the RF term may be treated to solve the LH problem or may be specified to work with electron cyclotron current drive. Many other aspects may be treated as well such as the DC field acceleration of electrons and fast electron transport. To illustrate this further, Figure 4-1 shows the different physics models which may be used when solving for the distribution function using CQL3D. CQL3D is a very complete code and has the capability to model all the important aspects of LHCD. Various codes have been developed in order to solve the distribution function which may be used for the LHCD problem. These are summarized in the next section.

4.1 Summary of Major FP Codes

There are four main codes used for simulating lower hybrid wave interactions within a tokamak plasma, ACCOME, CQL3D, DKE, and LSC. The codes are compared in Table 4.1. All the codes are written in Fortran with the exception of DKE, which is written in

Table 4.1: **Comparison of LH Simulation Codes**

	ACCOME	CQL3D	DKE	LSC
Native Language	Fortran	Fortran	Matlab	Fortran
Scope	LH only	All	Electron Waves	LH only
Ray Tracing	MLP	MLP	MLP, Pseudo	SLP
Absorption	Adjoint	Full FP	Full FP	Adjoint
HXR Simulation	No	Yes	Yes	Yes
Support Level	High	High[1]	High	None
Documentation	Low	Low	High	Medium

Matlab. The physics is really broken down into two pieces, the ray tracing, and the power absorption calculation. ACCOME and CQL3D have more complete ray tracing modules,

---

[1] One of CQL3d's primary authors, R.W. Harvey, who also maintains the code is available as a consultant.
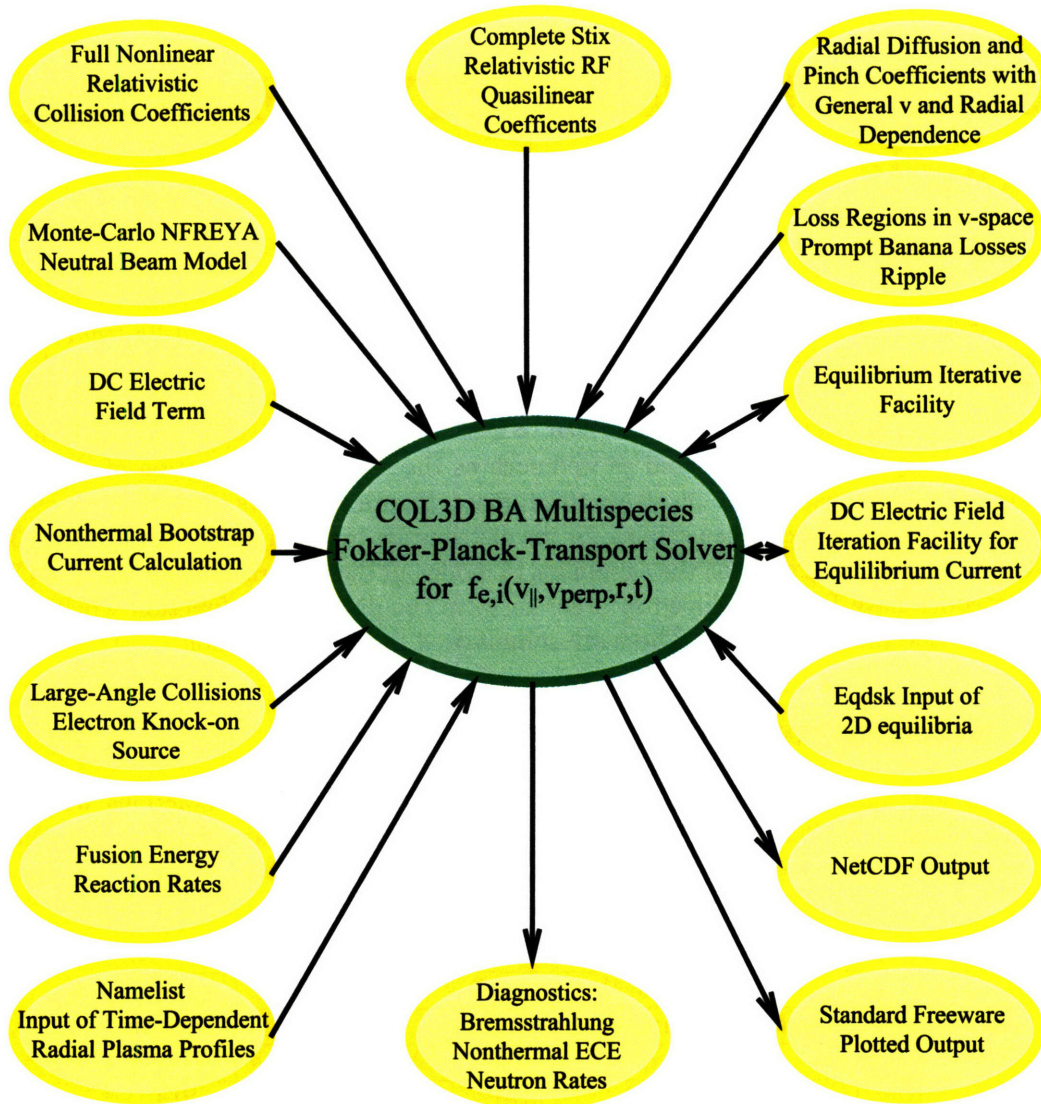
Figure 4-1: Physics models available for use when solving for the distribution function. Figure courtesy of R.W. Harvey.

allowing for multiple launch points (MLP) at different poloidal positions taking into account the physical extent of the LH antenna. LSC uses a single launch point (SLP).

DKE may be run in two ways, first it can be run with ray trajectories generated either by GENRAY, the same package used by CQL3D, or as a part of the CRONOS package. The second way uses a "pseudo" ray launched from a SLP with a single $n_\parallel$, and damps according to a profile input by the user. The user also inputs the level of D_{ql} as well as the velocity space width of the plateau into the calculation; doing so gives the power launched as an output instead of an input. This way of running the code is useful for quickly iterating between simulation and HXR experimental results to get the distribution function and the location of the driven current.

There are two primary methods to handle the power absorption calculation in the Fokker-Planck equation. The first method is to numerically solve it in two dimensions, parallel and perpendicular to the magnetic field. This was difficult to do in the past due to computing limitations. As a result a second method, known as the adjoint calculation was developed[86]. The adjoint calculation solves the FP equation using a Green's function technique, which accurately includes perpendicular and parallel velocity space effects, as well as effects due to particle trapping. The RF current density is computed from the Green's function using an approximate 1D ($v_\parallel$) form for the wave induced flux. As computing power increased and better algorithms were developed, solving the full 2D equation was no longer computationally prohibitive.

Recently, a direct comparison between a code using the adjoint technique, ACCOME, and a full 2D solver, CQL3D was performed. This comparison showed that using a full 2D solver predicts 35-50% more driven current than the adjoint method[74] under conditions characteristic of C-Mod plasmas. The difference was due to inaccuracies in the wave induced flux (used with the adjoint method), which did not properly capture 2D velocity space effects due to pitch angle scattering.

Once the distribution function is known, it is possible to reconstruct the HXR spectrum. This requires the bremsstrahlung cross sections and the geometry of the system. DKE has a very complete HXR modeling package, in which direct comparison with experimental results is made simple. CQL3D provides the chord emission, but detector effects must be included in a post processing routine. LSC has a simple model which was used on PBX-M[87] and ACCOME does not have this capability.

One of the final things to consider is how well each code is supported and documented. All of these codes are too complex to run without consultation to start. ACCOME, CQL3D, and DKE's primary authors are still active in the field, while LSC's author has retired. LSC does have a manual[64], and published papers[73][88], but is only supported within TRANSP, a transport simulation code. DKE is well documented in a 400 page manual[63] as well as other publications[89][90]. ACCOME is documented in published papers[61][91]. CQL3D is documented best in a conference proceedings paper[62], while more definitive documentation is currently being produced.

4.2 GENRAY

The general idea of ray tracing is to solve an initial value problem. The dispersion relation used in the ray equations to trace out a ray path must be real. This gives the actual location of the ray, but does not include any information about the damping or energy content of the wave. The damping information comes from the imaginary or anti-Hermitian part of
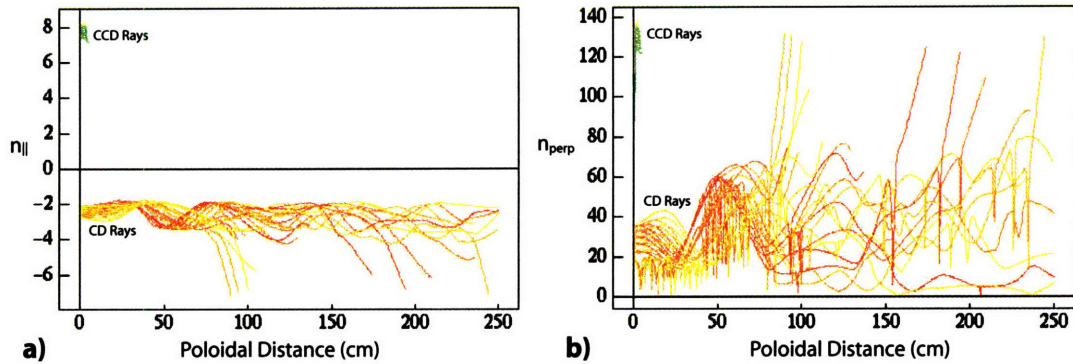
Figure 4-2: $n_{\parallel}$, panel a), and $n_{\perp}$, panel b) evolution as a function of poloidal distance traveled along the ray path.

the dispersion relation, or Fokker-Planck equation, and is calculated along the ray path. The path calculation for the ray is stopped when the wave energy reaches a small fraction of the initial value.

GENRAY[92] is a numerical ray tracing package that may be coupled into FP solvers. It is currently the ray tracing package used in CQL3D and preliminary work has been done to couple GENRAY to DKE. GENRAY uses magnetic equilibrium data in the form of an *eqdsk* file and the kinetic profiles to solve for the ray trajectories. Contrary to its name, GENRAY does not use a generalized form of the dispersion relation. Instead a number of options may be used depending on the type wave to be launched. For LH waves the choice is primarily between using the cold or hot plasma dispersion relation. In determining the trajectories, the difference between them is negligible so either form may be used.

The most important aspects of specifying the input parameters for GENRAY are to set the $n_{\parallel}$ launch spectrum, number of rays and poloidal distribution of ray bundles. The initial value of $n_{\parallel}$ is typically set to match a given phasing from the LH antenna. Both the CD and CCD spectral lobes may be set and their width specified. The stochastic nature of the trajectories requires a large number of rays to accurately model wave damping and current drive. Rays are launched in bundles which may be distributed over a number of poloidal locations, further allowing each rays' $k_{\parallel}$ to evolve differently. Figure 4-2 plots the evolution of $n_{\parallel}$ and $n_{\perp}$ as a function of poloidal distance traveled along the ray path. GENRAY results shown here are based on shot number 1030612013, a low density H-mode LH target plasma. Initial launch spectra consistent with 90° CD phasing. A poloidal cross sectional view of the plasma and ray trajectories calculated by GENRAY is shown in Figure 4-3.

GENRAY also calculates the Maxwellian damping along the ray by evaluating the imaginary part of the dispersion relation. The Maxwellian damping is significantly less then the quasilinear damping since there are very few particles present in the high velocity region where LH waves interact. The imaginary part of $k_{\perp}$ is shown as a function of major radius in Figure 4-4. Regions with large values of $\Im k_{\perp}$ indicate strong damping.

GENRAY outputs a data file containing all the information required by the FP code. This includes the ray trajectories, values of $n_{\parallel}$ and $n_{\perp}$ along the ray, as well as polarization. The FP code used then calculates the quasilinear damping and the distribution function.

86
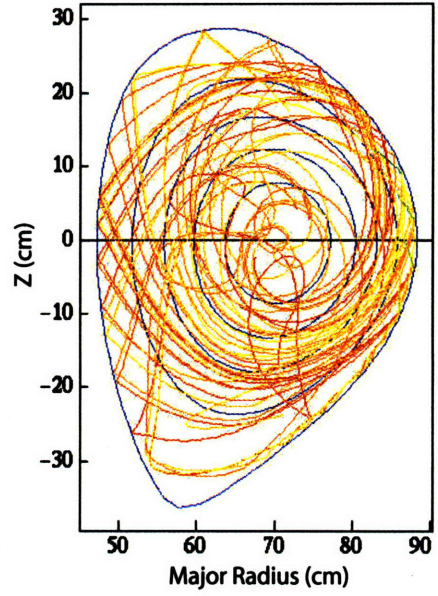
Figure 4-3: Poloidal cross section showing ray trajectories filling the plasma volume.
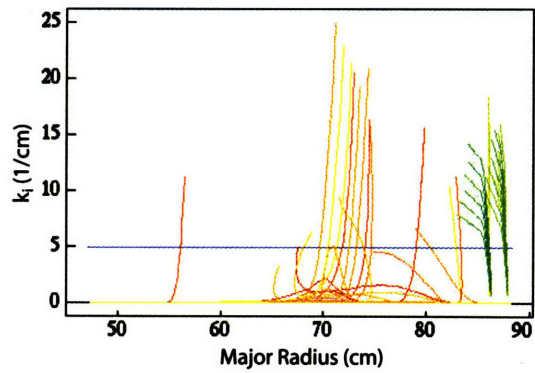
Figure 4-4: Imaginary part of $k_\perp$ used to calculate Maxwellian damping.

4.3 Bremsstrahlung Emission Models

Once the distribution function is known it is possible to solve for the bremsstrahlung emission from the plasma. The goal is to directly compare results from the hard x-ray camera presented in chapter 5 to the distribution function resulting from FP modeling. This type of analysis is very powerful when compared to simple inversion techniques, as in addition to the radial emissivity profile, information about the distribution function is recovered.

This modeling may be used in two important ways with different goals. First, when a ray tracing package is used, the primary purpose is to benchmark the FP code, making sure it is working properly and that the input parameters have been properly specified to match the experiment. Having the code well benchmarked gives confidence in its ability to correctly model cases where experimental verification becomes difficult. This is critical since meaningful HXR data may not be available in high performance plasmas due to low signal to noise.

Second, if ray tracing is not used, then the LH wave absorbtion may be specified along with LH parameters such as the plateau width and level of D_{ql} to generate a distribution function. The resulting HXR emission may be compared with experimental results and iterated until a distribution function that matches experimental results is found.

To calculate the expected emission seen by the detector the distribution function at each point along the viewing chord must be known as well as the chord geometry. In particular the angle of the magnetic field line and the direction of observation must be known to evaluate the bremsstrahlung cross sections.

The differential count rate observed at the detector may be written as

$$\frac{dN_E}{dtdE} = \int_0^\infty \eta_A(k)(1 - \eta_D(k))G(k, E)\frac{dN_k(t,k)}{dtdk}dk, \tag{4.1}$$

here E denotes the actual measured energy and k is the photon energy emitted from the plasma. $\eta_A(k)$ is the fraction of photons transmitted through any absorber present along the line of sight. In C-Mod's system this term would include the absorption from the 1 mm thick aluminum vacuum window. $(1 - \eta_D(k))$ is the fraction of photons that are stopped within the detector and $G(k, E)$ is the detector response function. This function models the photopeak as a Gaussian and describes Compton scattering within the detector as a Fermi-like function. Figure 4-5 plots the detector response function for a 70 keV incident photon. Since the detector size, shape, and material are nearly identical as in Reference[93], the same response function is used. $G(k, E)$ conserves energy such that

$$\int_0^\infty G(k, E)dk = 1. \tag{4.2}$$

$dN_k/dtdk$ is the differential number of photons emitted by the plasma inside a volume, ΔV for a given solid angle, $\Delta\Omega$ such that

$$\frac{dN_k(t,k)}{dtdk} = \int_{\Delta V} dV \int_{\Delta\Omega} \frac{dN_k(t,k,\bar{x},\hat{b}\cdot\hat{d})}{dtdkdVd\Omega}d\Omega. \tag{4.3}$$

ΔV and $\Delta\Omega$ may be functions of k if the aperture defining the chord is partially transmitting. Proper design of the aperture eliminates this dependency. $\hat{b}$ is the unit vector in the direction of the magnetic field and $\hat{d}$ is the unit vector of the viewing chord evaluated at position $\bar{x}$.
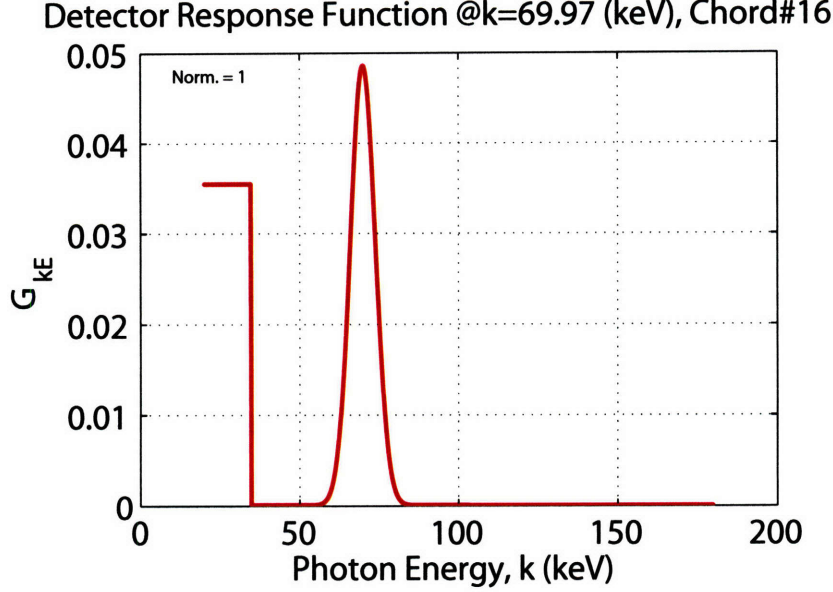
Figure 4-5: Detector response function, $G(k, E)$, for a 70 keV incident photon.

If the aperture is small such that the emissivity perpendicular to the chord may be neglected the integrals of Equation 4.3 may be reduced to a single integral over the chord length,

$$\frac{dN_k(t,k)}{dtdk} \simeq \int_{l_{min}}^{l_{max}} \varepsilon \frac{dn_k(t,k,\overline{x},\hat{b}\cdot\hat{d})}{dtdkd\Omega} dl, \qquad (4.4)$$

here, $l_{max} - l_{min}$ represents the extent of the chord within the plasma and ε is the éttendue of the system described by Equation 5.1. The photon density is $n_k = dN_k/dV$.

The photon density arises from both electron-ion and electron-electron collisions. Contributions from bound electrons may be neglected since free-free interactions dominate at energies much greater than the Rydberg energy, $Z^2 I_H = 13.6$ eV, for hydrogen. For heavier elements such as Mo, $Z = 42$, k must be much greater than 24 keV. Neglecting bound interactions the photon density may be written as

$$\frac{dn_k(t,k,\overline{x},\hat{b}\cdot\hat{d})}{dtdkd\Omega} = \sum_s \frac{dn_k^{ei}(t,k,\overline{x},\hat{b}\cdot\hat{d},Z_s)}{dtdkd\Omega} + \frac{dn_k^{ee}(t,k,\overline{x},\hat{b}\cdot\hat{d})}{dtdkd\Omega}, \qquad (4.5)$$

where the sum over Z_s represents contributions from all ion species.

The n_k^{ei} and n_k^{ee} may be expressed in terms of the differential bremsstrahlung cross sections, $d\sigma_{ei}/dtdkd\Omega$ and $d\sigma_{ee}/dtdkd\Omega$, and the velocity moment of the distribution function as

$$\frac{dn_k^{ei}(t,k,\overline{x},\hat{b}\cdot\hat{d},Z_s)}{dtdkd\Omega} = n_s(t,\psi) \int\int\int d^3\overline{p} \frac{d\sigma_{ei}(k,p,\hat{k}\cdot\hat{p},Z_s)}{dtdkd\Omega} v f(t,\overline{x},\overline{p}) \qquad (4.6)$$

and

$$\frac{dn_k^{ee}(t,k,\overline{x},\hat{b}\cdot\hat{d})}{dtdkd\Omega} = n_e(t,\psi) \int\int\int d^3\overline{p} \frac{d\sigma_{ee}(k,p,\hat{k}\cdot\hat{p})}{dtdkd\Omega} v f(t,\overline{x},\overline{p}). \qquad (4.7)$$

$n_s(t,\psi)$ is the ion density for species s as a function of flux surface and time, similarly $n_e(t,\psi)$ is the electron density. The velocity v is that of test particles, and $\hat{k}\cdot\hat{p}$ represents

the cosine of the angle between the direction of the incident electron of momentum p and the emitted photon of energy k.

Bremsstrahlung cross sections are well known[94] and may be projected onto Legendre polynomials to simplify their evaluation[63]. Cross sections exhibit relativistic behavior and are maximum in the direction of the electron's velocity. Figure 4-6 plots the evaluated cross sections for electron energies of 50 and 200 keV. Ion-electron collisions dominate at lower energies while electron-electron collisions become significant at the highest energies in the range of interest. The Bethe-Heitler model including the Elwert factor is used for electron-ion collisions and the Haug model is used for electron-electron collisions including the Coulomb correction factor.

4.4 Current Profile Modification Through $n_{\parallel}$ Spectral Variations Using CQL3D

CQL3D was used to study the current profile produced while varying the initial value of the launched $n_{\parallel}$. A coupling code, which is discussed in detail in Chapter 7, was used to calculate the $n_{\parallel}$ spectra used as inputs to CQL3D. Both CD and CCD spectral lobes along with their calculated amplitudes and widths were used. It should be mentioned that radial diffusion and electric field effects were not included in the model. The plasma used for the study was shot number 1030612013, a low density H-mode, specifically designed to be a LH target. Time traces of plasma quantities are shown in Figure 4-7. The plasma current was about 600 kA and 3 MW of ICRF heating were used to produce a central electron temperature of about 3.5 keV. The CQL3D analysis was performed for a single time slice, 1.0 s into the discharge. The density profile at 1.0 s is shown in Figure 4-8.

The amount of LH current produced along with the spatial location and width were studied using 60°, 90°, and 120° CD phasing with 2.0 MW of grill power. The power at the grill is divided spectrally according to results from the coupling code. The results are summarized in Table 4.2.

Table 4.2: **CQL3D Input Parameters and Results**

Run	Phasing (deg.)	P_{grill} (MW)	$n_{\parallel}$ CD	Power (MW)	$n_{\parallel}$ CCD	Power (MW)	I_{LH} (kA)	R_{max} (r/a)
7	90	2.0	2.33	1.42	6.98	0.44	202	0.75
8	90	2.7	2.33	1.92	6.98	0.59	287	0.75
9	120	2.0	3.09	1.14	6.20	0.48	120	0.80
10	120	2.7	3.09	1.54	6.20	0.65	159	0.80

It was found immediately that the 60° case could not be studied due to poor wave accessibility since the central value of $n_{\parallel}$ was low at 1.55 and the density was high from the H-mode edge. Waves from the 90° and 120° cases were accessible and able to drive current. The ray trajectories and quasilinear power absorption are shown for these cases in Figure 4-9. Blue indicates that the ray has most of its power while locations where the color changes along the trajectory designate power absorption. When the ray is red most of the power has been absorbed. Both cases have the same number of rays and use four poloidal launch points. Many of the rays trajectories for 120° are identical, but the evolution of the trajectories in the 90° case created many more distinct paths. The deviation between the two cases is purely a result of different initial values of $n_{\parallel}$, most of the rays for 90° are near 2.3 while rays for 120° are near 3.1.

90
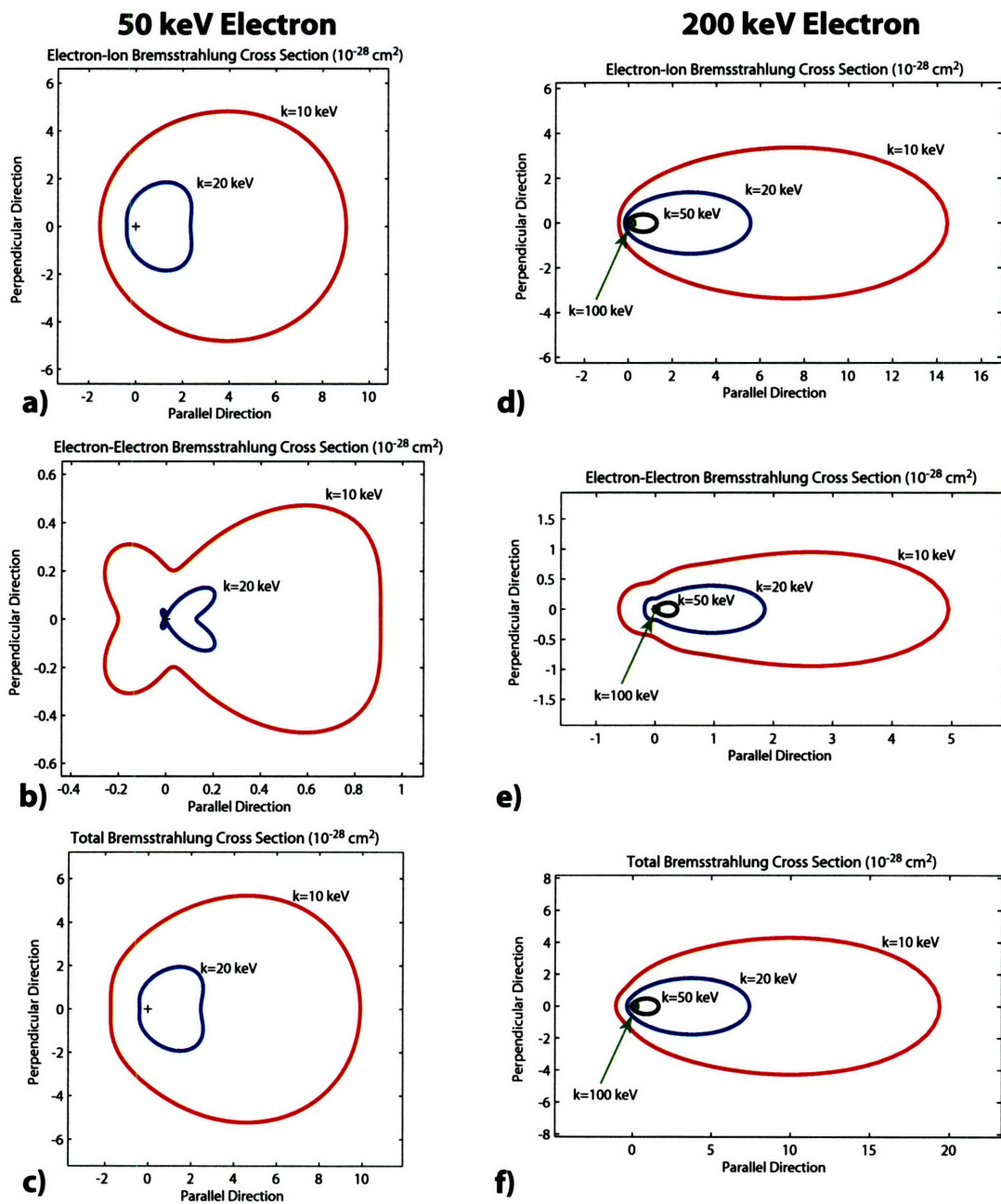
Figure 4-6: Bremsstrahlung cross sections for 50 and 200 keV electrons. Panels a), b), and c) plot the e-i, e-e, and total emission cross sections for a 50 keV electron radiating at 10 and 20 keV. Panels d), e), and f) plot the e-i, e-e, and total emission cross sections for a 200 keV electron radiating at 10, 20, 50, and 100 keV.
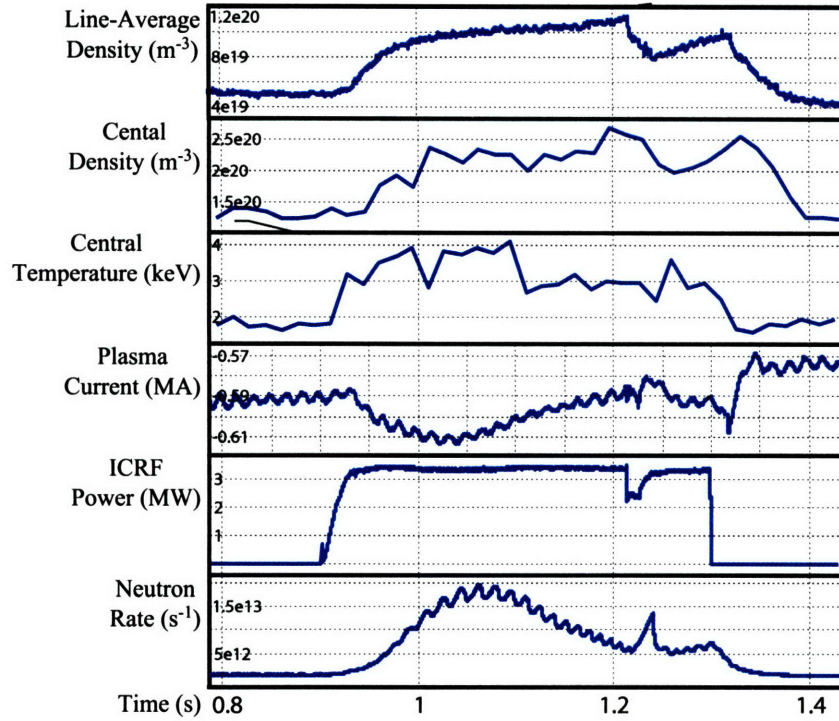
Figure 4-7: Time traces of plasma parameters for shot number 1030612013, a low density H-mode, designed for compatibility with LHCD.
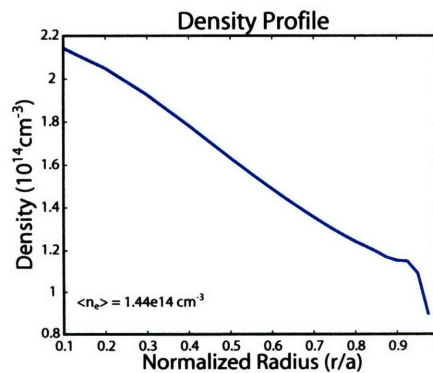
Figure 4-8: Density profile for shot number 1030612013, showing the H-mode edge and a central density of 2.1×10^{20} m^{-3}.

90 Degree CD Phasing
LH Power Absorption Along Rays

120 Degree CD Phasing
LH Power Absorption Along Rays
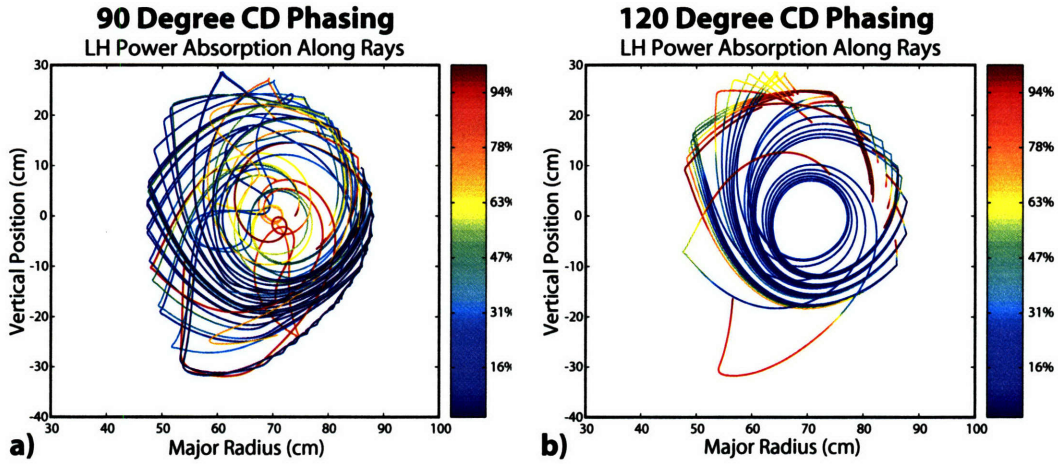
Figure 4-9: Ray trajectories and power absorption along the rays for 90 and 120 degree CD phasing.

In examining the ray trajectories it appears that most of the power is absorbed in the outer half of the plasma for both cases. This is made clearer by looking at the power deposition profiles which are plotted in Figure 4-10 along with the resulting current density profiles. The effect of the CCD spectral lobe is seen both in the power deposition and current density profiles. In the 90° power deposition, the outermost peak indicates that the high $n_{\parallel}$ CCD rays are damped near the edge. This is confirmed by the presence of negative current driven at the edge. 120° phasing exhibits a similar, but more subtle effect. The CCD spectral lobe in this case has a lower $n_{\parallel}$ meaning that the waves will not be as readily absorbed at the edge and this manifests itself as a broad single peak in the power deposition. The combination of the CD and CCD power deposition create an overall narrower current density profile than observed in the 90° case. The magnitudes of the total driven LH current scale well with the simple $1/n_{\parallel}^2$ dependence of the current drive efficiency.

The distributions functions and resulting HXR energy spectra may also be compared for these two cases. Figure 4-11 shows contours of the distribution, 90° in panel a) and 120° in panel b). The quasilinear plateau is wider for the 90° case as expected since the initial value of $n_{\parallel}$ is lower. This also leads to the generation of a harder bremsstrahlung energy spectrum. The energy flux emitted along a central channel of the HXR camera is shown for both phases. The flux at higher energies is much greater for 90° than 120° and is shown in Figure 4-12.

4.5 Compound Spectra Modeling Using CQL3D

A second LH antenna is planned for C-Mod allowing the use of compound spectra. A fourth klystron cart will also give an additional 1 MW of source power. CQL3D was used to explore the use of compound spectra to modify the current profile. This study was also based on shot 1030612013. Since 60° phasing was not accessible for this plasma it is not studied. The grill power was increased to 2.7 MW, in accordance with the extra power available from the fourth cart. One spectrum was kept fixed at 90° CD phasing while the second spectrum was systematically varied in 30° increments up to 180°. Two control cases, runs
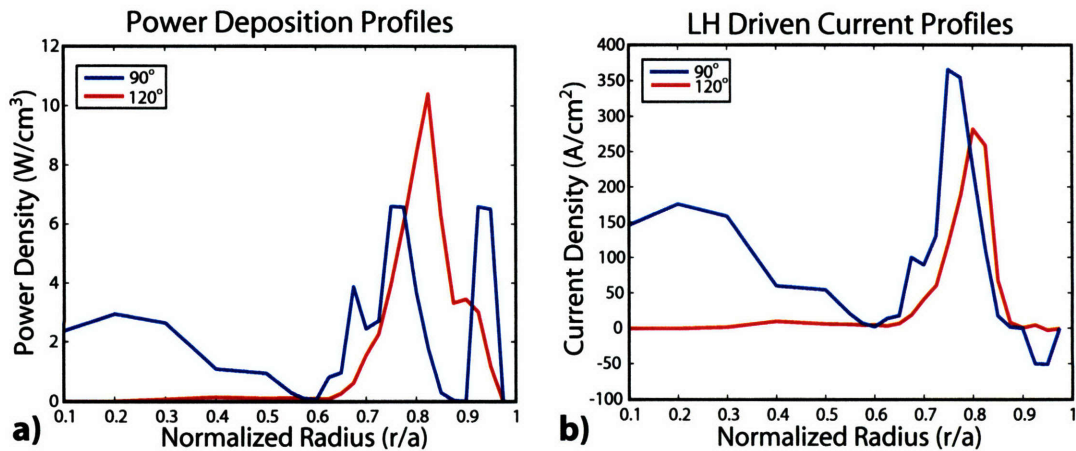
Figure 4-10: Radial profiles of power deposition and current density for 90 and 120 degree CD phasing.
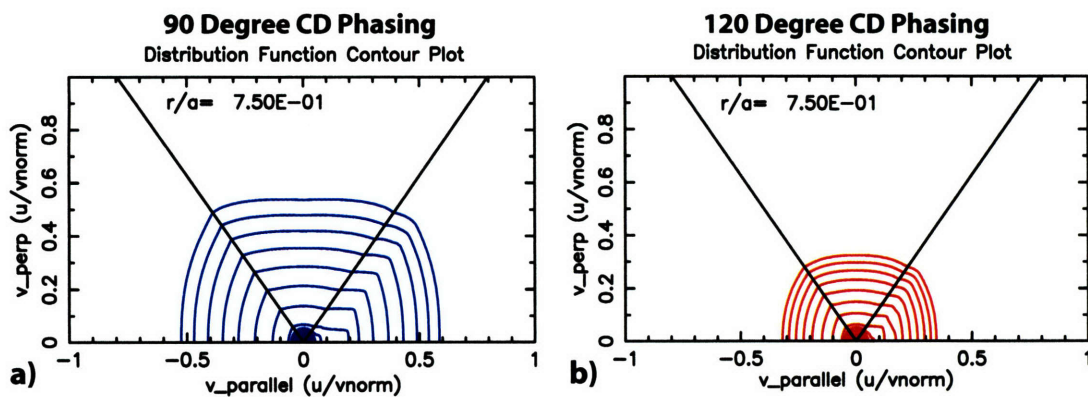
Figure 4-11: Contour plots of the distribution function for 90 and 120 degree CD phasing.
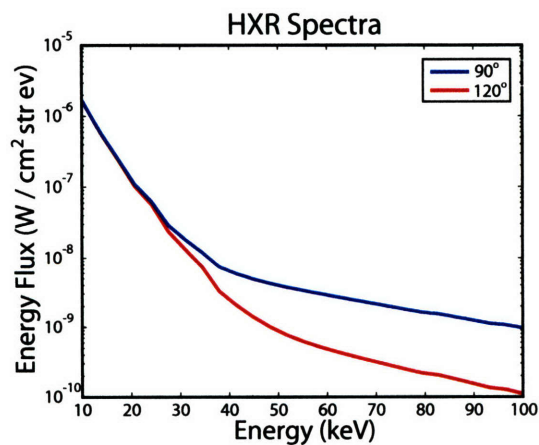
Figure 4-12: Bremsstrahlung energy flux emitted along a central viewing chord of the HXR diagnostic for 90 and 120 degree CD phasing.

8 and 10, were also run with 2.7 MW using purely 90° and purely 120° for comparison to the compound cases. Power division was also studied between using two klystron carts for each antenna in runs 11 through 13. Runs 20 through 22 split the power by using the 90° phasing on three carts while the fourth carts' phase was adjusted in 30° increments. This type of power division is consistent with keeping the current LH system as is and designing a second antenna based on using four klystrons. Results from the study are summarized in Table 4.3.

Table 4.3: **CQL3D Input Parameters and Results for Compound Spectra**

Run	Phasing (deg.)	P_{grill} (MW)	$n_\parallel$ CD	Power (MW)	$n_\parallel$ CCD	Power (MW)	I_{LH} (kA)	R_{max} (r/a)	FWHM (r/a)
8	90	2.7	2.33	1.92	6.98	0.59	287	0.75	0.08
10	120	2.7	3.09	1.54	6.2	0.65	159	0.80	0.08
11	90, 120	2.7	2.33	0.96	6.98	0.30	290	0.75	0.14
			3.09	0.77	6.20	0.32			
12	90, 150	2.7	2.33	0.96	6.98	0.30	252	0.55, 0.68	0.30
			3.87	0.63	5.42	0.43			
13	90, 180	2.7	2.33	0.96	6.98	0.30	189	0.68	0.06
			4.65	0.53	4.65	0.53			
20	90, 120	2.7	2.33	1.42	6.98	0.44	307	0.75	0.11
			3.09	0.40	6.20	0.17			
21	90, 150	2.7	2.33	1.42	6.98	0.44	294	0.68	0.09
			3.87	0.33	5.42	0.22			
22	90, 180	2.7	2.33	1.42	6.98	0.44	252	0.68, 0.78	0.16
			4.65	0.27	4.65	0.27			

Not surprisingly, the 90° and 120° control cases have the same shaped power deposition and current density profiles when going from 2.0 to 2.7 MW. The only difference is the increase in magnitude. The compound cases exhibit more interesting behavior. Figure 4-13 plots the ray trajectories and power absorption for runs 11, 12, and 13. Run 11, the 90° and 120° compound case, shows little change from the pure 90° case and is shown in panel a) of Figure 4-9. This is due to the initial values of $n_\parallel$ being relatively close, 2.3 to 3.1. In panel b) of Figure 4-13 the absorption is much broader than in the pure 90° case. When examining the 90° and 180° case in panel c) it is not clear what the change in deposition is and the radial profiles must be used. In all cases, however, ray trajectories cover the plasma volume well.

The power and current deposition profiles for the compound cases are shown in Figures 4-14 and 4-15. The 90° and 120° compound case looks like the superposition of the pure 90 and 120 degree cases for both profiles, since the $n_\parallel$ are near each other the interaction between the rays and absorption is not as strong as in other cases. The overall current is about the same, 290 kA, as the 287 kA driven by 2.7 MW at using pure 90° phasing.

The 90° and 150° compound case is very interesting in that the both profiles are much broader than the profiles of the non-compound spectra. This is most likely due to the 150° spectrum having a broad deposition profile which pushes more electrons to higher velocity over a broad spatial region. The low $n_\parallel$ from the 90° spectrum is then able to damp more readily across this broad spatial extent.

Interestingly enough, a similar argument as above may be used to explain the narrowing of the profiles for the 90° and 180° compound case. Here the 180° spectrum may populate the higher velocities of the distribution function over a narrow spatial extent. This time the low $n_\parallel$ from the 90° spectrum damps in this narrow region.
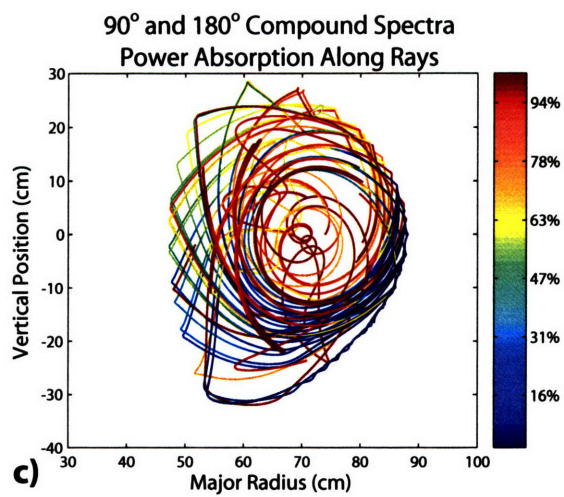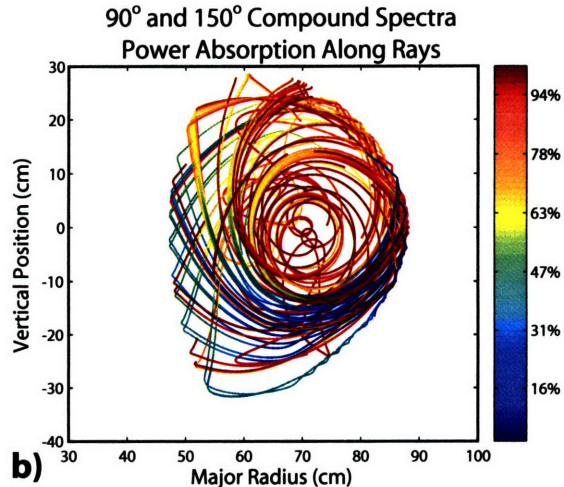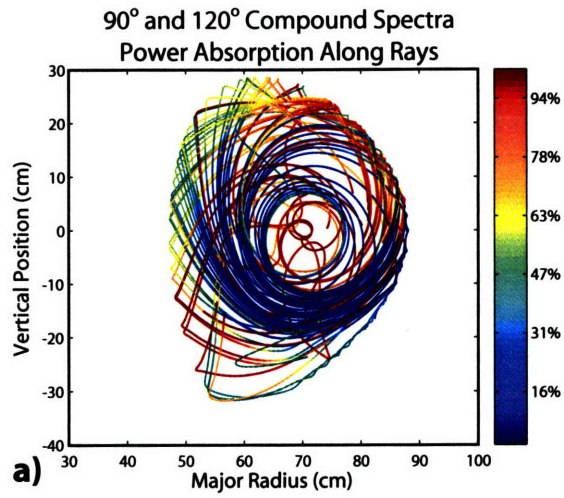
Figure 4-13: Compound ray trajectories and absorption for a) 90° and 120°, b) 90° and 150°, c) 90° and 180° phasing.
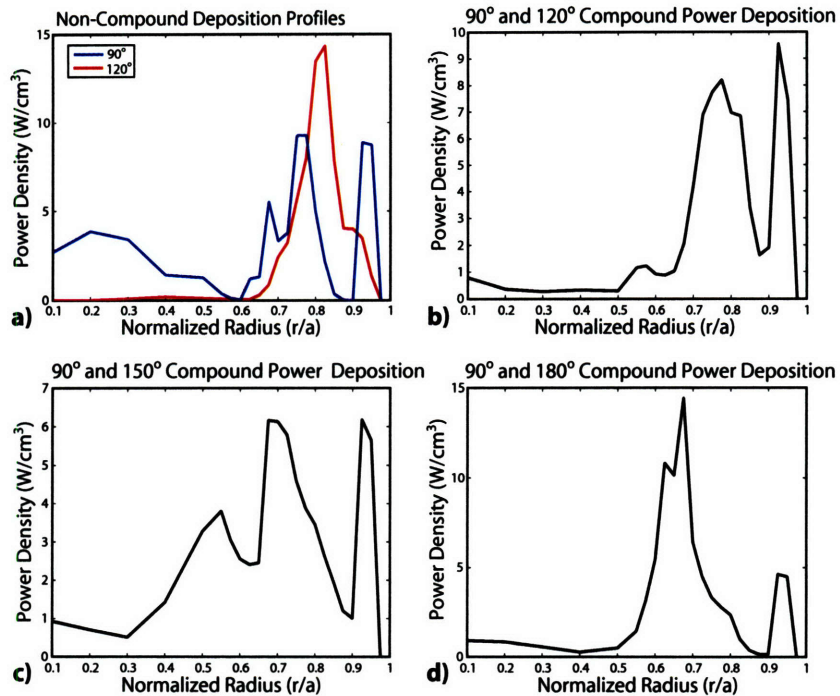
Figure 4-14: Power deposition profiles for a) 90° and 120° control cases, b) 90° and 120°, c) 90° and 150°, d) 90° and 180°.

The broad and narrow results in the profiles were somewhat unexpected and indicate that the interactions of the rays between the two antennas play a very important role in determining the resulting current profile. Comparing the results from Table 4.3 the power distribution between the two antennas also significantly affects the resulting current profile. Both the $n_{\parallel}$ spectra and the power level may be adjusted during compound experiments to modify the shape of the current profile.

4.5.1 Implications for the Design of a Second LH Antenna

The power division results of Table 4.3 allow for the comparison of two means to build the second antenna. The first way, option 1), divides the power equally between the two antennas so each grill has 2 MW of source power and two klyston carts. The second way, option 2) is to divide the power by having 3 MW (three carts) on one antenna and 1 MW (one cart) on the second.

Option 1) has the benefit that the power density at the grill may be lowered and reduce the risk of arcing. This method would give more utilization of the klystrons if a power limit is reached below each klystron's maximum output level. Option 1) also allows troublesome aspects of the current LH system to be addressed. Option 2) simplifies the system design, reducing the engineering burden while allowing the present LH system to stay intact.

CQL3D was used to study these two options and see if there were any compelling physics reasons to chose one option over the other. This is done by directly comparing runs 11, 12, and 13, which used option 1) to runs 20, 21, and 22, which used option 2).

First, runs 11 and 20 using 90° and 120° compound spectra may be compared. The total current driven was similar for both runs and there was very little difference between
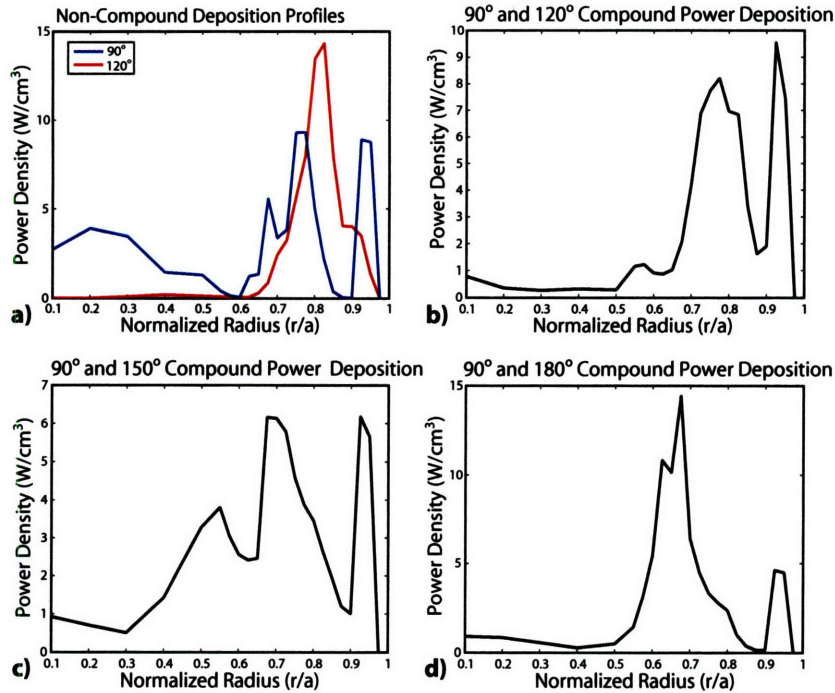
Figure 4-15: Current density profiles for a) 90° and 120° control cases, b) 90° and 120°, c) 90° and 150°, d) 90° and 180°.

the profiles. This was again a consequence of the $n_\parallel$ values being similar at 2.3 and 3.1. Spectra with a greater difference in $n_\parallel$ showed a more pronounced effect between option 1) and 2). Dramatic differences are observed when runs 12 and 21, which used 90° and 150° compound spectra are compared. The total current driven is 42 kA higher for option 2) and the profile went from being very broad in run 12 to very narrow in run 21. Comparing runs 13 and 22 also show significant changes using 90° and 180° compound spectra. Option 2) had 63 kA more current and the profile became broader from run 13 to run 22.

Option 2) drives more current since more of the total power is launched in the CD direction. Changes in the resulting current profile are significant, but do not exhibit a consistent pattern as one case went from broad to narrow while another case went from narrow to broad. From a physics standpoint driving as much current as possible is desirable in generating AT plasmas so option 2) is preferred.

4.6 LH Power Threshold Study for Meaningful Results from the HXR Diagnostic Using DKE

Setting up cases to run with DKE is relatively simple and each run takes only about 5 minutes to complete when performed on *pcdaqhxr2*, the time is about doubled when a typical C-Mod workstation is used. This makes adjusting parameters and iterating much easier than using CQL3D where runs are more cumbersome to set up and typically take hours to complete when many rays are used.

The count rate of the HXR diagnostic was studied as the LH power level was varied. This information allows the signal to noise to be estimated when compared to background
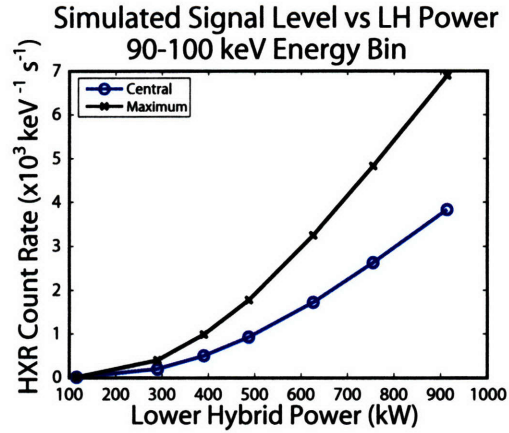
Figure 4-16: Count rate at the detector as a function of power for the 90-100 keV energy bin.
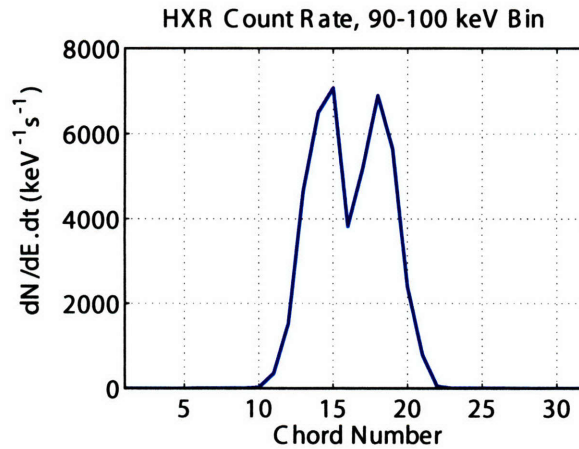
Figure 4-17: Count rate as a function of chord number for the 90-100 keV energy bin.

measurements in Chapter 5. A low density H-mode, shot 1030530014, was used for the study. This shot is very similar to 1030612013, which was used in the preceding CQL3D analysis. The power level was adjusted from 100 to 900 kW by setting the level of D_{ql}. The count rate at the detector is plotted as a function of LH power in Figure 4-16. The detector response function reduces this count rate by about a factor of two. Both the count rate at the central channel and the maximum count rate are shown for the 90-100 keV energy bin. Since the current is driven off-axis, the maximum count rate does not occur on the central channel, but rather is shifted out by about a channel or two as shown in Figure 4-17.

The count rate is a non-linearly increasing function of the LH power. Once the power level reaches about 500 kW, however, the count rate increases linearly as the power is further raised. It is important to point out that the signal to noise of the diagnostic is dependent on the other plasma quantities such as the density and ICRF power level. This parameter space must be explored experimentally to find the actual limits and requirements for reliable data from the HXR diagnostic.

Chapter 5

HXR Diagnostic

The purpose of the hard x-ray (HXR) diagnostic is to interpret lower hybrid performance in terms of controlling the current profile and modifying the electron distribution function. Antenna parameters such as $n_{\parallel}$, and forward and reflected power provide boundary conditions, but not a measurement of the wave when coupled to the plasma. The best means of measuring LH performance comes from examining the fast electron population on which the waves damp. The simplest and most easily observable process is bremsstrahlung emission. Fast electrons collide with ions or bulk electrons and radiate in the HXR region of the spectrum. Regions within the plasma will radiate more or less depending on where the waves are damping. This is characterized by the local plasma emissivity $j(h\nu, \bar{x}, \theta, t)$. Emissivity has units of $Jm^3 str^{-1} s^{-1}$ and is a function of energy, position, angle, and time. If the emissivity is known everywhere for a given energy bin, say 100-120 keV, then it gives the location of the fast electrons and by assumption, the location of the current drive. The energy dependence of the emissivity gives information about the electron distribution function when coupled to a model. A model is required since bremsstrahlung radiation is continuous, there are no characteristic spectral lines as particles can radiate at any frequency up to their total kinetic energy, meaning there is no direct mapping back to the distribution function. HXR modeling is discussed in detail in chapter 4.

This chapter covers the design and as built specifics of the HXR diagnostic. Section 5.1 discusses the application of of a pinhole camera for HXR emission and overall characteristics such as spatial resolution and geometry. The implementation on C-Mod and experimental layout is covered in section 5.2. Section 5.3 goes over the nuclear electronics needed to convert photons into useful data. The analysis software and data management are covered in sections 5.4 and 5.5. Section 5.6 discusses mechanical aspects of the HXR diagnostic such as shielding and the support structure. Section 5.7 wraps up the chapter by going over the final details needed before taking LHCD data such as alignment and calibration.

5.1   Pinhole Cameras

The ideal measurement is to have the local emissivity at every point in the plasma. A pinhole camera comes as close to this as possible by giving a number of chord integrated emissivities. Once these values are measured, an inversion technique such as Abel inversion or some other analysis is employed to recover the local emissivity mapped to a flux surface. To get the spectral information a technique known as pulse height analysis (PHA) is used. Detectors and electronics are coupled together to provide a system that produces a voltage

C-Mod Cross Section

HXR Diagnostic

a_c=5 mm a_d=5 mm

D=123 cm   d=40 cm
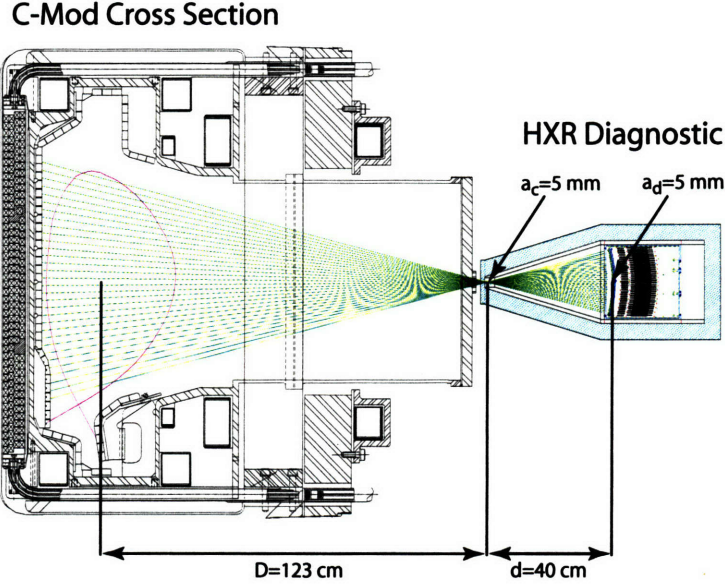
Figure 5-1: Cross sectional view of C-Mod with HXR diagnostic and viewing chords.

pulse corresponding in amplitude to the photon energy. Counting over time windows allows spectra to be built.

A pinhole camera is one of the simplest imaging devices possible, and is also well suited to applications with limited access. On C-Mod placing the pinhole near the port minimizes the space required for the diagnostic.

The three main characteristics of the camera are spatial, temporal, and energy resolution. All three quantities are linked through counting statistics. As typical of counting experiments, a Poisson distribution is assumed, meaning the standard deviation is just the square root of the number of counts. If the count rate is high enough good spatial, time, and energy resolution may all be obtained simultaneously, otherwise there is a trade off. Intuitively, increasing the pinhole size gives more signal at the expense of spatial resolution. Examining the geometry of a central channel distance d from an aperture of size a_c which is a distance D from the center of the plasma gives the expression

$$\Delta r = (1 + D/d)a_c.$$

In reality the measurement will combine a number of chords and involve a reconstruction so spatial resolution is not precisely defined. Δr may also be estimated as the plasma size divided by the number of chords $2a/N_{chords}$. The viewing chords are shown along with the geometry in Figure 5-1. Time and energy resolution are set either through counting statistics or detector resolution. Count rates are typically limited, so the ultimate resolution is determined by the bin size. Time resolution may be traded for energy resolution and vice versa through adjusting the bin size to attain the desired statistical accuracy.

The overall count rate is determined by the geometrical factor, or étendue of the system. The étendue is set by the pinhole and detector sizes and the distance between them

$$\varepsilon = a_c^2 a_d^2/d^2, \tag{5.1}$$

102
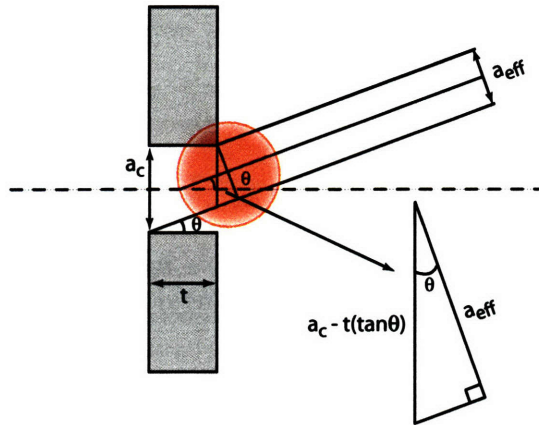
Figure 5-2: Geometry for determining the effective viewing area for a thick pinhole.

and has units of $m^2 str$. It is the area times the solid angle of the chord.

5.1.1 Design Features

C-Mod's HXR system geometry was designed to maximize the number of counts. To increase the étendue, d was made as small as possible such that the plasma still fills the view. The detector size was set by evaluating the array size and comparing it to the space available outside the port. The collimator size provides the desired spatial resolution which is 1.5-2 cm. Changing the collimator size is the knob for adjusting the spatial resolution if needed. HXR makes use of fast digitization signal processing so the bin sizes for time and energy are set in software and may be adjusted to maintain a balance of statistics and temporal resolution. Fast digitization is discussed in detail in Section 5.3.1. C-Mod's HXR system is composed of 32 channels as a balance between spatial resolution requirements and cost.

Using a pinhole camera for hard x-rays requires a few modifications, particularly with the shield and pinhole design. Shielding is needed to keep unwanted background from the detectors and is discussed in Section 5.6. The pinhole is better described as an aperture and needs to have some thickness to stop background emission and give the proper collimation for each chord. Adding thickness to the pinhole changes the geometrical factor by reducing the effective size of the aperture. This is shown in Figure 5-2. The étendue is now given by

$$\varepsilon = a_c a_{eff} a_d^2 / d^2,$$

with $a_{eff} = a_c \cos(\theta) - t \sin(\theta)$. Here θ is the angle from the center of the aperture to the center of a given detector. Each detector on the array is rotated to maximize a_{eff} forming an arc with the a radius of d, which is 40.4 cm. The geometry of the system with respect to the pinhole is listed in Table 5.1. The total viewing angle is 29°. For a pinhole with a thickness of 4 mm the étendue varies 23% from the central channels, 16 and 17, to the outer channels 1 and 32. Measurements of detector position are taken to the substrate of the detector and have an uncertainty of 0.8 mm. The distance from the center of the cental column to the pinhole is 187 cm, the inner wall position is 38 cm, and the magnetic axis is about 64 cm. The port layout and experimental setup is covered in the next section.

Table 5.1: **Detector geometry relative to center of pinhole.**

Channel	x (cm)	y (cm)	θ (degrees)	ε (10^{-3}mm^2 str)
1	39.08	10.15	14.5	2.94
2	39.24	9.51	13.6	3.00
3	39.39	8.86	12.6	3.07
4	39.53	8.22	11.7	3.13
5	39.66	7.57	10.8	3.19
6	39.78	6.91	9.8	3.25
7	39.88	6.26	8.9	3.31
8	39.98	5.61	8.0	3.37
9	40.07	4.95	7.0	3.43
10	40.14	4.29	6.1	3.48
11	40.21	3.63	5.1	3.54
12	40.26	2.97	4.2	3.59
13	40.30	2.31	3.3	3.65
14	40.34	1.65	2.3	3.70
15	40.36	0.98	1.4	3.75
16	40.37	0.32	0.5	3.80
17	40.37	-0.34	-0.5	3.80
18	40.36	-1.00	-1.4	3.75
19	40.34	-1.67	-2.4	3.70
20	40.30	-2.33	-3.3	3.65
21	40.26	-2.84	-4.2	3.59
22	40.21	-3.65	-5.2	3.54
23	40.14	-4.31	-6.1	3.48
24	40.06	-4.97	-7.0	3.42
25	39.97	-5.62	-8.0	3.37
26	39.88	-6.28	-8.9	3.31
27	39.77	-6.93	-9.9	3.25
28	39.65	-7.59	-10.8	3.19
29	39.52	-8.23	-11.7	3.13
30	39.38	-8.88	-12.7	3.06
31	39.23	-9.53	-13.6	3.00
32	39.07	-10.17	-14.5	2.94
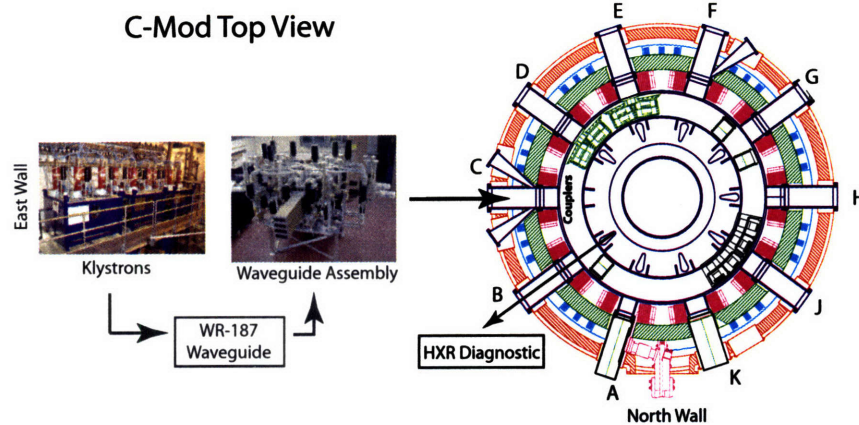
Figure 5-3: C-Mod cell layout showing port arrangement and the location of the lower hybrid and HXR diagnostic.

5.2 Experimental Layout

C-Mod has 10 horizontal ports labeled A through K and excluding I. Ports D,E, and J are filled by ICRF heating antennas and C-port now houses the LH grill. The HXR diagnostic is located at B-port with a midplane view of the poloidal cross section. Figure 5-3 shows a top view of C-Mod and the port layout. HXR diagnostics for current drive can be implemented using a tangential or perpendicular view with respect to the toroidal magnetic field, or more appropriately the current. A tangential view is not possible on C-Mod since there are no tangential ports available. A tangential view may become available in the future if the D and E ICRF antennas are combined to use a single port. One possible benefit of looking tangentially is increased signal, bremsstrahlung cross sections are about a factor of 2-10 greater, depending on the energy. The degree to which tangential geometry is favorable for increased signal must be evaluated carefully while considering the actual viewing geometry. The emission is chord integrated and electrons along the view will not be moving in the favorable direction throughout. Another benefit to looking tangentially that the reconstruction simplifies since the flux surfaces now look circular, and techniques like Abel inversion may be used. A tangential view was used for diagnosing the lower hybrid current drive on PBX-M[95]. The HXR measurements may also be made using a perpendicular view as shown with great success on Tore Supra[96]. Perpendicular measurements are also used on ASDEX[97], JET[98] and JT60-U[99]. HXR measurements on Alcator C were made using individually collimated channels viewing up from underneath the machine[100].

B-port itself is very crowded, many diagnostics and systems are forced to share this space. The flange and an internal view of the port extension are shown in Figure 5-4. The names and locations of other diagnostics sharing the flange are also shown in this figure. Chief among them are the lithium pellet injector (LPI) with stereo cameras and the HiRex. LPI is used to make internal field measurements as well as study zonal flows and ablation physics. HiRex measures toroidal plasma rotation. The ports labeled "periscope" and "gas jet" contain a reentrant tube and a gas line, both of which could possibly block part of the view for HXR. A system was included in the HXR diagnostic for alignment to make sure the views are clear from obstruction and also give an accurate location of the chords for mapping data and reconstruction. Details of the alignment system are covered in section
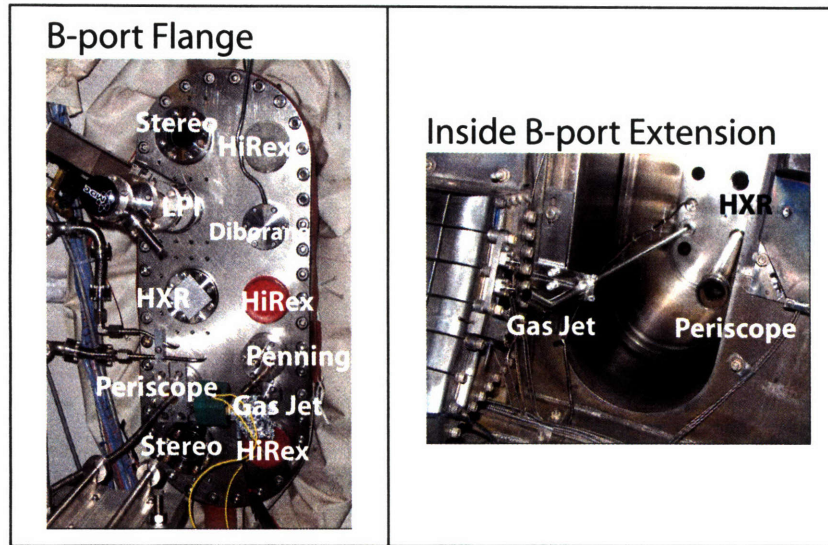
Figure 5-4: External and internal photographs of B-port with key diagnostics labeled.

5.7. HXR has a 3 3/8" flange on the C-side of the port. The vacuum window is 1 mm thick aluminum and has an aperture of 1.5". B-port is also the emergency exit port which complicates the structural support design and alignment procedures. This also means that whenever there is a manned entry into C-Mod, HXR, along with all the other diagnostics on the port, must be completely removed.

5.3   Nuclear Electronics

The simplest way to describe the electronics for nuclear spectroscopy is to follow what happens to a photon as it strikes a semiconductor detector in a typical pulse height analysis setup. Ideally the photon is absorbed through the photoelectric effect and produces a number of electron-hole pairs corresponding to the incident energy. The bias voltage accelerates the charges to a set of electrodes that are attached to a charge sensitive preamplifier. The preamplifier integrates the current and raises the signal level to millivolts. The shaping amplifier steps the signal up to volts and also shapes the pulses for amplitude measurement. The height of the pulse is proportional to the incident energy and is measured by discriminators and then binned by a counter. Steps in pulse processing are shown graphically in Figure 5-5. A typical experimental setup has the preamplifier located near the detector and the rest of the electronics located in a rack in the form of separate NIM bin modules. These methods were perfected in the 1960's and have seen little change since.

This type of system works great in applications where a small number of channels are needed. In systems where a large number of channels are required, such as on C-Mod, this setup becomes extremely costly. Cost and spatial constraints as well as the desire for updated technology allowing for greater flexibility guided the design of C-Mod's HXR system.

C-Mod's HXR system is composed of 32 channels as a balance between spatial resolution requirements and cost. Detectors and pulse processing electronics are integrated into a

106
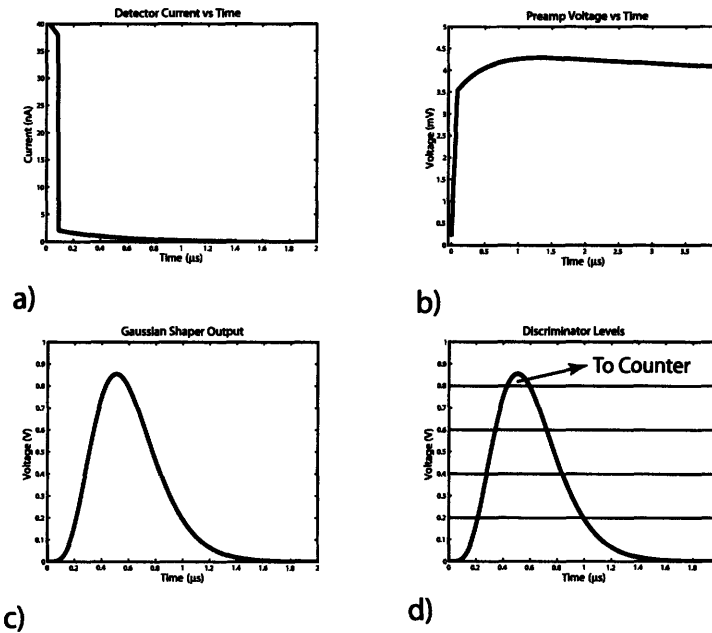
Figure 5-5: Typical pulse shapes during different stages of signal processing for a PHA system. a) Detector current pulse, b) Integrated preamplifier voltage output, c) Shaped signal, d) Discriminator levels measuring pulse height

compact and modular package making extensive use of printed circuit board and surface mount technology. The system also makes use of fast digitization and software signal processing techniques described in sections 5.3.1 and 5.4. Sections 5.3.2 through 5.3.6 give more background into preamplifier and shaping circuits as well as discuss the details of C-Mod's electronics including detectors. The final two sections, 5.3.7 and 5.3.8, go over other relevant technology and the possibility of real time feedback control for the LH using HXR measurements.

5.3.1 Fast Digitization

As mentioned above, applying the usual nuclear electronics for a multichannel system not only becomes costly, but bulky as well. Figure 5-6 shows the signal flow in a traditional system and fast digitization system. The front end electronics for both the traditional and fast digitization methods, are identical, the difference is changing the final destination of the pulses. In a typical setup each channel goes to a discriminator or a multichannel analyzer (MCA). For a 32 channel system this means an additional rack of either antiquated NIM bin technology or a bank of expensive MCAs.

Fast digitization[101] solves this problem by digitizing the raw pulses from the shaper and storing them for later analysis. For C-Mod this is done using two 16 channel D-TACQ boards, described in detail in section 5.3.2. This makes the system much cheaper and more compact. Fast digitization also allows for flexible binning in both time and energy. This means that if the signal level is low the counting time may be increased and the energy bins widened to ensure good statistics. If the signal level is high, finer bins may be used, giving

a) Typical PHA Electronics

Photons

Preamp

Shaping Amplifier

Discriminator/Counter or MCA

Detector

b) Fast Digitization

Photons

Preamp

Shaping Amplifier

Fast Digitizer

Detector
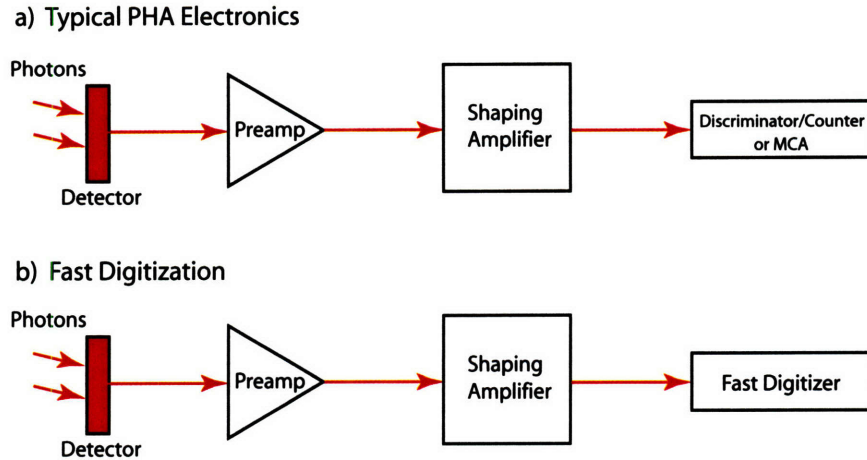
Figure 5-6: a) Typical signal flow for nuclear spectroscopy. b) Fast digitization signal flow is identical up to the back end electronics where the MCA is replaced by a digitizer capable of recording individual pulses.

higher temporal and energy resolution. Since the raw pulses are digitized it is possible to reduce pile up by fitting the pulses in question through software and recovering the information. This reduces the overall dead time of the system and allows access to higher counting rates. Traditional systems discard or reject these counts leading to increased dead time. Seeing the raw signal is also valuable in diagnosing any noise problems. Electronic noise may be distinguished from background by examining the shape and frequency of the raw voltage signal. Background pulses may be identified directly while electronic noise is typically oscillatory in character. In the C-Mod cell the HXR voltage time history can be compared to other events to identify sources of pickup. For example an increase in noise at a frequency of 10 kHz was observed during the 50 ms firing of the old diagnostic neutral beam.

5.3.2 Detectors

There are two main types of detectors used for hard x-ray spectroscopy, scintillators and semiconductors. Scintillators are based on fluorescence, a process of exciting molecular states in a crystal and observing the photons released during decay to the ground state. The net effect is to convert a short wavelength photon into a longer one, typically visible, that can be easily collected. In semiconductor detectors incident photons create conduction electron-hole pairs that are accelerated to electrodes by an applied electric field. Both detector types have been used extensively so choice depends upon the specifics of the measurement to be made.

As discussed in section 5.2, space near the machine is very limited so the whole diagnostic needs to be as compact as possible. The use of cryostats or magnetic shielding should be avoided leading to choosing a detector that operates at room temperature and in the presence of a magnetic field. A large number of detectors will be operated together as an imaging device, requiring a modular and easily reproducible package. Good absorption efficiency in the energy range of 20-250 keV is also necessary to achieve both compact size and high count rates. The constraint on energy resolution is not nearly so restricting.

Bremsstrahlung emission is continuous so a resolution around 10% for the energy range of interest should not limit the performance of the diagnostic.

Scintillators such as NaI have long been used in conjunction with photomultiplier tubes, or PMTs to make such measurements. PMTs are very sensitive to magnetic fields and require careful shielding to avoid perturbing the photoelectrons. The PMTs are of large size themselves and thus scintillators coupled to PMTs are not considered viable options. It is possible, however, to couple a scintillator and Si diode into a photodiode detector, to overcome the shielding and size difficulty. The scintillator most commonly used for this is CsI since it emits light in a region where the Si photodiode has high quantum efficiency. CsI is inherently too slow for the desired count rate with a rise time of about $4\mu s$. The second problem arises from the noise induced from the Si diode. The noise level restricts the lowest energy that can be resolved to around 100 keV[102].

Semiconductors such as Ge and Si have been used extensively. Ge in particular has found widespread use in spectroscopy because of its excellent energy resolution. Si works well for low energy applications. Properties of commercially available semiconductor detectors are listed in Table 5.2. Detectors made of materials such GaAS and PbI_2 are not considered since they are mostly in the research stage of development. The detector type is chosen by comparing different physical properties to best match the design requirements. Comparing absorption efficiencies it is apparent that Si has too low a value owing to low Z and low density. In practice Si detectors are used up to about 30 keV and are not applicable to measuring the desired range of 20-250 keV. The other detectors that are considered have reasonable stopping efficiencies, and are composed of materials with high Z and high density.

Table 5.2: **Summary of semiconductor detector properties**

Detector	CZT[1]	CdTe	Ge	Si	HgI$_2$
Atomic Number	49.1	50	32	14	62
Density (g/cm^3)	5.78	5.85	5.33	2.33	6.4
Linear Attenuation[2](cm^{-1})	9.3,1.2,0.3	9.8,1.3,0.3	3.0,0.7,0.3	0.4,0.3,0.1	22,2.5,0.4
Absorption Efficiency[3](%)	94,31,9	95,32,10	58,19,9	12,8,4	100,53,11
Energy Resolution[4](%)	6[5]	4-10[6]	0.5-2[7]	NA	2-10[8]
Band Gap (ev)	1.572	1.5	0.67	1.12	2.13
Pair Creation Energy (eV)	4.64	4.43	2.95	3.62	4.2
Resistivity (Ωcm)	3×10^9	10^9	50	¡10^9	10^{13}
Electron Mobility (cm^2/Vs)	1350	1100	3900	1400	100
Hole Mobility (cm^2/Vs)	120	100	1900	480	4
Electron Lifetime (s)	3×10^{-6}	3×10^{-6}	$>10^{-3}$	$>10^{-3}$	10^{-6}
Hole Lifetime (s)	10^{-7}	2×10^{-6}	10^{-3}	2×10^{-3}	10^{-5}
$(\mu\tau)_e$ Product (cm^2/V)	$3\text{-}5\times10^{-3}$	3×10^{-3}	>1	>1	10^{-4}
$(\mu\tau)_h$ Product (cm^2/V)	8×10^{-5}	2×10^{-4}	>1	≈1	4×10^{-5}

The next property to consider is the band gap energy. The band gap needs to be high enough to prevent thermal electrons moving to the conduction band. Ge's low band gap requires cooling to liquid nitrogen temperature for operation. Thus Ge detectors require cryostats, and due to size constraints Ge detectors cannot be used. All other detectors have large enough band gaps making them suitable for room temperature operation.

The final property to consider is the electron and hole mobilities. HgI$_2$ has a low electron mobility and an extremely low hole mobility. From the hole mobility the count rate may be estimated. Taking a voltage of 500 V across two mm gives a hole velocity of about 6700 cm/s and so maximum charge collection time is 30 μs. If the pulses were packed as densely as possible without pileup this would give a rate of about 30 kHz which is too low. For this reason HgI$_2$ is ruled out. That leaves CZT and CdTe. All physical properties are similar with CZT having a slight advantage in all categories except hole mobility. In the past CZT has achieved better performance because of less impurities present from the manufacturing process. Manufacturing processes of CdTe have been improved to the extent that the difference in quality for CZT to CdTe can be negligible. The final choice comes down to choosing between the specific products of different manufacturers. Nearly all CZT detectors in the United States are made by eV Products. CdTe is primarily produced internationally with the major vendors being Eurorad in France and Acrorad in Japan. In terms of support and contacting a company it is much more practical to buy from the American vendor so CZT from eV Products was chosen.

Now that CZT has been chosen for the detector material it is important to examine its performance characteristics to understand its response to photons and practical considera-

---

[1]Cd$_{0.9}$Zn$_{0.1}$Te
[2]at 100, 250, 1000keV
[3]3mm thickness at 100, 250, 1000keV
[5]at 122keV
[6]eV Products
[7]Eurorad
[8]Ortec
[9]estimated from Constellation Technology

CZT Detector Efficiency
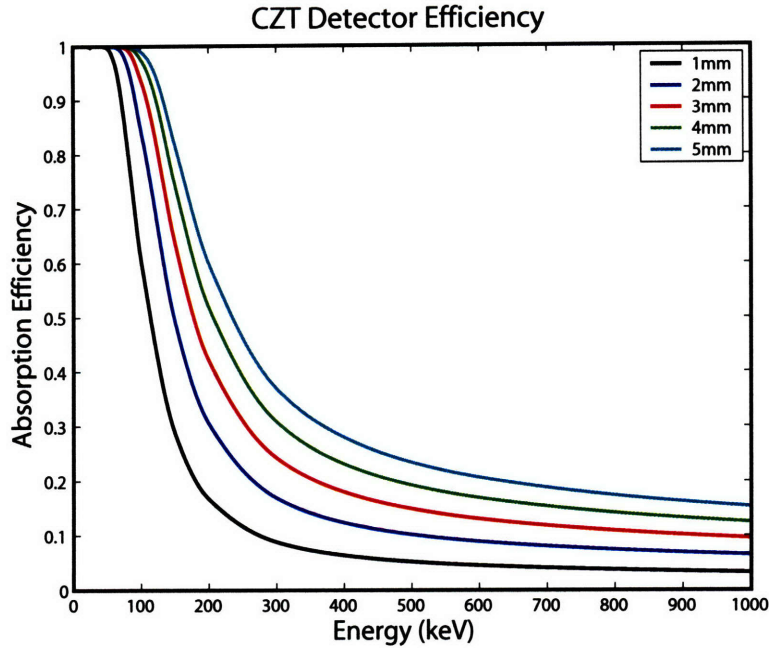
Figure 5-7: CZT absorption for for thicknesses one to five mm at energies up to one MeV. Data is from the NIST XCOM database.

tions such as determining the proper crystal dimensions. The cross sections and coefficients for CZT were obtained from the NIST XCOM database. With the cross sections the absorption as a function of thickness may be determined. This is shown in Figure 5-7. The ideal response of the detector would be complete absorption up to the maximum energy of 250 keV and then fall to zero for energies beyond this value. Absorption of higher energy photons increases the noise level and the effective dead time of the detector. It is therefore important to keep the detector as thin as possible while maintaining an acceptable level of absorption. For CZT in the energy widow up to 250 keV the appropriate thickness is two to three mm.

Examination of the charge transport helps to specify the thickness and appropriate shaping time for the electronics, as well as gaining understanding of overall detector response. Consider a photon of energy $h\nu$ being absorbed in a CZT crystal as in Figure 5-8. The photon is absorbed at a depth x from the cathode out of a total thickness d. A bias of V volts is applied. As soon as the photon is absorbed a current is induced on the electrodes. The charge created at position x is given by

$$Q = q\frac{h\nu}{W}$$

where q is the electron charge and W is the pair creation energy. Once the charge is liberated it begins to flow, but may become trapped due to impurities within the crystal. Not all the electron-hole pairs will reach the electrodes and the loss is characterized by the electron and hole lifetime, τ_e and τ_h, and is usually expressed in the form of a "$\mu\tau$" product, with μ being the mobility. The length the charge travels before it is trapped is given by the mean free path

$$\lambda_{e,h} = \mu_{e,h}\tau_{e,h}E,$$

111
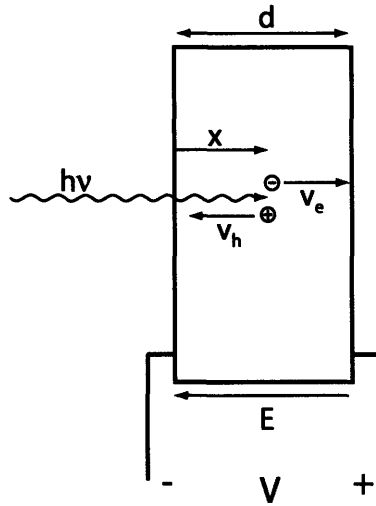
Figure 5-8: Semiconductor detector photoelectric absorption schematic.

where E is the electric field, V/d. Looking at CZT properties in Table 5.2 it is clear that electrons and holes flow at vastly different speeds, and as a consequence, the location where the photon is absorbed determines the charge collection time and efficiency.

The charge collection time is plotted in Figure 5-9 for a 100 keV incident photon, V_{bias}=200 V, d=2 mm, $\mu_{e,h}$ from table 5.2, and $\mu_e \tau_e = $ at 5×10^{-3} and $\mu_h \tau_h = $ at 8×10^{-5} cm^2 s/V are estimated from CZT simulation[103]. It should be noted that the $\mu\tau$ products can vary over an order of magnitude from detector to detector for holes and up to about a factor of five for electrons[104]. The collection time is limited by the hole mobility, and can be at most $d^2/\mu_h V$, or 1.7 μs; the transit time for holes to cross the full thickness of the detector. Using the same parameters above, the individual currents arising from electrons and holes are shown with and without trapping in Figure 5-10. The charge collection time is less than 100 ns for electrons, while it is over 600 ns for holes. Trapping reduces the total charge collected, and in particular the hole contribution for detector events near the anode.

Having as complete a charge collection as possible in the shortest amount of time means that as thin of a detector as possible should be used. C-Mod's camera uses two mm thick crystals as a trade off between absorption efficiency and charge transport considerations. The charge collection time needs to be reasonably matched with the shaping time of the electronics. If the electronics are too fast an incomplete amount of charge will be collected and lead to spectral degradation in an effect known as the ballistic deficit. Since hole collection is poor for higher energies in the range of interest a minimum shaping time of around one μs should be used.

One final thing to consider about the detector when matching it to electronics is the leakage current. The detector can either be AC or DC coupled to the preamplifier. DC coupling has better noise characteristics, but does not work for detectors with too high a leakage current. The leakage can be estimated as $V_{bias}/\Omega d$, where Ω is the resistivity and d is the detector thickness. From the properties of Table 5.2 the leakage current for a two mm CZT detector is about 300 nA. Typically leakage currents need to be less than about
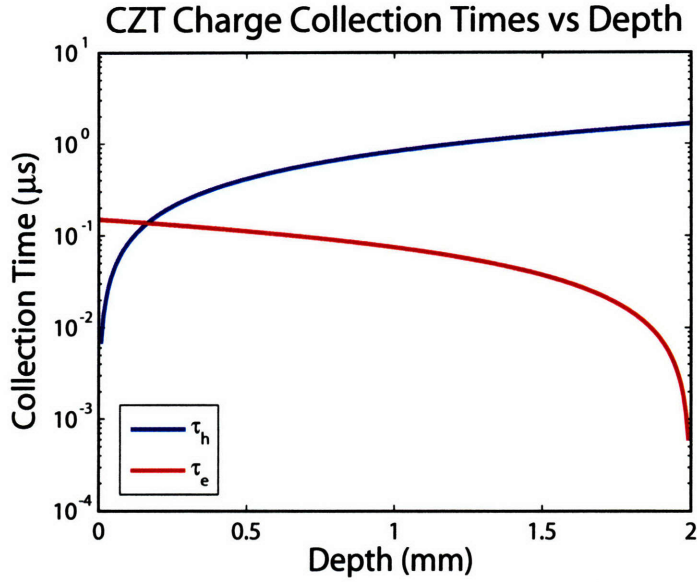
Figure 5-9: Collection times for electrons and holes for two mm thick CZT detector neglecting trapping.
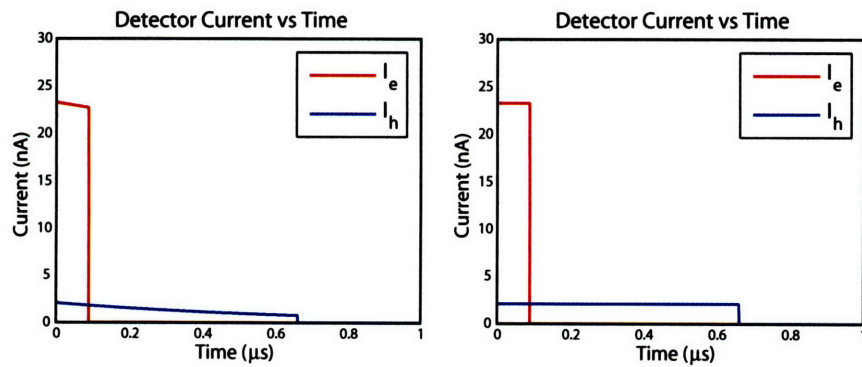
Figure 5-10: Charge collection times for electrons and holes with and without trapping for $\mu_e \tau_e =$ at 5×10^{-3} and $\mu_h \tau_h$ at 8×10^{-5} cm$^2 \times$s/V, $V_{bias} = 200$ V, and d=2 mm.
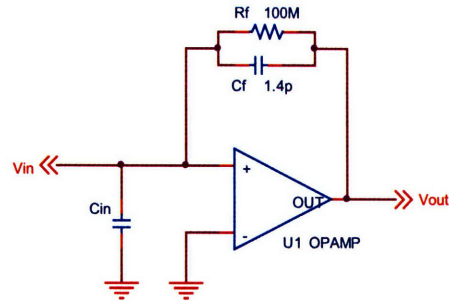
Figure 5-11: Simplified preamplifier schematic with representative values for C_f and R_f.

10 nA in order to avoid having the DC offset from saturating the preamp output, therefore AC coupling is used.

5.3.3 Preamplifiers

The preamplifier converts the detector current to a voltage and brings the signal to the level of millivolts. A general sketch of a preamplifier circuit is shown in Figure 5-11. C_{in} represents the input capacitance. R_f and C_f provide the integration and the fall time constant. If R_f and C_{in} are disconnected it is apparent that $V_{out} = Q/C_f$ where Q is the charge from the detector. This is the idea behind a charge sensitive preamplifier. This also means that if V_{out} is to be measurable then C_f must be quite small. To make the fall time long then requires a large value for R_f. In practice $C_f \sim 1$ pF and $R_f \sim 100$ MΩ.

The three most important characteristics of a preamp are its sensitivity, fall time, and noise level. The sensitivity measures the gain of the circuit and is usually given in units of mV/keV or V/pC. Going from one set of units to the other is just a matter of using the pair creation energy for a given detector material. Say the gain of a given preamp is 1.4 mV/pC. The pair creation energy for CZT is 4.64 eV giving rise to a total charge of 1.6e-19 C. This converts to 0.048 mV/keV. So for a 100 keV photon the preamp produces a 4.8 mV pulse. Often times sensitivities are quoted for Si detectors. The conversion factor from Si to CZT is just the ratio of pair creation energies, 3.62/4.64 or 0.78. Fall time is the characteristic time it takes for a pulse from the detector to decay away on the preamp output. Fall times are much longer than pulse widths and thus lead to a piling up of pulses on the output. Shaping separates out the pulses, but there is the possibility for saturation at high count rates. If too many pulses with high enough energy reach the detector the DC level of the preamp output may go beyond the rails and cause large distortions, lost counts, or blindness. Faster fall times are desirable for high count rates. Slower fall time amplifiers typically have lower noise values since the feedback resistor value is larger, reducing Johnson noise. Another contributor to noise is input capacitance. Input capacitance arises from the detector itself and the connections between the detector and preamp. C-Mod's system uses 30 AWG wire with gold connectors and 0.007" traces to minimize this capacitance.

Table 5.3 gives the important parameters for commercially available preamps from a number of manufacturers. The noise level of all preamps shown is fairly constant at about 2 keV in Si for an input capacitance of about 10 pF. They all can operate at ± 12 V. For C-Mod's HXR system high gain and fast fall time are desirable. Higher gain reduces the amount of amplification needed from the shaper and fast fall time allows access to high

114

Table 5.3: **Sample preamp properties from different manufacturers.**

Vendor	Model	S (mv/fC)	S (mV/keV)	t_{fall} (μs)
eV Products	eV-5091	1.0	0.034	25
	eV-5093	3.6	0.123	1030
Cremat	CR-110	1.4	0.048	140
Eurorad	PR-304	2.0	0.069	1000
	PR-16	6.6	0.226	50

counting rates. Given these criteria the Eurorad PR-16 seems to offer the best balance of gain and fall time. The only other factor is actual cost. The CR-110 from a little known company called Cremat is about a quarter of the cost compared to products from well known vendors such as eV and Eurorad. Since there are 32 channels it is worth adding more gain into the shaper and using the cheaper CR-110.

Integrating the preamp and shaper into a single module is possible, but the small value of C_f and large value of R_f make it difficult to make a viable preamp in practice. Integration could also introduce other noise issues such as capacitive coupling that would have to be debugged adding to development time.

5.3.4 Pulse Shaping

Many different shaping schemes are used to take preamplifier output and transform it into a useful shape for measurement. Shaping methods typically start by using a RC circuit to take a derivative and remove the DC level from the preamp. From there the pulse can be transformed into shapes such as a trapezoid, a triangle, or a Gaussian. A good introductory discussion on pulse shaping is included in Reference [105].

Since fast digitization techniques are used it is important to select a shape that is both easy to fit, and has a gentle slope near the maximum, and has no undershoot. Gaussians are easy to fit given a few parameters and offer good noise characteristics when compared to other shapes. The slope near the peak is gentle enough to give accurate results during fast analysis. Choosing the width of the pulse is a trade off between complete charge collection and high counting rates. A longer pulse allows for more complete charge collection thus gives better energy resolution. Longer pulses also allow more data points per pulse for a given digitization rate, making it easier to find the peak quickly in software. Shorter pulses, however, reduce pile up and are good for counting at higher rates. A compromise between the competing effects for CZT detectors was to set the width at 1 μs.

The simplest way to make an approximate Gaussian is to use a RC-(CR)^n network. The output can be approximated by $V_{out} = V_0 (t/\tau)^n exp(-t/\tau)$. Generally n=4 is used and this is the shape shown in Figure 5-5 panel c). A better means is direct frequency synthesis[106].

The general idea of direct frequency synthesis is to create a filter that takes in the preamp signal and returns a Gaussian pulse shape. The key is to find the poles that accomplish this and then to apply these poles to a real circuit. In the time domain a Gaussian is simply represented by

$$f(t) = a_0 \exp\left(\frac{-t^2}{2\sigma^2}\right). \tag{5.2}$$

Table 5.4: **Pole locations for Gaussian filter**

$\Re_e$	$\Im_m$
$A_0 = 1.661$	$W_0 = 0.000$
$A_1 = 1.622$	$W_1 = 0.502$
$A_2 = 1.496$	$W_2 = 1.044$
$A_3 = 1.234$	$W_3 = 1.712$

Transforming to the frequency domain gives another Gaussian with the form

$$F(\omega) = a_0\sqrt{2\pi}\sigma \exp\left(\frac{-\sigma^2\omega^2}{2}\right).$$ (5.3)

Now let $s = j\omega$ and require that the magnitude of the transfer function of some filter results in a Gaussian, $H(s)\cdot H(-s) = F^2(\omega)$. Continuing, rather generally, take the transfer function to be

$$H(s) = \frac{H_0}{Q(s)},$$ (5.4)

where $Q(s)$ is a Hurwitz polynomial containing the poles of the filter. Using this expression with the Gaussian gives

$$Q(s)\cdot Q(s) = \left(\frac{H_0}{a_0\sigma}\right)^2 \exp(-\sigma^2 s^2)$$ (5.5)

Taylor expanding the exponential using $p = \sigma s$ gives

$$\exp(-p^2) = 1 - p^2 + \frac{p^4}{2!} + \ldots + (-1)^n\frac{p^{2n}}{n!},$$ (5.6)

with the roots being the poles needed to construct the filter. The number of terms to keep determines how close the filter output really is to a Gaussian. n=7 gives very Gaussian shapes that are ideal for fast digitization and software fitting. Using n=7 gives 14 roots. Since the roots are from a Hurwitz polynomial they have special properties. The roots form a mirror image of each other in the complex plane and are such that only the left-hand plane roots need to be considered when taking the magnitude since all the phase information cancels out, i.e. $Q^2(s) = Q(s)\cdot Q(-s)$. The roots are solved for numerically and are given in Table 5.4 with the A_i as the real parts and the W_i as the imaginary parts.

Now that the poles are known the next step is to apply these values to a real circuit. The real pole, A_0, is simply a differentiator which can be produces by a RC circuit. A Sallen-Key filter is used for its simplicity and versatility in producing conjugate pole pairs. Figure 5-12 shows a single stage of the filter. Using basic frequency domain circuit analysis the generic transfer function is

$$H(s) = \frac{G}{s^2 C_1 C_2 R_1 R_2 + s(C_2 R_2 + C_2 R_1 + C_1 R_1(1 - G)) + 1},$$ (5.7)

where

$$G = 1 + \frac{R4}{R3},$$

the gain of a non-inverting amplifier. To simplify, take $C_1 = C_2 = C$ and set the gain to two by requiring $R_3 = R_4$. Now

$$H(s) = \frac{2}{s^2 C^2 R_1 R_2 + sCR_2 + 1}$$ (5.8)

116
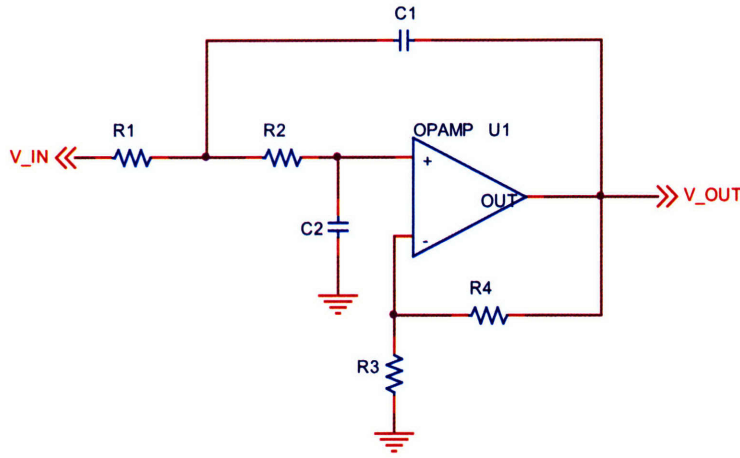
Figure 5-12: Sallen-Key filter schematic.

which may be factored using the quadratic formula. The poles are

$$s = \frac{1}{2CR_1}(-1 \pm j(4\frac{R_1}{R_2} - 1)^{\frac{1}{2}}). \tag{5.9}$$

The roots are conjugate pairs on the left hand plane, just as desired. Next write the roots in terms of the A_i, W_i. Take $\sigma = \sigma_0\tau_0$, with $\sigma_0 = \exp(1)/\sqrt{2\pi}$ a constant and τ_0 the pulse width. This allows direct comparison to $RC - (CR)^n$ Gaussian filters. The real and imaginary Gaussian roots in terms of circuit parameters are

$$A_i = \frac{\sigma_0\tau_0}{2CR_1} \text{ and } W_i = \frac{\sigma_0\tau_0}{2CR_1}\sqrt{4\frac{R_1}{R_2} - 1}. \tag{5.10}$$

R_1 may be chosen to satisfy the opamp requirements and then C and R_2 may be written as a function of R_1,

$$C = \frac{\sigma_0\tau_0}{2A_1R_1} \text{ and } R_2 = \frac{4R_1}{W_i^2/A_i^2 + 1}. \tag{5.11}$$

A_0, is given by the constants of the RC circuit, $RC = \sigma_0\tau_0/A_0$.

The Sallen-Key filter makes up the heart of the shaper, but there are a number of other functions that still need to be considered. These include amplification, pole-zero cancelation, DC offset adjust, 50 Ω line driver, and power supply filtering. The complete circuit is shown in Figure 5-13 with actual values of components. The preamp output sees an optional impedance matching resistor, R_1 and is AC coupled into the first opamp. The time constant of the coupling stage is 2 ms. The first opamp gives a gain of seven. The pulse then goes to the differentiator, pole A_0 formed by C_2 and R_6, and through the pole zero cancelation.

Pole-zero cancelation adds a zero to cancel out the unwanted pole from the preamp. This reduces undershoot and improves the overall shape of the pulse. The resistor, R_5, is chosen such that R_5C_2 matches the fall time of the preamp which is 140 μs.

After the pole-zero cancelation, the signal is amplified by a factor of six. The signal is then AC coupled by C_3 and R_9 to remove any DC offset that may have occurred during

117

amplification. R_{10} and C_4 provide an optional stage of filtering before the signal enters the Sallen-Key filters.

After the filters make the pulses Gaussian, the signal goes to an optional DC offset circuit. The output is related to the input as

$$V_{out} = \left(1 + \frac{R_{28}}{R_{26}} + \frac{R_{28}}{R_{27}}\right) V_{in} - \frac{R_{28}}{R_1} V_{off}. \tag{5.12}$$

Choosing $R_{26} = R_{28}$ makes the gain independent of the offset voltage and reduces to

$$V_{out} = \left(2 + \frac{R_{28}}{R_{27}}\right) V_{in} - V_{off} \tag{5.13}$$

as shown in the circuit diagram.

The final stage is a buffer used to drive the 50 Ω inputs of the digitizers and includes the option of AC or DC coupling.

Printed circuit board (PCB) technology is now readily available and is fairly easy to use. C-Mod's system was designed using OrCAD's design suite of Capture for schematics, PSPICE for simulation, and Layout for making the physical board design. Once the files for a circuit board have been generated they may be uploaded to one of many companies offering PCB manufacturing services through the internet. Once a company receives the files, they can typically produce and ship a complicated, multilayer board in less than a week. This makes design iterations easier so that a final revision may be realized quickly and relatively cheaply. PSPICE is used to simulate the performance of the circuit. The colored markers in Figure 5-13 are PSPICE test points where the simulated voltage is plotted. PSPICE can simulate currents, power consumption in the time domain, as well as examine the frequency characteristics of a circuit. PSPICE models non-ideal behavior of opamps through the use of model files supplied by the manufacturers. The shaper's response to a simulated preamp pulse, Figure 5-14, is shown in Figure 5-15. The output pulse is very Gaussian and has a full width across the base of slightly less than one μs.

The shaper board is small, 5.6×2.5 cm, and makes use of dual opamps and 0805 surface mount components. The board has three layers, components on the top and bottom with traces for test points and power busses on the internal layer. The layout of the board is shown in Figure 5-16. The board is designed to be very flexible offering optional filtering between stages, the ability to set the output impedance, and AC or DC coupling. These features are a great asset during testing.

During testing a number of things were changed from Figure 5-13. In spite of using PSPICE and earlier tests, the circuit had to be modified to function properly. The most significant change is in the filtering between stages. The decision was made to use a dual opamp for the final revision and make the cards even more compact. The LMH6628 can not drive as much capacitance as the previous opamp and led to oscillations. This led to the following modifications: R_1, R_9, R_{25}, C_4, C_9 and C_{14} are all not connected. C_{17} and C_3 are shorted. The output is DC coupled at low output impedance so R_{29} is not connected and C_{26} is shorted. The DC offset circuit is not currently used so R_{26} is not connected. The power filtering is done by resistors instead of inductors, L_1 through L_4 are 4.7 Ω. More gain was needed so R_{28} was increased to 600 Ω.
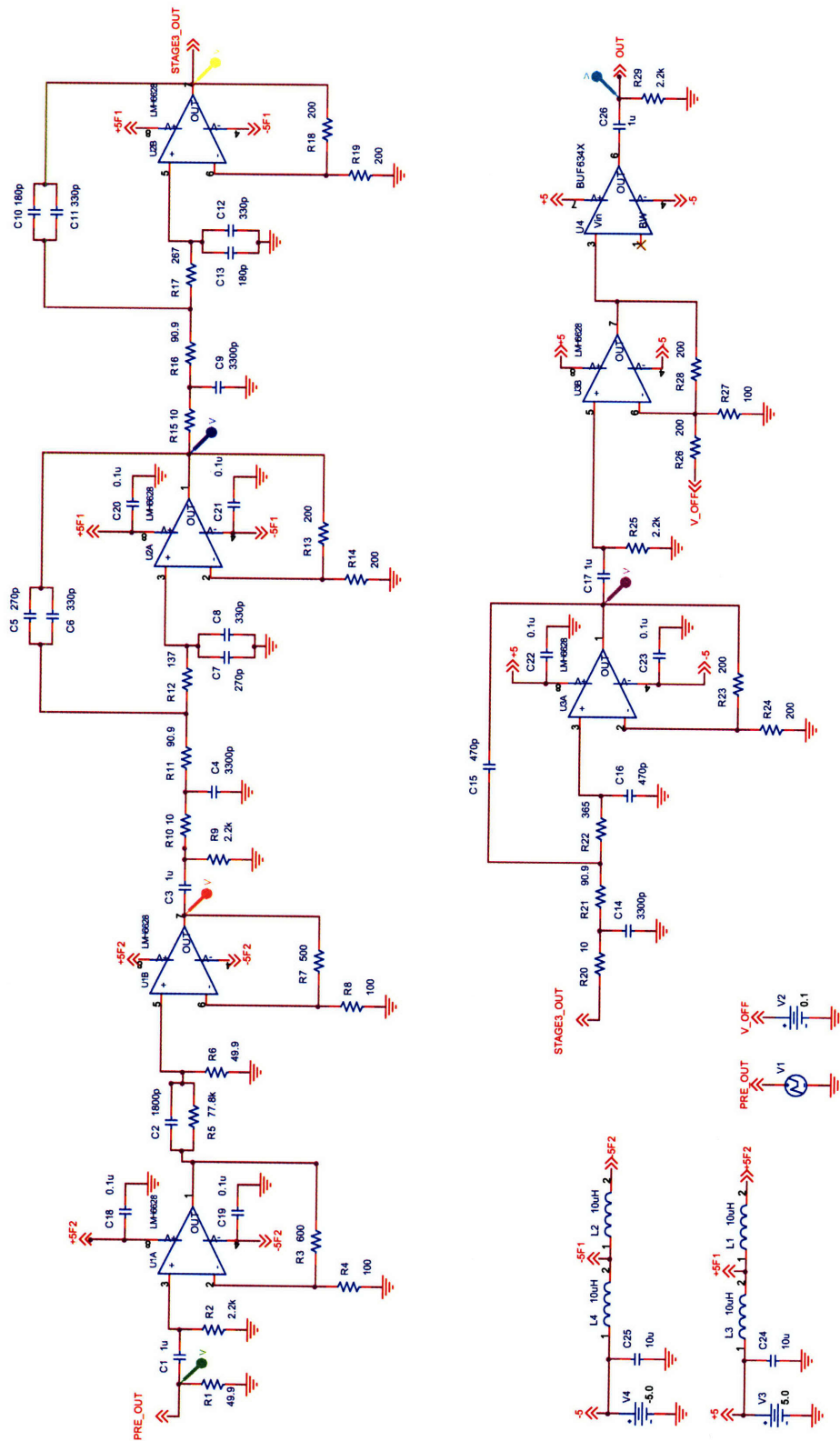
Figure 5-13: Complete shaping circuit schematic showing all components and values. Colored markers denote PSPICE voltage test points. The PSPICE predicted signal at each point is shown in Figure 5-15.

119
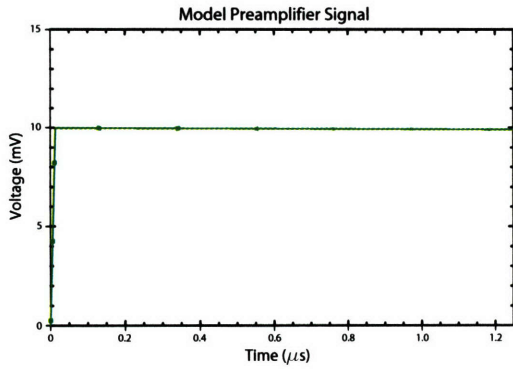
Figure 5-14: Model preamp signal in based on the rise and fall time of the Cremat CR-110 preamplifier, which makes the input nearly a step function.
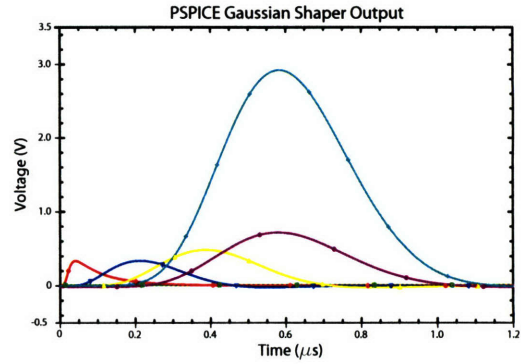
Figure 5-15: Voltage outputs at test points showing the filter amplify and create Gaussian pulse.
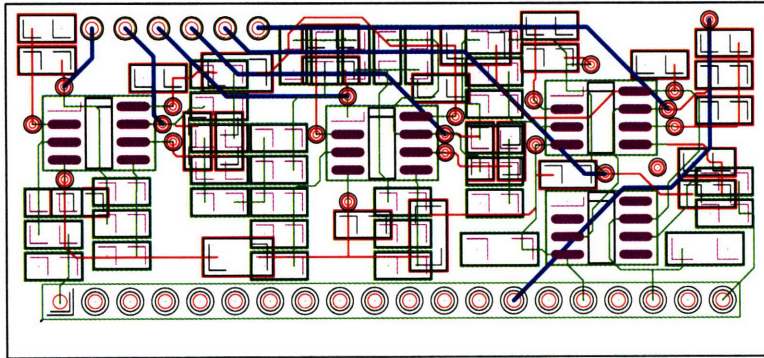
Figure 5-16: Shaper circuit layout showing component pads and internal routing. Top mounted components and traces are shown in green, while bottom components and traces are shown in red. Blue represents internal traces for test point outputs and power routing.
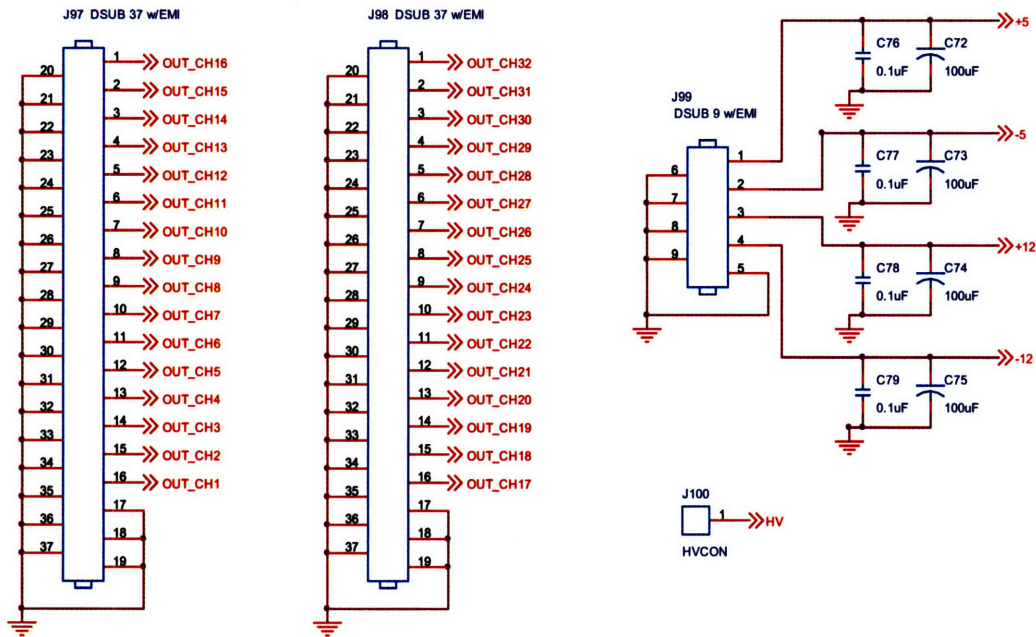
Figure 5-17: Motherboard pinouts for signal output and power input.

5.3.5 Motherboard

A motherboard based system offers an efficient means to incorporate many components into a small space. This allows for modular packages that can be easily replaced due to failure or upgraded if need be; similar to personal computers. A motherboard also trades the wiring of traditional systems for traces and ground planes, reducing the capacitance and overall noise levels.

The overall size of the board is 8.25" by 9.00" and is composed of four layers. The internal layers are used primarily for signal routing and power bussing. Components are spaced 0.270" center to center. Pinouts are shown in Figure 5-17. Filtered D connectors provide an efficient means for power entry and signal output. The high voltage enters through a SHV feed through connector. Internal traces and busses are shown in Figure 5-18.

Besides containing sockets for preamps and shapers the motherboard also has power supply filtering and, more importantly, a high voltage bias circuit. The circuit used is shown in Figure 5-19.

The high voltage is typically around 200 V and is mostly dropped across the detectors given their high resistivity. R_2 and C_2 of Figure 5-19 form a low pass filter with a time constant of one ms for further reducing and ripple and any high frequency that may be left on the bias voltage. C_1 and R_1 form a high pass filter that sends the detector pulse to the preamp. This circuit is repeated for each channel in parallel with the bias voltage originating from a NIM bin linear high voltage supply. The initial prototype motherboard had an EMCO high voltage switching supply which was small enough to be mounted on

121
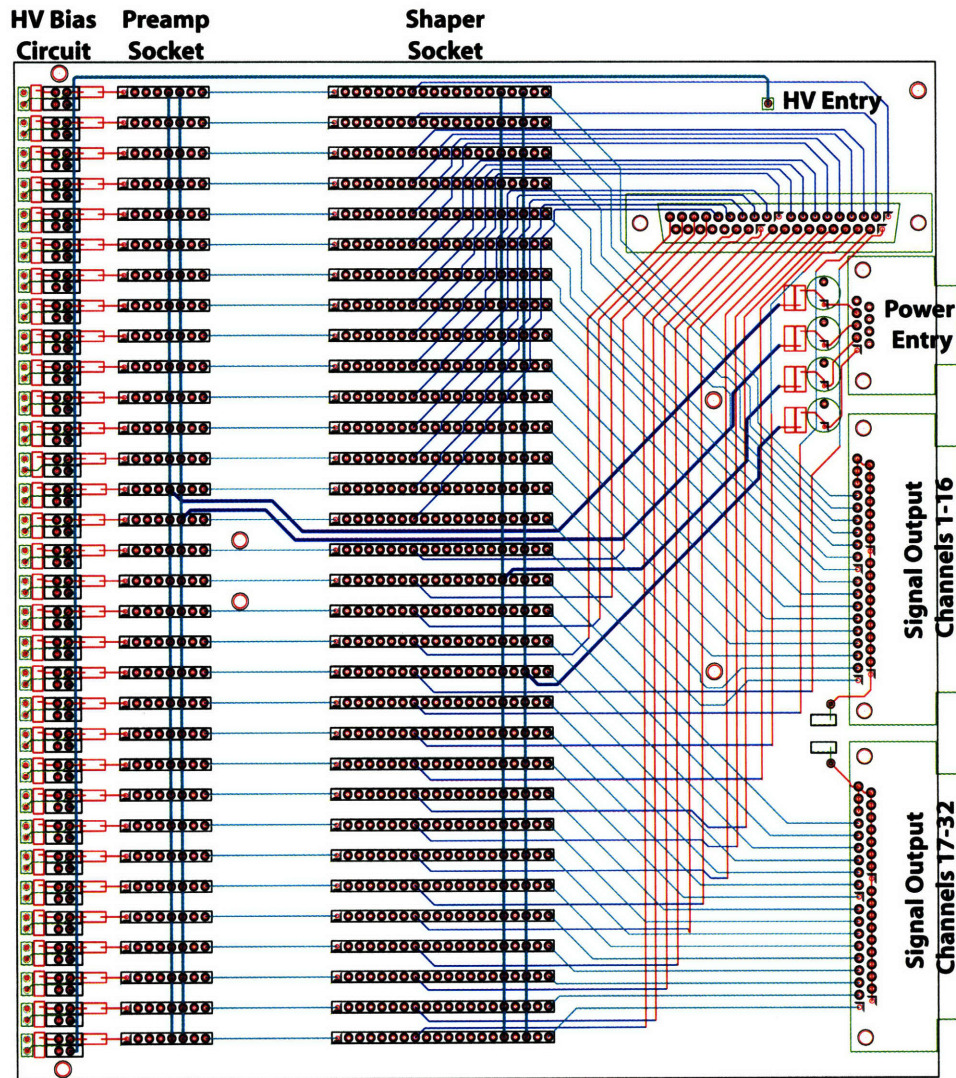
Figure 5-18: Location of internal traces and busses from Layout file.
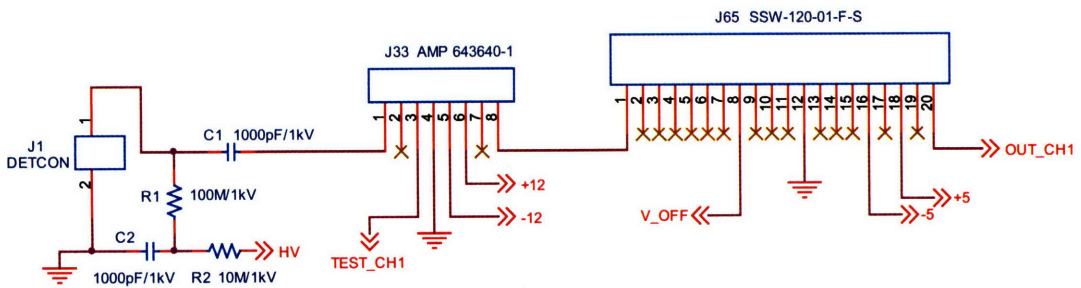
Figure 5-19: Motherboard bias circuit and pinouts for preamps and shapers.

122
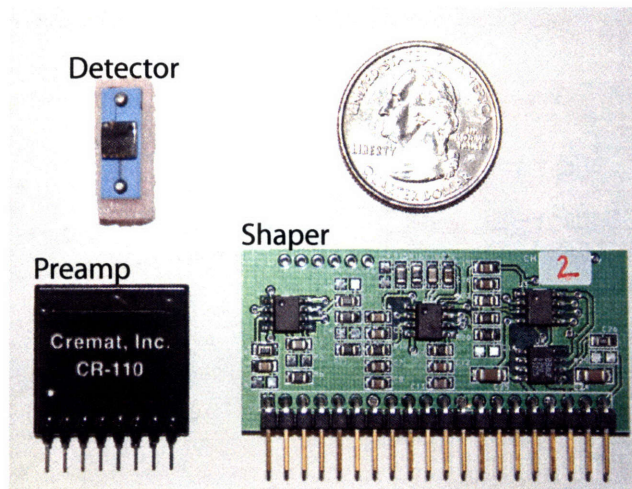
Figure 5-20: CZT detector, preamplifier and shaper composing a single channel of PHA electronics.

the board, but ended up producing oscillations about five mV in amplitude and 280 kHz in frequency. This noise level was too high to get any meaningful results from the preamp and shaper.

Modular motherboard components, the detector, preamp, and shaper, are shown in Figure 5-20. The complete board is shown in Figure 5-21. Detectors are connected using low capacitance 30 AWG wire and gold connectors. The leads are soldered onto the motherboard and the connectors slide over the detector pins.

5.3.6 Digitizers

The critical component to be able to do the analysis through software is the digitizer. The HXR diagnostic requires a large number of channels at a fast rate and consequently large on board memory. D-TACQ Solutions of Scotland was the only company that could meet these requirements. The ACQ216 is a 16 channel board capable of 10 MHz per channel. The board can operate at faster rates with less channels, eight channels at 20 MHz or four channels at 40MHz. A typical pulse from the shaper digitized at 10 MHz is shown in Figure 5-22. The board is 14 bit and has one GB of memory, which makes it possible to digitize for the length of current C-Mod discharges, about 2.8 s total when all channels are used. The boards come in a 6U CompactPCI form factor with dual pin Lemo connector inputs. Other features include software control of the voltage input range with ±2.5, ±4.0, and ±6.6 volts available. This feature and others are controlled through a web page interface accessible by logging into the local server(*pcdaqhxr2*), starting a browser, and typing the IP addresses of each card. The IPs are 192.168.0.7 and 192.168.0.8. The digitizer also has the ability to sub-sample the data stream, and has some resources available on a FPGA which will be further discussed in the section 5.3.8.
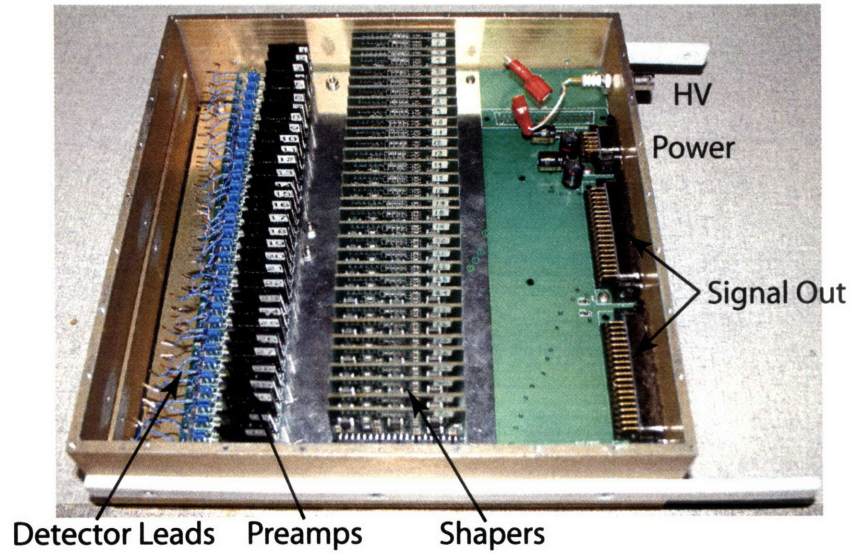
Figure 5-21: Electronics box showing motherboard with preamps and shapers.
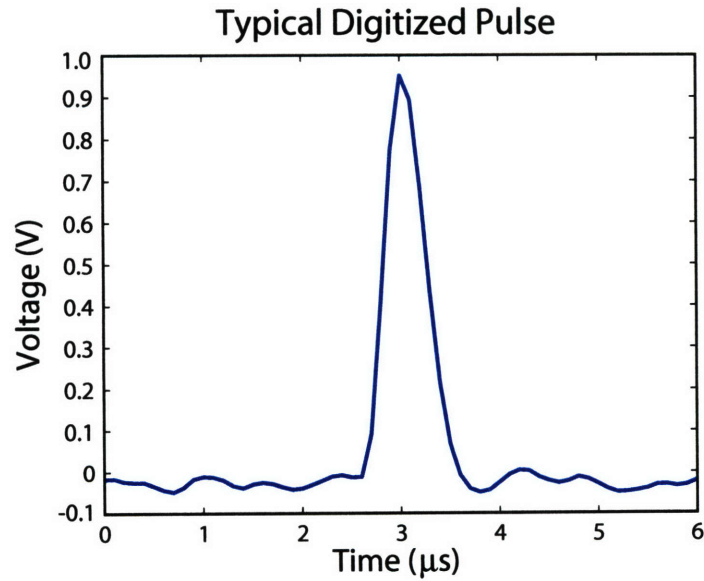
Figure 5-22: Digitized output pulse from HXR electronics showing the full width across the base to be slightly more than one μs.

5.3.7 Other Technology

A number of other technologies exist for nuclear electronics. Two of the most useful are ASICs and FPGAs, which allow direct digital processing. ASICs are applied specific integrated circuits, which are engineered to accomplish a certain task. For nuclear electronics this typically means incorporating the preamplifier and shaper all on one chip. In most circumstances many channels are replicated into a small package giving a very high channel density for use with pixilated detectors. Early cell tests were done using an eV Products ASIC[107] with a pixilated detector. 5×5 mm pixels are currently too large to be manufactured and so individual planar detectors must be used in an array. Unfortunately, the planar detectors are incompatible with using the ASIC for obscure reasons that are not fully known, even by the manufacturer. That said, ASICs are very useful in imaging devices with small pixels or may be applied in the future to C-Mod if larger pixels sizes can be made.

The second piece of technology is a FPGA or field programable gate array. FPGAs are highly flexible devices that may be configured to be everything from processors to digital spectrometers. The basic idea is to use the FPGA as a sort of hardware shaping and processing device that combines the flexibility of fast digitization with access to real time spectra[108]. After a pre-ADC stage the pulses are digitized out of the preamp. Once digitized they can be shaped and binned into spectra. The only drawbacks are long development time and cost. FPGA programming of this complexity is time consuming alone, but the system would have to be integrated with a fast ADC, pre-ADC stage and replicated into a multichannel device. A couple of vendors, XIA and Amptek, market commercial single channel digital pulse processors that are currently about three times the price per channel of C-Mod's HXR system. The individual channels would require integration into a multichannel system and software development or modification to perform as desired. Recently, however, companies such as Mathworks have developed higher level software tools for FPGAs, facilitating programming and possibly shortening development time for such a device.

5.3.8 Real Time Feedback Control

Real time control of plasma quantities such as the current profile would provide a means to operate indefinitely in AT regimes and optimize performance. Recently JET achieved a simple form of q-profile control[109]. The initial results use LHCD power level as the actuator with real time magnetics, and interferopolarimetry data as the feedback. To be successful the plasma conditions had to be contrived from previous dedicated experiments. In spite of this, this represents a good start to using real time feedback control to regulate an important plasma quantity. On TCV a single channel real time PHA using a XIA card for processing achieved 10 ms resolved electron temperature measurements[110]. Combining a real time PHA for feedback with LHCD as an actuator would provide a much more direct means of current profile control and this is a future goal on C-Mod.

It is conceivable to use the emissivity profile, PHA results or simply the count rate on a given channel as the information to control the antenna phasing. Present implementations of the LH control system and HXR diagnostic are limited and would need to be upgraded to accomplish this end. The LH control system is designed to take in a preprogrammed waveform and the HXR data is not accessible in real time. HXR data can be made available in real time either by upgrading to a digital pulse processing system or by possibly modifying the ACQ216s. The ACQ216 digitizers are FPGA based and have some resources available.
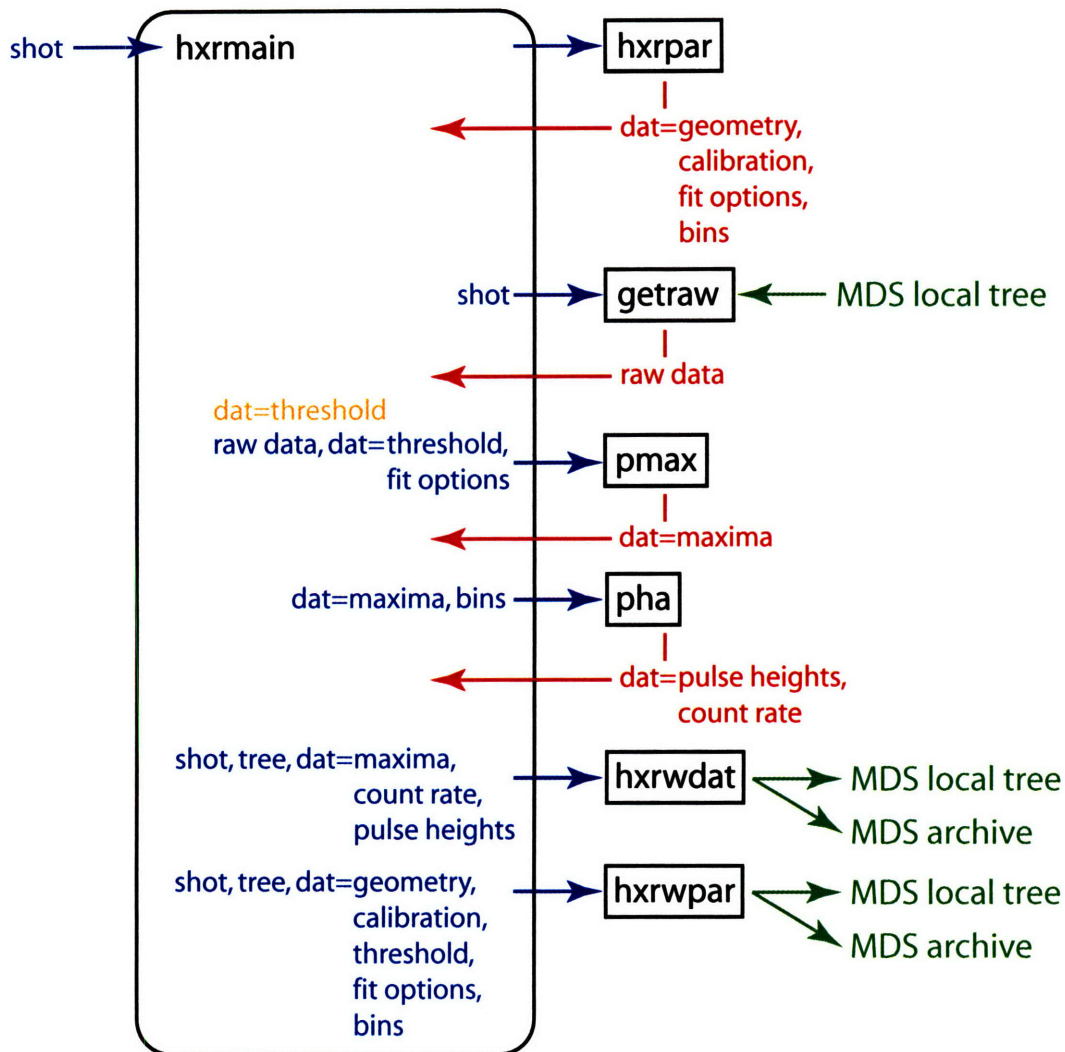
Figure 5-23: Control flow of analysis routines.

It may be possible to modify the digitizer to do the pulse processing onboard and output the spectra in almost real time.

5.4   Analysis Software

Pulse analysis is performed locally using a number of Matlab routines. The main routine, *hxrmain*, is called from the store action of the digitizer and takes in the shot number from the Linux environment variables. A flow chart of the routines is shown in Figure 5-23. Blue arrows and blue text indicate inputs and red arrows and red text are outputs. Green text and arrows denote interaction with MDSplus. *hxrmain* first calls *hxrpar*, a routine that contains all the knobs needed for the analysis, such as fit options, time and energy bins, calibration data, etc. *hxrpar* consolidates all the parameters that may need adjustment into a single file. This information is returned to *hxrmain* in the form of a data structure.

hxrmain then enters a loop where the data is gathered and processed for each channel. The shot number is used to call *getraw* which accesses the local tree and returns the raw data. *hxrmain* then takes the average of the signal and adds a specified offset to get the energy threshold for which peaks will be calculated. The threshold is added to the data structure and used in *pmax*, the routine that finds the peaks and does fitting if need be. *pmax* adds the maxima to the data structure and is described in more detail in section 5.4.1. Once the maxima are known, *hxrmain* calls *pha*. *pha* takes in all the bin information, and the maxima and generates pulse height histograms and calculates the total count rate. *hxrwdat* then writes the maxima, the pulse heights, and the count rate back to the local and archival trees. After all 32 channels have been processed, *hxrmain* calls *hxrwpar* which writes all the parameters used to perform the analysis to both the local and archival tree.

5.4.1 Peak Finding

pmax is the primary routine for analysis since it finds the location of the pulses and performs fitting and pile up rejection. The routine is based on examining the curvature of the signal through numerical derivatives. Looking at the sign of the curvature determines if the data has a maxima or a minima. Maxima above the threshold level are recorded and examined for pileup. The width of the pulses and the spacing between maxima and minima are used to determine if pileup exists. Five options have been implemented for pileup rejection and fitting:

1. No fit and no pile up rejection

2. No fit while rejecting double and triple peaks

3. Fit doubles and reject triples peaks

4. Fit triple and double peaks

5. Fit triple, double, and single peaks

Options 1 and 2 are the fastest to perform while option 5 may be used to reduce the entire signal into fit parameters alone. Figure 5-24 plots 30 ms of raw signal in blue and overlays maxima found from *pmax* in red circles. The threshold is indicated by the black line. Option 2 is typically used for fast intershot analysis. The error in amplitude from digitization can be estimated from the digitization rate and the pulse width. The full pulse width is 1.1 μs. The FWHM is 0.45 μs giving $\sigma = 0.191$ μs. At 10 MHz the most the peak may be missed by is 0.1 μs and this corresponds to an error of 13%. If on average the peak is missed by 0.05 μs then the error is only 3%. Fitting is used to gather data from pulses that would normally be rejected. Figure 5-25 shows a pile up event and the results from the automated fit procedure.

5.5 Data Management and Storage

With up to two GB of data per shot data management, processing, and storage become very important issues. Data taken from a typical C-Mod shot is currently about two GB, and is increasing exponentially. This data is permanently archived on a very large RAID array. Adding two GB per shot just for the HXR diagnostic would place too great a demand on
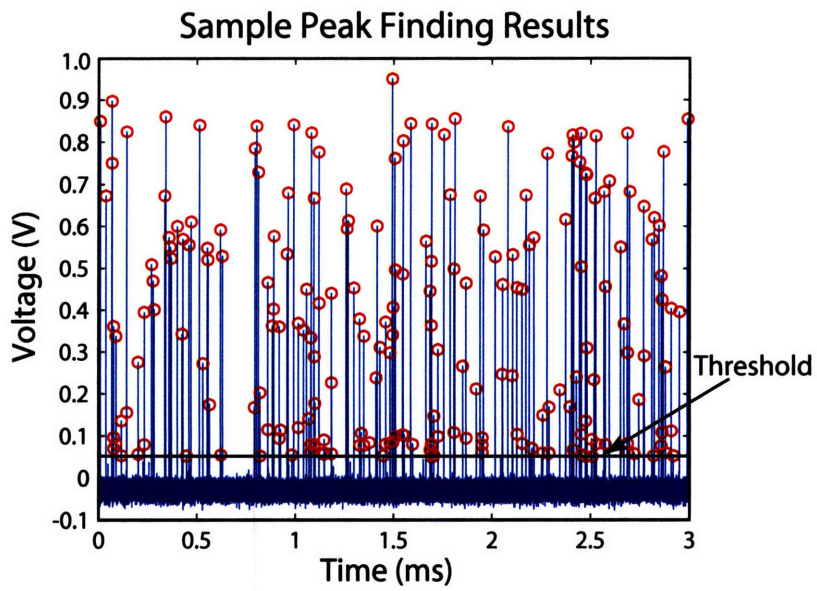
Figure 5-24: Sample peak finding result using option 1, without any fitting or pile-up rejection. Raw data is plotted in blue while found peaks are indicated by red circles.
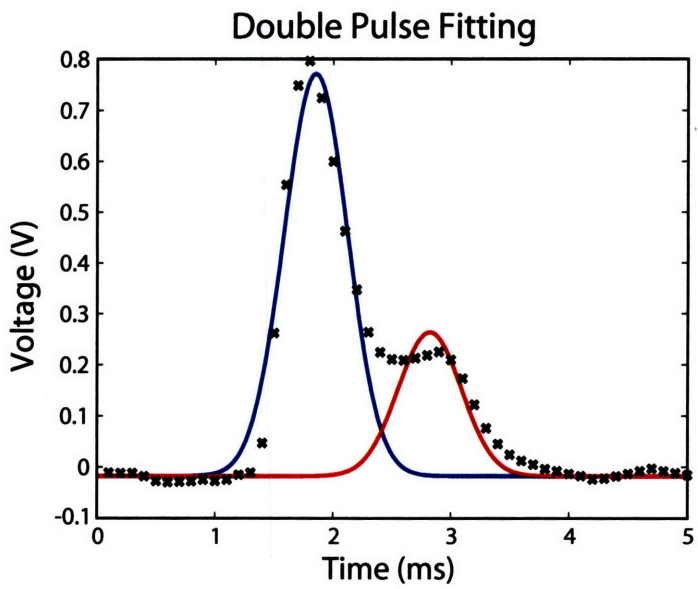
Figure 5-25: Sample double peak fit from shot data.
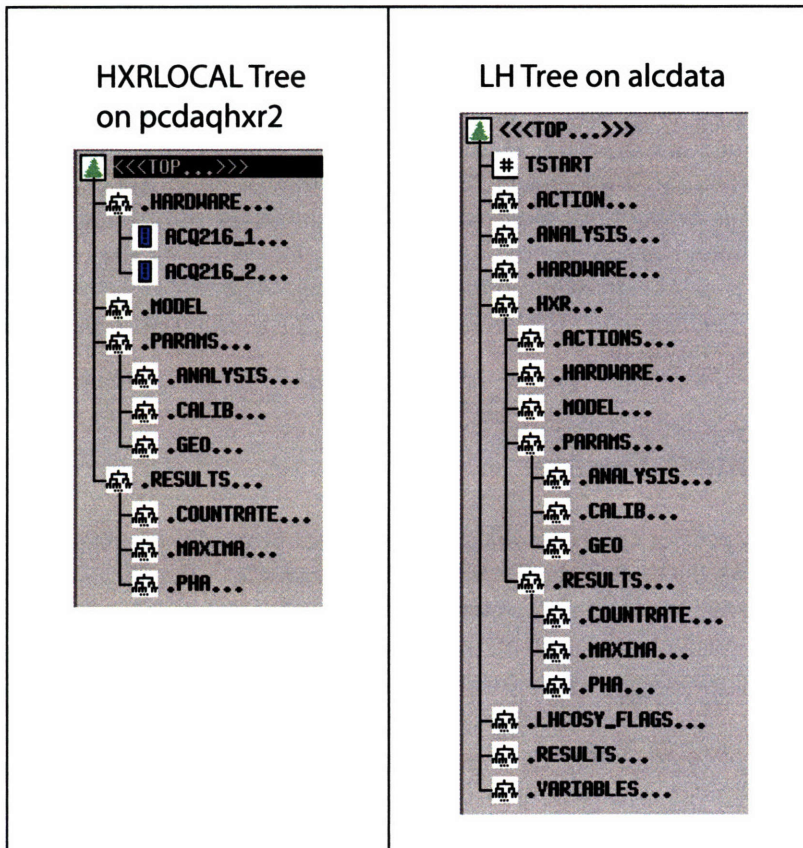
Figure 5-26: MDSplus local and archive trees showing subnodes for the HXR diagnostic.

system and network resources. The best solution is to store and process the data locally. The processed data may then be archived in the C-Mod RAID array.

The local system consists of three main parts, a server, a local gigabit network, and the digitizers. The server is where all the processing occurs and where the data is stored. The local gigabit network connects the digitizers to the server for fast data transfers. The server is a Dell PowerEdge 2850 with dual Xeon 3.2 GHZ processors, 4 GB of RAM, and 478 GB of SCSI disk space. The operating system is Linux, which boots from the network. These components as well as power supplies, high voltage, and triggers are all housed in a RF shielded rack located underneath the LH antenna at C-port.

HXR uses MDSplus to organize and access data as well as issue commands during the shot cycle. The local data is organized on a tree called HXRLOCAL, which is physically on the Dell server named *pcdaqhxr2*. The permanent storage location is the HXR branch of the LH tree, which is physically located on the C-Mod data server, *alcdata*. The trees with branches are shown in Figure 5-26. The two trees are nearly identical with the main difference being that the raw data is stored on the local tree and the permanent tree contains actions for the data analysis. Processed data such as the maxima, count rate, and PHA spectra are available as well as important parameters such as the method used to find the peaks, the energy calibration, and the geometry. Model parameters and results are also recorded for a given shot.

129

To minimize processing time during post shot analysis a separate store action for each digitizer may be used. This allows for parallel reading of the digitizer memory and writing to hard disk and cuts in half the amount of time required. The time to read and write is about 1.5 minutes for every second of data taken when all channels are used. Embedded in each store action is a call to the Matlab analysis routines. Two instances of Matlab are used simultaneously as well and begin the analysis after the store is complete. Processing time depends on the fitting options chosen and also the count rate. Using option 2 for fast analysis usually allows the analysis to be completed at less than 10 s per channel. This puts the processed data on the trees in about five minutes. The store action log files include the store time for each channel and processing times for the Matlab routines, and may be viewed in */usr/local/cmod/logs*.

5.6 Mechanical Design

The mechanical aspect of the HXR diagnostic consists primarily of shielding and support structure as well as packaging the detectors and electronics. Section 5.6.1 briefly covers neutron and photon interactions of interest when considering shielding. A Monte Carlo code was used to estimate the neutron and photon energy spectra in Section 5.6.2. The shield and support structure are discussed in Sections 5.6.3 and 5.6.4. Section 5.6.5 goes over the pinhole. The final two sections, 5.6.6 and 5.6.7 discuss the detector mounting structure and the electronics box.

5.6.1 Neutron and Photon Interactions

Background signal may arise from both neutrons and photons generated in the cell through a number of nuclear and atomic processes. D-D fusion neutrons are born at 2.45 MeV and can slow down through collisions and be absorbed by structural materials or the detector itself and produce γs. Fast neutrons may also make γs through inelastic scattering. Photons are generated through neutrons or created by bremsstrahlung.

The neutron energy distribution in the cell contains many more thermal than fast neutrons and for most elements, this means a greater cross sections for reactions. Thermal neutrons may be absorbed directly by an element and elevate it to an excited state. When the excited state decays a characteristic γ ray is produced. Thermals may interact with materials in the cell which contain H, B, Cu, Mo, Al, Fe, Cu, and Mo. C, Cr, Ni, and Br are also present. It is also possible for the neutrons to interact with the Cd and Te in the detector itself. Cd in particular has a very high thermal neutron absorption cross section.

Most high energy background photons are produced by (n,γ) reactions. Lower energy photons arise through Compton scattering of higher energy gammas and K-shell fluorescence within the shielding material. Photons may also be reflected off the inner wall[111].

These interactions are summarized for most elements of interest in Figure 5-27. Elemental information as well as isotope abundances are listed. Each isotope responds differently to thermal neutrons. (n,γ) cross sections as well as mean free paths are tabulated. Cross section data is taken from the National Nuclear Data Center (NNDC). The number of gammas generated and the three strongest prompt transitions are listed with energy and absolute intensity referenced to k_0. k_0 is the intensity normalized by the 2.2 Mev Hydrogen transition. Data is from the Prompt Gamma Activation Analysis, or PGAA database.

Element	Z	Weight amu	Density g/cm3	k Shell keV	Isotope	Abundance %	(n,gamma) cs barns	mfp cm	# gammas	Three strongest transitions MeV (k0)		
										I1	I2	I3
H	1	1.01	8.90E-05	NA	nat	100	0.33	57105	1	2.22(1.0)		
					1	100	0					
					2	0	0.00052		1	6.25(1.5e-3)		
B	5	10.81	2.34	NA	nat	100	0.1	77	10	0.478(2.0e2)	4.44(1.1e-2)	7.01(9.2e-3)
					10	0.5	0.5		0			
					11	0.005	0.005		0			
Al	13	26.97	2.72	1.6	nat	100	0.23	72	216	1.78(2.6e-2)	0.031(9.0e-3)	7.72(5.5e-3)
Fe	26	55.85	7.86	7.1	nat	100	2.6	4.5				
					54	5.8	2.3		33	9.30(4.1e-3)	5.51(1.3e-4)	0.412(1.2e-3)
					56	91.8	2.6		193	7.63(3.5e-2)	7.65(3.0e-2)	0.352(1.5e-3)
					57	2.1	2.5		35	0.811(1.5e-3)	3.49(6.2e-4)	0.864(3.9e-4)
					58	0.3	1.3		67	0.287(1.2e-4)	6.29(9.2e-5)	0.726(4.1e-5)
Cu	29	63.54	8.94	9.0	nat	100	3.8	3.1				
					63	69.2	4.5		305	0.278(4.3e-2)	7.92(4.1e-2)	0.159(3.1e-2)
					65	30.8	2.2		306	0.186(1.2e-2)	0.465(6.4e-3)	0.386(6.3e-5)
Mo	42	95.94	10.22	20	nat	100	2.5	6.2				
					92	14.8	0.019		5	0.943(2.4e-4)	1.4(1.4e-4)	7.13(1.0e-4)
					94	9.3	0.015		13	0.204(3.7e-4)	0.820(2.9e-4)	2.22(1.5e-4)
					95	15.9	13		139	0.778(6.4e-2)	0.850(1.4e-2)	0.848(1.0e-2)
					96	16.7	0.5		36	0.481(1.9e-3)	4.32(3.3e-4)	0.719(3.2e-4)
					97	9.6	2.5		110	0.787(5.3e-3)	0.723(1.6e-3)	6.62(9.0e-4)
					98	24.1	0.14		56	0.140(8.7e-4)	0.198(3.4e-4)	0.0977(2.7e-4)
					100	9.6	0.2		332	0.181(5.4e-5)	0.238(4.7e-5)	0.157(4.1e-5)
Cd	48	112.41	8.65	26.7	nat	100	2522	0.0086				
					106	1.3	1		0			
					108	1	0.72		0			
					110	12.5	11		191	0.245(7.4)	0.342(2.7)	0.171(1.5)
					111	12.8	24		5	0.618(7.8e-2)	0.851(6.0e-3)	0.798(4.8e-3)
					112	24.1	2.2		0			
					113	12.2	20600		134	0.558(51)	0.651(9.7)	0.806(3.6)
					114	28.7	0.34		0			
					116	7.5	0.75		0			
Te	52	127.6	6.24	31.8	nat	100	4.6	7.4				
					120	0.9	2.3		0			
					122	2.6	3.9		113	0.440(2.4e-4)	0.159(2.2e-4)	0.473(1.8e-4)
					123	0.9	418		162	0.602(5.8e-2)	0.723(1.2e-2)	0.646(6.2e-3)
					124	4.7	6.8		280	0.444(7.1e-4)	1.85(7.1e-4)	0.380(5.1e-4)
					125	7.1	1.6		8	0.666(1.1e-3)	0.754(3.2e-4)	1.21(1.9e-4)
					126	18.8	1		2	6.29(5.5e-5)	0.061(1.5e-5)	
					128	31.7	0.2		23	3.72(5.0e-4)	0.180(4.8e-4)	2.36(4.4e-4)
					130	34.1	0.3		258	0.296(6.9e-4)	3.35(6.4e-4)	2.29(4.2e-4)
Pb	82	207.21	11.34	88	nat	100	0.162	187				
					204	1.4	0.66		35	6.73(4.7e-5)	4.61(9.9e-6)	4.92(8.9e-6)
					206	24.1	0.027		6	6.74(1.0e-4)	0.570(1.6e-6)	0.898(1.5e-6)
					207	22.1	0.63		23	7.37(2.0e-3)	2.61(5.9e-6)	4.75(3.4e-6)

Figure 5-27: k-shell and (n, γ) reaction data for elements of interest. Data taken from NNDC and PGAA databases.

131

5.6.2 MCNP

The first step taken when designing the shield was to identify the type and energy of the radiation to be shielded. C-Mod's diagnostics provide some information into the background, but specifics like the the neutron and photon spectra are unavailable. To better identify the sources present in the experimental cell under operating conditions a code was used to simulate the environment in which the HXR camera would be placed in.

MCNP[112] is the most widely used Monte Carlo code in the field of nuclear engineering where it is used from studying everything from nuclear fuel geometry to radiation therapy. MCNP stands for Monte Carlo N-Particle and is capable of tracking neutrons and photons through almost every possible reaction in arbitrary geometry. MCNP has well developed cross section libraries making it a powerful and very versatile tool. A fairly elaborate model of the C-Mod experimental cell was developed as part of a nuclear safety survey[113]. The main features are the concrete experimental cell, vacuum vessel, coils, and igloo. This model was used to simulate the neutron and photon energy spectrum at the position where the HXR diagnostic is located. The initial source was a ring of 2.45 MeV neutrons from D-D fusion events in the plasma core.

The resultant neutron spectrum was primarily due to slowing down, whereas the photon spectrum is produced from (n,γ) reactions and scattering. The spectra tallied in the cell just outside a port extension are plotted in Figures 5-28 and 5-29. The most notable feature of the neutron spectrum was the high proportion of thermal and low energy neutrons. Cd has a large cross section for absorption of thermal neutrons. Experimentally on Tore Supra[93] direct neutron reactions in the detector are rare and do not significantly impact the performance of the diagnostic. High energy peaks are observed, but the peaks can not be distinguished as originating from either photons or neutrons. In either case the count rate is low enough that it does not impact the performance of the diagnostic. The photon spectrum showed many clear peaks associated with (n,γ) reactions for materials in the cell such as, iron or copper. MeV level peaks are more difficult to shield, but the CZT detector is fairly insensitive at high energies since it was made as thin as possible. The high photon flux in the energy range of interest, 20-250 keV, was the main concern and needed to be addressed through shielding. Fortunately it is not difficult to get orders of magnitude of attenuation through the use of thick, high Z, and high density materials such as lead.

MCNP was also used for a simple slab geometry study of Pb thickness. One major concern about using thick pieces of Pb for shielding is the generation of fluorescent k-shell hard x-rays at 88 keV. The neutron spectrum in Figure 5-28 was used as the source and the volume photon production and flux through the boundary were tallied. The results are shown in Figure 5-30 for one, two, and three cm slabs. Photons were produced in the volume through (n,γ) reactions and scatter and produce k-shell x-rays. As the volume increased the photon production increased, as expected. The photon flux out slightly increases from one to two cm, but is roughly constant from two to three cm. This indicates that lead is self shielding, particularly for the 88 keV k-shell, such that only reactions in the outer portion of the lead will be able to escape and contribute to the background. This means that as much lead may be used as necessary for shielding without concern of increasing the background.
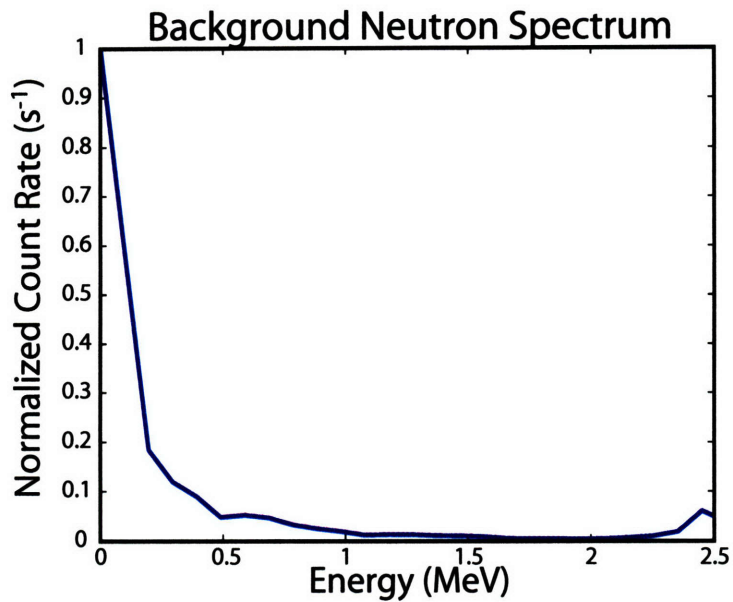
Figure 5-28: MCNP background neutron spectrum generated by D-D fusion events at 2.45 MeV. A large population of near thermal neutrons are present due to slowing down in the structural material surrounding the machine.
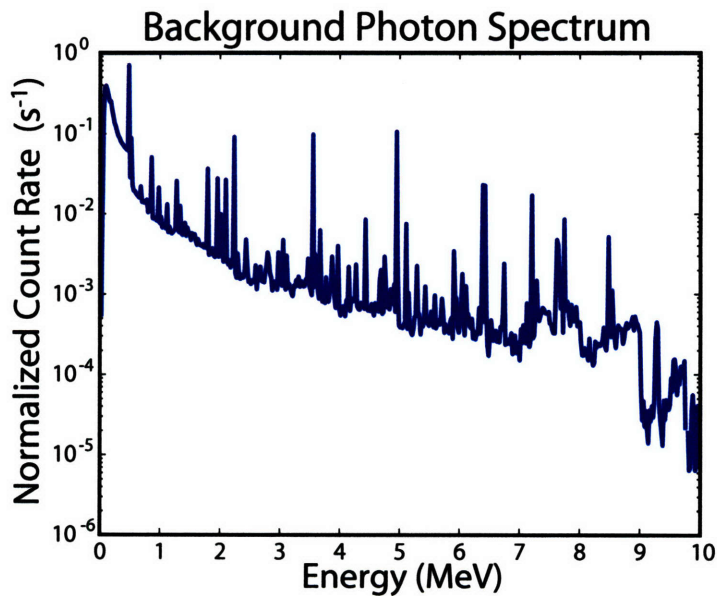
Figure 5-29: MCNP background photon spectrum showing a large number of well defined peaks from (n,γ) reactions in the various materials composing Alcator C-Mod.
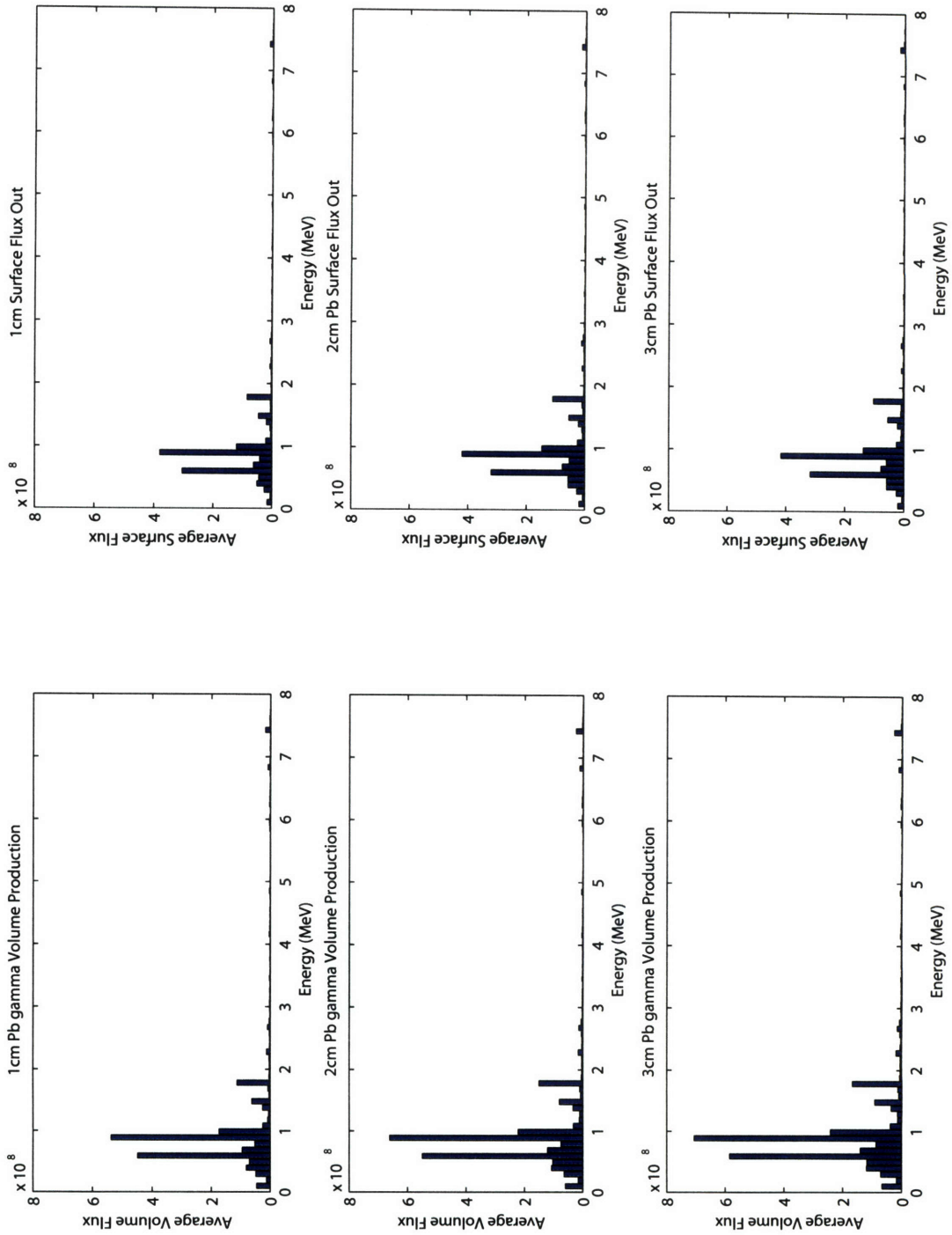
Figure 5-30: Volume photon production and surface flux for varying Pb thickness
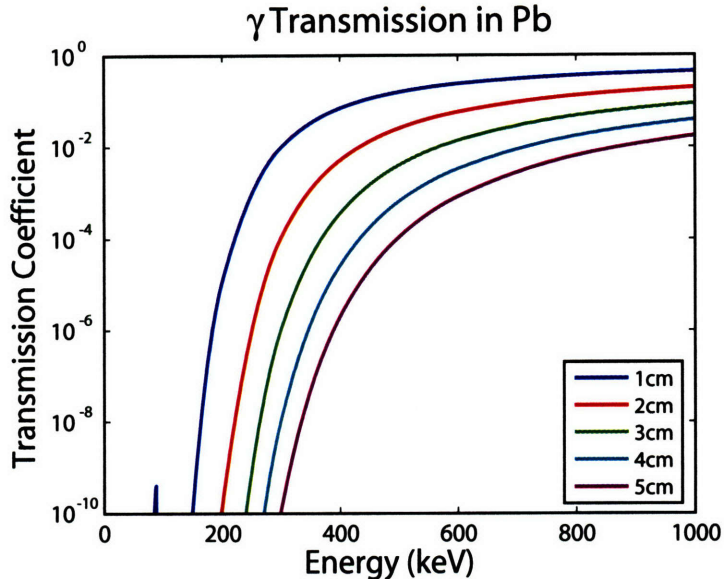
Figure 5-31: Transmission coefficient of Pb for thickness of 1-5 cm.

5.6.3 Shield

Design of the shield was based upon background measurements, expected signal levels, and the predicted background spectra from MCNP. From the spatial requirements for the diagnostic there is little room for bulky neutron shielding. At best a thin layer of Cd may be wrapped around the shield for thermal absorption. The primary function of the shield is to stop gammas. Pb is an excellent shielding material for gamma rays since it has a very high density and a high Z. The attenuation for lead of varying thickness is shown in Figure 5-31.

The main questions to answer are how thick to make the Pb and how to hold it together in a structurally sound package. The overall thickness was set by the size of the electronics box on the inside and the spatial constraints of B-port on the outside. The resulting space is enough for about 3 cm of lead. This gives about ten orders of magnitude in attenuation up to 250 keV.

The shield can either be fashioned out of interlocking plates or cast as a single solid piece. The later method was used since it produced a monolithic structure without the complexity of bolting many odd shaped and overlapping plates together. The shield itself consists of a pyramidal front section that contains the pinhole and a rectangular rear section for the electronics box. The shield was made through casting between two 0.125" aluminum shells. The engineering drawing for the pour is shown in Figure 5-33. The inner shell and electronics box provides some shielding against the lead k-shell radiation. Figure 5-32 shows the transmission coefficient for aluminum of one, three, and six mm. Shielding of the lead k-shell is further augmented through 0.125" stainless steel plates that cover the front end of the electronics box.

The shells were held at a fixed distance through a dowel at the nose of the shield and tack welded spacers in the rear. The pour was done by ABM lead in Huffman, Texas. The overall weight of the shield is about 480 lbs, not including the rear door. The shield also features rails and stops for positioning the electronics box. A 3D model of the shield is shown in Figure 5-34 and a photograph in Figure 5-35. Once the lead has been poured the
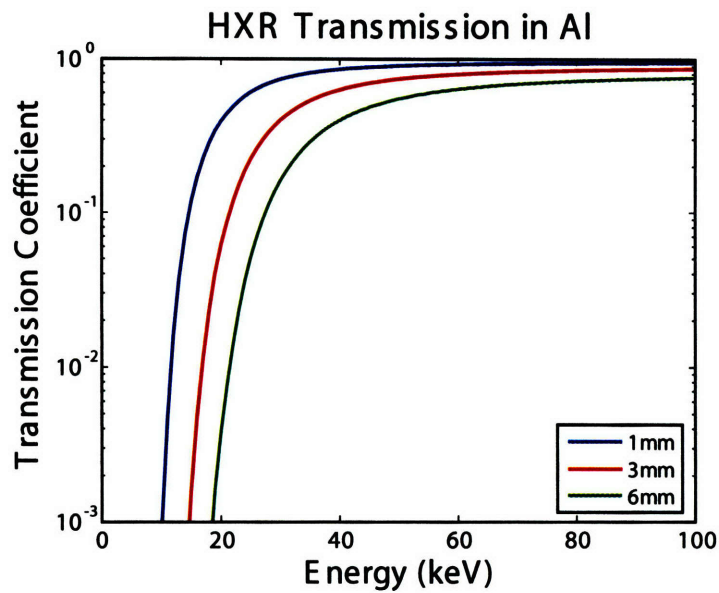
Figure 5-32: Transmission coefficient of Al for thickness of one, three, and six mm; corresponding to the thickness of the vacuum window, the inner shell, and the inner shell and electronics box combined.
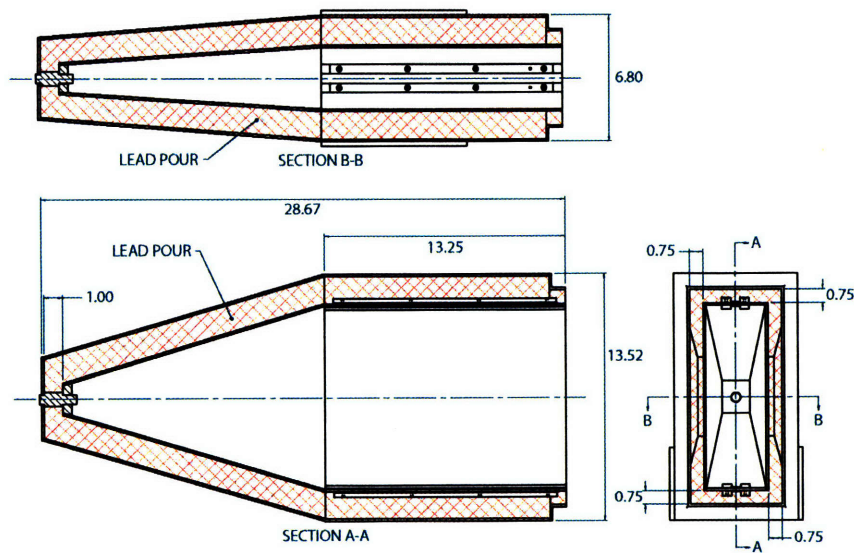
Figure 5-33: Engineering drawing of lead shield, all units are in inches.
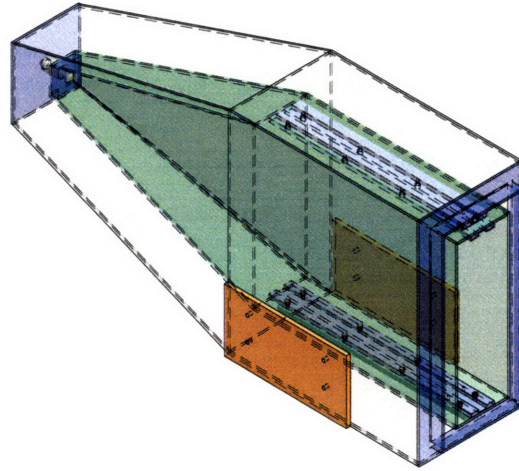
Figure 5-34: SolidEdge drawing of multilayered shielding composed of aluminum shells and lead.
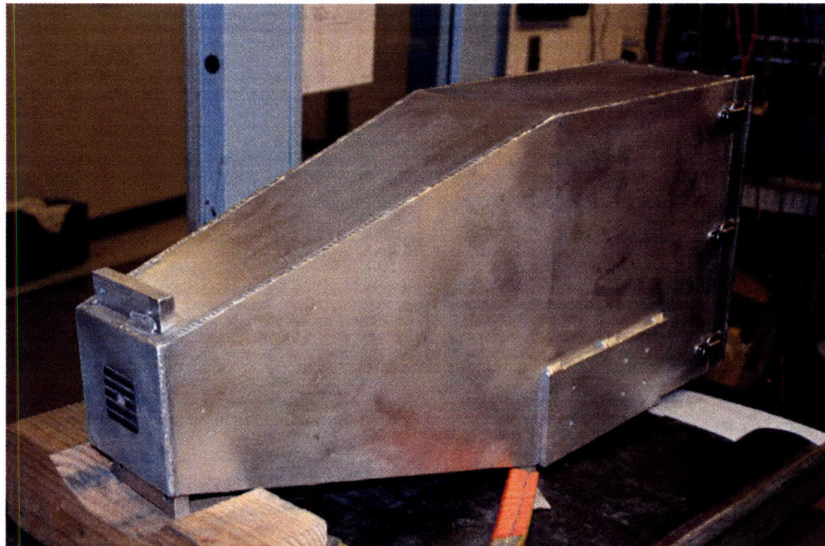
Figure 5-35: Photograph of complete shield with pinhole and rear door.

cutout from the pinhole needed to be machined. This proved difficult due to slight bowing and bulging of the aluminum from the pouring process. There were no square or true surfaces to reference. A special plate fixture was made to slide into the rails and provide a good reference. This ensures that the pinhole cutout is centered with respect to the rails so that the detectors will be in the proper position with respect to the pinhole. A hinged rear door completes the shield and contains the cable feedthrough.

5.6.4 Support Structure

The lead shield is mounted on a support structure that is mounted directly to the igloo. The base consists of an sturdy aluminum box with a number of cutouts for cable feedthroughs. Four jack screws connect the rail table to the base and allow for vertical and tilt adjustment. The rail table provides translation in and out of the port. A sled with pillow blocks and rail locks attaches the lead shield to the rails. The whole mounting structure is shown in Figure 5-36.
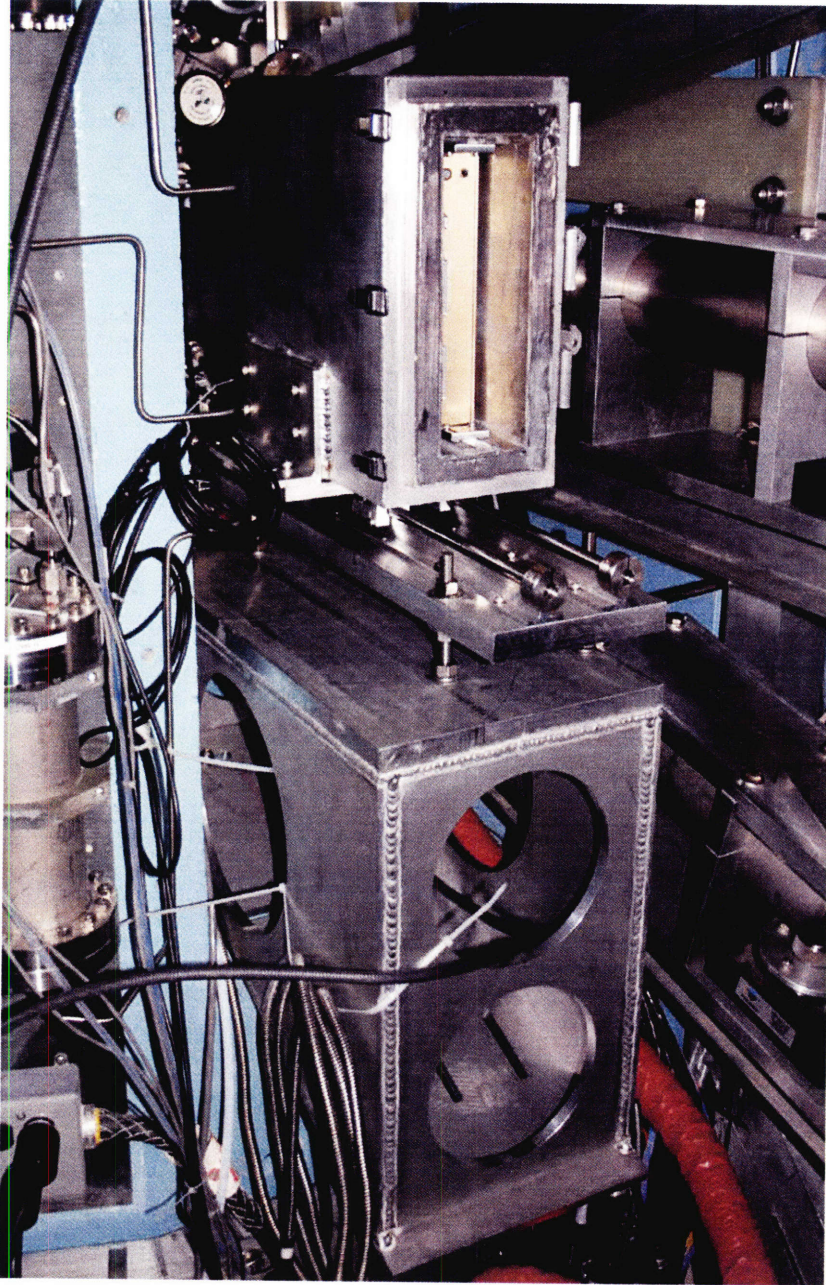
Figure 5-36: Shield and structural support installation at B-port. Circular cutouts allow cable access for other diagnostics.
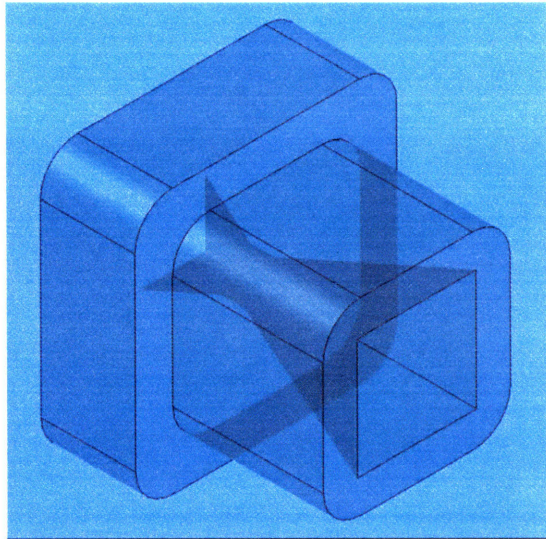
Figure 5-37: SolidEdge drawing of 5 mm square pinhole.

5.6.5 Pinhole

The pinhole design was based on the aperture analysis of Section 5.1.1 and the work in Reference[93]. The pinhole has a stepped square shape to prevent background photons from having a direct path to the detectors and to ensure the proper orientation. The overall size of the pinhole is 4.4×4.4×4.1 cm where the aperture itself is 5×5×4 mm. The aperture is tapered at 16° allowing the full viewing angle to see the plasma. A drawing of the pinhole is shown in Figure 5-37. The pinhole was formed from a two piece aluminum cast, an outer stepped cup an the inner piece with the tapers. After the lead was poured and the aperture removed from the outer cup the inner aluminum was removed through drilling and dissolving in sodium hydroxide. Different size apertures may be made in a similar fashion as count rate and resolution requirements dictate.
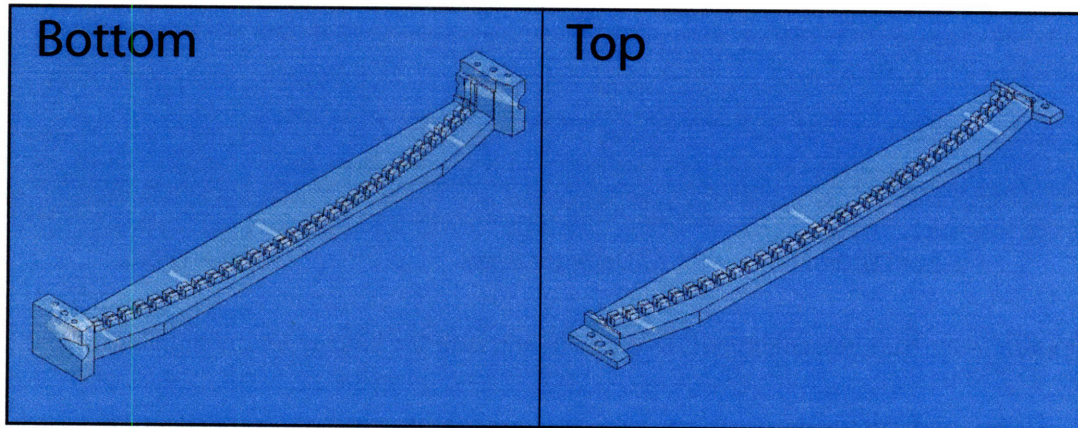
Figure 5-38: SolidEdge drawing of top and bottom detector mount pieces. Detectors slide in between the teeth-like slots and are held in compression.

5.6.6 Detector Mount

The design of the detector mount was challenging as it incorporates not only all the detectors, but also alignment lasers. The detectors are mounted on substrates that are $6.0 \times 15.6 \times 0.7$ mm. Stacking 32 detectors without any spacing gives a minimum height of 19.3 cm. The shape of the substrates and the position of the electrodes make mounting difficult. This was further compounded by the need for the detectors to be mounted on a radius.

While it is possible to machine such a mount it would take a large amount of time and the complexity of the part would most likely lower the overall quality. A fairly new process called stereo lithography (SLA) or 3D printing can generate a complete part from a CAD file. SLA takes the drawing file and converts it to movements for a UV light source. This source traces out the pattern over a bath of chemicals that cure when exposed to the UV. After a pass the bath is lowered allowing more liquid to cover the surface and the light traces out another path. This continues until the complete part is built up. SLA is typically used for building prototypes and visualizing parts since the product is not very mechanically rigid. The structural integrity requirements for the detector mount are almost negligible since there is no weight bearing or other stress that needs to be taken into account so the part may be used as received. The HXR mount is made from a high resolution process with ± 0.08 mm layers. The mount is made in two parts, a top and bottom, as shown in Figure 5-38. The detectors are loaded into the bottom piece and are held in compression by the top piece. The lasers are angled to mark the extent of the view in plasma and are secured by set screws after alignment. Figure 5-39 shows a picture of the fully assembled mount.

5.6.7 Electronics Box

All electronics are housed in an iridized aluminum box. The box's primary purpose is to provide RF shielding for the electronics. The box also protects the electronics from handling and is structurally rigid to install the detector mount and motherboard. Teflon runners are attached to the outside to mate with the mounting tracks on the Pb shield. The box is $9.75 \times 9.5 \times 2.75$" and 0.125" thick. The detector mount is attached directly to the box and the detectors view the plasma through a 0.25" diameter slot.
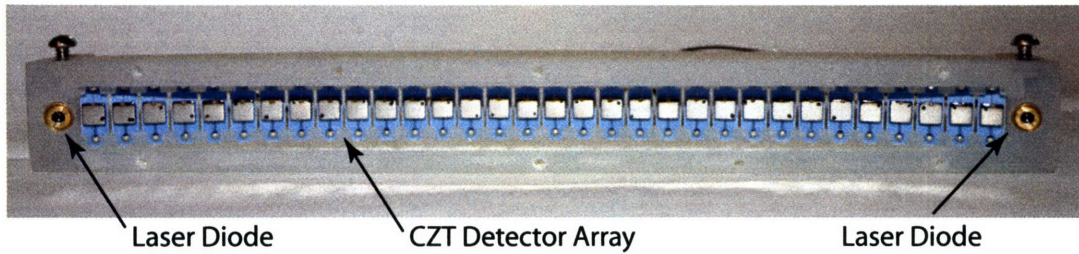
Figure 5-39: SLA manufactured detector mount with CZT array and alignment lasers.

An internal RF shield is also incorporated into the box to prevent against channel to channel crosstalk. The internal shield is composed of an upper and lower section. The upper section has three rails with slots for panels to create a separate compartment for each preamplifier and shaper. The lower section is an Al plate with slots milled to isolate the pins of the through hole components. The motherboard has exposed copper allowing the ground plane to come into direct contact with the internal shield. The rails fasten to the lower shield compressing the motherboard and giving good contact. The complete electronics box with internal shield is shown in Figure 5-40.
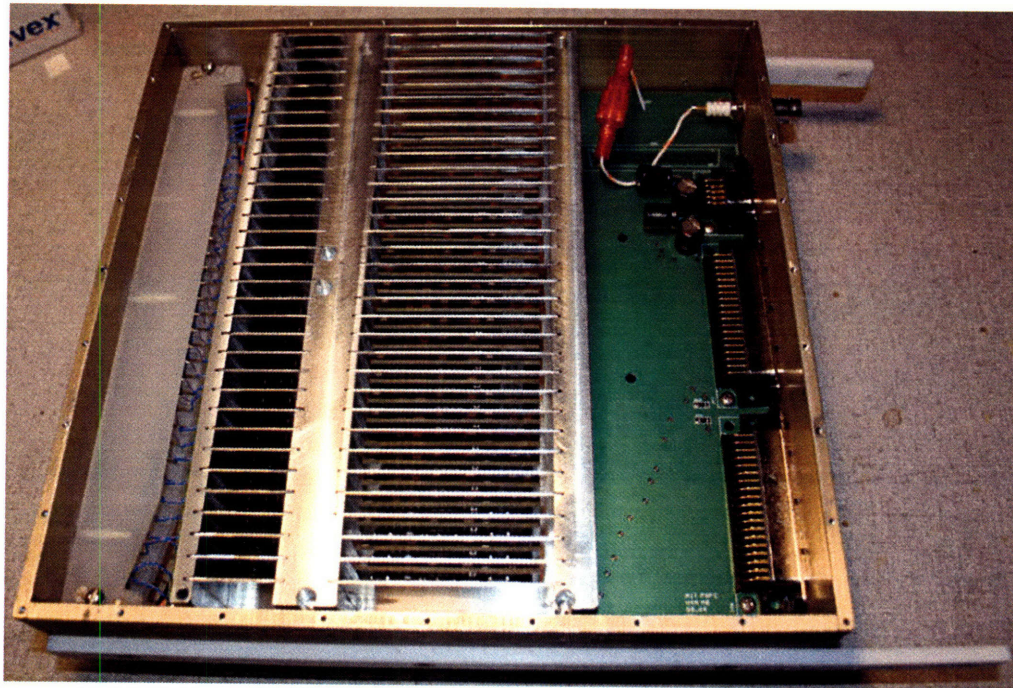
Figure 5-40: Complete electronics box assembly with detector mount and internal shielding.
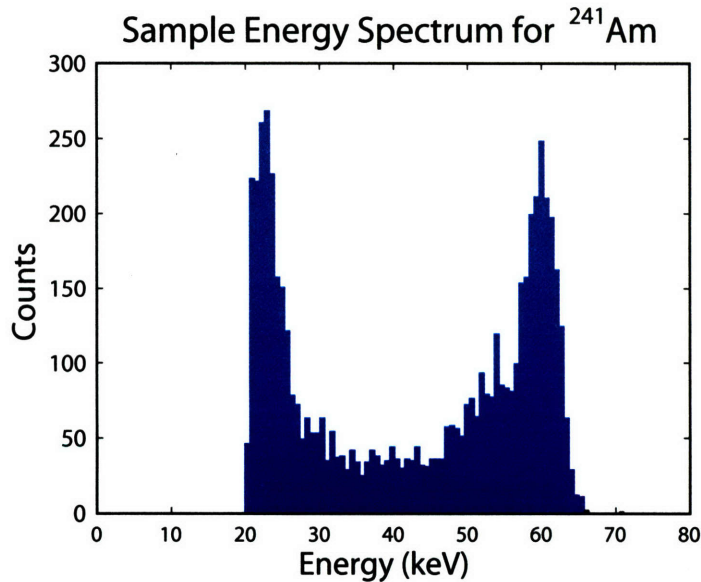
Figure 5-41: Energy calibration spectrum for channel 32 using ^{241}Am.

5.7 Calibration and Alignment

Before plasma data can be taken the diagnostic needs to be calibrated and aligned. The energy calibration was performed by using two very active sources, ^{241}Am and ^{57}Co. Two energy points were needed to give a linear relation for the energy. Using just one source and assuming that the energy is linear and passes through zero keV and zero volts ignores the well known threshold that CZT detectors have. These two sources provide energy points within the desired energy range with good separation. The ^{241}Am has a peak at 60 keV and an activity of 400 μCi and the ^{57}Co has a peak at 122 keV and an activity of 5 mCi. The ^{241}Am is a long lived source with a half life of 432 years, which is regularly accessible. The ^{57}Co on the other hand has a relatively short half life of 272 days, and had to be borrowed from the Physics Department's junior lab Mossbauer effect experiment.

Such strong sources were needed since the digitizers can only digitize for about three seconds at a time. Multiple shots are added together to produce the spectra with reasonable statistics and resolution. The sources were independently placed in front of the full electronics box assembly. The bias voltage was set to 200 V and then the data acquisition system is initialized, triggered, and stored. C-Mod style shot numbers were used to separate the good calibration data from a number of other test shots. Three shots at 2.8 s each were used to build up the spectra. Numbers 1050128001-3 are used to build the cobalt spectrum while shots 1050128006-8 are the americium. Sample spectra are plotted against the energy calibration obtained and are shown in Figures 5-41 and 5-42.

The complete linear calibration numbers are shown in Table A.1. The slope in keV/V and intercept in keV allows the conversion of voltage data to energy for each channel. The standard deviation in the slope is 5.2 keV/V and 1.1 keV for the intercept.

The lack of a good reference surface on the shield lead to the development of an alignment system. The general position of the view could be estimated by measuring the position of the shield, but the actual view would be unknown. It is important to ensure that the plasma

Table 5.5: **Energy calibration results**

Channel	Slope(keV/V)	Int.(keV)
1	132.8	9.9
2	123.3	8.0
3	130.0	10.3
4	128.6	8.3
5	130.0	9.0
6	135.7	9.5
7	137.2	9.0
8	138.7	9.8
9	138.7	7.0
10	137.2	8.3
11	138.7	7.7
12	130.0	9.0
13	128.6	7.6
14	121.3	9.8
15	119.7	8.3
16	132.8	7.3
17	135.7	9.5
18	137.2	8.3
19	124.8	11.1
20	131.4	9.2
21	134.2	8.1
22	130.0	9.0
23	132.8	8.6
24	132.8	8.6
25	130.0	6.4
26	122.3	8.4
27	131.9	9.3
28	133.3	6.1
29	130.5	9.2
30	130.0	9.0
31	124.5	9.3
32	134.2	10.1
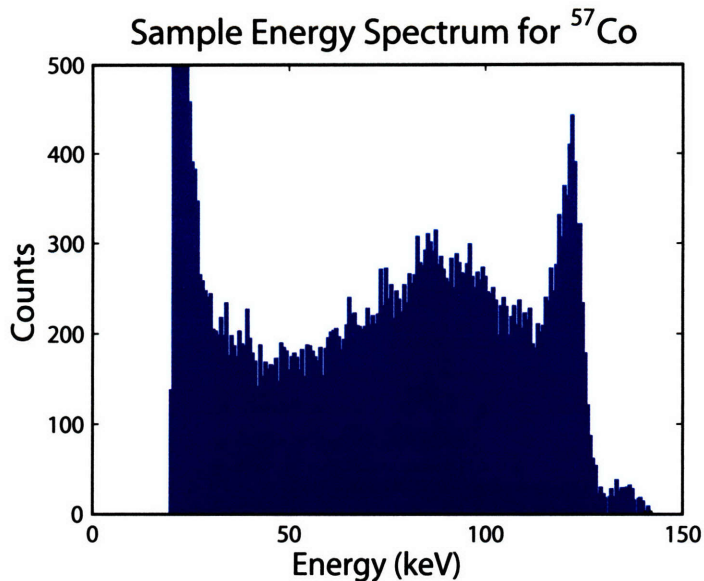
Figure 5-42: Energy calibration spectrum for channel 1 using ^{57}Co.

view is not obstructed by the periscope or gas injection line. It also helps a great deal for interpretation of results and modeling to know the exact view. A set of two laser diodes are used to give the extent of the view as measured on the central column. The tiles on center column are the best position reference on the machine. This allows any tilts and angles to be taken into account during the analysis. The only downside is that it requires a manned entry when the machine is up to air. The vacuum window must be off since it is opaque and the flange must be in place before the mounting structure is attached to the igloo. B-port is the emergency exit port so the alignment is one of the last things done before C-Mod is closed up and pump down begins.

The laser diodes themselves are centered in the detector mount and the electronics box. The two beams were internally aligned to intersect at a distance of 38.15 cm from the front face of the electronics box and have an angle of 14.8°. The position of the laser spots may be used to completely determine the geometry of the system. Typically the HXR camera is aligned with about a 3° angle toward A-port to avoid any obstructions. The exact geometry changes from campaign to campaign.

5.8 Background Measurements

A number of different setups were used to gather background spectra data during the run campaigns leading up to lower hybrid operation. The first setup used a pixilated CZT detector with an ASIC. Next, two channels of planar detectors with an early revision of the Gaussian shaper were tied. Finally all 32 channels were used inside the lead shield and it is these results that will be presented here.

In all cases the detectors were sensitive to counts from runaway electrons and counts generated during ICRF heating. The primary source of background is neutron capture reactions in the material surrounding the HXR diagnostic. The neutron rate and HXR background signals track the ICRF heating power. Figure 5-43 shows the time history of

146
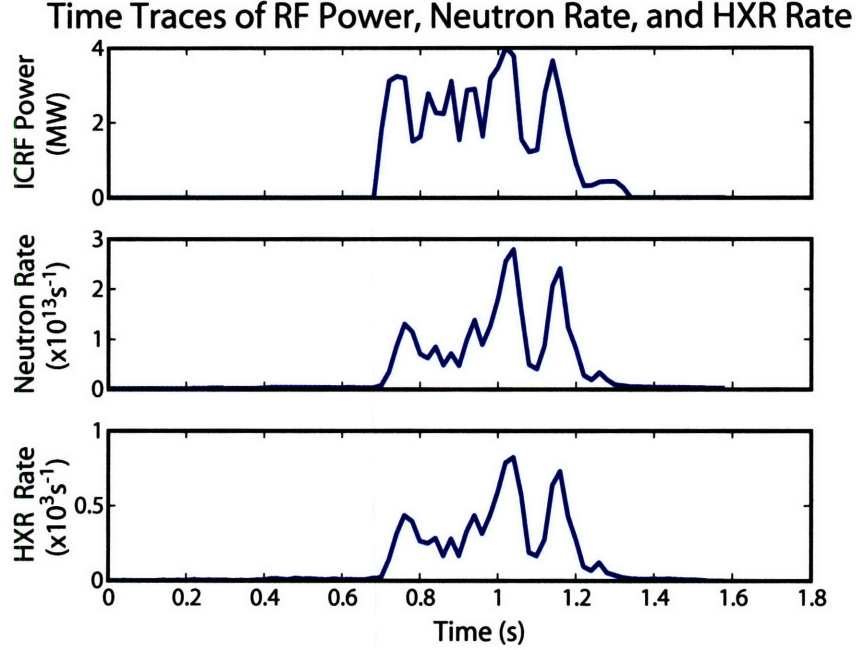
Figure 5-43: Time traces showing the background tracking with RF power and neutron rate for shot 1050804025 with $n_e = 1 \times 10^{20}$ m^{-3} and $T_{e0} = 2$ keV.

the RF power, neutron rate, and HXR background. High energy counts, greater than 300 keV, are also observed corresponding to the neutron rate. They could either be from (n, γ) reactions, or possibly neutron absorption. In either case the result of their presence is to increase the dead time of the system. At the highest neutron rates observed thus far the dead time due to all counts above 200 keV is only 8%.

The background observed is fairly consistent from channel to channel indicating the flux in the area of the camera is uniform. Figure 5-44 shows the spectra from all channels. The majority of the spread occurs at the low energy channels where the thermal bremsstrahlung from the varying plasma views may contribute.

Figure 5-45 shows the background count rate in the 90-100 keV energy bin as a function of neutron rate. The background rate is linear, but with greater uncertainty at higher neutron rates from limited data and counting statistics. Results from DKE simulations indicate that the bremsstrahlung signal level is a nonlinearly increasing function of lower hybrid power, but is near the levels shown in Figure 5-45. Operating conditions, particularly the plasma density, LH power level and ICRF power level will determine the signal to noise of the HXR diagnostic. From the H-mode plasma used in DKE about 500 kW of LH power is needed to give a signal to noise ratio of one for a neutron rate of 10^{13} s^{-1}.
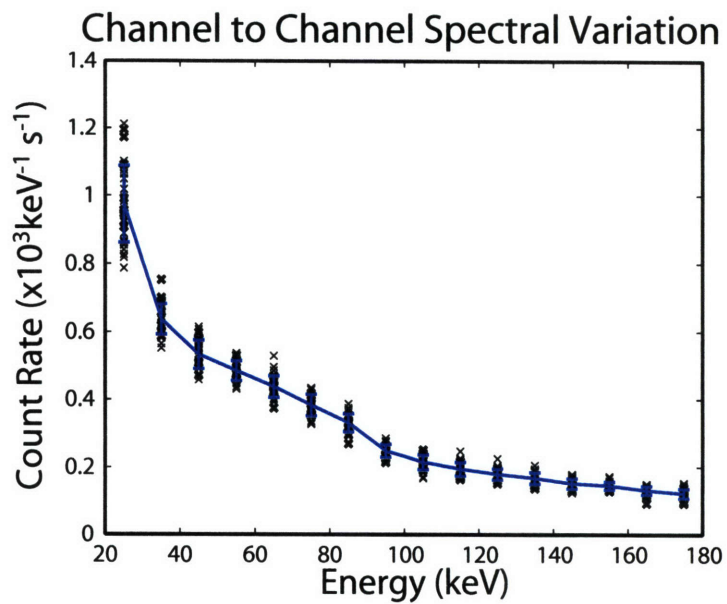
Figure 5-44: Typical background spectrum for a neutron rate of $5 \times 10^{12}\ s^{-1}$ for all 32 channels. Each channel is represented by an x while the average is plotted as a solid line.
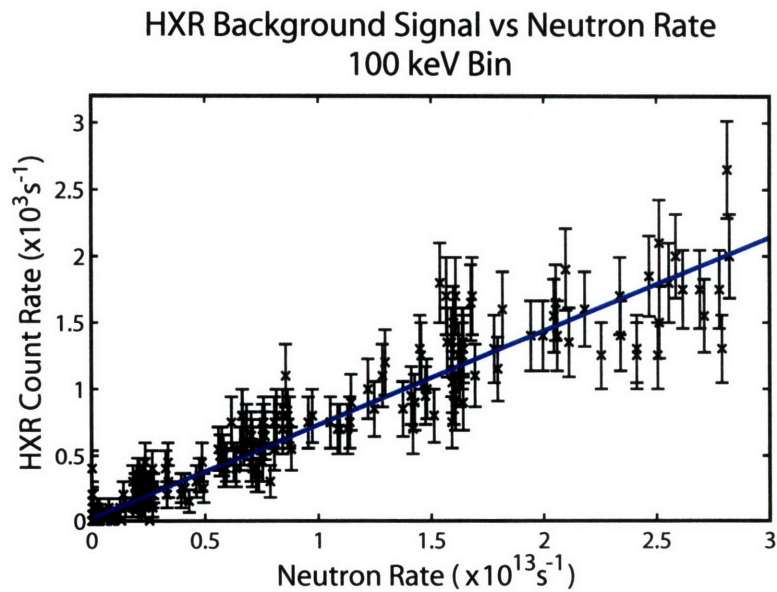
Figure 5-45: Background signal level vs neutron rate for the 90-100 keV energy bin from six shots.

Chapter 6

HXR Results and Experimental Observations

LH generated fast electrons were first observed on C-Mod during the first LH run day, 1060307, of the Spring 2006 campaign. This run was dedicated to coupling studies, but on shot 12 the density was low enough that fast electron bremsstrahlung was observed on the HXR camera. Shot 16 had a slightly higher power and gave even more signal. After the coupling studies were completed, the main focus was to increase power and pulse length to create a measurable fast electron population and drive current. This meant that a reliable means of arc protection had to be developed and tested; runs 1060406 and 1060413 were devoted to this purpose. The method that was ultimately decided upon was to compare the reflected and forward power signals of the RINTs and FINTs. If the RINT/FINT ratio for a given klystron exceeded the 30% threshold value, then all klystrons would be switched off. A re-strike system was also implemented that attempts to restart the klystrons 20 ms after a fault. The re-strike will try up to six times to restart the LH power. The RINT/FINT signals by themselves do not provide complete protection. Arcs are possible and have been observed that do not raise the RINT/FINT ratio so further protection is needed. Circuits are being added, which will compare the ratio of reflected and forward power on the jungle gym couplers with the goal of fully protecting the launcher and couplers.

Given that the system was not fully protected for initial current drive experiments, less than half of the full source power was used in run 1060420, which had the goal of producing measurable plasma current. In fact about one megawatt was generated at the source, and given the losses and coupling efficiency, this produced a maximum coupled power of about 430 kW. The maximum pulse duration achieved was 400 ms. As will be shown below this type of power and pulse length drove current and generated copious amounts of HXR photons.

LH power has been used thus far in low density L-mode discharges, typically with plasma currents of 700 kA, a 5.4 T magnetic field, central electron temperatures of 2-3 keV and integrated densities of $3\text{-}5\times10^{19}$ m^{-2}. This corresponds to a line-average density of about $5\text{-}8\times10^{19}$ m^{-2}. Since the current drive efficiency is roughly inversely proportional to the density[44], reducing the density is like increasing the power. The grill was moved in to be approximately flush with the LH limiter for run 1060420 in order to maximize coupling.

Run 1060420 had a discontinuity in the phase between carts 2 and 3, which produced compound-like spectra shown in Figure 6-1. The phase progression remained the same and will be used to label each spectra.
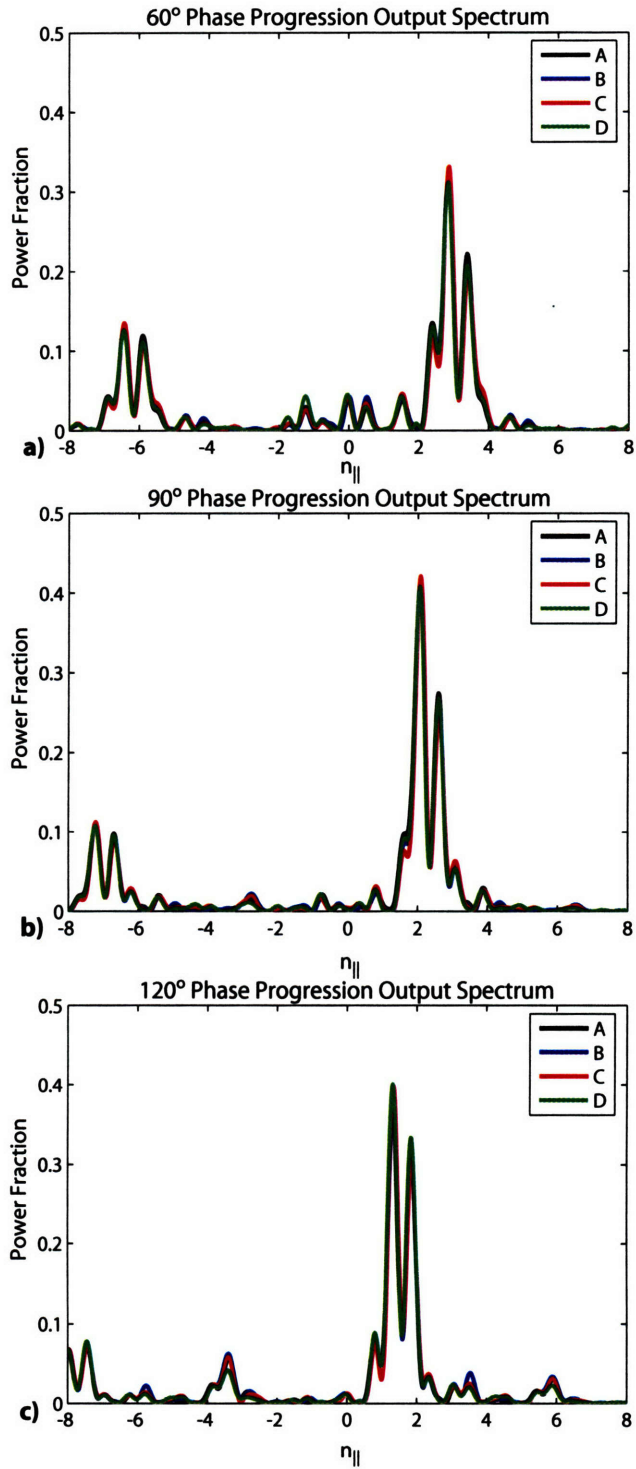
Figure 6-1: Spectra for 60°, 90°, and 120° CD phase progressions. Note that the 60° phase progression has the highest $n_{\parallel}$ of the compound spectra. For non-compound spectra, 60° phasing has the lowest value of $n_{\parallel}$.

150

Changes in the loop voltage and a reduction of the internal inductance were observed as LH power was applied using CD phasing. This is shown for shot 1060420026 in Figure 6-2.

The reduction in l_i corresponds to a broadening of the current profile due to LHCD.

The HXR camera was aligned during the last manned entry into C-Mod, before the beginning of the campaign. The laser spots were aligned to +39.5 and -39.5 cm above and below the machine midplane, with a 3.7 cm tilt towards A-port with respect to the center of the B-port. The tilt angle is 3.4°. A top view showing the tilt of the viewing chords and the direction of the plasma current and magnetic field is shown in Figure 6-3. A poloidal cross sectional view of the HXR viewing chords is show in Figure 6-4.

6.1 CD and CCD Phase Progression Results

The effect of changing the phase progression direction was studied by comparing changes in the loop voltage and HXR spectra for two discharges with 400 kW of coupled power. Shots 1060420026 and 1060420009 launched waves in the CD and CCD directions respectively, with 90° phase progressions. Time traces of plasma parameters are shown in Figure 6-5. The top panel shows the coupled LH Power in kW, the second panel displays the line-integrated density, the third panel shows the magnitude of the loop voltage, while the bottom panel plots the total HXR count rate for channel 16. The loop voltage was digitized at 5 kHz and was smoothed using 83 points to reduce 60 Hz noise. Changing the launch direction produced dramatic differences. The loop voltage was virtually unchanged by CCD phasing, while a drop of about 0.4 V, or 50% was seen for CD phasing. The drop in voltage means that actual current was being driven by the lower hybrid waves, since a lower voltage was needed to maintain a constant plasma current. Both CD and CCD phasing HXR count rate signals are sensitive to the changes in density. As the density decreased the HXR total count rate increased.

A rough estimate of the spatial distribution of the fast electron population may be made by plotting the HXR count rate for a given energy bin against channel number. This is shown in Figure 6-6 for the 48 to 58 keV energy bin. This energy range was chosen since there was a negligible contribution to the count rate above about 40 keV by thermal electrons. Channel 1 views the bottom of the plasma while channel 32 sees the top. For both phase progressions the emission is peaked broadly in the center, which seems to indicate that the fast electrons are located over a wide spatial extent centered near the magnetic axis. Such a broad profile may be the result of the compound spectra used and spatial diffusion of the fast electron population. The CD phase progression had a much higher count rate due to the ohmic electric field, which accelerated the fast electrons to even higher energies. Conversely, the electric field decelerated the CCD driven electrons.

The effect of the electric field is even clearer when examining the PHA results for a central channel; this is shown in Figure 6-7. CD phasing generates a much more energetic population of electrons, which is seen in both the slope and and magnitude of the count rate at higher energies.
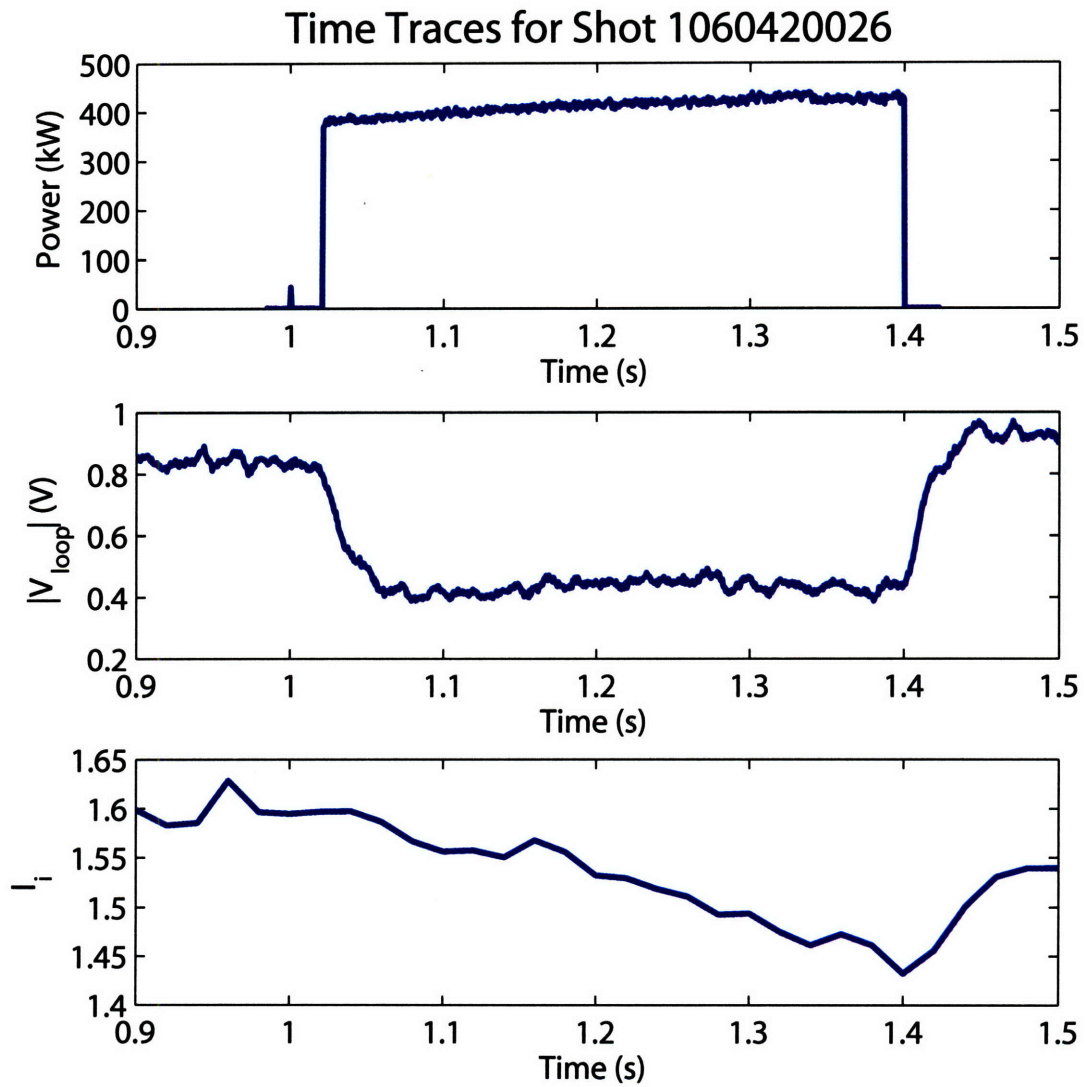
Figure 6-2: Time traces of coupled LH power, loop voltage, and internal inductance.

Top View of HXR Chords
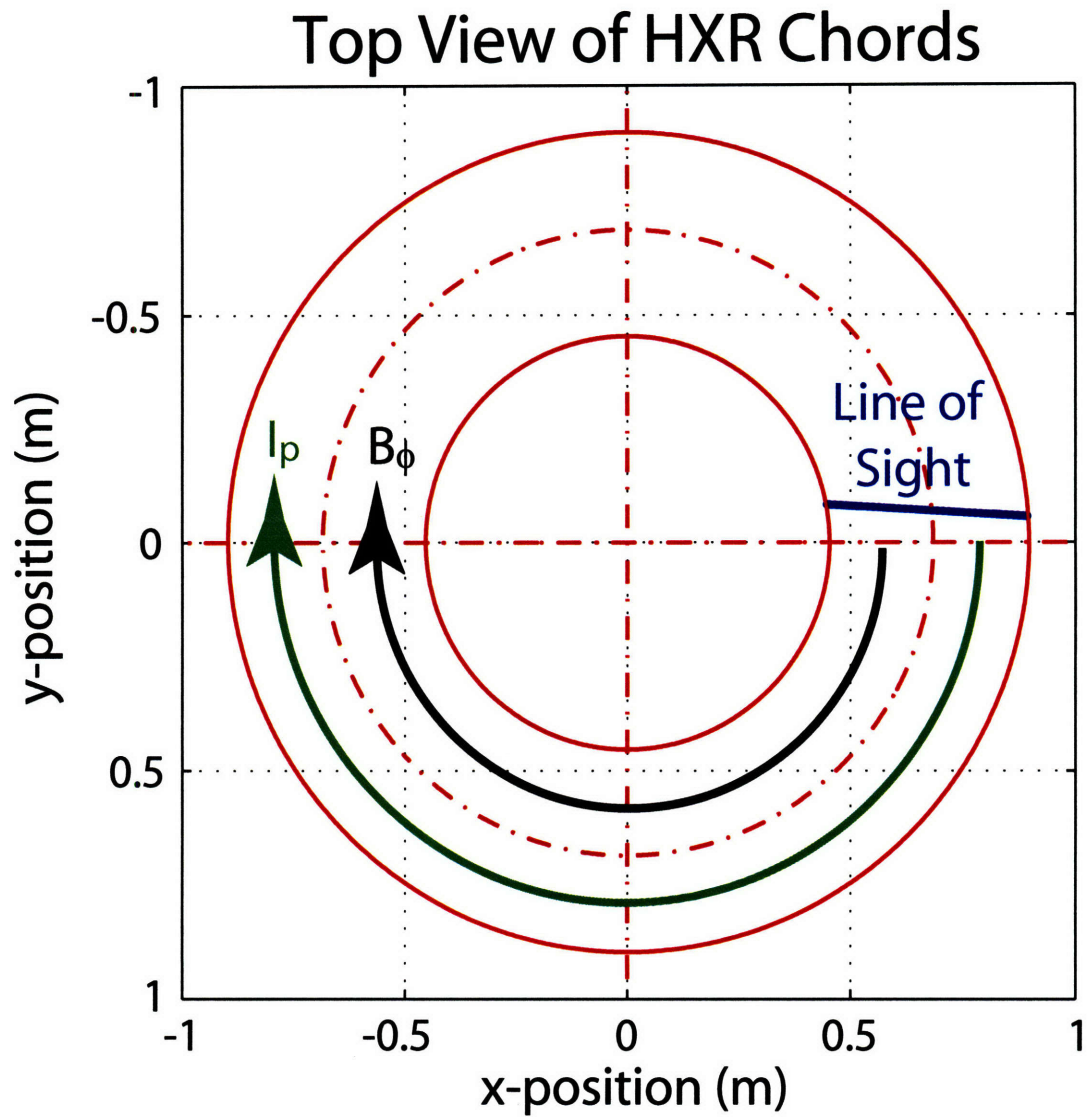
Figure 6-3: Top view of the plasma and HXR geometry. The HXR view is shown in blue, plasma current direction in green, and toroidal field direction in black.
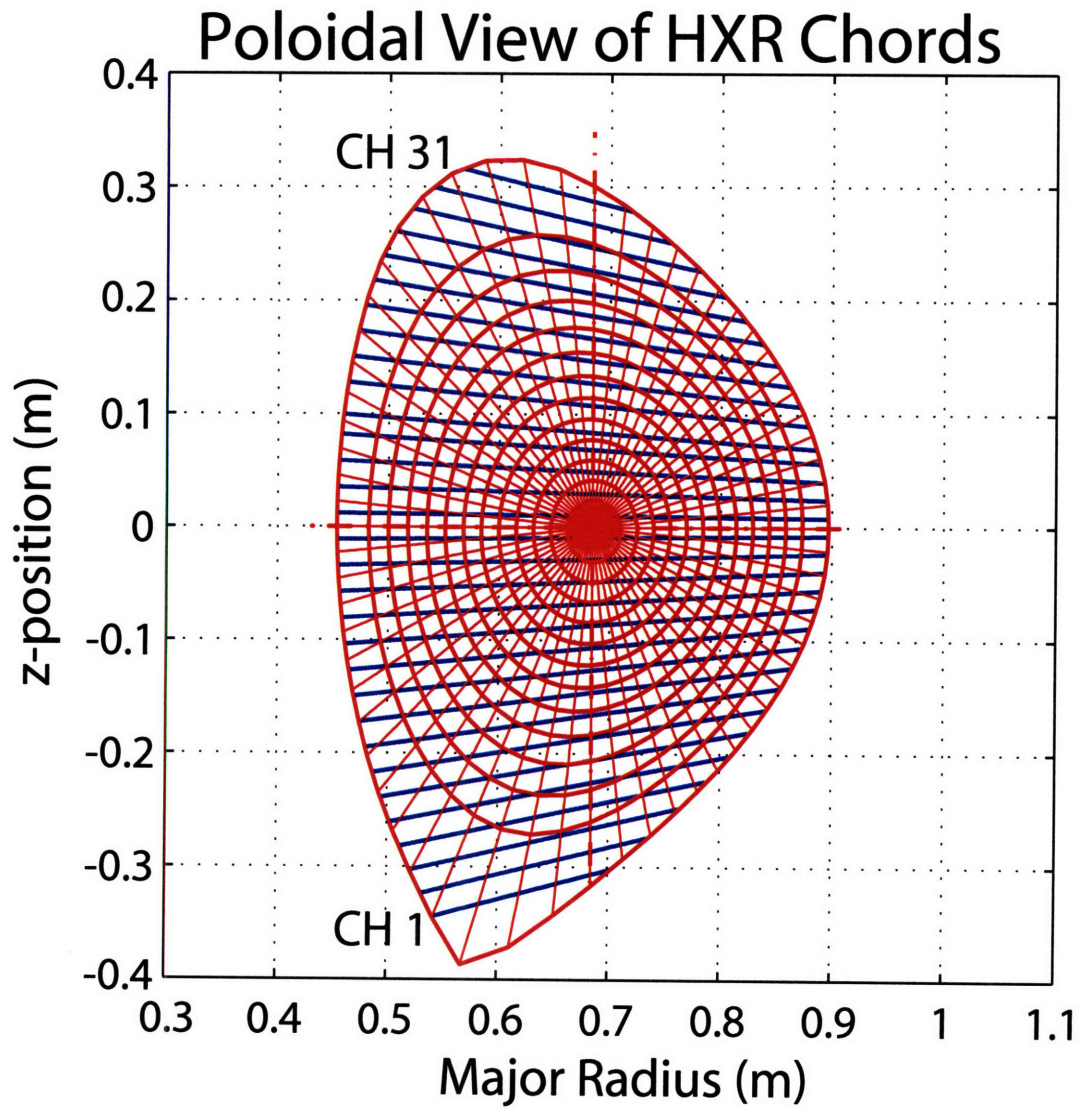
Figure 6-4: View of HXR chords for shot 1060420026 at 1.2 s. Channel 32 does not view any closed flux surfaces.
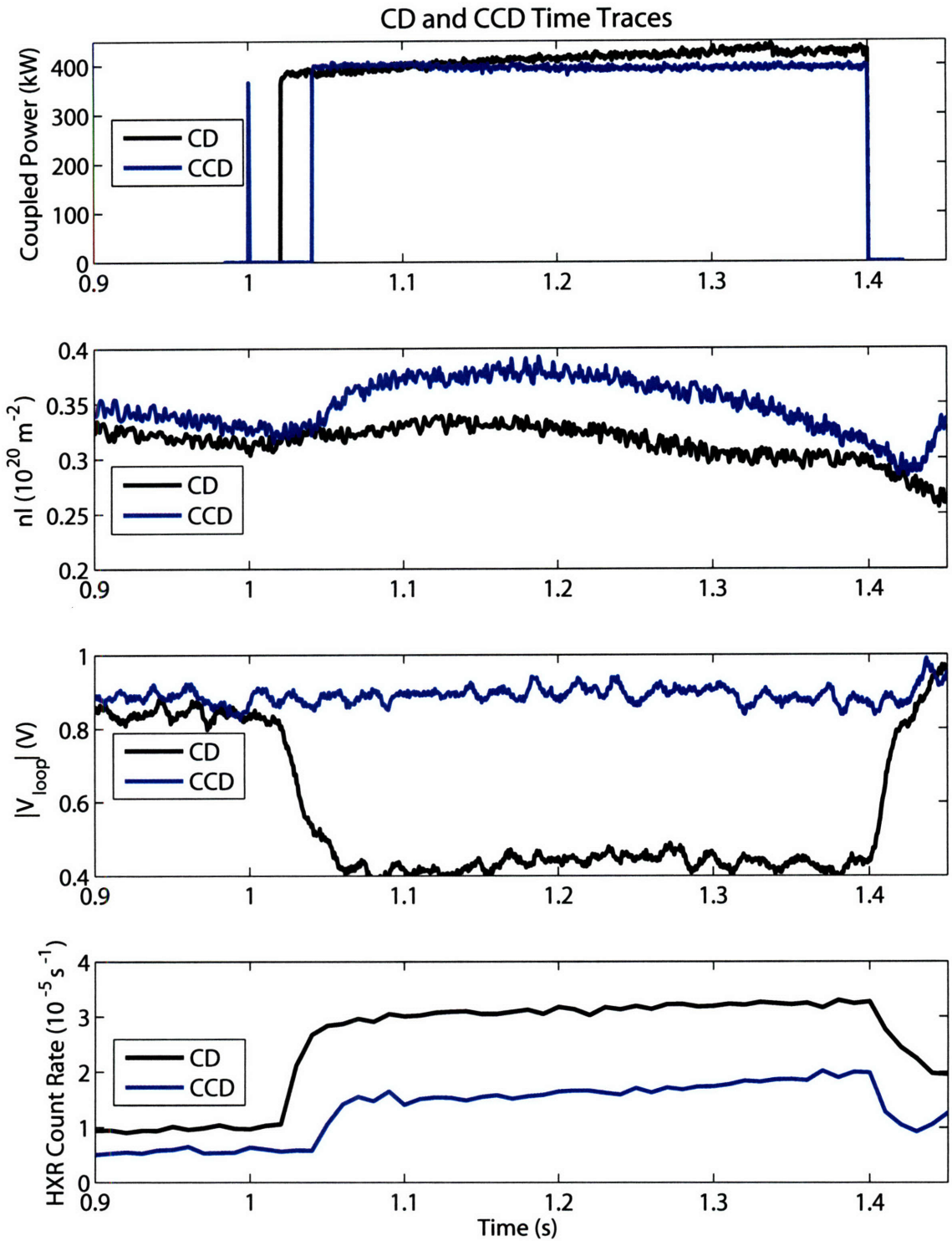
Figure 6-5: Time traces for shots 1060420026 and 1060420009, which had 90° phase progressions in the CD and CCD directions respectively. Shot 1060420009 was at 5.4 T, while 1060420026 was at 6.5 T.
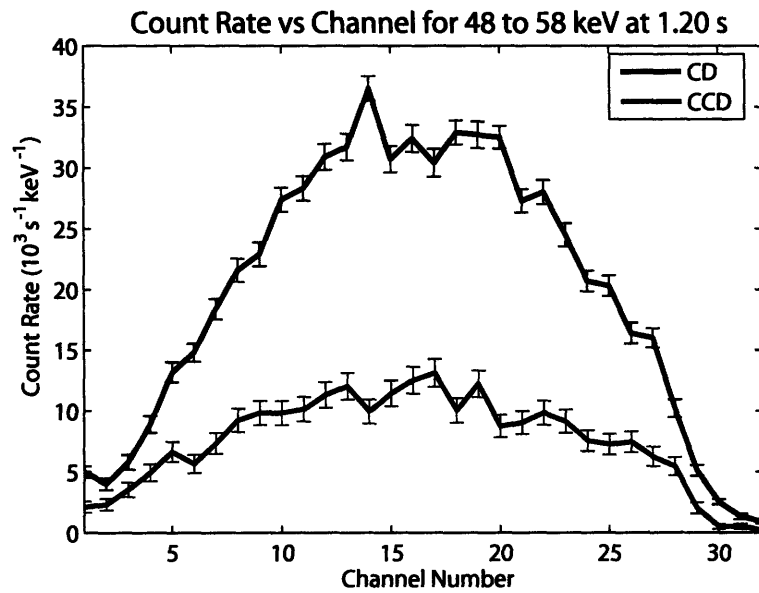
Figure 6-6: Count Rates for CD and CCD phase progressions for the 48 to 58 keV energy bin at 1.20 s.
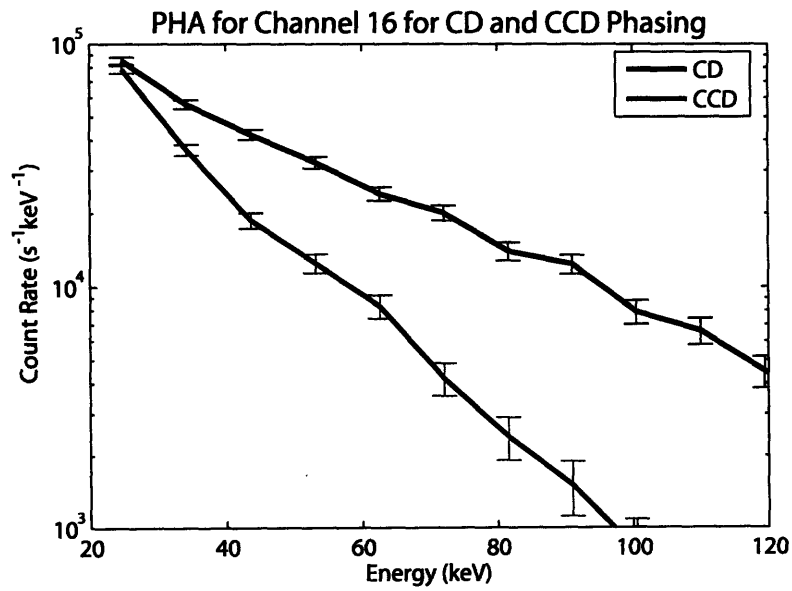
Figure 6-7: PHA spectra for CD and CCD phasing for channel 16 at 1.20 s.

6.2 Phase Scan Results

CD phase progressions of 60, 90, and 120 degrees were used to study the effect on the plasma of varying the $n_\parallel$ spectrum. Figure 6-8 shows time traces of the relevant quantities. Differences in the coupled power for each phase are observed in the top panel due to different reflection coefficients at the grill. Unfortunately, the density was significantly higher for the 120° phase progression, making a direct comparison of this result difficult. Density control at these levels is difficult on C-Mod, and some drift is expected shot to shot and even during a shot. Decreases in the loop voltage were observed for all phase progressions with 90° causing the largest reduction. 90° also produced the highest HXR count rate.

The 90° phase progression also produced the most counts in the 48 to 58 keV bin as shown in Figure 6-9. As was the case when comparing CD and CCD shots, the emission seems to be spatially broad, with slight variations in shape. The magnitude of the count rates depends on the density and phase. A time of 1.38 s was chosen in Figure 6-9 where the 60° and 90° progression have similar densities. 60° phasing has a lower count rate and narrower shape than the 90° result.

Pulse height analysis for each phase progression is shown in Figure 6-10. The count rate is again highest for 90° phasing at all energies. The spectra are remarkable in that they all have similar slopes, or photon temperatures. The count rate is related to the height of the quasilinear plateau of the LH distribution function, while the slope is related to the plateau width. It is expected that spectra with lower values of $n_\parallel$ would produce more energetic electrons and a harder bremsstrahlung spectrum. This is not evident from the PHA results, most likely due to the width and compound nature of the spectra produced.

6.3 6.5 T Results

Experiments at 6.5 T were also performed to compare to the 5.4 T results. Increasing the field should improve wave accessibility, and possibly change the spatial distribution of the fast electron population. Shots 1060420021 and 10600420023 used 60° and 90° phase progressions. Time traces of the coupled power, line-integrated density, loop voltage, and total HXR count rate are plotted in Figure 6-11. 60° phasing had a fault to start and a lower coupled power due to a higher reflection coefficient. The density of the shots was matched fairly well, with 90° phasing being slightly higher. 90° phasing produced the greater drop in loop voltage which may be due to a slightly higher power level, or more efficient current drive, or a combination of both. The 60° spectra has most of the power at $n_\parallel > 2$, while the 90° spectrum is more centered around $n_\parallel = 2$. Lower $n_\parallel$ values are expected to drive current more efficiently since the resonant electrons are more energetic and less collisional. Total HXR count rates are very similar as well.

The spatial distribution of the fast electron populations appear to be similar for the two phasings, which can be seen when count rate is plotted against channel number in Figure 6-12. A time of 1.2 s was chosen to minimize the effects of power and density on the spectra. At this time the 90° case has a higher density than the 60° case which may partially compensate for the difference in input power levels. The shape and magnitude of the count rates for the two phasings are very similar.

Comparing Figure 6-12 to Figure 6-9 allows the 6.5 T results to be compared to the 5.4 T results at similar powers and densities. The 90° phasing is mostly unchanged, except that the outer channels have slightly higher count rates at 6.5 T. The 60° phasing showed
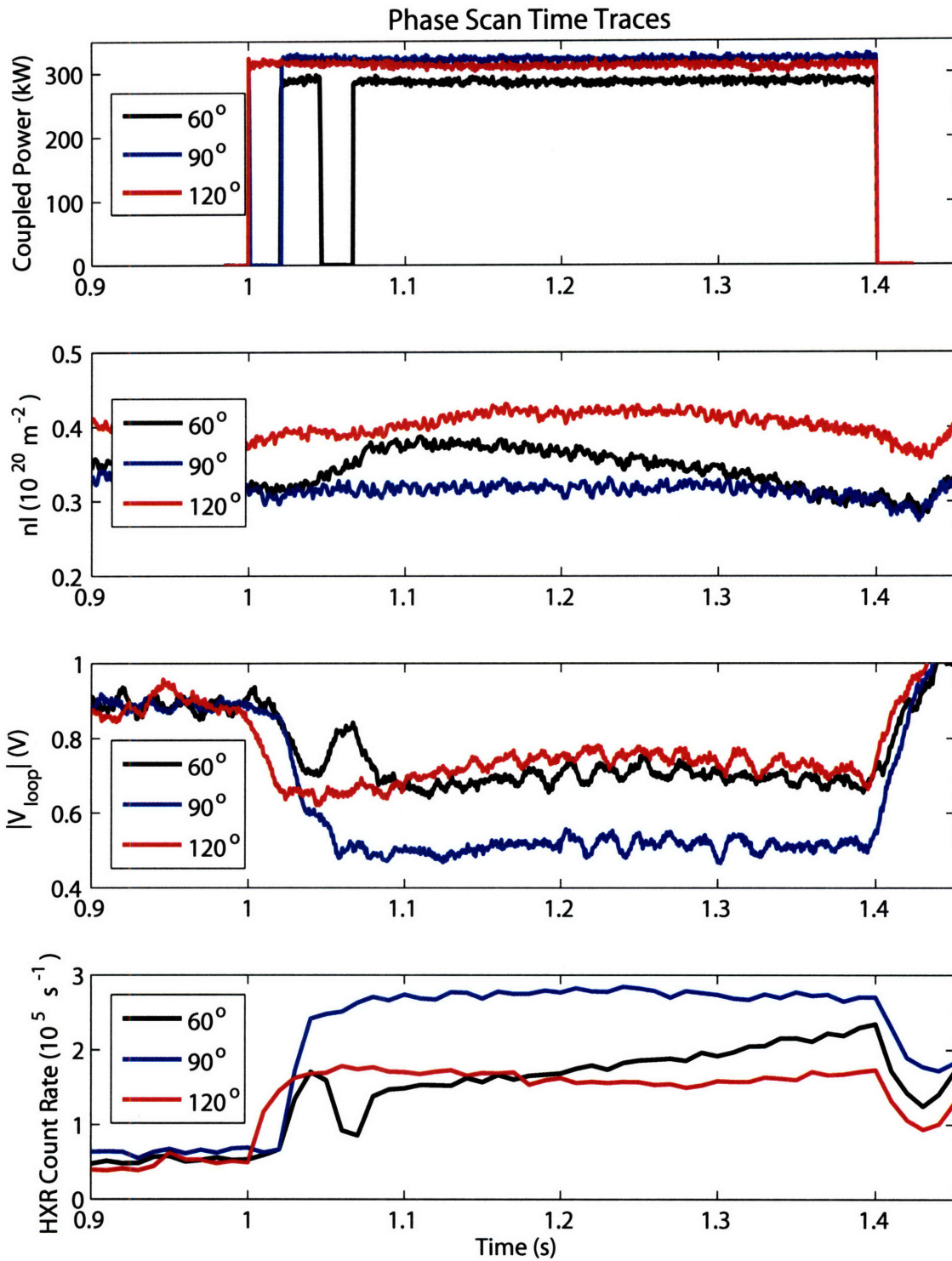
Figure 6-8: Phase progression time traces for shots 1060420020, 1060420015, and 1060420018, which had 60°, 90°, and 120° CD phase progressions at 5.4 T.
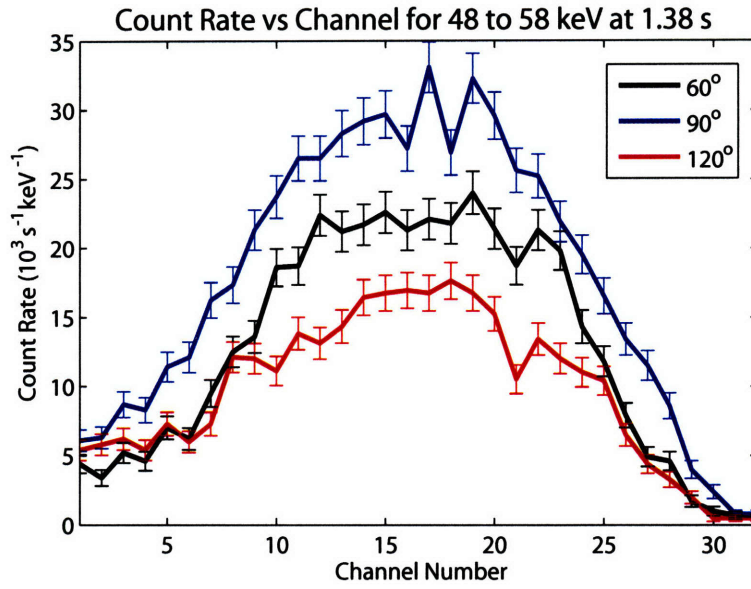
Figure 6-9: Count Rates for 60°, 90°, and 120° phase progressions for the 48 to 58 keV energy bin at 1.38 s.
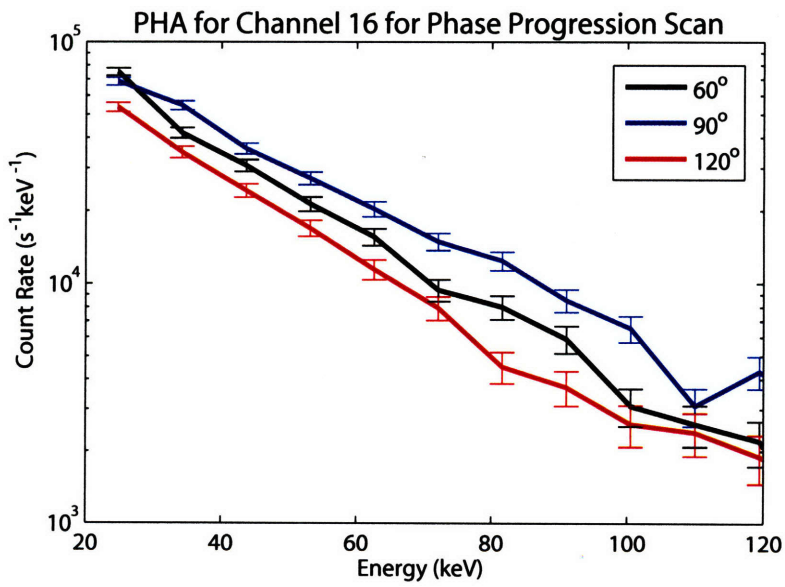
Figure 6-10: PHA spectra for 60°, 90°, and 120° phase progressions at 1.38 s.
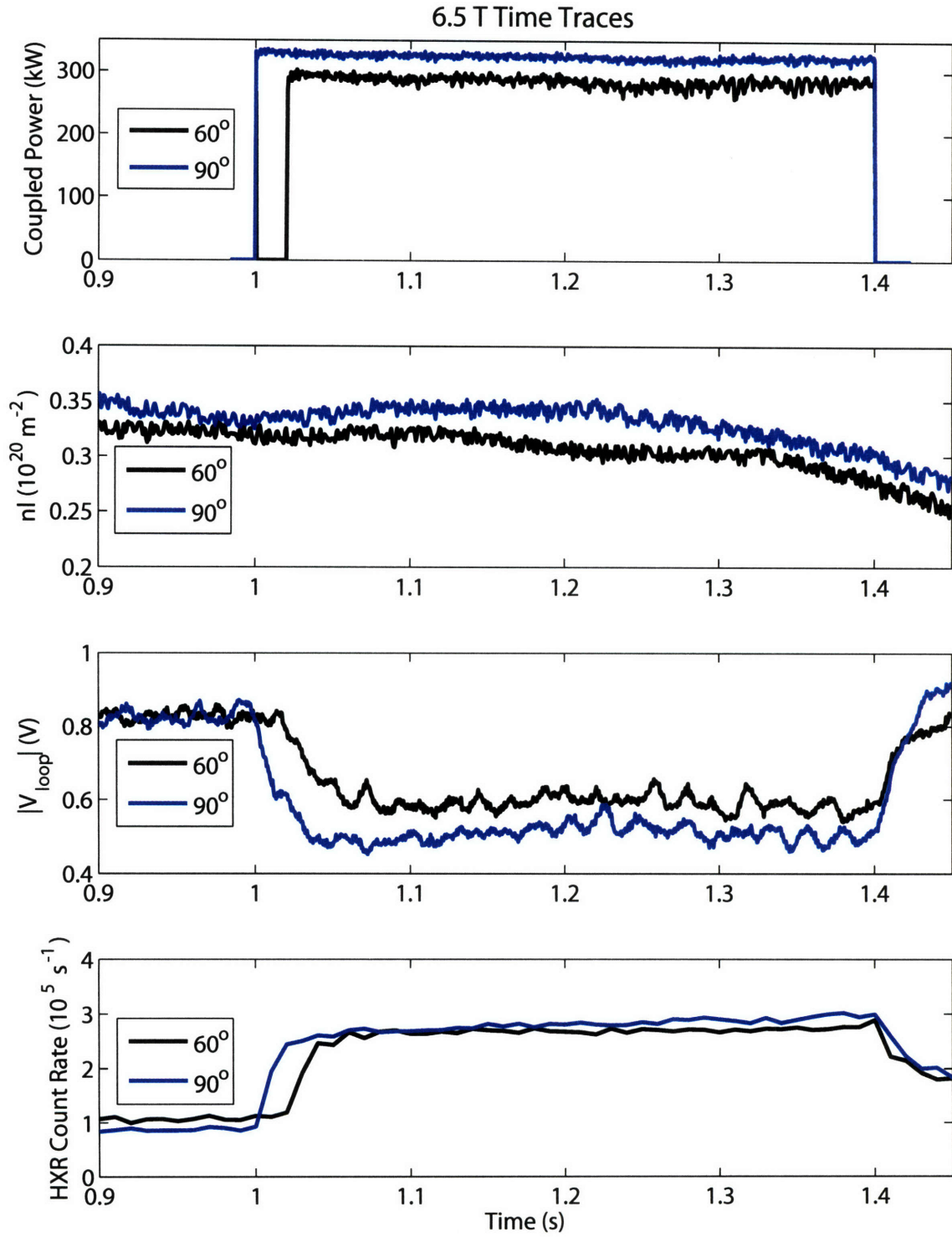
Figure 6-11: Time Traces for shots 1060420021 and 1060420023, which were 60° and 90° phase progressions at 6.5 T.

an increase in count rate in the central channels. The change in the loop voltage for the two fields and phases are comparable as are the pulse height analysis results.

6.4 Density Scan Results

A density scan was also performed over threes shots. As mentioned previously, density control is difficult on C-Mod at such low levels. As such regular steps in density are difficult to produce and the density drifts in time. The density was increased incrementally for shots 1060420027, 1060420028, and 1060420029, while the phase progression was fixed at 90°. In this section the shot numbers will be used to label each density and referenced by the last two digits. On all shots the coupled power level was ramped from about 380 to 430 kW. Shots 27, 28, and 29 the had line-average densities of about 0.3, 0.4, and 0.6 $\times 10^{20} m^{-3}$. Time traces of the relevant quantities are shown in Figure 6-14. Examining the loop voltage shown in the third panel clearly shows that as the density increases the change in loop voltage lessens meaning less current was driven. Effects from the increasing power level in time as well as the drifting density level can be seen on both the loop voltage and the total HXR count rate.

The fast electron spatial distribution, as indicated by plotting the count rate vs. channel number, is shown in Figure 6-15 for each shot at 1.10 s. The density was increased by a factor of two from shot 27 to shot 29, which caused about a factor of seven drop in the bremsstrahlung emission level. Since LHCD efficiency is roughly inversely proportional to the density for a given power, about 800 kW of coupled power would be needed to increase the signal level from that in shot 29 to that in 27. The drop in efficiency can also be seen in the change in magnitude of the PHA spectra. shown in Figure 6-16. The photon temperature stays roughly constant indicating a constant width of the quasilinear plateau.
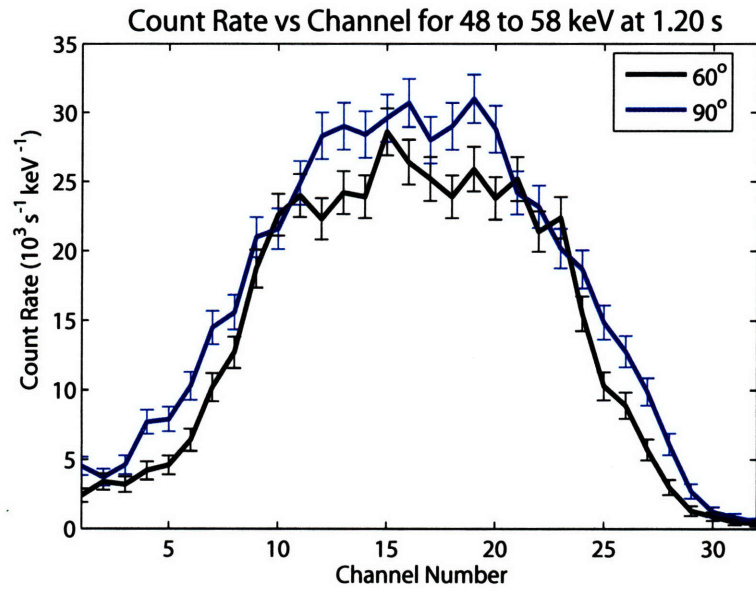
Figure 6-12: Count Rates for 60° and 90°, phase progressions for the 48 to 58 keV energy bin at 6.5 T and 1.20 s.
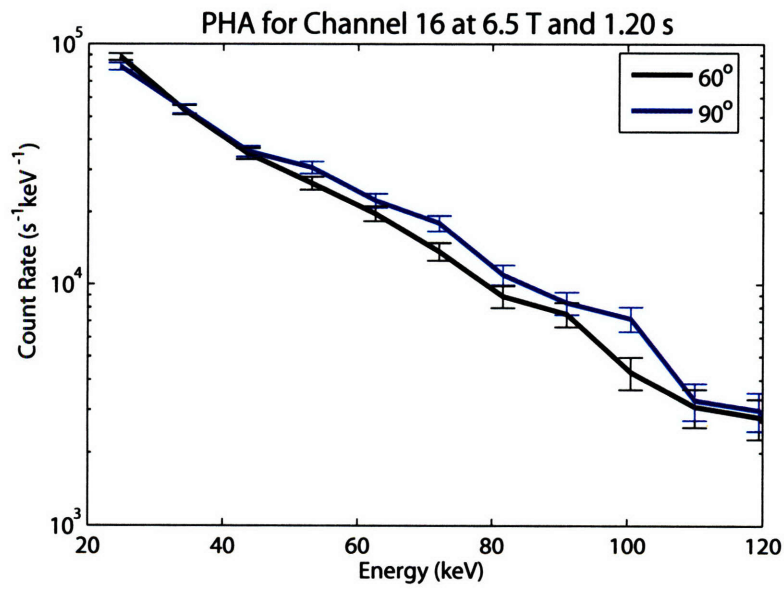
Figure 6-13: PHA spectra for 60° and 90° phase progressions at 6.5 T and 1.20 s.
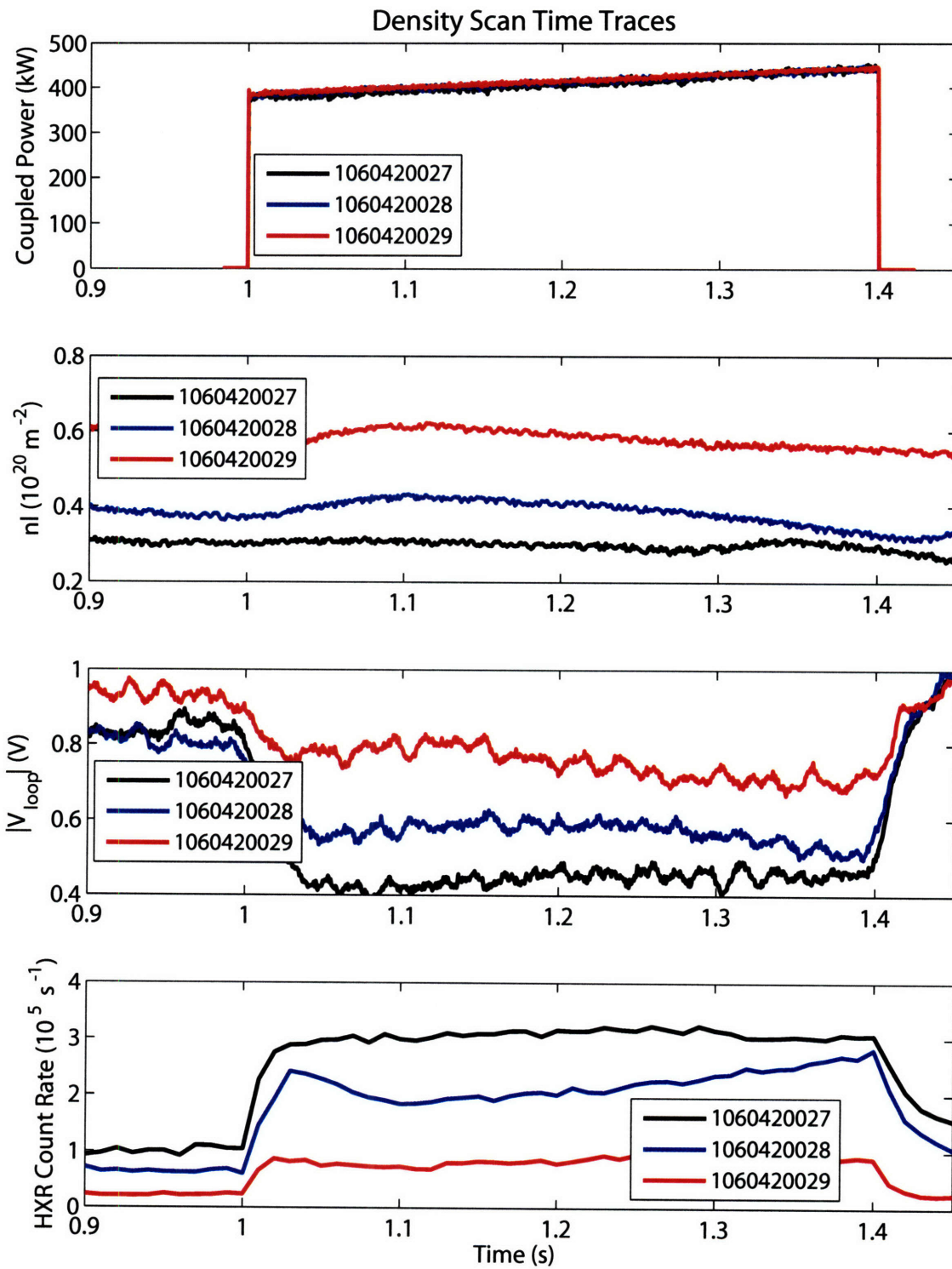
Figure 6-14: Time Traces for shots 1060420027, 1060420028, and 1060420029 with varying density at 6.5 T and 90° phase progression.
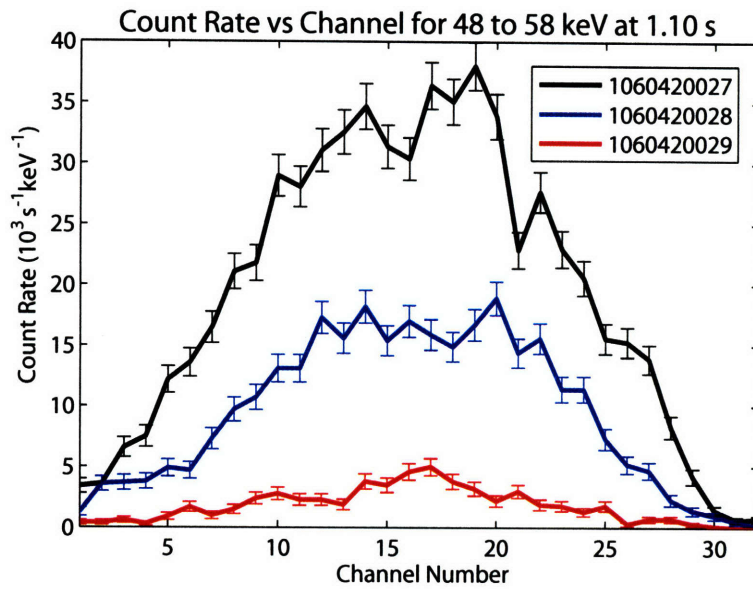
Figure 6-15: Count Rates for varying density with a 90° phase progression at 6.5 T. The 48 to 58 keV energy bin is shown at 1.10 s.
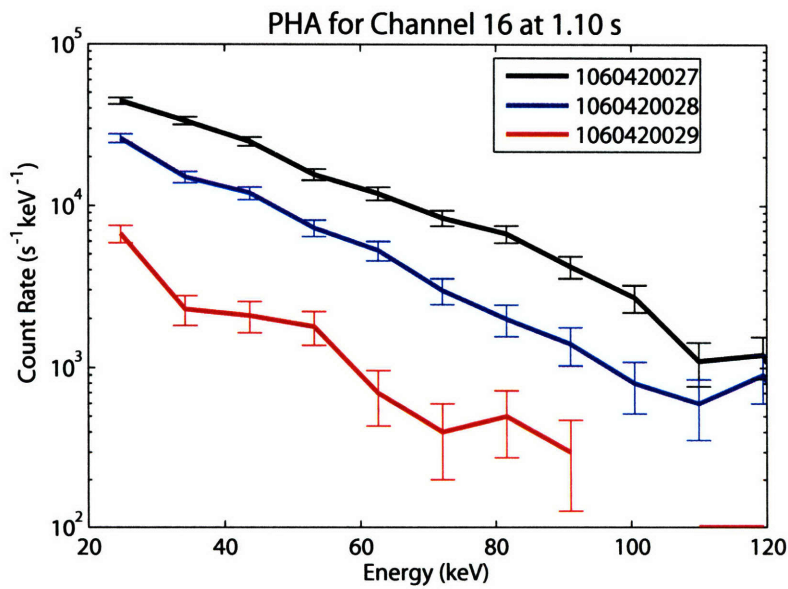
Figure 6-16: PHA spectra for varying density with a 90° phase progression at 6.5 T and 1.10 s.

6.5 CQL3D Analysis of Shot 1060420026

Discharge 1060420026 was chosen at a time of 1.20 s for detailed CQL3D analysis. Time traces for this shot were shown in Figure 6-5, as the CD case. At this time 410 kW of power was coupled, which decreased the loop voltage by about 50%, to 0.45 V. The temperature, density, and Z_{eff} profiles input into CQL3D are shown in Figure 6-17. The temperature and density profiles were obtained through Thomson scattering and the Z_{eff} profile through Thomson and visible bremsstrahlung emission. The compound $n_{\parallel}$ spectrum was modeled as CD and CCD Gaussians, centered at 2.4 and -7.0 respectively. Broad widths were used corresponding to the spectral widths determined from measurements as in panel b) of Figure 6-1.

CQL3D runs were made with and without an electric field in order to assess the importance of the ohmic field in accelerating LH produced fast electrons. Figure 6-18 shows the power deposition and current density profiles with a constant electric field of 0.0011 V/cm. This value for the field was calculated from the experimentally measured loop voltage divided by $2\pi R_0$. This value of electric field is also consistent with the electric field calculated with $q_0 = 1$ using Spitzer resistivity. The total current produced by CQL3D matched the experimentally observed value of 718 kA, which gives a degree of confidence in the quality of the CQL3D results. Lower hybrid current drive is clearly present at $r/a \sim 0.5$.

The power deposition and current density profiles without an electric field are shown in Figure 6-19. Lower hybrid driven current was produced both at $r/a \sim 0.5$ and near the magnetic axis. The total LH driven current was 167 kA.

With these two results the current drive efficiency,

$$\eta_{CD} = \frac{\bar{n}_e[10^{20}m^{-3}]I_{LH}[A]R_0[m]}{P_{LH}[W]},$$

may be calculated and compared to other experiments.

The efficiency without the electric field can be calculated by taking I_{LH} to be 167 kA, which gives η_{CD}=0.15 ($10^{20}Am^{-2}/W$). Experiments on Alcator C[19] were performed with nearly identical values of line-average density. On Alcator C η_{CD} was found to vary with magnetic field strength, having a value of 0.12 at 10 T and 0.08 at 8 T. C-Mod's efficiency is nearly twice that of the 8 T Alcator C result. Even though the densities were comparable, many parameters were different. Although Alcator C had a lower value of central $n_{\parallel}$ that would result in more efficient LH current generation, the antenna directivity was lower. C-Mod plasmas are also hotter, by about a factor of two. Increasing the temperature has been observed empirically on many experiments to increase the current drive efficiency[55]. This can be explained by the hotter plasma having more electrons at higher energy, making it easier for the lower hybrid waves to pull out a tail on the distribution function. More difficult to compare are the density and temperature profiles of each experiment, both contribute to the location where the fast electrons are produced and can influence the overall efficiency. Central current drive was observed on C based on hard x-ray emission, while CQL3D results indicate off-axis current drive on C-Mod. One of the most important factors, however, may be C-Mod's improved confinement with respect to C. The C experiments were completed with only LH current, typically about 180 kA, compared to ~700 kA on C-Mod. The increased current could improve the confinement of the fast electrons and lead to higher efficiency.

More recently a detailed study of current drive efficiency at high density was completed on FTU[55], where values of 0.12-0.24 were obtained under a variety of conditions. C-Mod's
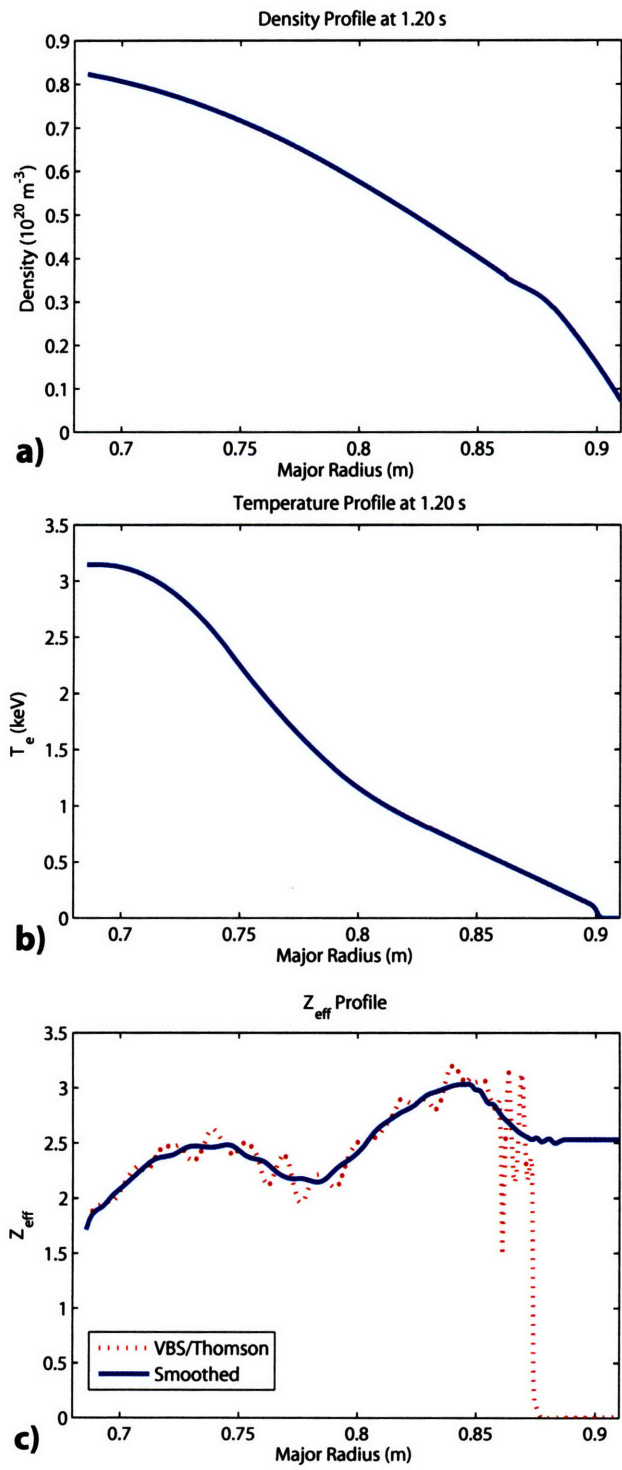
Figure 6-17: Density, Temperature, and Z_{eff} profiles for shot 1060420026 at 1.20 s. Profiles were interpolated onto CQL3D grid.
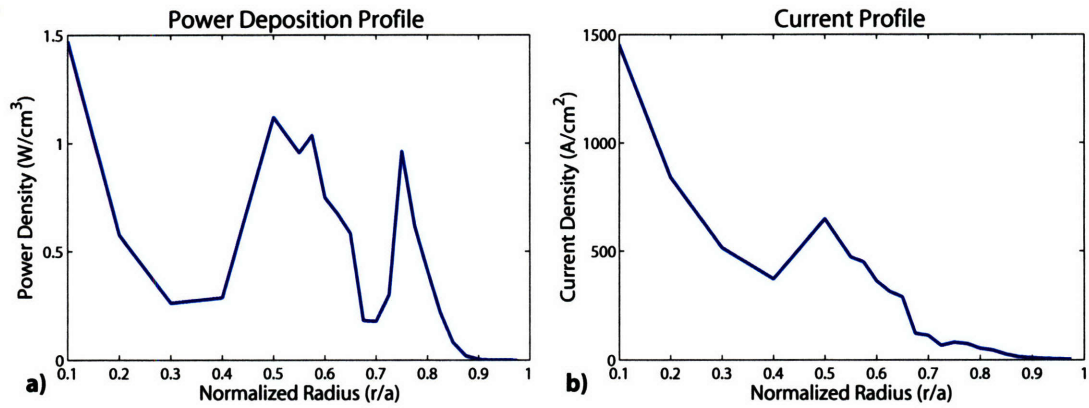
Figure 6-18: CQL3D LH power deposition and current density profiles with a constant electric field of 0.0011 V/cm. The total current was 718 kA, which matches the experimental total current.
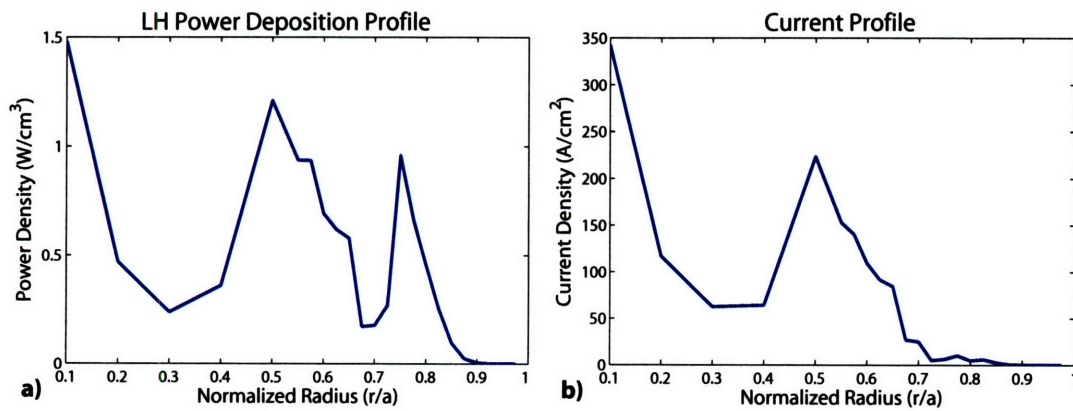
Figure 6-19: CQL3D LH power deposition and current density profiles without an electric field. The total LH generated current was 167 kA.

value of 0.15, obtained without an electric field, is toward the lower range observed in FTU. Some of the FTU data had a small residual electric field, with $\Delta V_{loop}/V_{loop} \geq 80\%$, which was claimed not to affect the efficiency. In C-Mod $\Delta V_{loop}/V_{loop} = 53\%$ was observed and the effect of the electric field should be significant in this case. An analysis identical to that in FTU was performed to compare the electric field enhanced current and efficiency to that observed in FTU. First the plasma current is defined to be the sum of the LH, ohmic, and bootstrap as

$$I_p = I_{LH} + I_{OH} + I_{BS}. \tag{6.1}$$

The ohmic current is calculated by comparing the loop voltages, with and without LH power and taking into account any bulk heating or changes in Z_{eff} as

$$I_{OH} = I_p \frac{V_{l,LH}}{V_{l,OH}} \frac{\langle T_{e,LH}^{3/2}\rangle}{\langle T_{e,OH}^{3/2}\rangle} \frac{Z_{eff,OH}}{Z_{eff,LH}}. \tag{6.2}$$

I_{OH} is evaluated to be 370 kA. The bootstrap current was calculated by CQL3D to be 40 kA, and so the enhanced lower hybrid current is 308 kA. Using this value, the voltage-aided current drive efficiency is 0.28, which is slightly higher than the maximum efficiency observed on FTU. The effect of the residual electric field was to about double both the LH current driven and the efficiency due to the ohmic acceleration of the LH produced fast electrons. The FTU team also derived a scaling for the current drive efficiency as a function of plasma parameters,

$$\eta_{CD} = 0.1543 \langle T_e \rangle^{0.517} \bar{n}_e^{0.0796} q_a^{-0.393} B_{T0}^{0.775} P_{LH}^{-0.364} n_{\parallel 0}^{-0.296}. \tag{6.3}$$

Evaluating this expression for C-Mod parameters gives an efficiency of 0.31. It should be pointed out that Equation 6.3 was developed for a fixed machine size and is of limited use for non-FTU plasmas.

CQL3D also has a synthetic hard x-ray diagnostic which may be used to compare the code results to the experiment. The detector response function was not included in the comparison so the output from CQL3D was normalized to give the same number of total counts for a given energy bin. For 48 to 58 keV, the CQL3D output had to be divided by a factor of 4.12, which is not unreasonable when the detector efficiency and Compton scattering events are considered. Figure 6-20 compares the code result to the experiment. Clearly, the experimental profile is much smoother and slightly broader and does not exhibit the three peaked features of the CQL3D result. Spatial diffusion of the fast electron population may be able to account for the discrepancies.

6.6 Experimental Observations

During initial LH experiments LH waves were observed to interact with runaway electrons. If the runaway population was negligible , then the LH waves would act as a seed to increase the runaway population. This is not surprising as the electron Landau damping would create a fast electron population that may then be accelerated by the loop voltage and become runaways. A second, more interesting phenomena was observed with a large initial runaway population and CCD phasing.

This effect was most visible on shot 1060310015, where the LH power was launched in pulses into a large population of runaway electrons. The LH power reduced the runaway
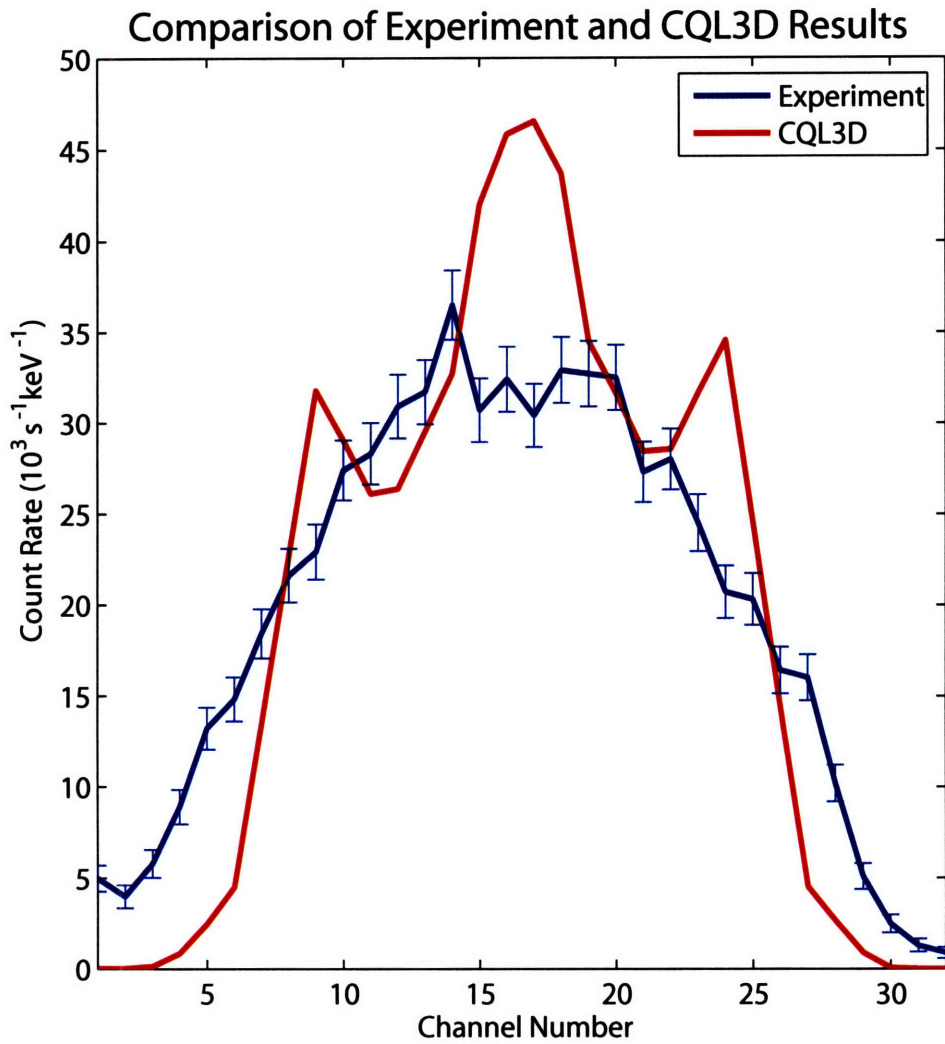
Figure 6-20: Comparison of the measured HXR profile and CQL3D's synthetic diagnostic for 48 to 58 keV.

emission measured by the "neuts-hard" signal, which is a photon detector that has a tangential view from K-port. Time traces of LH power, neuts-hards count rate, total HXR count rate, and electron cyclotron emission are shown in Figure 6-21. Along with the reduction in runaway electrons, visible light was observed on a camera. The timing seems to be correlated with the LH power as shown in Figure 6-22. The light was brightest while the runaway population was high and diminished in intensity as the LH power pulses reduced the runaway level. The phase was changed from 60, 90, and 120 degrees and then repeated for the second three pulses.

A visible camera views the LH antenna to help determine if there is any arcing or other phenomena occurring near the grill. The camera used has a 5 ms integration time and takes frames every 50 ms. On some shots a diffuse glow or flash was observed near the grill. Three frames from the camera are shown in Figure 6-23 for power levels of 50, 60, and 70 kW/klystron. As the power level was increased the visible light increased in intensity. This does not seem to be related to any arcing at the grill or in the launcher as there were no sudden jumps in the reflection powers. The visible emission may be due to gas being expelled from the LH antenna, being ionized, and then recombining. At times striation patterns are observed which seem to follow the field lines. This is most clearly seen in Figure 6-24 for shot number 1060406010 which had a power level of 20 kW/klystron.

One final observation is that spatial information about the birth of runaway electrons can be obtained by examining the bremsstrahlung emission with the HXR camera. Runaway electrons appear to be born in a very localized region in the plasma center during startup, and are quickly accelerated to energies greater than can be seen with the HXR camera. The spatial distribution and PHA spectrum for shot 1060310015 are shown in Figure 6-25. A time of 0.205 s was chosen for the plot, which corresponds to the maximum runaway signal for this discharge.
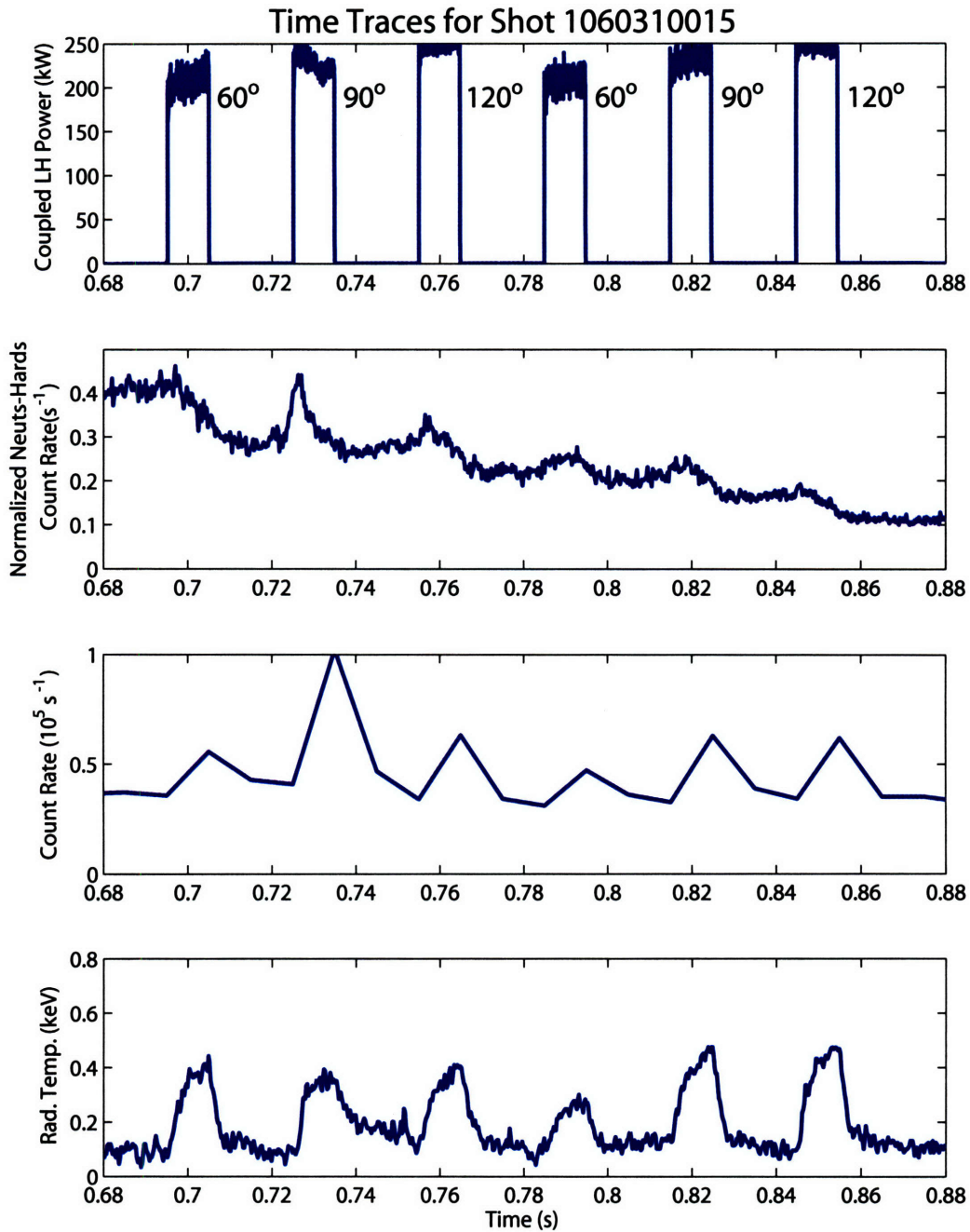
Figure 6-21: Time traces for shot 1060310015 showing coupled LH power, neuts-hard, HXR, and ECE signals.
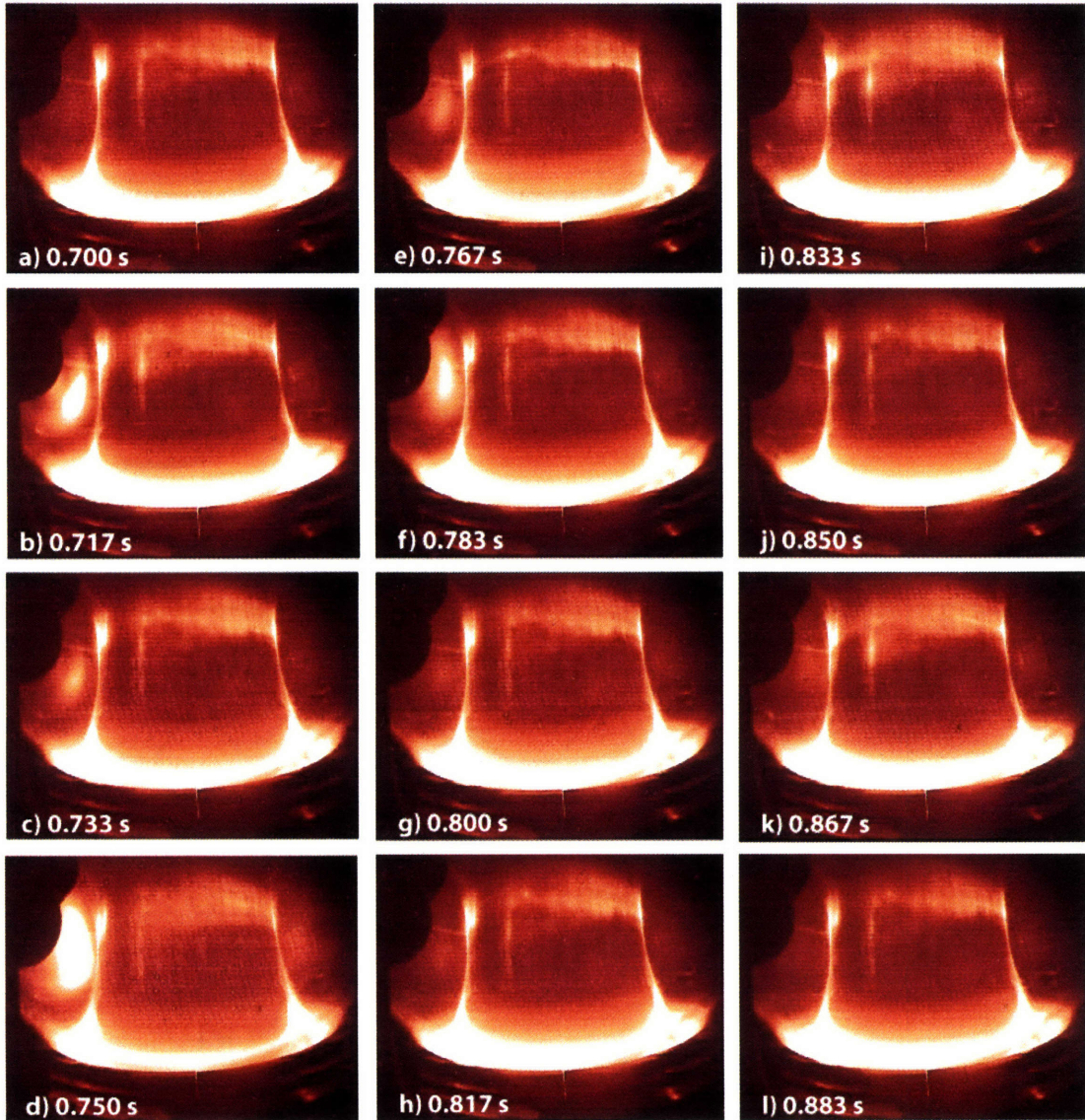
Figure 6-22: Visible camera frames for shot 1060310015. Some frames show visible light emission on the left hand side of the picture, which is opposite the location of the LH grill.
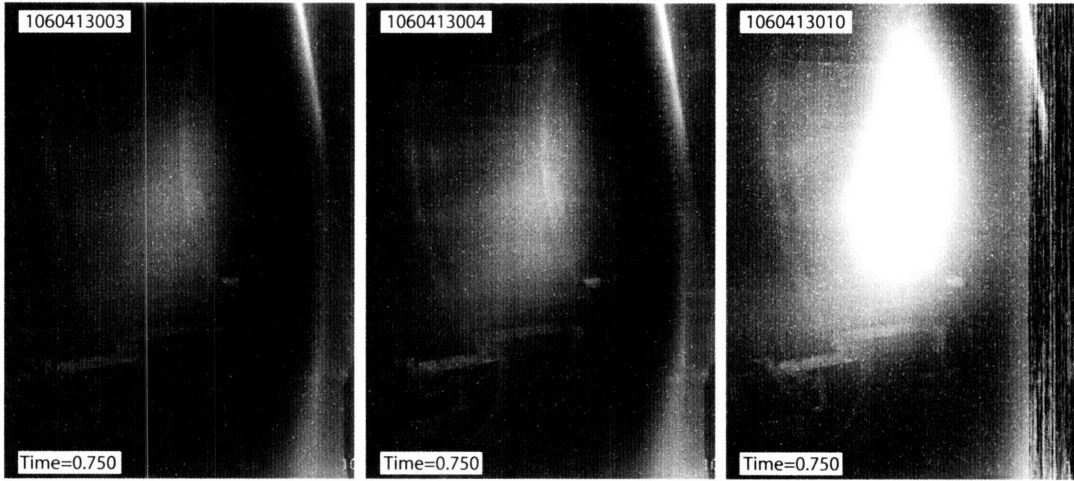
Figure 6-23: LH camera frames for three 1060413003, 1060413004, and 1060413010, where the power level was 50, 60, and 70 kW/klystron respectively.
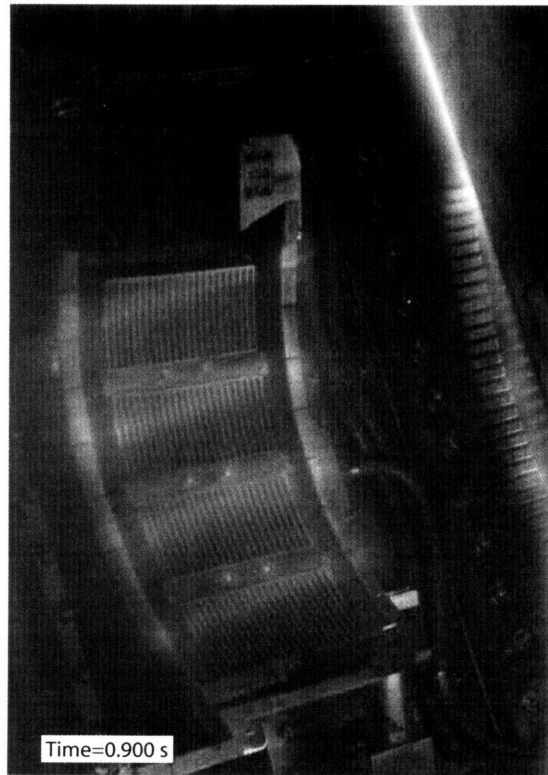
Figure 6-24: Visible light frame from LH camera on shot 1060406010 at 0.900s, just after last power pulses.
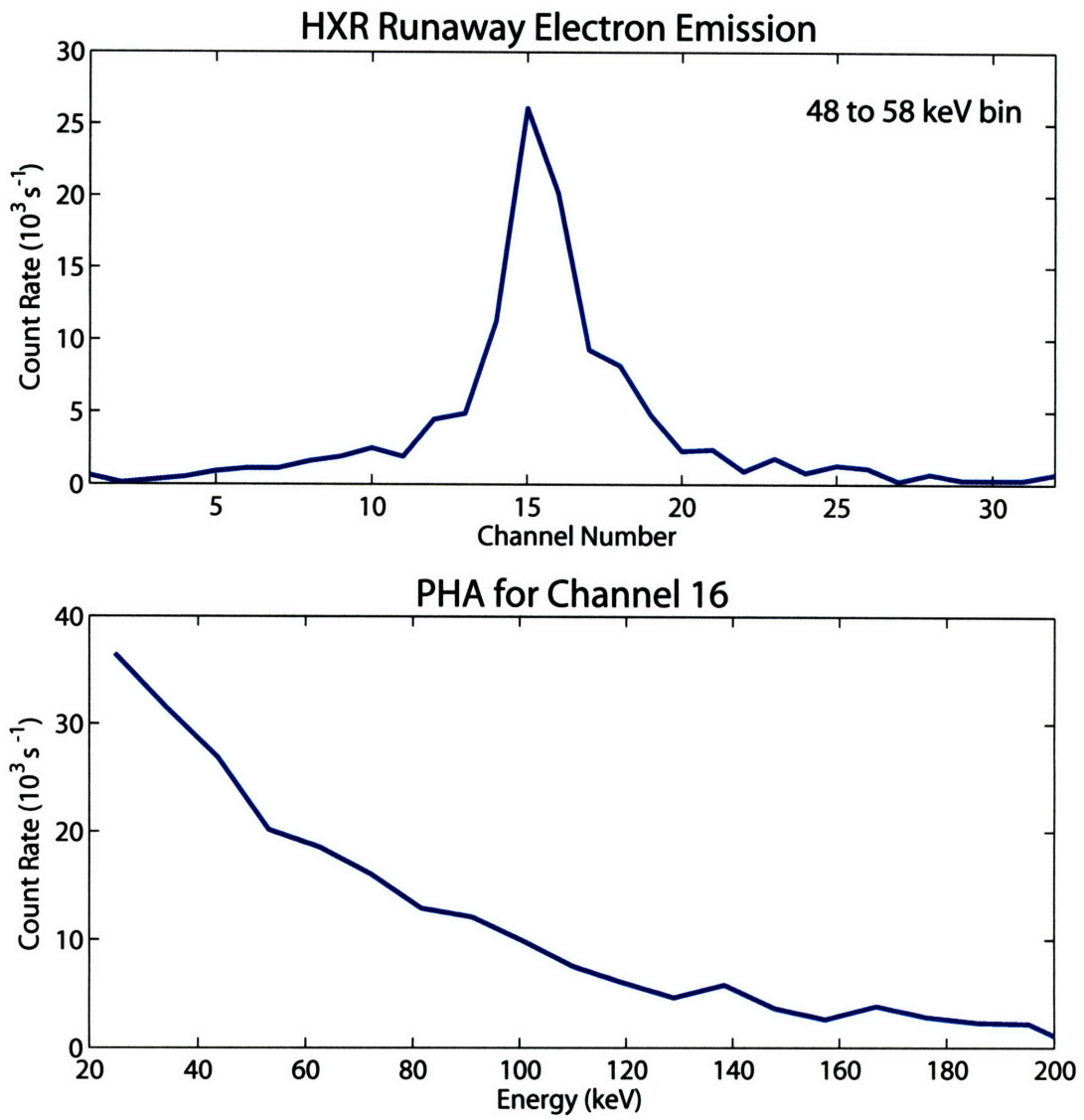
Figure 6-25: Runaway electron spatial distribution and PHA spectrum for channel 16. Data shown for shot 1060310015 at 0.205 s, which is the maximum count rate.

Chapter 7

Grill Modeling and Coupling Results

The simple Fourier analysis of the LH grill presented in Section 2.3 provides the location of the CD and CCD $n_\parallel$ peaks and and an estimate of the power fraction. To really study the coupling of LH waves to the plasma a more complicated model is required. This model was put forth by Brambilla[114] in 1976 for coupling LH waves with the purpose of plasma heating. Brambilla's model was expanded upon by Stevens[115] who added a step density model with a vacuum gap, which has also proved valuable in comparing the coupling theory to experiment. Additional physics has been studied such as finite Larmor radius effects[116] and coupling to the fast wave[117], but Brambilla's linear theory with Stevens' density model gives reasonable agreement with experiment[118].

The coupling model is essentially a field matching problem through three regions, the plasma, vacuum, and waveguide. The result is a set of equations which may be solved numerically in a so-called coupling code. An outline of the key equations and relationships of the coupling model is presented below following Reference[118]. The starting point is Ampere's and Faraday's laws with the plasma dielectric tensor of Equation 2.10

$$\nabla \times \nabla \times \overline{E} - \frac{\omega^2}{c^2} \overline{\overline{\epsilon}} \cdot \overline{E} = 0. \tag{7.1}$$

The goal is to derive a wave equation that describes the propagation of the wave in the plasma. Take the equilibrium magnetic field to be in the $\hat{z}$-direction and the density gradient to be in the $\hat{x}$-direction. Assuming infinite extent in the $\hat{y}$-direction, while ignoring E_y, and neglecting ϵ_x gives an equation for the slow wave of the form

$$\frac{\partial^2 E_z}{\partial x^2} - \frac{\omega^2}{c^2} \epsilon_\parallel (n_\parallel^2 - 1) E_z = 0. \tag{7.2}$$

The density profile near the grill may be modeled as a step plus a gradient, that is

$$n(x) = \frac{dn}{dx} x + n_0, \tag{7.3}$$

where n_0 is the step density and dn/dx is the gradient. The gradient may be written as n_c/L, with n_c defined as the density at which the plasma frequency is equal to the generator frequency and L is a scale length. Using this relation with the substitution of

$$u(x) = \left(\frac{\omega^2}{c^2 L^2} (n_\parallel^2 - 1) \right)^{1/3} (L(\frac{n_0}{n_c} - 1) + x), \tag{7.4}$$

gives the following differential equation

$$\frac{\partial^2 E_z}{\partial u^2} - uE_z = 0, \tag{7.5}$$

which has Airy function solutions

$$E_z(u) = -iA_i(u) + B_i(u). \tag{7.6}$$

The magnetic field of the wave can be determined from Faraday's law and the wave electric field as

$$B_y(u) = \frac{ic}{\omega(n_\parallel^2 - 1)} \left(\frac{\omega^2}{c^2 L^2}(n_\parallel^2 - 1)\right)^{1/3} \left(-i\frac{\partial A_i(u)}{\partial u} + \frac{\partial B_i(u)}{\partial u}\right). \tag{7.7}$$

Now that the wave fields are known the wave impedance may be defined as

$$Z_p = \frac{E_z(u)}{B_y(u)}. \tag{7.8}$$

Matching the plasma impedance to the waveguide impedance minimizes the reflection coefficient.

Now that the fields in the plasma have been defined, equations for the vacuum region may be written. Typically the fields are represented in terms of Fourier integrals as

$$E_z(x, z) = \int_\infty^\infty \frac{\omega}{c} \left(\sigma(n_\parallel)e^{ik_\perp x} + \rho(n_\parallel)e^{-ik_\perp x}\right) e^{i(\omega/c)n_\parallel z} dn_\parallel \tag{7.9}$$

and

$$B_y(x, z) = \int_\infty^\infty \frac{i\omega/c}{(n_\parallel^2 - 1)^{1/2}} \left(\sigma(n_\parallel)e^{ik_\perp x} - \rho(n_\parallel)e^{-ik_\perp x}\right) e^{i(\omega/c)n_\parallel z} dn_\parallel, \tag{7.10}$$

with $\sigma(n_\parallel)$, and $\rho(n_\parallel)$ being coefficients representing the field incident and reflected from the plasma. The two coefficients are two of the three parameters that must be solved for numerically.

The third parameter is another coefficient that represents the reflected field in the waveguide, β_{np}. Assuming infinite height waveguides, the fields in the guides may be represented as

$$E_z^{wg}(x, z) = \sum_{p=1}^N e^{i\phi_p} \Theta_p(z) \left(\sum_{n=0}^\infty (\alpha_{np}e^{ik_n x} + \beta_{np}e^{-ik_n x}) \cos\frac{n\pi(z - z_p)}{b}\right) \tag{7.11}$$

and

$$B_y^{wg}(x, z) = \sum_{p=1}^N e^{i\phi_p} \Theta_p(z) \left(\sum_{n=0}^\infty \frac{-\omega}{ck_n} (\alpha_{np}e^{ik_n x} + \beta_{np}e^{-ik_n x}) \cos\frac{n\pi(z - z_p)}{b}\right) \tag{7.12}$$

where the p sum is over the number of waveguides and the n sum is over the number of waveguide modes. As in chapter 2, $\Theta_p(z)$ is the box function which is one over the width of the pth guide and zero elsewhere. k_n is the waveguide mode vector and for the nth mode and is given by

$$k_n = \left(\omega^2/c^2 - n^2\pi^2/b^2\right). \tag{7.13}$$

α_{np} is the coefficient of the incident waveguide field, and is usually constrained by the waveguide to be the TE_{10} mode, making α_{np} zero for $n \neq 1$, and is assumed to be known through calibration and measurement.

Matching the equations at the plasma-vacuum and vacuum-waveguide boundaries uniquely determines $\sigma(n_\parallel)$, $\rho(n_\parallel)$, and β_{np}, knowing these quantities the total and waveguide reflection coefficients may be determined. The power spectrum produced from the fields may be evaluated by calculating the Poynting flux at the plasma-vacuum boundary, that is

$$S_x(n_\parallel) = \frac{1}{2\mu_0}\Re(E_z B_y^*),$$

which may be written in terms of $\sigma(n_\parallel)$ and $\rho(n_\parallel)$ as

$$S_x(n_\parallel) = \frac{1}{\mu_0}\frac{|\sigma(n_\parallel)|^2}{(n_\parallel^2 - 1)^{1/2}}\Im(\frac{\rho n_\parallel}{\sigma(n_\parallel)}). \qquad (7.14)$$

7.1   Sensitivity of Reflection Coefficient to Input Parameters

The output phase from C-Mod's LH system may be characterized as either "ideal" or "approximate", depending on the relation between the klystron phasing and the settings of the mechanical phase shifters. The phase between adjacent columns fed by the same klystron is controlled by the mechanical phase shifter. Setting the phase shifter and the klystron phase such that the phase difference from column to column is constant is known as ideal phasing. For example ideal 90° phasing would be a repeating progression of 90°, 0°, 270°, 180°, and repeat.

The mechanical phase shifters must be adjusted by hand, requiring about 30 minutes of access to the C-Mod experimental cell. Typically the mechanical phase shifter is set for the desired phasing before the run begins for the day. The $n_\parallel$ spectrum may be adjusted by controlling the klystron phase only, which may be changed electronically. In this case the column to column phase difference is not constant, and is known as approximate phasing. For example if the phase shifters are set at 90°, then ideal 120° phasing may be approximated as a repeating pattern of 90°, 0°, 210°, 120°, 330°, and 240°. A detailed description of antenna phase settings is presented in Appendix A.

The sensitivity of the coupling model to the input plasma parameters was studied by scanning parameters over the range expected on C-Mod experiments. The key parameters are density, density gradient, vacuum gap width, and phase. The difference between ideal and approximate phasing in terms of the resulting spectra and reflection coefficients is shown in Figures 7-1 and 7-2.

Comparing the ideal and approximate spectra for the same model parameters in Figure 7-1 shows that the location of the $n_\parallel$ peaks are identical, but that approximate phasing cases have lower power fractions. As the deviation from 90° increases, the power fraction of the approximate peaks decreases relative to the ideal case. This is a result of having more power located in the region of $|n_\parallel| < 1$, which will not propagate in plasma, and the increase of higher order lobes in the spectrum.

The total reflection coefficient, R, which is the defined as the total reflected power divided by the total incident power is plotted as a function of ideal and approximate phase for a wide range of model parameters in Figure 7-2. Over all parameters, the ideal and approximate reflection coefficients are comparable, except at 150° and 180°. For these
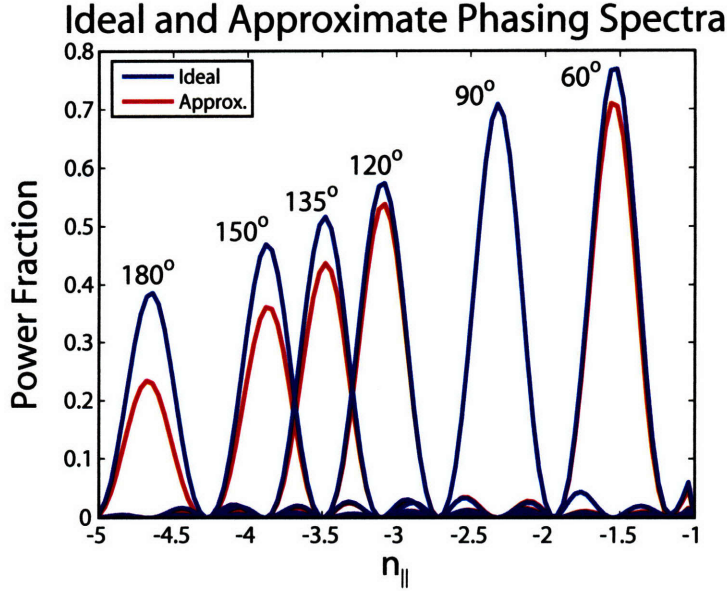
Figure 7-1: Coupled power fraction between ideal and approximate phasing $n = 3 \times 10^{12}$ cm^{-3} and $dn/dx = 6 \times 10^{12}$ cm^{-4} and no vacuum gap.

phases the reflection coefficient is much higher, which lowers the spectral power density, as seen in Figure 7-1. This indicates that if these phases are desired experimentally that the phase shifters should be changed such that ideal spectra are generated. This also seems to show that there is little difference between ideal and approximate phasing for 60° through 120°, which may be readily generated through adjusting the klystron phase.

Comparing the panels of Figure 7-2 gives a sense for the relative sensitivity model parameters. Reducing the density by a factor of six from panel a) to b) increases the R by 10% at 90° and by 30% at 180°. Increasing the vacuum gap from zero to 1 mm, panels a) and c), also raises R by 10% at 60° and 50% at 180°. When the density gradient was decreased by a factor of six from panels a) to g) there is very little change in the total reflection coefficient.

The total reflection coefficient strongly depends on both the plasma density and vacuum gap. The reflection coefficient increases at low densities as it nears the cutoff at the plasma frequency. The critical density is

$$n_c[m^{-3}] = 0.0124 f^2, \tag{7.15}$$

where f is the source frequency in Hz. For C-Mod this puts the critical density at 2.6×10^{11} cm^{-3}. At densities lower than this there is effectively a vacuum region that the wave must tunnel through. The increasing reflection coefficient as a function of phase may be explained by examining $n_\perp$ or more appropriately, the corresponding perpendicular wavelength. Writing the simple electrostatic dispersion relation in the LH limit, $\omega_{ce}^2 \gg \omega^2 \gg \omega_{ci}^2$, and assuming low density, $\omega \sim \omega_{pe}$ gives

$$\left(1 - \frac{\omega_{pe}^2}{\omega^2}\right) n_\parallel^2 + n_\perp^2 = 0.$$

178
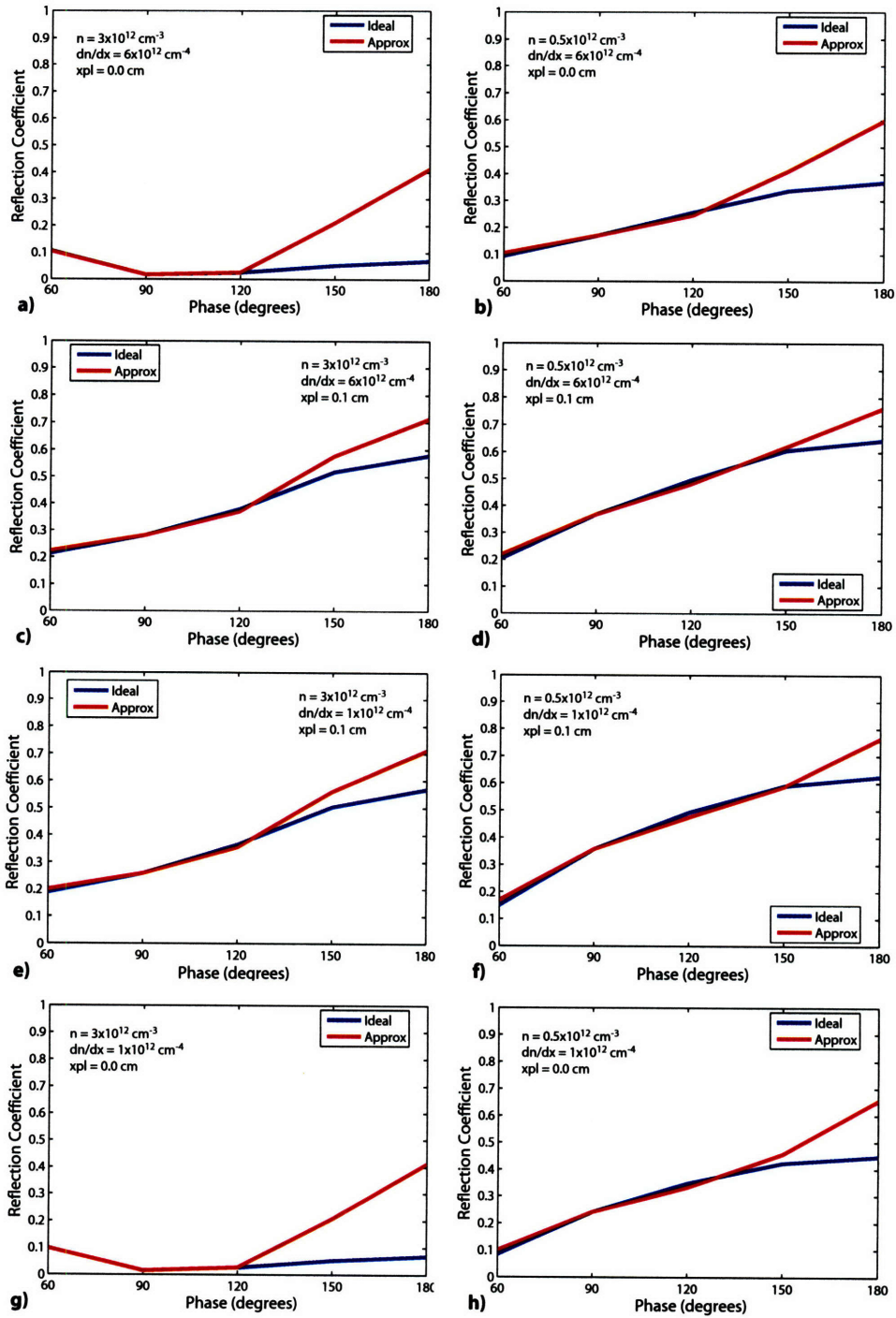
Figure 7-2: Variation of total reflection coefficient vs ideal and approximate phasing while scanning over model parameters. n is the density at the grill, or at the end of the vacuum region if present. dn/dx is the density gradient, and xpl denotes the length of the vacuum region.
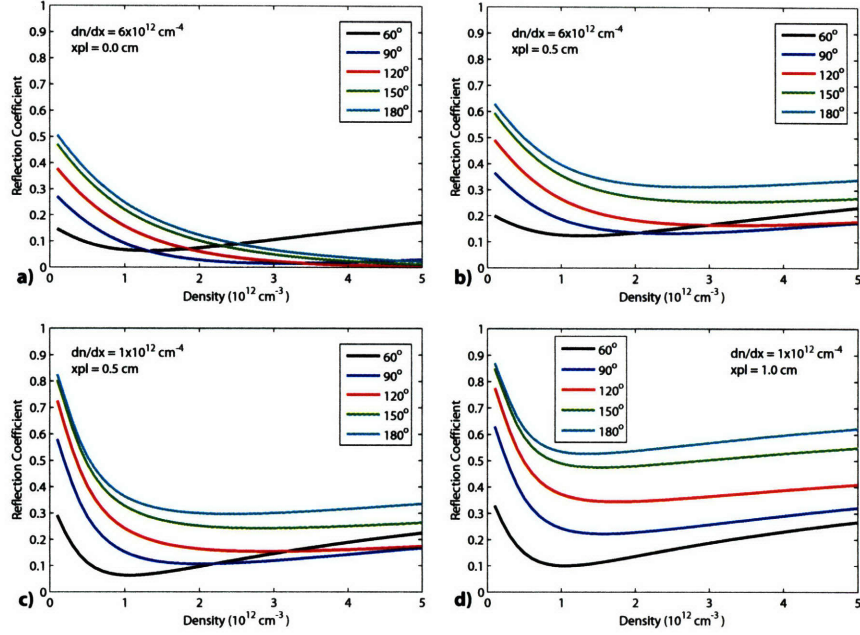
Figure 7-3: Reflection coefficient as a function of density for ideal phasing.

This may be written in terms of the perpendicular wavelength as

$$\lambda_\perp = \frac{2\pi c^2}{n_\| \sqrt{\omega_{pe}^2 - \omega^2}},$$

(7.16)

which is inversely proportional to $n_\|$. This means that as the phase increases the perpendicular wavelength decreases, making it more difficult for the waves to propagate into the plasma by increasing the impedance mismatch. In general a rule of thumb for the optimum density to minimize the reflection coefficient is given by[115]

$$n_o = n_c n_\|^2,$$

(7.17)

which provides the best match of the waveguide and plasma impedance.

The sensitivity of the coupling model was further studied by scanning the range of model parameters for C-Mod experimental conditions for ideal phasing. The density, vacuum gap, and density gradient dependencies are shown in Figures 7-3, 7-4, and 7-5 respectively. In general good coupling, R less than 10%, is possible under the right conditions. In particular the density must be high enough while a vacuum region is not present. The most sensitive parameter is the size of the vacuum region, such a strong dependence is not surprising since as the gap becomes larger the wave must tunnel through a larger evanescent region before reaching the plasma and propagating. The reflection coefficient seems to weakly depend on the density gradient. This is helpful as the gradient is often the most difficult parameter to measure reliably.

180
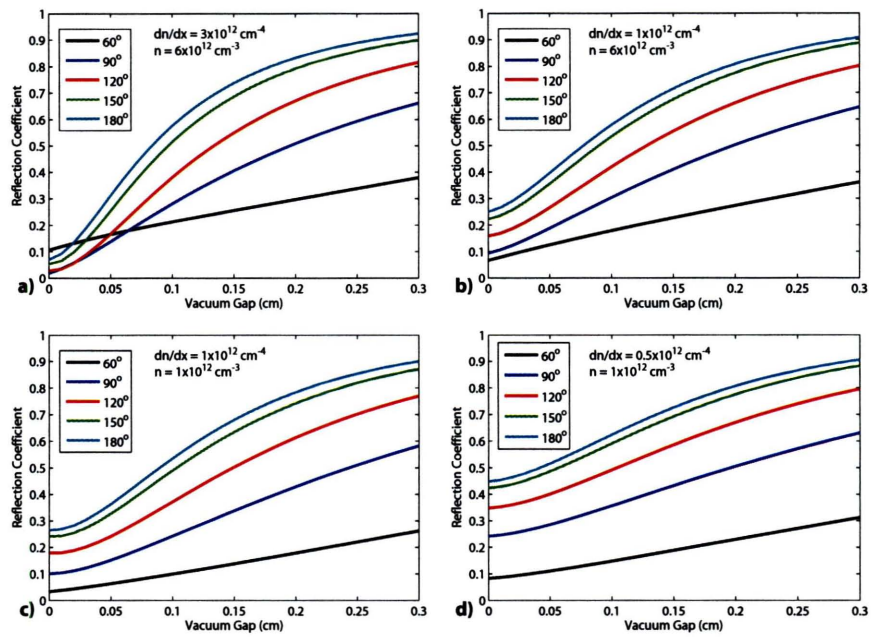
Figure 7-4: Reflection coefficient as a function of vacuum gap for ideal phasing.
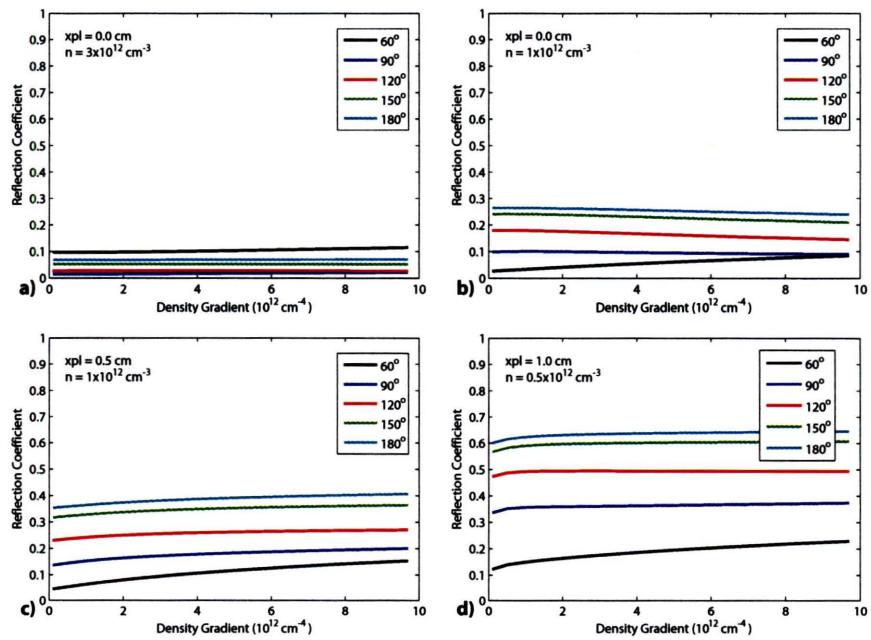
Figure 7-5: Reflection coefficient as a function of density gradient for ideal phasing.

181

90° Phase Progression Output Spectrum
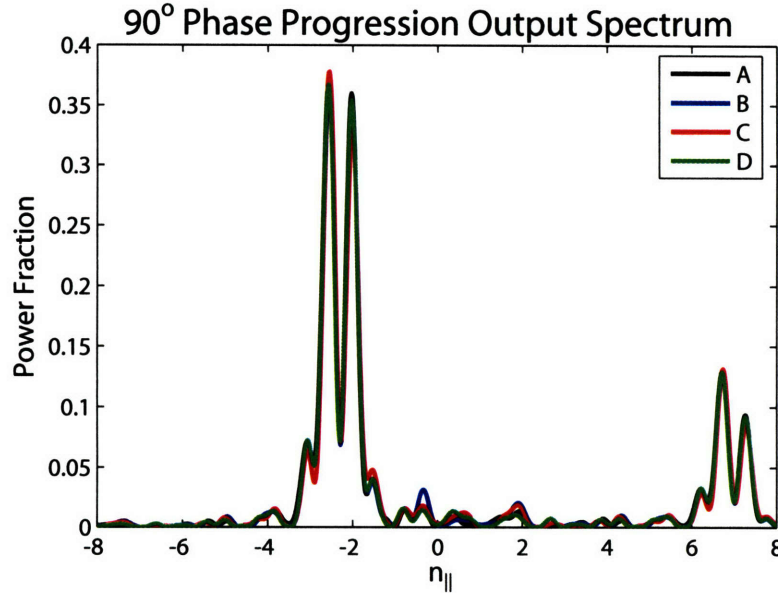
Figure 7-6: Spectrum produced for a 90° phase progression with a discontinuity in phase between carts 2 and 3.

7.2 Experimental Results

Initial coupling studies were carried out on C-Mod by using two types of plasmas at a low power level of 20 kW/klystron. The first study kept the density constant while a complete scan of approximate phasing was performed on a single shot. The phase of the antenna may be controlled in programmable segments in time, as described in Appendix B. 10 ms pulses every 20 ms were used as the phase was changed from 60° through 180° in 30° increments. These shots were repeated at different grill positions to change the density and measure the gradient.

The second type of plasma used an outer gap scan to adjust the density at the grill for ideal phasing. This type of plasma was produced for 60, 90, 120, 150, and 180 degree ideal phasing. The measurements presented in this section used phasing which had a discontinuity between carts 2 and 3, but with the same phase progression. The net result was to produce a compound spectrum as shown for a 90° phase progression in Figure 7-6. The compound spectra produced will be labeled by the type of phase progression used.

7.2.1 Density Measurements

As part of the coupling studies the density at the grill was measured using the six Langmuir probes. Figure 7-7 shows the measured gradient behind the LH limiter in panel a) and the measured probe densities as a function of line-integrated density and outer gap in panels b) and c). The line-integrated density and outer gap data had to be restricted to a narrow range in order to produce a meaningful gradient result. Under these conditions a gentle gradient of 6×10^{12} cm^{-4} was measured. This was somewhat unexpected since the LH limiter is located about 0.5 cm behind the main limiter and the gradient was expected to be

182

steeper given the small connection length. It should be mentioned at this point as well that the position of the grill relative to the LH limiter is known only approximately. The stops that were intended to keep the grill position at or behind the LH limiter were lost, so there was not an absolute reference for position. The probe density is a nonlinearly increasing function of the line average density and roughly linearly decreasing function of the outer gap.

Two probes are positioned between each coupler one on the B-port side and one on the D-port side. The probes between the A and B, B and C, and C and D couplers are known as the top, middle, and bottom probes respectively. Figure 7-8 plots the measured density, averaged over the B-port and D-port side probes for the top, middle, and bottom probes. Measurements from B and D-port probes are labeled with B and D markers. Shots 1060307007, 1060307014, and 1060406009 were approximate phase scans at estimated limiter positions of 0.44, 0.3, and 0.11 cm respectively. The density is highest in the middle of the grill and lower at the top and bottom, possibly due to a mismatch in the shape of the plasma compared to the shape of the LH limiter and grill. The deviation from the central probe density to the top and bottom can be well over 50%. The variation from the B-port to D-port side probes may also indicate a degree of toroidal asymmetry. The most notable and surprising feature is that the density measured by the probes goes down as the antenna is moved in from about 3 mm to 1 mm behind the LH limiter. The probes themselves are 3 mm long, and protrude beyond the LH limiter, which was expected to raise the density further. The reason for the decrease in density is currently unknown.

7.2.2   Approximate Phase Progression Coupling

The approximate phase progression coupling experiments were done while the density was maintained at a constant level. This is shown in Figure 7-9 as a function of phase for each coupler position. The error bars represent the standard deviation, which is mostly due to the top to middle and bottom to middle density variation.

The reflection coefficients on C-Mod may be measured two ways, using RF probes or the jungle gym couplers. RF probes located on rows A and D of the end of the rear waveguide assembly measure the forward and reflected power on each waveguide. This allows for the reflection coefficient of each individual guide to be calculated as well as the total reflection coefficient. Unfortunately, the directivity of the RF probes is much less than desired, which is most likely due to how each probe is seated in the waveguide. The probes were found to work well on the test bench where each one was held in place by two screws. Access to the launcher made this means of fastening nearly impossible so the probes are held down by three bars that span the width of the launcher. Loss from the forward waveguide assembly and the couplers themselves needs to be accounted for when calculating the total reflection coefficient.

Amplitude data from phase calibrations performed in the summer of 2005 and the fall of 2006 may be used to estimate the loss in the forward waveguide. In 2005 the average loss was measured to be 10.3±0.3 dB measured from the top of the pant leg splitter to the end of the rear waveguide assembly. In 2006 the same measurement was performed going to the end of the forward waveguide. This time the average loss was found to be 11.0±0.5 dB. This seems to indicate that the average loss in the FWG assembly is about 0.7 dB. This number should be treated with caution because a significant change was made to the waveguide assembly. In 2005 rows B and C were shorted with a plate, which was replaced in 2006 by a water load. Microwave simulations of the launcher indicated that a load was
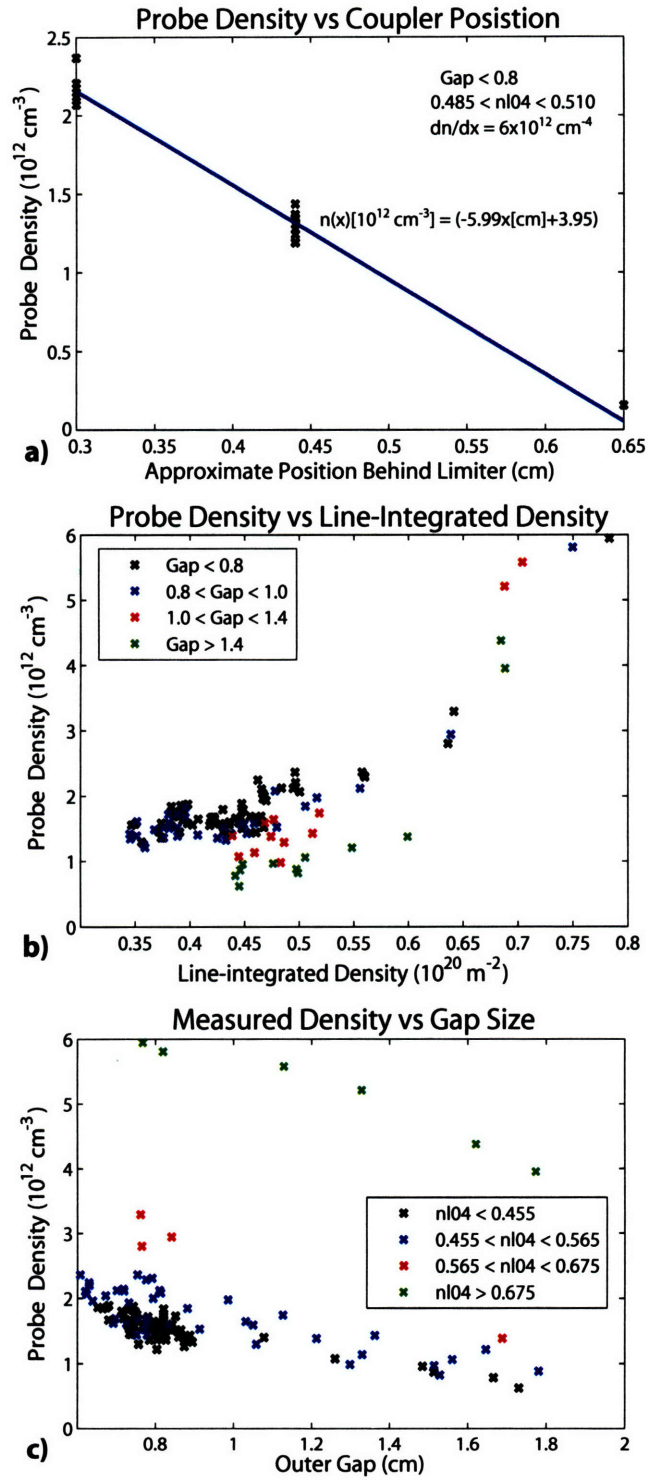
Figure 7-7: Panel a), measurement of density gradient for a narrow range of parameters with the probe tips at or behind the LH limiter. Panel b) measured density as a function of line-integrated density. Panel c) measured density as a function of outer gap.
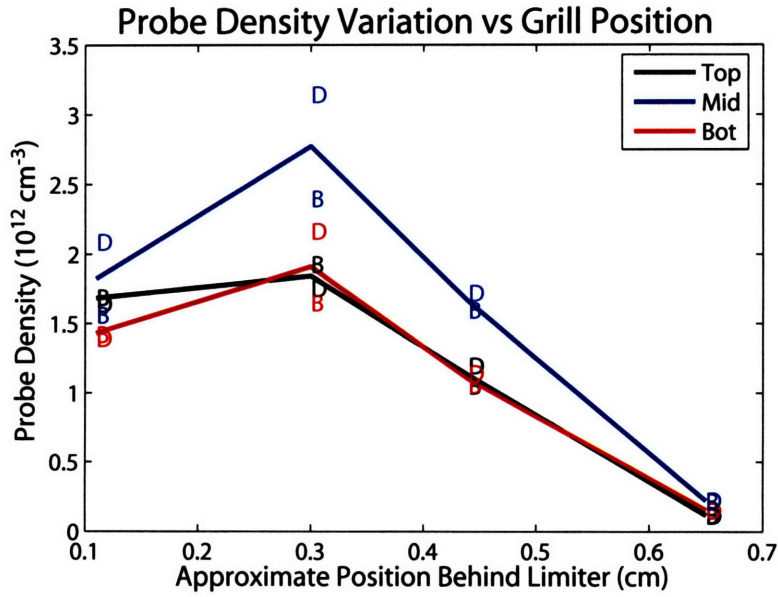
Figure 7-8: Top, middle, and bottom probe density as a function of position behind limiter. The average for the B-port and D-port probes over all segments are denoted by the letters "B" and "D" respectively.
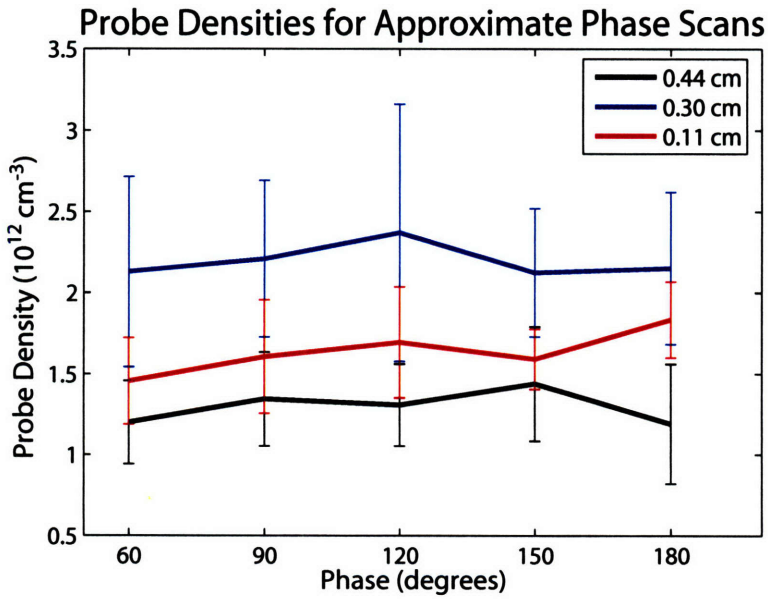
Figure 7-9: Probe density as a function of phase at grill positions of 0.44, 0.30, and 0.11 cm. Density is maintained at nearly a constant value for each phase scan.

Approximate Phasing Reflection Coefficients
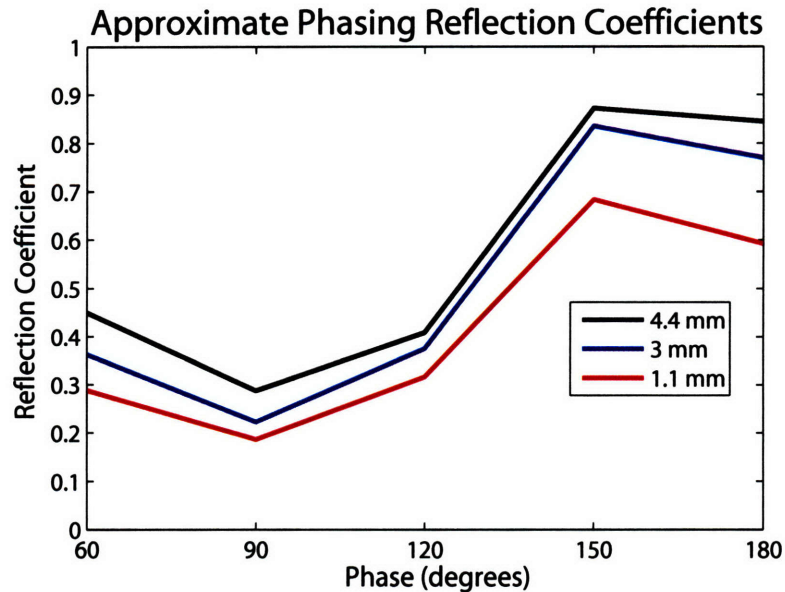
Figure 7-10: Approximate phase coupling measurements at various grill positions using RF probe measurements.

required so that the 3 dB splitter in the RWG would work properly.

Even though the couplers are short, loss may be significant as they are made from unplated stainless steel. Losses in stainless waveguide are estimated to be 0.7 dB/m[1] giving about a 0.1 dB loss in the coupler. The exact loss has not been measured and is currently neglected. Neglecting the loss in the coupler makes the calculations of the total reflection coefficient and coupled power an upper bound.

Results using the RF probes are shown in Figure 7-10. Here the losses in the FWG and couplers have been neglected. The total reflection coefficient plotted is the average of the total reflection coefficient calculated for rows A and D. Rows A and D typically see the lowest density, as shown in Figures 7-8 and 7-9, and therefore should have higher reflection coefficients than in rows B and C, which partially offsets the increase that would be incurred if waveguide losses were known and included. The reflection coefficients are high in general ranging from about 20% to 88%. As the coupler position was moved in from 4.4 to 1.1 mm the reflection coefficient decreases by at least 10%. 90° and 120° phasing exhibit the lowest reflection, while the 150° and 180° are particularly high.

Given the number of uncertainties with the probes a more accurate, but less direct means of calculating the total reflection coefficient is to use the jungle gym couplers. The jungle gym couplers measure the forward and reflected power just outside the rear waveguide assembly. To use these couplers the waveguide losses must be estimated as well as the amount of power being absorbed into the water load. Using the amplitude attenuation from the 2006 phase calibration, shown in Table A.1, the average loss from the top of the pant leg splitter to the end of the FWG is 11.0±0.5. Losses from the splitter to the jungle

---

[1]Calculated by G. Wallace.

186
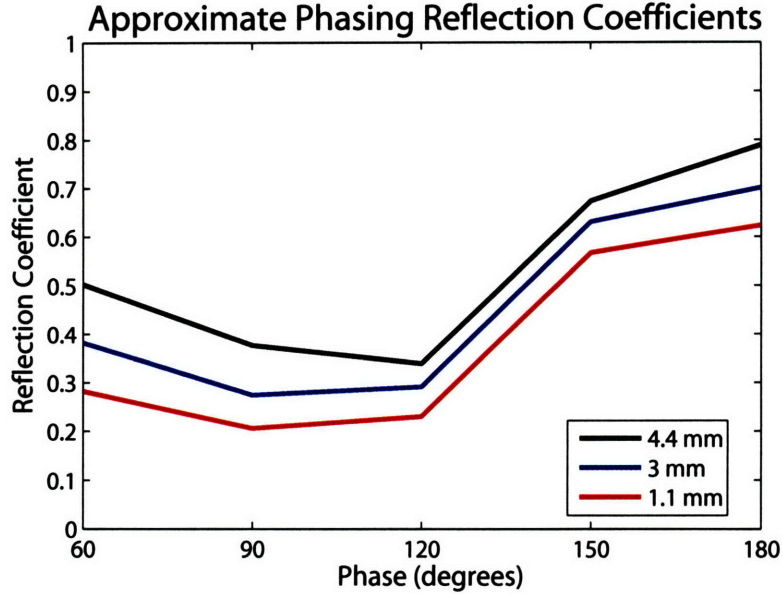
Figure 7-11: Approximate phase coupling measurements at various grill positions using jungle gym couplers and waveguide loss estimates.

gym couplers may be estimated by comparing the total FINT power to the total forward jungle gym power. Using data from runs 1060307 and 1060310 the loss is 0.5±0.1 dB. Accounting for the power division in the RWG, the loss from the jungle gym couplers to the end of the forward waveguide is about 1.5 dB. This means that the power delivered to the end of the FWG is 29% less than the forward jungle gym power, and that the reflected power at the end of the FWG is 29% higher than the reverse jungle gym power. The power into the water load must also be accounted for. Fortunately, the RF probes on rows B and C near the water load work reliably and may be used to measure this power. In terms of signals the total reflection coefficient is

$$\Gamma_{tot} = \frac{1 + P_{loss}}{1 - P_{loss}} \sum_{p=2}^{23} \frac{REVT_p + REVB_p + BR_p + CR_p}{FWDT_p + FWDB_p}, \tag{7.18}$$

where P_{loss} is the loss fraction from the jungle gym to the end of the FWG and the sum is over the column number p. $FWDT$ and $FWDB$ are the forward power from the top and bottom jungle gym couplers. $REVT$ and $REVB$ are the reverse or reflected power from the top and bottom jungle gym couplers. BR and CR are probe measurements of the power into the water load. The net power coupled into the plasma may be calculated as

$$P_{net} = \sum_{p=2}^{23} (1 - P_{loss})(FWDT_p + FWDB_p) - (1 + P_{loss})(REVT_p + REVB_p + BR_p + CR_p). \tag{7.19}$$

Reflection coefficients estimated from the jungle gym couplers for the approximate phase scan are shown in Figure 7-11. The jungle gym results are qualitatively similar to the results obtained by the probes and quantitatively similar for 90° and 120° phasing. As seen with

the probes better coupling is obtained when the launcher is moved in closer to the plasma. Approximate phase scan data is summarized in Table 7.1.

Table 7.1: **Approximate Phase Progression Coupling Data**

Shot	Segment Number	Position (mm)	PS Set (deg)	Phase (deg)	Avg. Phase Error (deg)	nl04 $(10^{20}m^{-3})$	Outer Gap (cm)	Probe Density $(10^{18}m^{-2})$	FINT Tot.(kW)	RINT Tot.(kW)	FWD Tot.(kW)	REV Tot.(kW)	Ref. Coef.
1060307007	1	4.4	90	60	10.9	0.47	0.74	1.20	217.9	11.6	202.9	45.7	0.50
	2	4.4	90	90	8.9	0.49	0.66	1.34	216.7	8.3	191.3	31.6	0.37
	3	4.4	90	120	9.2	0.50	0.64	1.31	209.7	13.1	191.2	28.4	0.34
	4	4.4	90	150	9.3	0.50	0.68	1.44	210.7	32.3	195.1	65.1	0.67
	5	4.4	90	180	8.6	0.49	0.70	1.19	211.9	57.3	197.5	77.9	0.79
1060307014	1	3.0	90	60	13.8	0.48	0.70	2.13	222.2	10.0	206.5	34.9	0.38
	2	3.0	90	90	11.1	0.50	0.63	2.21	222.3	7.1	196.7	22.0	0.27
	3	3.0	90	120	11.6	0.50	0.61	2.37	212.6	12.2	193.8	24.4	0.29
	4	3.0	90	150	12.2	0.49	0.72	2.12	217.2	30.7	200.4	63.5	0.63
	5	3.0	90	180	10.7	0.50	0.72	2.15	216.4	53.1	201.6	71.3	0.70
	6	3.0	90	90	12.2	0.50	0.62	2.07	218.3	9.9	203.5	34.5	0.39
1060406009	1	1.1	90	60	17.1	0.46	0.93	1.45	200.5	8.6	201.4	27.7	0.28
	2	1.1	90	90	15.4	0.46	0.87	1.60	194.5	5.7	190.4	17.3	0.20
	3	1.1	90	120	14.5	0.47	0.86	1.69	195.0	9.2	194.2	20.2	0.23
	4	1.1	90	150	15.2	0.46	0.85	1.59	189.2	24.9	194.6	56.7	0.57
	5	1.1	90	180	14.9	0.45	0.95	1.83	192.8	42.3	196.3	64.5	0.62
	6	1.1	90	90	14.8	0.45	0.86	1.70	191.1	5.5	187.2	16.6	0.21

For runs after 1060310 the FINT and RINT signals had attenuators placed in line which slightly changes the power calibration. The power calibration has not yet been updated, so the FINT and RINT signals from shot 1060406009 are lower than they actually are. The actual waveguide loss remains unchanged.

It should be mentioned that calculating the total reflection coefficient requires a large number of signals. With 22 columns there are 88 jungle gym signals and 176 probe signals. It is also likely with so many channels that some will not be working properly. In calculating the reflection coefficients above, bad or missing channel data was replaced by average values. A GUI interface was written to help manage and display the data. A screen capture from the GUI for the 90° segment of shot 1060406009 is shown in Figure 7-12. Each plot panel represents a coupler row, A through D from top to bottom. All data plotted was averaged over the segment length in time. The forward and reverse directions are defined to be toward and away from the plasma. Examining the middle two panels shows that the water load is a very good match and that there was very little reflected power. Negative values for the forward direction probes on rows B and C are an artifact of the calibration meaning that a near zero power was measured.
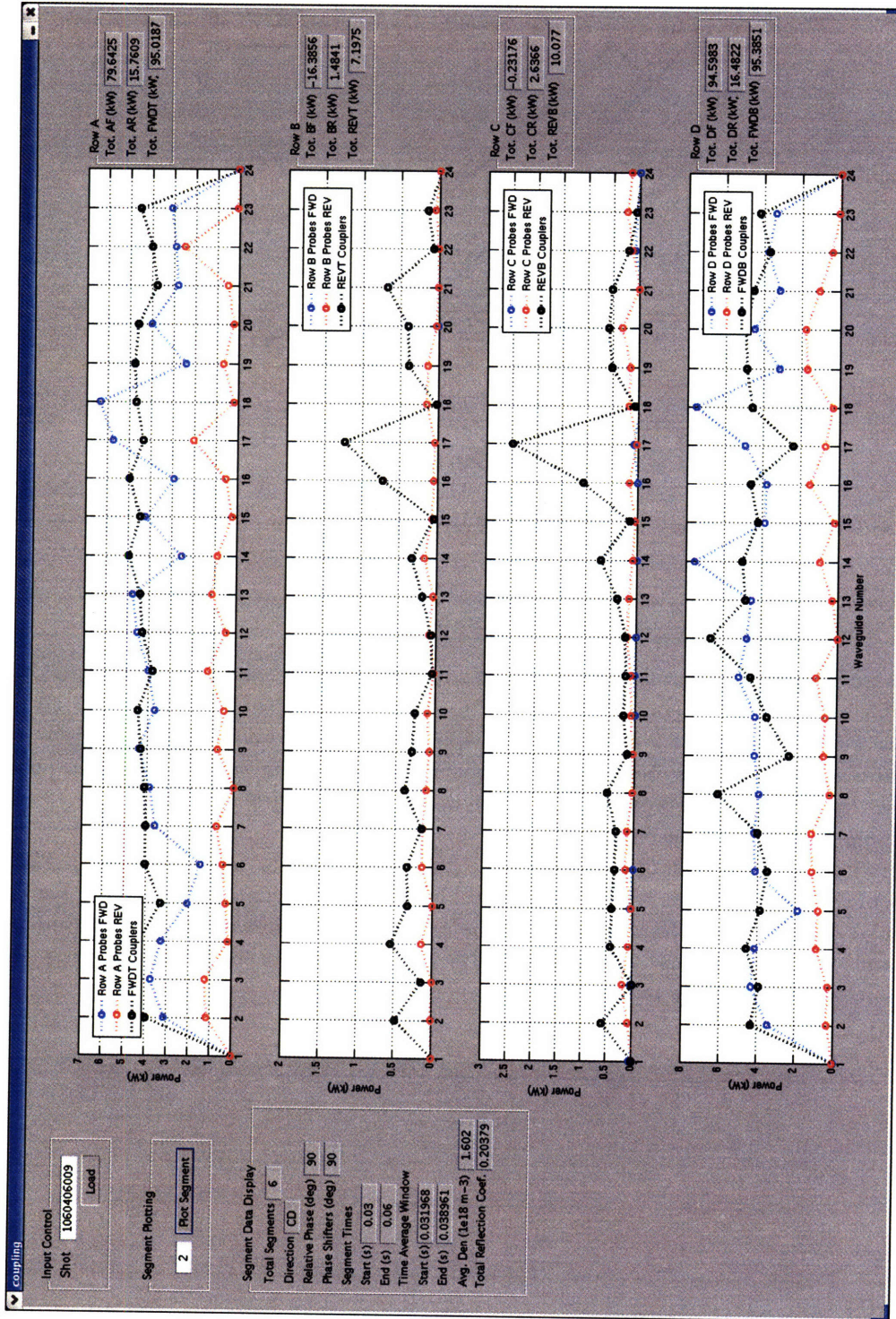
Figure 7-12: Screen capture from the Coupling GUI used to organize and display jungle gym and RF probe data. Each plot panel represents a coupler row and relevant information is displayed in text boxes.
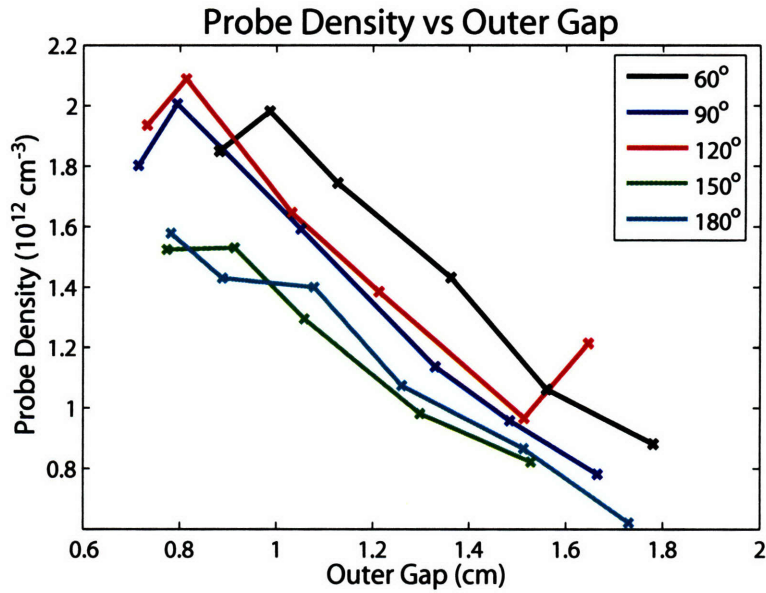
Figure 7-13: Probe density as a function of outer gap for ideal phase coupling study.

7.2.3 Ideal Phase Progression Coupling

Ideal phase progression coupling was studied with the couplers about 3 mm behind the LH limiter while the outer gap was increased to lower the density at the grill. Six 10 ms segments with a spacing of 20 ms with the same phase were used. The outer gap was increased by about 2 mm in between each segment. The resulting densities for each phase are shown in Figure 7-13. Typically the probe density decreased by about a factor of two for a gap increase of about 1 cm.

The reflection coefficients obtained from the jungle gym coupler analysis are plotted as a function of density in Figure 7-14 and phase in Figure 7-15. The data are also summarized in Table 7.2. As the probe density increases the reflection coefficients decrease, the amount of decrease depends on phase. A change of 3% was observed for 120° phasing while the 180° case changed by about 15%.
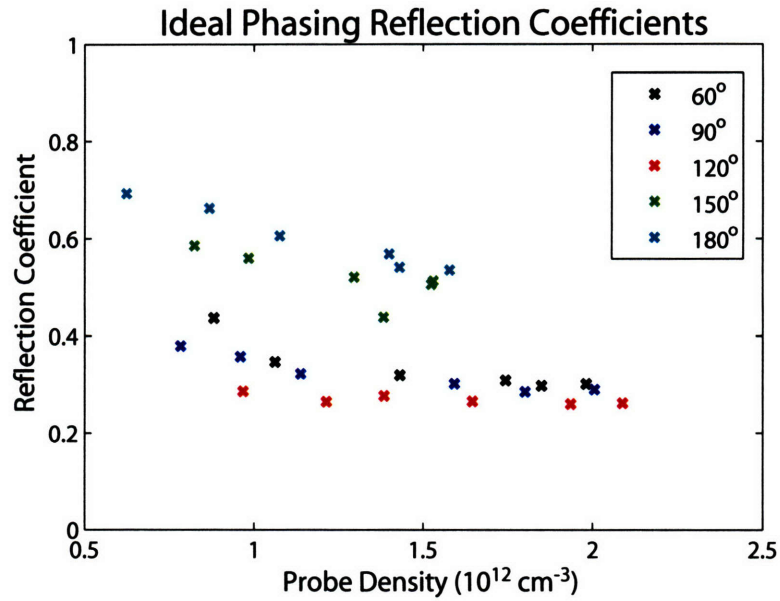
Figure 7-14: Ideal phase coupling measurements at various densities produced by changing the outer gap. The reflection coefficient calculation uses the jungle gym couplers and waveguide loss estimates.
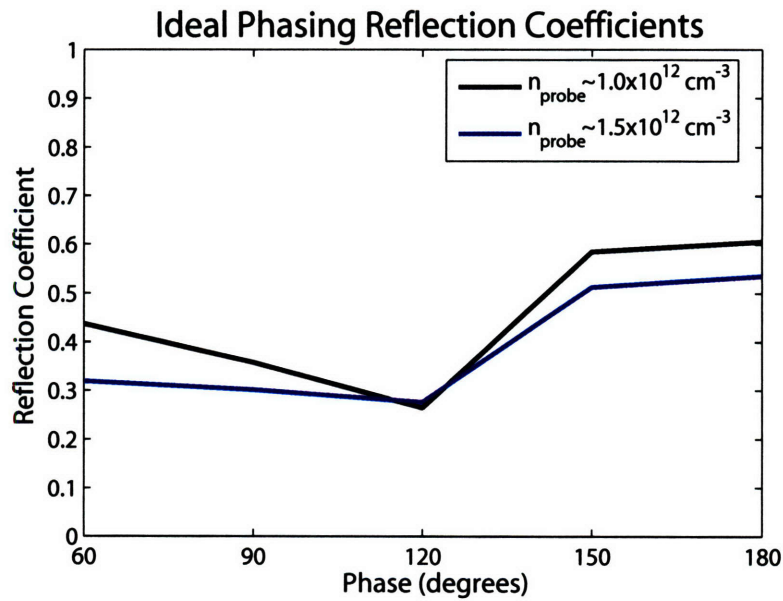
Figure 7-15: Ideal phasing reflection coefficients as a function of phase for densities of ≈ 1 and $\approx 1.5 \times 10^{12}$ cm^{-3}.

Table 7.2: Ideal Phase Progression Coupling Data

Shot	Segment Number	Position (mm)	PS Set (deg)	Phase (deg)	Avg. Phase Error (deg)	nl04 ($10^{20} m^{-2}$)	Outer Gap (cm)	Probe Density ($10^{18} m^{-3}$)	FINT Tot.(kW)	RINT Tot.(kW)	FWD Tot.(kW)	REV Tot.(kW)	Ref. Coef.
1060307015	1	3.0	90	90	14.0	0.45	0.71	1.80	226.0	7.6	199.5	24.2	0.28
	2	3.0	90	90	12.5	0.47	0.79	2.01	224.1	7.4	198.1	24.7	0.29
	3	3.0	90	90	12.3	0.47	1.05	1.59	222.1	7.6	196.4	25.9	0.30
	4	3.0	90	90	12.2	0.46	1.33	1.14	221.6	7.8	196.0	28.3	0.32
	5	3.0	90	90	12.0	0.45	1.48	0.96	220.8	7.9	195.0	31.7	0.36
	6	3.0	90	90	11.9	0.44	1.67	0.78	221.0	7.9	195.0	33.6	0.38
1060307017	1	3.0	180	180	15.1	0.42	0.78	1.58	212.9	43.7	192.1	47.0	0.53
	2	3.0	180	180	13.8	0.44	0.89	1.43	211.3	43.9	190.7	47.2	0.54
	3	3.0	180	180	13.6	0.44	1.08	1.40	210.9	45.9	190.3	49.7	0.57
	4	3.0	180	180	13.4	0.44	1.26	1.08	210.8	48.4	190.2	52.8	0.61
	5	3.0	180	180	13.4	0.45	1.51	0.87	209.8	52.4	189.3	57.8	0.66
	6	3.0	180	180	13.3	0.45	1.73	0.62	208.9	54.5	188.4	60.5	0.69
1060307019	1	3.0	150	150	17.3	0.47	0.77	1.52	217.1	31.4	201.6	49.1	0.51
	2	3.0	150	150	15.7	0.48	0.91	1.53	215.3	31.9	199.9	49.3	0.51
	3	3.0	150	150	15.4	0.49	1.06	1.30	214.0	32.2	199.3	49.6	0.52
	4	3.0	150	150	15.2	0.48	1.30	0.98	214.1	35.0	199.7	53.1	0.56
	5	3.0	150	150	15.3	0.50	1.53	0.82	212.7	36.5	198.2	55.4	0.58
	6	3.0	150	150	15.1	0.60	1.69	1.38	213.6	26.3	197.9	42.8	0.44
1060307021	1	3.0	120	120	17.9	0.47	0.73	1.94	217.5	15.7	199.5	28.4	0.26
	2	3.0	120	120	16.2	0.48	0.81	2.09	214.6	15.7	197.0	28.2	0.26
	3	3.0	120	120	16.0	0.48	1.03	1.65	213.2	16.1	195.6	28.4	0.27
	4	3.0	120	120	15.8	0.47	1.21	1.38	212.7	17.0	195.1	29.6	0.28
	5	3.0	120	120	15.6	0.48	1.51	0.97	212.1	18.0	195.3	30.6	0.29
	6	3.0	120	120	15.5	0.55	1.65	1.21	212.9	15.9	195.1	28.2	0.26
1060310003	1	3.0	60	60	26.0	0.51	0.88	1.85	228.5	6.5	205.2	28.7	0.30
	2	3.0	60	60	24.3	0.52	0.99	1.98	225.6	6.5	202.7	29.2	0.30
	3	3.0	60	60	23.9	0.52	1.13	1.74	224.7	6.4	202.2	29.6	0.31
	4	3.0	60	60	23.6	0.51	1.36	1.43	223.6	6.1	201.2	30.6	0.32
	5	3.0	60	60	23.4	0.51	1.56	1.06	224.5	6.1	201.9	33.0	0.35
	6	3.0	60	60	23.6	0.50	1.78	0.88	224.8	6.1	201.7	37.9	0.44
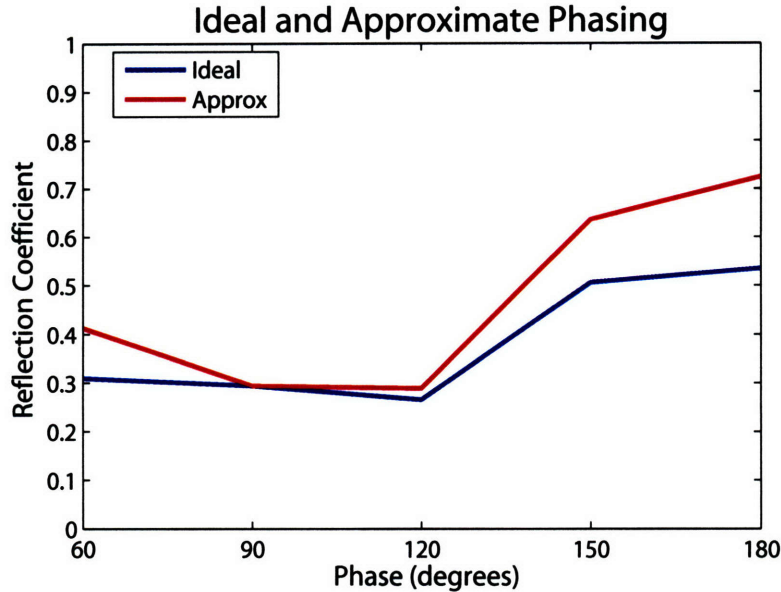
Figure 7-16: The approximate phase scan of shot 1060307013 is shown with data points chosen from the gap scans that match the probe density of $\approx 1.6 \times 10^{12}$ cm^{-3}.

Shot 1060307013 was an approximate phase scan with a near constant probe density of 1.6×10^{12} cm^{-3}. Comparing this shot to ideal phase segments with similar density allows ideal and approximate phase progressions to be compared. The results are plotted in Figure 7-16. Using an ideal phase gives the same or better coupling than approximate phasing. The deviation increases as the phase moves away from 90°.

7.2.4 Sensitivity to Phase Error

The sensitivity study of the coupling model assumed no phase error, that is the phase that was demanded was delivered. In the experiment, however, phase errors of 10 to 20 degrees are common. This error is due primarily to temperature variations in the experimental cell which change the electrical length of cabling. When the electrical length changes the phase calibrations are no longer valid, leading to error. Another GUI was written to display the most important signals involved in controlling the LH system, including the phase error and resulting $n_\parallel$ spectrum as calculated by the Fourier analysis developed in chapter 2. A screen capture from this GUI is shown in Figure 7-17 for shot 1060406009, where the demanded phase is plotted in the top right panel in blue. Over plotted in red is the phase measured by the IQ detectors and the difference is shown in the adjacent text box. Amplitude information is shown in the bottom right panel.
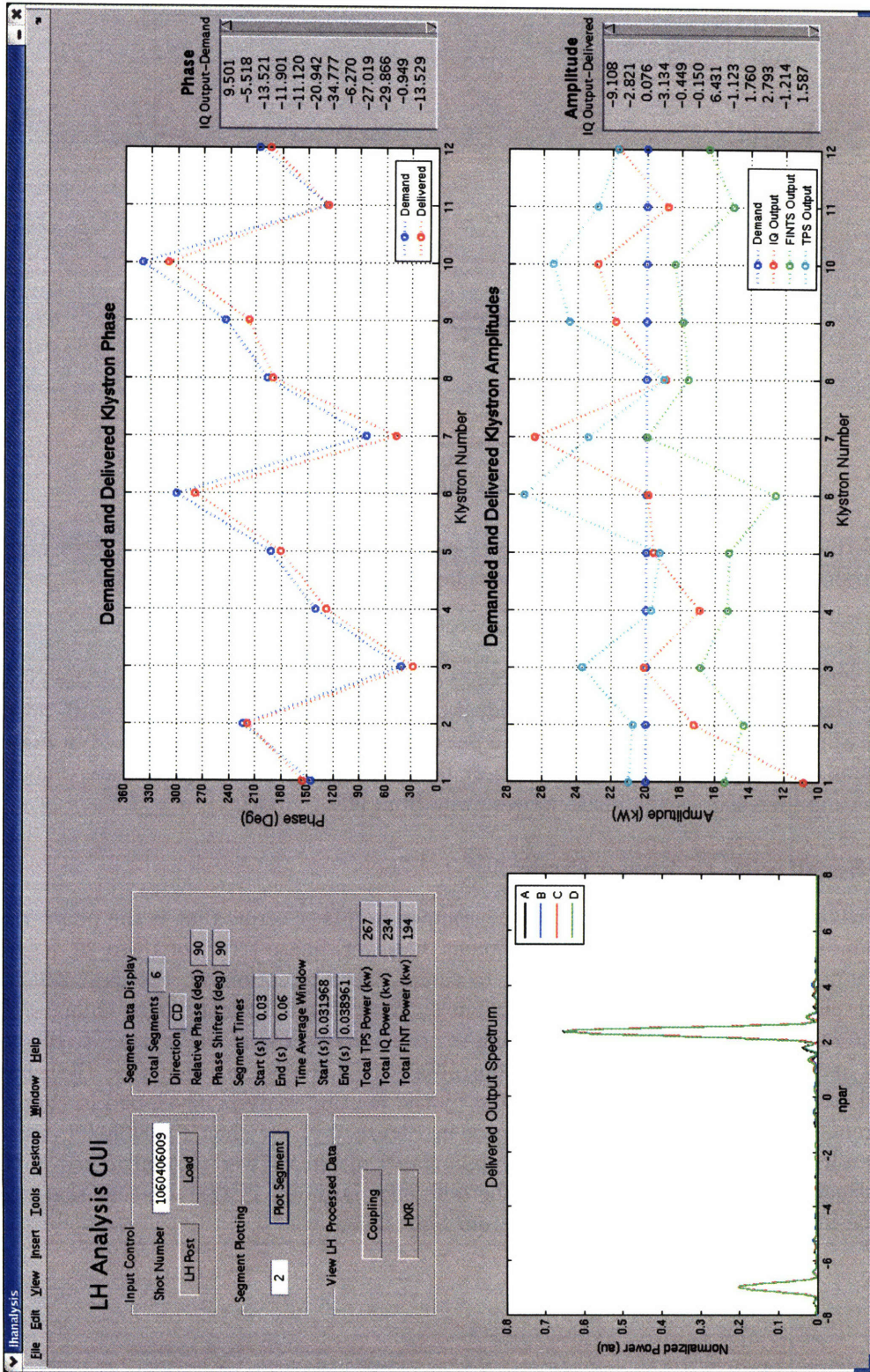
Figure 7-17: Screen capture from the LH analysis GUI used to organize and display amplitude and phase data. The top right panel plots the demanded and delivered phases. The bottom left panel shows the resulting output spectrum using equation A.7.
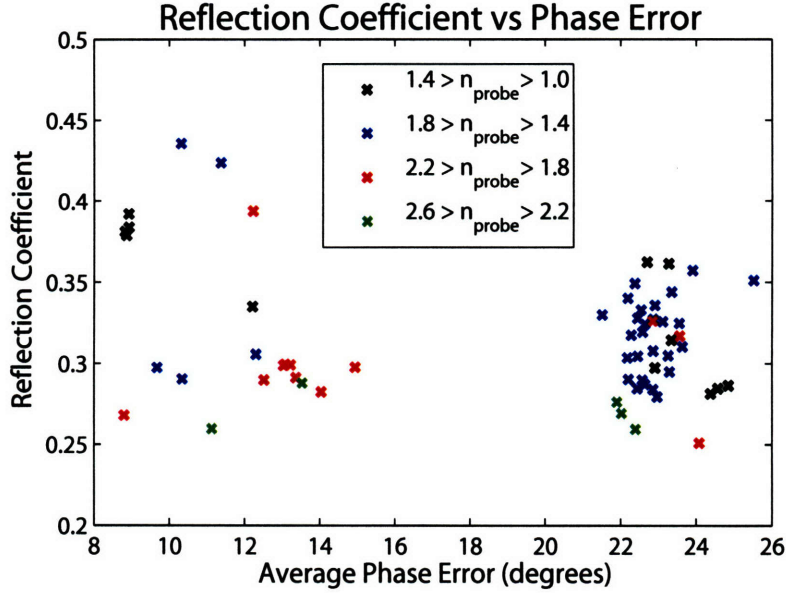
Figure 7-18: Reflection coefficients for 90° phasing as a function of average phase error for a variety of densities. Densities are in units of 10^{12} cm^{-}3

The $n_\parallel$ spectrum using the measured phase without accounting for the discontinuity between carts 2 and 3 is shown in the bottom left panel for all for rows of the coupler. Even with the phase error the resulting $n_\parallel$ spectra are nearly identical to spectra produced without phase error, implying that the $n_\parallel$ spectrum is very robust, and is not affected by errors of this magnitude.

Phase errors also do not seem to impact the reflection coefficient as shown in Figure 7-18. The reflection coefficient is plotted against the the average phase error for 90° phasing and over a number of density ranges. The data was gathered for runs 1060307 and 1060310 over which the temperature changed a couple of °C. The data clustered on the left of the plot was from 1060307, while the data clustered to the right was from 1060310.

7.3 Coupling Model and Experiment Comparison

The first step in comparing the experimental results to coupling theory is to interpret the probe density measurements in terms of the density profile that is used in the model. Typically a step function is used with a linear density gradient. This is shown in Figure 7-19. The position, x, is measured with respect to the location of the grill. A vacuum region of width x_{gap} precedes the step to a density of n_0, where the density increases with a slope of dn/dx. The probe, which is 3 mm long, is too large to measure the density locally at the grill, it instead measures the average density at a centroid defined by the density profile. The density profile may be described mathematically as

$$n(x) = \begin{cases} 0 & \text{for } x_{gap} > x \geq x_{grill} \\ \frac{dn}{dx}(x - x_{gap}) + n_0 & \text{for } x_{probe} \geq x \geq x_{gap}. \end{cases},$$

197
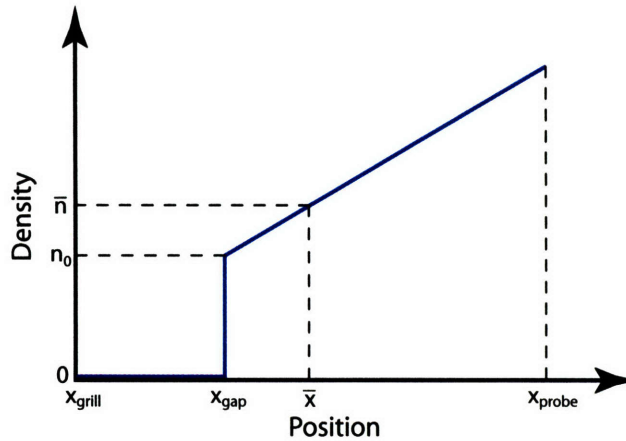
Figure 7-19: A model of the density profile near the grill is needed to interpret the probe density measurements. A step model was chosen to be consistent with the coupling model.

where x_{probe} is the probe length. The average density measured by the probe is given by

$$\overline{n} = \frac{1}{x_{probe}} \int_{x_{gap}}^{x_{probe}} n(x)dx,$$

which allows the step density, n_0 to be written in terms of the measured density $\overline{n}$ as

$$n_0 = \frac{1}{x_{probe} - x_{gap}} \left(x_{probe}\overline{n} - \frac{1}{2}\frac{dn}{dx}(x_{probe}^2 - x_{gap}^2) + x_{gap}\frac{dn}{dx}(x_{probe} - x_{gap}) \right). \quad (7.20)$$

The step density is one of the inputs for the coupling model.

The coupling code was run for the approximate phasing shots 1060307007, 1060307014, and 1060406009, which had the coupler located ad 4.4, 3.0 and 1.1 mm behind the LH limiter. The inputs to the code are phase, step density, density gradient, and vacuum gap width. The step density may be calculated from the probe density and the vacuum gap, which is a free parameter.

A simple linear extrapolation from the density gradient measurements give a density at the grill above the critical density, giving no vacuum gap. During experiments high reflection coefficients were measured, which can only be reproduced in the coupling model by the presence of a vacuum region. The coupling code was used with the measured phase and density gradient, while scanning the vacuum gap until reasonable agreement with the experiment was observed. The step density was calculated to be consistent with the chosen vacuum gap and the measured density gradient. The resulting input parameters are summarized in Table 7.3.

As can be seen in the table, the required vacuum gap to fit the results decreased as the launcher was moved closer to the plasma. A comparison of the experimental results to the model is shown in Figure 7-20 as a function of phase progression. Excellent agreement is observed, which is remarkable considering the complexity of the launch spectra. The spectra produced from the model using the parameters from Table 7.3 for shot 1060406009 are shown in Figure 7-21.

198

Approximate Phase Progression Reflection Coefficients
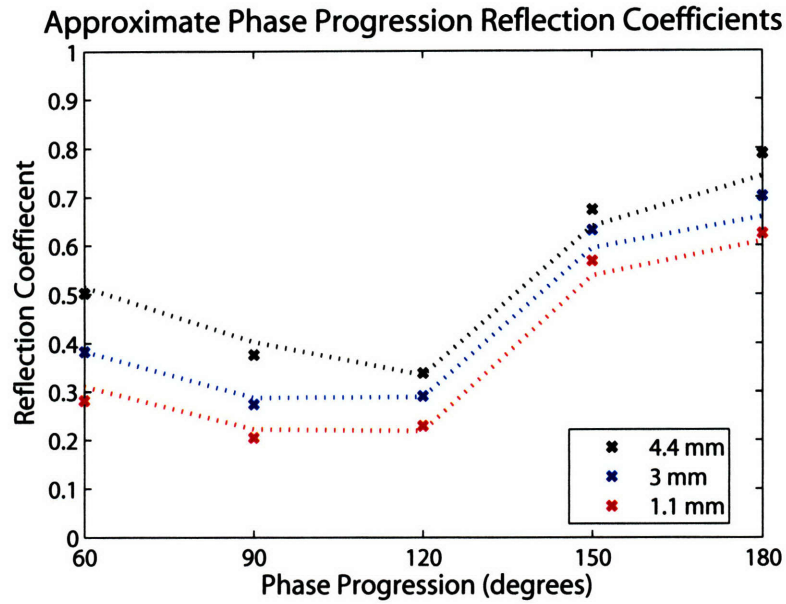
Figure 7-20: Comparison of coupling theory and experiment for approximate phasing at various coupler positions. Experimental points are marked as x's while the theory curves are shown as dashed lines.

Coupling Code Spectra for 1060406009
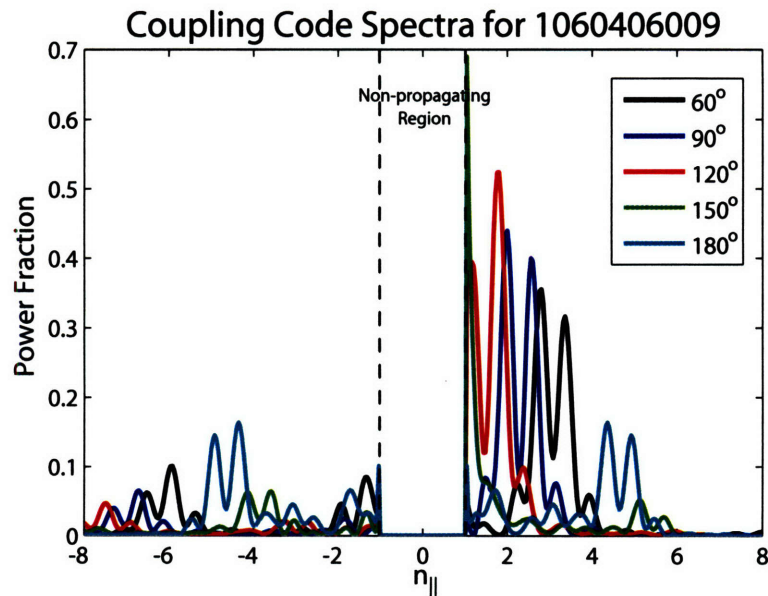
Figure 7-21: Output spectra produced by the coupling code for 1060406009 using the measured phase with model parameters of $n_0 = 1.3 \times 10^{12}$ cm^{-3}, $dn/dx = 6 \times 10^{12}$ cm^{-4}, and a 0.6 mm vacuum gap.

Table 7.3: **Approximate Phase Scan Parameters**

Shot	Position (cm)	$\langle \bar{n} \rangle$ (10^{12} cm^{-3})	n_0 (10^{12} cm^{-3})	x_{gap} (cm)	dn/dx (10^{12} cm^{-4})
1060307007	0.44	1.3	2.0	0.14	6.0
1060307014	0.30	2.2	2.5	0.09	6.0
1060406009	0.11	1.6	1.3	0.06	6.0

Similar modeling was done for the ideal phase progression gap scan plasmas, this time as a function of step density. The model parameters used are summarized in Table 7.4. A vacuum gap of 1 mm is needed to match the experimental results. These numbers are

Table 7.4: **Ideal Phase Scan Parameters**

Shot	Phase (°)	Position (cm)	x_{gap} (cm)	dn/dx (10^{12} cm^{-4})
1060307015	90	0.30	0.09	6.0
1060307017	180	0.30	0.11	6.0
1060307019	150	0.30	0.09	6.0
1060307021	120	0.30	0.08	6.0
1060310003	60	0.30	0.07	6.0

nearly identical to the 0.9 mm gap needed for the approximate phase progression case at the same position behind the limiter. Figure 7-22 compares the experimental results to the model. Again remarkable agreement with the model is observed given the spectra produced. The spectra produced for a step density of $n_0 = 1.5 \times 10^{12}$ cm^{-3} are shown in Figure 7-23.

Vacuum gaps have been required to describe results in the past, and results from ASDEX[119] are particularly relevant to what was observed on C-Mod. Reflection coefficients of 20-40% were observed with their grill located 3 mm behind the limiter. Here the presence of a vacuum gap was described as a consequence of the short connection length between the limiter tiles and the ponderomotive force from the grill electric field pushing the plasma away. In a later campaign the grill was moved to be flush with the limiter and the reflection coefficient dropped by about factor of two.

On C-Mod a similar drop in reflection coefficient was observed when the launcher is moved from 4.4 mm to 1.1 mm behind the limiter as shown in Figure 7-11. Since there is ambiguity about the actual position of the antenna behind the limiter, the launcher has not been moved in further, but doing so may provide better coupling.

Examining time traces from C-Mod's Langmuir probes do not show a significant change in density from when the power is switched on and off for any launcher position. Figures 7-24, 7-25, and 7-26 compare the time history of the LH power and Langmuir probes for grill positions of 4.4, 3.0 and 1.1 mm respectively behind the limiter.

The probe data points are asynchronous since bad I-V characteristics are rejected. The sweep time of the probes are similar to the LH pulse length used during the coupling study, however, no effect is seen when long duration pulses are examined as well. Even though the probes do not show a change in the density it is still possible that a vacuum gap may be present. As mentioned above, the probe is 3 mm long, which is much longer than the width of the vacuum gaps needed to match the results with the model.

The ponderomotive force becomes significant when the energy density of a waveguide

Ideal Phase Progression Reflection Coefficients
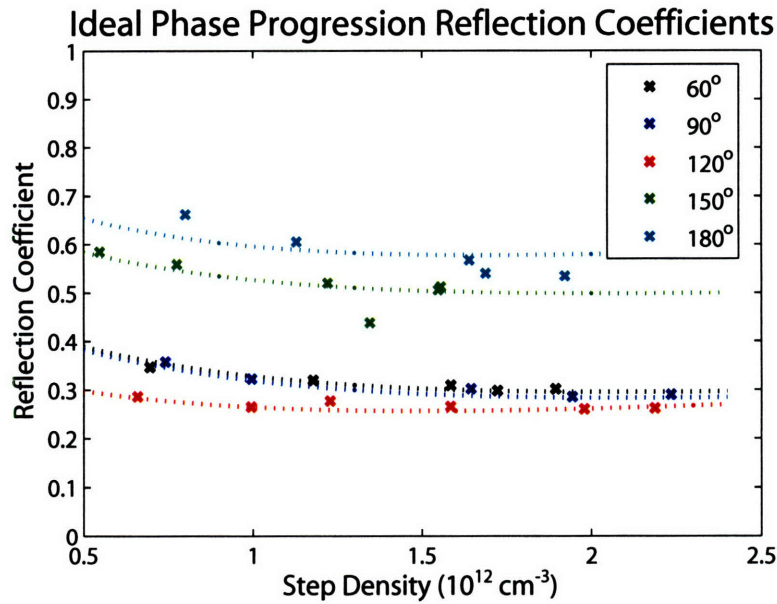
Figure 7-22: Comparison of coupling theory and experiment for ideal phasing as a function of density. Experimental points are marked as x's while the theory curves are shown as dashed lines.

Coupling Code Ideal Spectra
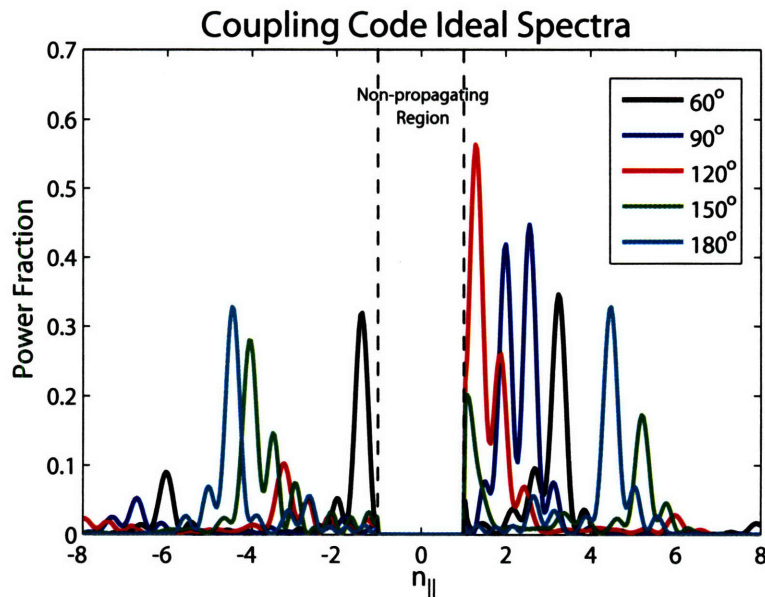
Figure 7-23: Output spectra produced by the coupling code for ideal phasing using the measured phase with model parameters of $n_0 = 1.5 \times 10^{12}\ cm^{-3}$, $dn/dx = 6 \times 10^{12}\ cm^{-4}$. Vacuum gaps of 0.7, 0.9, 0.8, 0.9, and 1.1 mm for 60°, 90°, 120°, 150° and 180° phasing.
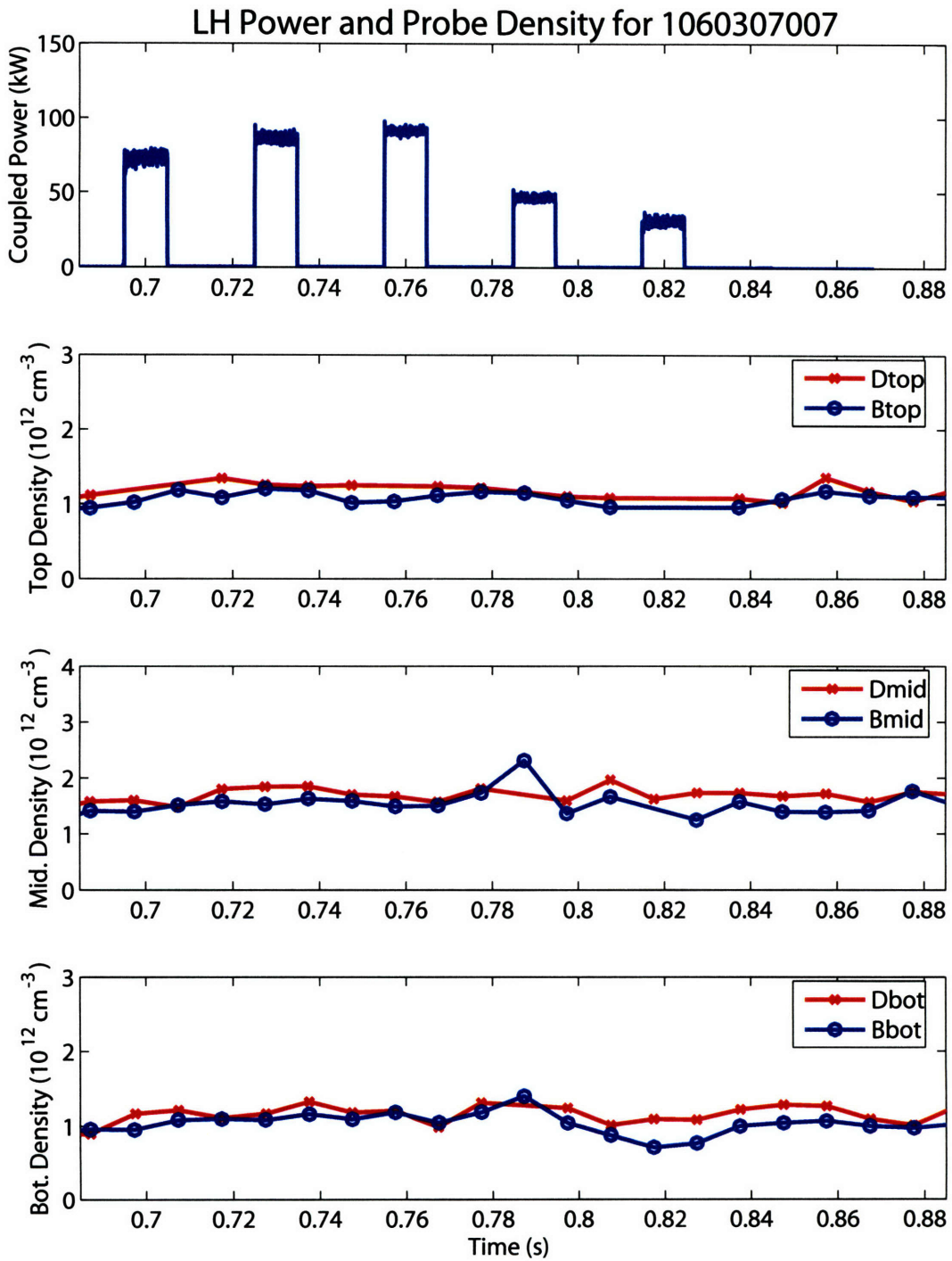
Figure 7-24: Time traces of the coupled LH power and probe density for 1060307007, in which the grill is approximately 4.4 mm behind the LH limiter.
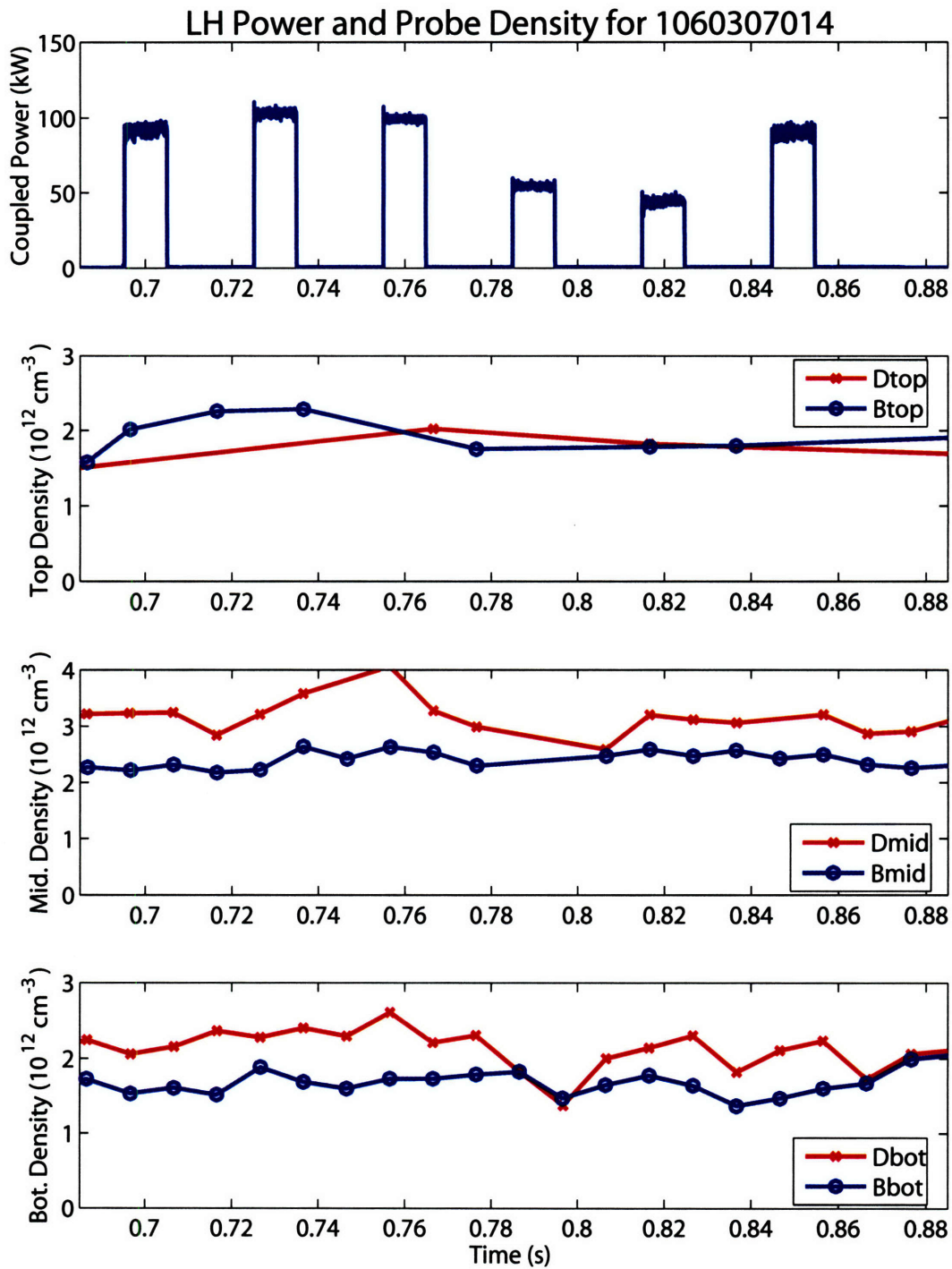
Figure 7-25: Time traces of the coupled LH power and probe density for 1060307014, in which the grill is approximately 3 mm behind the LH limiter.
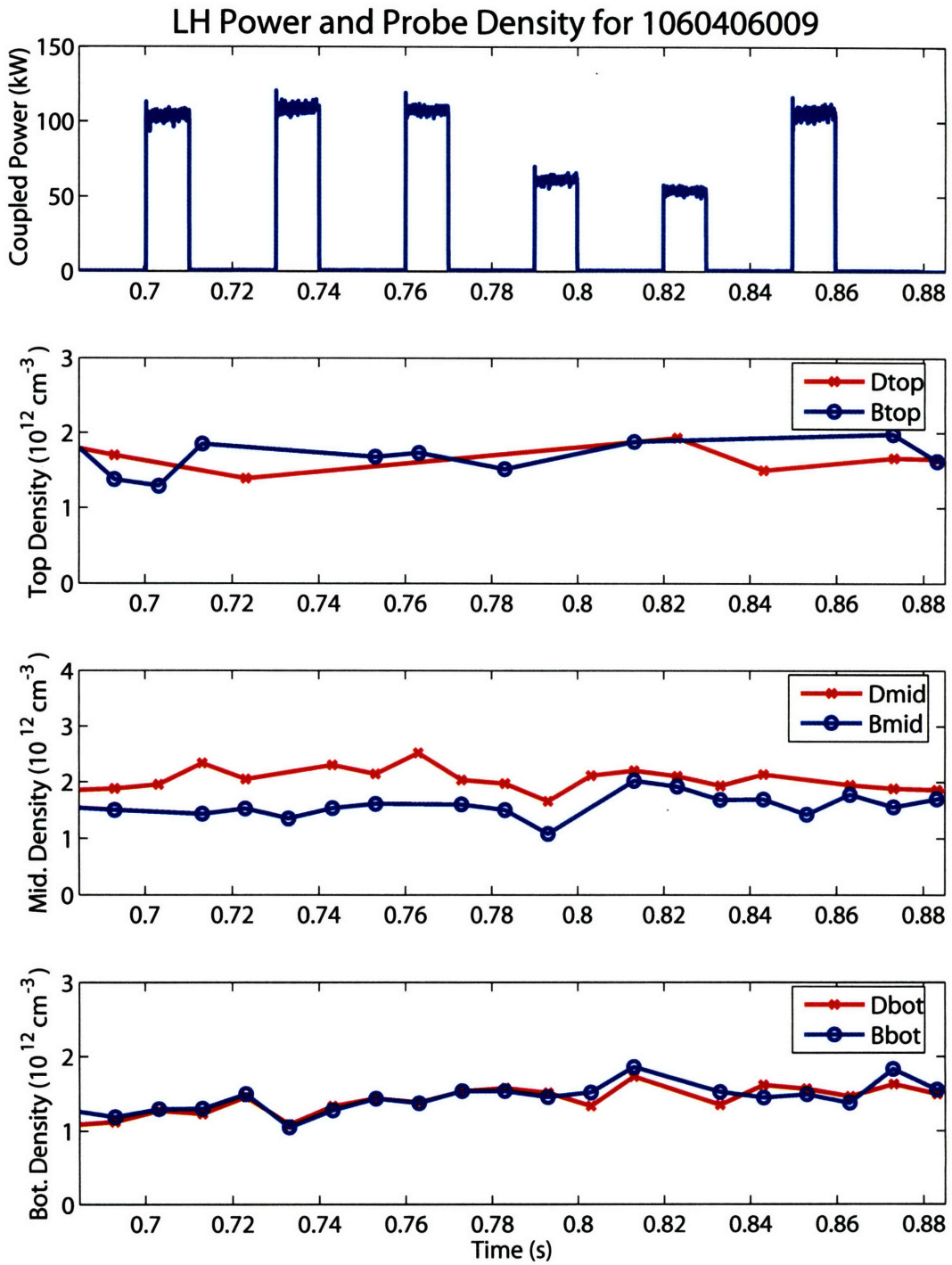
Figure 7-26: Time traces of the coupled LH power and probe density for 1060406009, in which the grill is approximately 1.1 mm behind the LH limiter.

comparable to the energy density of the plasma, that is

$$\frac{W_{wg}}{W_{plasma}} \sim \frac{\epsilon_0 E_{wg}^2}{2nT}.$$

The electric field of the waveguide may be estimated by

$$E_{wg} \sim \left(\frac{2P_{wg}Z_{coup}}{A_{wg}}\right)^{1/2} \tag{7.21}$$

where P_{wg} is the power in the waveguide at the coupler, A_{wg} is the area of the guide, Z_{coup} is the coupler impedance and C-Mod's coupler has an impedance of 450 Ω. For 200 kW of grill power the waveguide field is 7.5×10^4 V/m. This gives as energy density of about 0.03 J/m^3. The peak field may be significantly higher. For a 10 eV plasma at the critical density the plasma energy density is 0.4 J/m^3. This means that the ponderomotive effect may play a role in determining the conditions at the grill, but is not likely the dominant factor.

In general, the results obtained agree very well with the linear coupling model. This was a good test of the model as the spectra launched were fairly complex in nature, yet the model was still able to match the observed total reflection coefficients. The uncertainty in R is estimated to be 20-40%, increasing as the magnitude of R increases. This estimate assumes a 5% error in the jungle gym coupler measurements and propagates the error through the sums and divisions required to calculate the total reflection coefficient. Probe density measurements typically have standard deviations within 50%, mainly due to the discrepancy between the top and bottom measurements as compared to the middle probe measurements. Detailed evaluation of the model is difficult given the free parameter and the propagation of many small errors incurred when calculating the total reflection coefficient. This means that even if the RF probes on the end of the RWG are working extremely well, the total reflection coefficient would still be difficult to measure accurately enough to constrain the model.

Chapter 8

Summary and Future Work

Advanced tokamaks appear to be a promising approach to thermonuclear fusion energy and can be characterized by high performance, steady state operation. The bootstrap current can be used to generate much of the plasma current required for confinement by careful control of the current and pressure profiles. Lower hybrid current drive is a very efficient means of producing the off-axis current needed for creating large bootstrap fractions.

Alcator C-Mod is a high density, high magnetic field, diverted tokamak capable of studying AT plasmas in regimes relevant to ITER and fusion reactors on quasi-steady state time scales. A lower hybrid system has been implemented on C-Mod with 3 MW of source power at 4.6 GHz, with the goal of attaining current profile control and studying AT operation. The initial value of $n_\parallel$ is a key parameter in determining the location and efficiency of the driven current. The $n_\parallel$ spectrum can be varied over a wide range of values by controlling the phase of the LH antenna. The phase may be controlled dynamically, which gives flexibility in the values of $n_\parallel$ produced during a discharge with the goal of tailoring the resulting current profile.

In support of lower hybrid experiments, extensive modeling was carried out to provide a basis of what could be expected. Time dependent modeling of integrated scenarios was preformed using a transport code. An internal transport barrier scenario formed from a current ramp was simulated while parameters such as LH and ICRF power as well as density were varied. Results indicate that fully non-inductive operation is possible with bootstrap fractions of about 75%.

Detailed Fokker-Planck modeling of current profile control with various antenna phasings was performed using a low density H-mode target plasma. Results indicate that about 200 kA of plasma current can be driven using 2 MW of lower hybrid power at the grill. This result was obtained without including an ohmic electric field. Compound spectra were also investigated for a planned second lower hybrid antenna. Results showed that a variety of current profile shapes are possible depending on the phasing of the two antennas.

Wave coupling between the antenna and the plasma was studied using a coupling code, which was modified for use with C-Mod's LH system. A sensitivity study was performed over the parameter ranges of C-Mod experiments with the result that low total reflection coefficients are possible, under certain conditions. For example using 90° phasing with no vacuum gap and a density at the grill of 3×10^{12} cm^{-3}, a total reflection coefficient of about 3% is expected.

The location of fast electron population created through electron Landau damping of the LH waves may be inferred by measuring the nonthermal bremsstrahlung emission in

the hard x-ray region. The HXR measurement provides experimental results to compare with the results from the modeling and a means to benchmark code parameters. A pinhole camera using an array of 32 CdZnTe detectors was developed to image energies in the 20-200 keV range. Detectors and pulse processing electronics were integrated into a compact and modular package making extensive use of printed circuit board and surface mount technology. The system also make use of fast digitization and software signal processing techniques. An ambient environment of neutrons, gammas, and high RF power requires careful shielding. Shielding was studied using the neutron and photon transport code MCNP.

Initial experiments have been completed to study the wave coupling between the grill and plasma. The coupling experiments were performed first at low power and short pulse length. Dynamic phase control was implemented for these experiments allowing for complete phase scans to be completed during a single discharge. A discontinuity in the phase between carts 2 and 3 was found to produce compound spectra and raise the reflection coefficients observed. The coupling code was used to model the reflection coefficients from compound spectra. Remarkable agreement was observed between the theory and experiment when a vacuum gap was included in the model. As the coupler was moved closer to the plasma the vacuum gap required to match the experiment decreased.

Initial current drive experiments were also completed by coupling about 400 kW for 400 ms into low density L-mode discharges. Clear evidence of current drive was seen as the loop voltage decreased by about 50%. Studies were performed by varying the phase, density, and magnetic field as well as changing the direction that the waves were launched. HXR results indicate a spatially broad and centered fast electron population under all conditions. This is most likely due to the broad nature of the $n_\parallel$ spectra produced and spatial diffusion of the fast electron population. The presence of an ohmic electric field greatly increases the energy of the HXR spectra observed and leads to high count rates as seen through Fokker-Planck analysis of shot 1060420026. The current drive efficiency was determined to be 0.15 ($10^{20}m^{-2}A/W$) by driving 167 kA of LH current with 410 kW at a line-average $5.5 \times 10^{19}m^{-3}$, without an electric field. A constant electric field calculated from the residual loop voltage, 0.45 V, was then included in the Fokker-Planck analysis. The LH current and efficiency nearly double to 308 kA, and 0.28 respectively. Hard x-ray profiles predicted by a synthetic diagnostic differ from the observed profiles, possibly requiring spatial diffusion of the fast electron population for agreement.

8.1 Future Work

Coupling experiments should be performed using non-compound spectra to try and find the minimum reflection coefficient possible and compared to results from the coupling code. Similarly, the L-mode current drive experiments should also be performed using non-compound spectra, with particular emphasis on changing the phase and examining the spatial distribution of the fast electron population. Current drive experiments with ICRF power would be of interest to see the effect of increased temperature on the spatial location and efficiency of LHCD. Using ICRF would also create a background gammas, which may be used to begin to map out the operational space for good S/N from the HXR camera. Another experiment that would be of use and does not require high power is a coupling study of H-mode discharges. Once full protection and higher power is available then AT experiments may begin in earnest.

In the future real time feedback control of the $n_\parallel$ is possible. If results from HXR camera are favorable and lend themselves to fast interpretation, then HXR data may be used as an actuator in controlling the $n_\parallel$ spectrum. Doing so would necessitate upgrading the HXR diagnostic to a digital, real time spectrometer.

Appendix A

Lower Hybrid Antenna Phase Settings

This appendix includes all the phasing information for the lower hybrid antenna. It is meant to be a record of how the antenna calibrations were done as well as how to set the antenna phase to generate a given $n_\parallel$ spectrum. The main tables are hyperlinked in the electronic version of this document to specific cases to aid navigation.

The calibration data is used by the Matlab script *nspectrum* to generate the correct settings for the klystrons and mechanical phase shifters for a given type of phasing and direction. The phasing is either "ideal", meaning that the phase between adjacent waveguides is always the same or "approximate", which takes into account the mechanical phase shifters set at a fixed location. The direction is either "CD" for current drive, with the plasma current or counter current drive, "CCD", against the plasma current. The code is located in */home/jliptac/matlab/nspectrum*. *nspectrum* also performs a quick analysis using equation A.7. Of course to get more accurate information the coupling code must be used to take into account the plasma parameters. A more general version of *nspectrum* is included in the set point generator used to control the antenna phase.

The couplers now have 22 columns, so the information for waveguides 1 and 24 may be disregarded.

A.1 Calibration Data

The lower hybrid antenna was calibrated by taking phase and amplitude measurements at two locations, the intermediate 50 dB coupler and at the coupler end of the forward waveguide assembly. Each waveguide has a characteristic phase shift which needs to be taken into account when phasing the antenna to control the $n_\parallel$ spectrum. The calibration phase and amplitude numbers collected in November 2005 are summarized in Table A.1.

Since each klystron feeds eight waveguides in two columns and four rows, each waveguide is not independent. The phase is controlled with respect to a reference, row A.

To launch a given $n_\parallel$ spectrum, the phase progression must be known. Setting the phase change between columns, ϕ_{dph}, and the direction of the phase progression determines where the main lobes of the power spectrum are located and the direction the wave is launched. To launch a wave in the CD direction the phase progression must decrease from column 1 to 24, conversely an increasing progression launches a wave in the CCD direction. The output phase on row A is given by ϕ_α^{out} and ϕ_β^{out}, with the subscripts α and β representing

the columns with and without the mechanical phase shifter respectively. The phase shifters are located on odd columns for carts 1 and 2, and even columns on cart 3.

For columns without the mechanical phase shifter, the required klystron phase, ϕ_k is related to the requested output phase as

$$\phi_k = \phi_{idc} + \phi_\beta^{out} - \phi_{fwg}. \tag{A.1}$$

Here ϕ_{idc} and ϕ_{fwg} are the measured calibration numbers in Table A.1 for a given column number.

The output phase for a column with the phase shifter is

$$\phi_\alpha^{out} = \phi_\beta^{out} + \phi_{ps}, \tag{A.2}$$

where ϕ_{ps} is the phase shift introduced by the mechanical phase shifter.

For a given column each row has a slightly different phase shift, which may be partially compensated for when setting the mechanical phase shifter. This is done by calculating the average difference between each row as

$$< \Delta_{\beta\alpha} >= \frac{1}{4} \left(\phi_{\beta A} - \phi_{\alpha A} + \phi_{\beta B} - \phi_{\alpha B} + \phi_{\beta C} - \phi_{\alpha C} + \phi_{iD} - \phi_{jD} \right), \tag{A.3}$$

where the subscripts A, B, C, and D represent the row. The required phase shifter phase is then

$$\phi_{ps} = \phi_{dph} + < \Delta_{\beta\alpha} > . \tag{A.4}$$

Now ϕ_{dph} must be defined more precisely to account for the direction the wave is to be launched and the asymmetry of having the phase shifters on the even columns of cart 3,

$$\phi_{dph} = \begin{cases} |\phi_\alpha^{out} - \phi_\beta^{out}|C_{dir} & \text{for carts 1 and 2} \\ -|\phi_\alpha^{out} - \phi_\beta^{out}|C_{dir} & \text{for cart 3.} \end{cases} \tag{A.5}$$

Here C_{dir} is +1 for the CD direction and -1 for the CCD direction.

The mechanical phase shifters are adjusted using a depth gauge with the calibration of 1.13" giving 360°. Making the length shorter adds phase lag while increasing length subtracts phase lag

$$PS_{pos} = PS_0 + \phi_{ps}c_{ps}. \tag{A.6}$$

Here PS_0 is the zero position in inches, ϕ_{ps} is the desired phase shift and c_{ps} is the calibration number, 0.003139"/degree. Table A.1 also includes the zero position of each phase shifter.

All of this is made much clearer by going through an example. Say 90° CD phasing is desired with 90° output phase on column 1 and 0° output phase on column 2. The klystron phase would be

$$\phi_k = -155.1° + 0° - 59.4° = 145.5°.$$

This sets the phase for column 2 on all rows. CD means that C_{dir} is +1 and columns 1 and 2 correspond to cart 1, so $\phi_{dph} = 90°$. The average difference phase is $< \Delta_{21} >= 5.24°$ and so the needed phase adjustment from the phase shifter is

$$\phi_{ps} = 90° + 5.24° = 95.24°.$$

Now the phase shifter position may be calculated as

$$PS_{pos} = 2.738" + 95.24° \frac{1.13"}{360°}, \text{ or } 3.037".$$

212

The resulting $n_\parallel$ spectrum may be formed from $P(k) = E(k) \cdot E(k)^*$ with

$$E(k) = \frac{2}{k}\sin\left(\frac{kL}{2}\right)e^{-i\frac{kL}{2}}\sum_{p=2}^{23}E_p e^{i(kpL+kp\Delta+\phi_p)}. \qquad (A.7)$$

The electric field, E_p, for each waveguide is given from the amplitude calibration, A_p, in Table A.1 and the conversion from dB, $E_p = \sqrt{10^{(A_p/10)}}$. The phase ϕ_p is the output phase of the pth column. Equation A.7 accurately calculates the $n_\parallel$ of the spectral peaks and provides an estimate of the amplitude. To get a more accurate value for the amplitude a coupling code is needed to take into account the plasma interaction. Differences in amplitude from Equation A.7 and the coupling code can be $\sim 10\%$ for $n_\parallel$ below 90° with the differences decreasing at higher waveguide phasings, as the spectra become less directional.

Table A.1: Antenna Calibration Numbers

	Column	1	2	3	4	5	6	7	8	9	10	11	12
	$\phi_{idc}(°)$	-155.1	-155.1	-163.5	-163.5	-165.8	-165.8	-159.1	-159.1	-161.9	-161.9	-155.3	-155.3
Row A	$\phi_{fwg}(°)$	65.3	59.4	145.1	152.8	162.9	152.5	-110.2	-119.4	11.6	6.1	88.4	84.6
	Amp. (dB)	-10.5	-10.4	-10.9	-10.4	-11.3	-10.9	-11.8	-11.9	-11.4	-11.2	-12.0	-11.2
Row B	$\phi_{fwg}(°)$	-37.2	-33.5	40.2	53.7	70.9	72.4	141.7	129.0	-79.3	-96.9	-4.7	-16.9
	Amp. (dB)	-10.5	-11.4	-10.9	-10.9	-11.3	-11.0	-11.1	-11.3	-11.1	-10.7	-10.7	-10.8
Row C	$\phi_{fwg}(°)$	-50.2	-33.5	58.2	55.2	63.5	75.5	144.4	158.5	-80.7	-91.9	2.5	-11.4
	Amp. (dB)	-11.3	-11.3	-10.7	-11.0	-11.3	-11.0	-12.0	-12.4	-11.9	-10.6	-10.9	-10.6
Row D	$\phi_{fwg}(°)$	48.3	54.8	140.7	152.3	153.7	164.9	-120.7	-117.2	-4.1	-3.0	86.1	79.3
	Amp. (dB)	-10.4	-10.7	-10.4	-10.6	-11.2	-11.0	-10.8	-11.1	-11.0	-10.5	-11.5	-11.0
	PS_0 (in)	2.738		2.754		2.777		2.706		2.939		2.786	

	Column	13	14	15	16	17	18	19	20	21	22	23	24
	$\phi_{idc}(°)$	-157.6	-157.6	-155.3	-155.3	-162.9	-162.9	-155.0	-155.0	-155.5	-155.5	-157.0	-157.0
Row A	$\phi_{fwg}(°)$	119.7	120.0	-165.6	-171.8	42.2	48.0	135.5	127.1	166.3	152.7	-93.2	-90.9
	Amp. (dB)	-11.7	-11.5	-11.5	-12.2	-11.4	-11.9	-11.3	-11.3	-12.1	-11.7	-11.4	-11.1
Row B	$\phi_{fwg}(°)$	24.6	17.0	97.4	86.4	-56.2	-52.2	31.0	17.4	65.9	55.1	162.5	159.0
	Amp. (dB)	-11.0	-10.8	-10.8	-11.1	-11.1	-10.8	-10.8	-10.4	-11.0	-10.6	-10.9	-10.4
Row C	$\phi_{fwg}(°)$	29.0	19.2	100.7	93.2	-37.3	-43.8	28.7	22.3	60.2	41.1	168.5	163.2
	Amp. (dB)	-11.3	-10.9	-11.0	-10.9	-10.6	-10.7	-10.6	-10.6	-11.2	-11.4	-11.5	-11.0
Row D	$\phi_{fwg}(°)$	120.7	116.3	-162.8	-176.3	53.3	51.3	119.2	132.5	147.1	140.0	-98.2	-86.7
	Amp. (dB)	-11.0	-11.0	-11.1	-11.4	-10.8	-10.5	-10.3	-10.6	-10.4	-10.8	-10.1	-10.1
	PS_0 (in)	2.943		2.739		2.803		2.790		2.757		2.823	

A.2 Ideal Phasing

Ideal phasing has the mechanical phase shifters set to produce a constant change in phase from column to column. For example, 90° CD phasing with an initial phase of 90°, would have a phase progression of 90°, 0°, 270°, 180°, and then repeat. Decreasing the phase launches the wave in the CD direction. The CD direction is the direction of the electrons, or opposite the plasma current. If the phase progression is increasing, for example 270°, 0°, 90°, 180°, etc. then the wave would be primarily launched in the CCD direction, or with the plasma current.

The spectral properties for a given ideal phasing in the CD direction are shown in Table A.2 and includes the peak $n_\parallel$ and power distribution. The numbers in the table are the result of running the coupling code with $n = 2 \times 10^{12}$ cm^{-3}, $dn/dx = 5 \times 10^{12}$ cm^{-4}, and no vacuum gap. The table begins at 60°, since this puts the primary peak near the minimum accessible $n_\parallel$ of 1.5 for standard operating conditions at 5.4 T. Ideal CD klystron and phase shifter settings are shown in Sections A.2.1 through A.2.7 for 60° through 180° phasing. These sections also include plots of the $n_\parallel$ spectrum generated using Equation A.7.

The spectral properties for the CCD direction are identical to the CD direction, but in the opposite direction, ie the sign of $n_\parallel$ changes. The settings for $\phi_{klystron}$ and PS_{pos} are also different and are tabulated in Sections A.3.1, A.3.2, and A.3.3. *Note that changing direction from CD to CCD, or vice versa, requires adjusting the mechanical phase shifters.*

Table A.2: **Ideal Current Drive Phasing Spectral Properties**

ϕ	$n_\parallel$ CD	Power (%)	$n_\parallel$ CCD	Power (%)
60	1.52	70.0	7.76	13.3
72	1.84	68.2	7.44	15.4
90	2.32	61.9	6.96	18.9
120	3.12	54.7	6.20	22.1
135	3.48	48.3	5.80	26.0
150	3.88	43.6	5.40	28.9
180	4.64	35.5	4.64	35.5

A.2.1   60° Ideal CD

60°			
WG	ϕ_{out}	ϕ_k	PS_{pos}
1	60	145.5	2.943
2	0	145.5	
3	300	283.7	2.966
4	240	283.7	
5	180	161.7	2.977
6	120	161.7	
7	60	320.3	2.891
8	0	320.3	
9	300	71.95	3.101
10	240	71.95	
11	180	240.1	2.946
12	120	240.1	
13	60	82.4	3.115
14	0	82.4	
15	300	256.5	2.897
16	240	256.5	
17	180	334.9	
18	120	334.9	2.614
19	60	129.5	
20	0	129.5	2.614
21	300	338.2	
22	240	338.2	2.608
23	180	116.2	
24	120	116.2	2.631
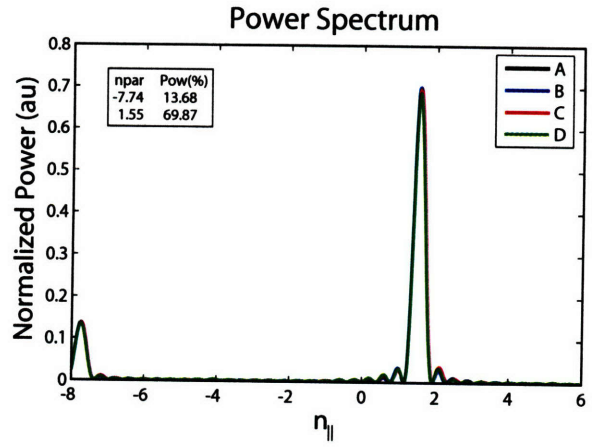
Figure A-1: Ideal spectrum for 60°.

A.2.2   72° Ideal CD

72°			
WG	ϕ_{out}	ϕ_k	PS_{pos}
1	72	145.5	2.980
2	0	145.5	
3	288	259.7	3.004
4	216	259.7	
5	144	113.7	3.014
6	72	113.7	
7	0	248.3	2.929
8	288	248.3	
9	216	336.0	3.139
10	144	336.0	
11	72	120.1	2.983
12	0	120.1	
13	288	298.4	3.152
14	216	298.4	
15	144	88.5	2.935
16	72	88.5	
17	0	154.9	
18	288	154.9	2.576
19	216	285.5	
20	144	285.5	2.576
21	72	110.2	
22	0	110.2	2.571
23	288	224.2	
24	216	224.2	2.593
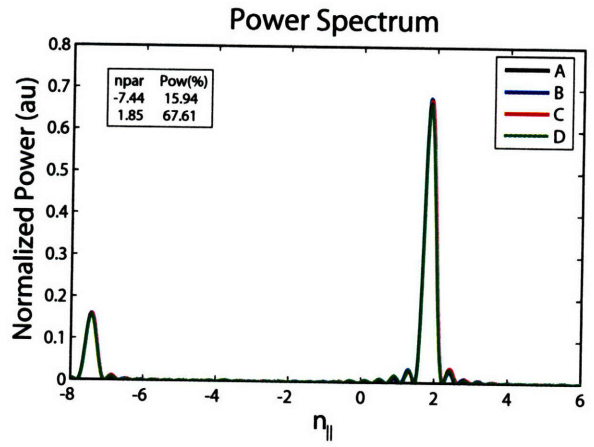
Figure A-2: Ideal spectrum for 72°.

A.2.3 90° Ideal CD

90°			
WG	ϕ_{out}	ϕ_k	PS_{pos}
1	90	145.5	3.037
2	0	145.5	
3	270	223.7	3.060
4	180	223.7	
5	90	41.7	3.071
6	0	41.7	
7	270	140.3	2.985
8	180	140.3	
9	90	192.0	3.196
10	0	192.0	
11	270	300.1	3.040
12	180	300.1	
13	90	82.4	3.209
14	0	82.4	
15	270	196.5	2.992
16	180	196.5	
17	90	244.9	
18	0	244.9	2.519
19	270	339.5	
20	180	339.5	2.519
21	90	128.2	
22	0	128.2	2.514
23	270	206.2	
24	180	206.2	2.537
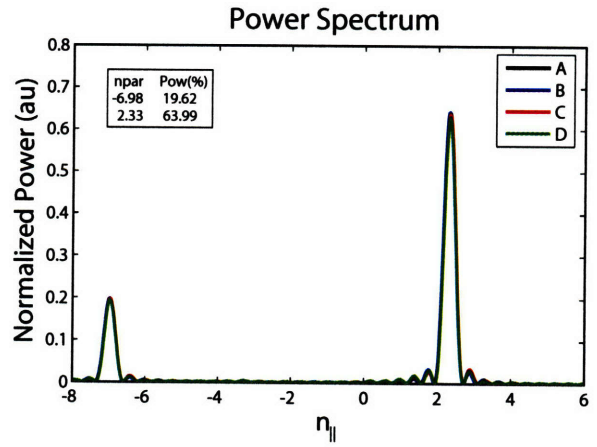
Figure A-3: Ideal spectrum for 90°.

A.2.4 120° Ideal CD

120°			
WG	ϕ_{out}	ϕ_k	PS_{pos}
1	120	145.5	3.131
2	0	145.5	
3	240	163.7	3.154
4	120	163.7	
5	0	281.7	3.165
6	240	281.7	
7	120	320.3	3.079
8	0	320.3	
9	240	312.0	3.290
10	120	312.0	
11	0	0.1	3.134
12	240	0.1	
13	120	82.4	3.303
14	0	82.4	
15	240	136.5	3.086
16	120	136.5	
17	0	154.9	
18	240	154.9	2.425
19	120	189.5	
20	0	189.5	2.425
21	240	278.2	
22	120	278.2	2.420
23	0	296.2	
24	240	296.2	2.442
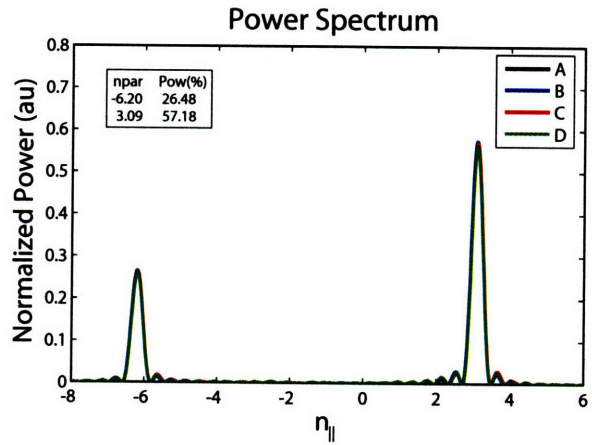
Figure A-4: Ideal spectrum for 120°.

A.2.5 135° Ideal CD

135°			
WG	ϕ_{out}	ϕ_k	PS_{pos}
1	135	145.5	3.178
2	0	145.5	
3	225	133.7	3.201
4	90	133.7	
5	315	221.7	3.212
6	180	221.7	
7	45	230.3	3.126
8	270	230.3	
9	135	192.0	3.337
10	0	192.0	
11	225	210.1	3.181
12	90	210.1	
13	315	262.4	3.350
14	180	262.4	
15	45	286.5	3.133
16	270	286.5	
17	135	289.9	
18	0	289.9	2.378
19	225	294.5	
20	90	294.5	2.378
21	315	353.2	
22	180	353.2	2.373
23	45	341.2	
24	270	341.2	2.395
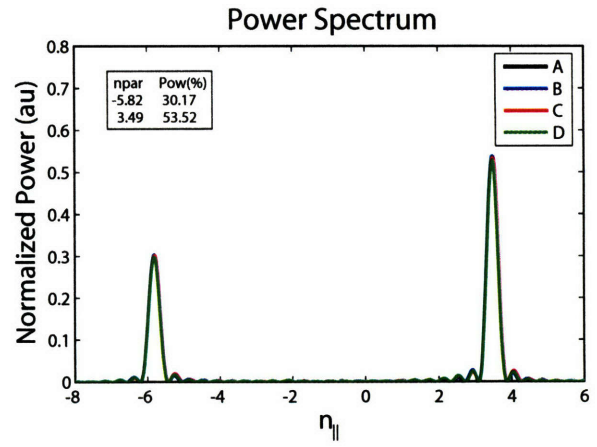
Figure A-5: Ideal spectrum for 135°.

A.2.6 150° Ideal CD

150°			
WG	ϕ_{out}	ϕ_k	PS_{pos}
1	150	145.5	3.225
2	0	145.5	
3	210	103.7	3.248
4	60	103.7	
5	270	161.7	3.259
6	120	161.7	
7	330	140.3	3.174
8	180	140.3	
9	30	72.0	3.384
10	240	72.0	
11	90	60.1	3.228
12	300	60.1	
13	150	82.4	3.397
14	0	82.4	
15	210	76.5	3.180
16	60	76.5	
17	270	64.9	
18	120	64.9	2.331
19	330	39.5	
20	180	39.5	2.331
21	30	68.2	
22	240	68.2	2.326
23	90	26.2	
24	300	26.2	2.348
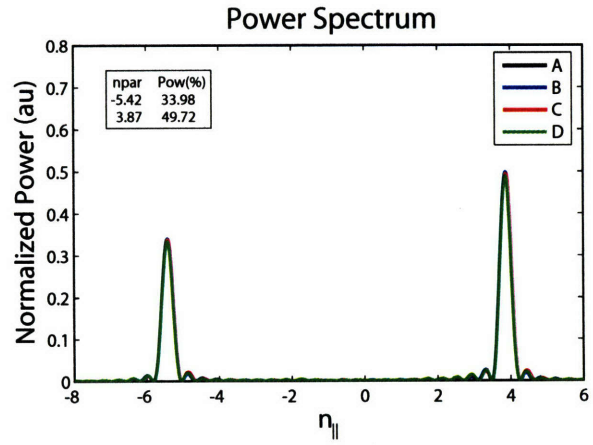
Figure A-6: Ideal spectrum for 150°.

A.2.7 180° Ideal

WG	ϕ_{out}	ϕ_k	PS_{pos}
1	180	145.5	3.320
2	0	145.5	
3	180	43.7	3.343
4	0	43.7	
5	180	41.7	3.353
6	0	41.7	
7	180	320.3	3.268
8	0	320.3	
9	180	192.0	3.478
10	0	192.0	
11	180	120.1	3.322
12	0	120.1	
13	180	82.4	3.491
14	0	82.4	
15	180	16.5	3.274
16	0	16.5	
17	180	334.9	
18	0	334.9	2.237
19	180	249.5	
20	0	249.5	2.237
21	180	218.2	
22	0	218.2	2.232
23	180	116.2	
24	0	116.2	2.254

(Table header: 180°)
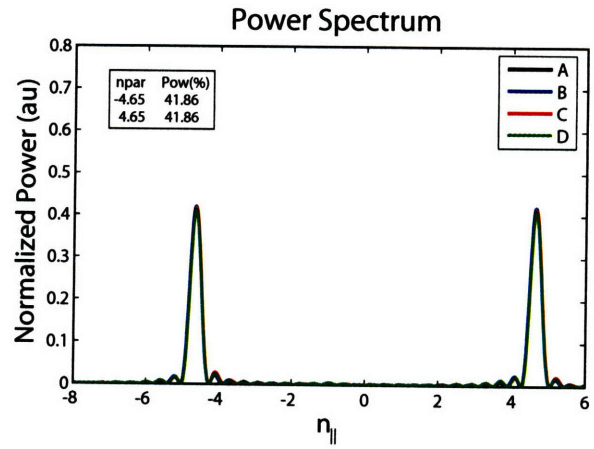
Figure A-7: Ideal spectrum for 180°.

A.3 Ideal Phasing, CCD

A.3.1 Ideal Phasing 60° and 72°, CCD

WG	ϕ_{out}	ϕ_k	PS_{pos}	WG	ϕ_{out}	ϕ_k	PS_{pos}
1	300	145.5	2.566	1	288	145.5	2.528
2	0	145.5		2	0	145.5	
3	60	163.7	2.589	3	72	187.7	2.551
4	120	163.7		4	144	187.7	
5	180	281.7	2.600	5	216	329.7	2.562
6	240	281.7		6	288	329.7	
7	300	320.3	2.514	7	0	32.3	2.477
8	0	320.3		8	72	32.3	
9	60	312.0	2.725	9	144	48.0	2.687
10	120	312.0		10	216	48.0	
11	180	0.1	2.569	11	288	120.1	2.531
12	240	0.1		12	0	120.1	
13	300	82.4	2.738	13	72	226.4	2.700
14	0	82.4		14	144	226.4	
15	60	136.5	2.521	15	216	304.5	2.483
16	120	136.5		16	288	304.5	
17	180	334.9		17	0	154.9	
18	240	334.9	2.990	18	72	154.9	3.028
19	300	9.5		19	144	213.5	
20	0	9.5	2.990	20	216	213.5	3.028
21	60	98.2		21	288	326.2	
22	120	98.2	2.985	22	0	326.2	3.023
23	180	116.2		23	72	8.2	
24	240	116.2	3.008	24	144	8.2	3.045

(Table headers: 60° | 72°)

A.3.2 Ideal Phasing 90° and 120°, CCD

90°				120°			
WG	ϕ_{out}	ϕ_k	PS_{pos}	WG	ϕ_{out}	ϕ_k	PS_{pos}
1	270	145.5	2.472	1	240	145.5	2.378
2	0	145.5		2	0	145.5	
3	90	223.7	2.495	3	120	283.7	2.401
4	180	223.7		4	240	283.7	
5	270	41.7	2.506	5	0	161.7	2.412
6	0	41.7		6	120	161.7	
7	90	140.3	2.420	7	240	320.3	2.326
8	180	140.3		8	0	320.3	
9	270	192.0	2.631	9	120	72.0	2.536
10	0	192.0		10	240	72.0	
11	90	300.1	2.475	11	0	240.1	2.381
12	180	300.1		12	120	240.1	
13	270	82.4	2.644	13	240	82.4	2.550
14	0	82.4		14	0	82.4	
15	90	196.5	2.427	15	120	256.5	2.332
16	180	196.5		16	240	256.5	
17	270	64.9		17	0	154.9	
18	0	64.9	3.084	18	120	154.9	3.179
19	90	159.5		19	240	309.5	
20	180	159.5	3.084	20	0	309.5	3.179
21	270	308.2		21	120	158.2	
22	0	308.2	3.079	22	240	158.2	3.173
23	90	26.2		23	0	296.2	
24	180	26.2	3.102	24	120	296.2	3.196

A.3.3 Ideal Phasing 135° and 150°, CCD

135°				150°			
WG	ϕ_{out}	ϕ_k	PS_{pos}	WG	ϕ_{out}	ϕ_k	PS_{pos}
1	225	145.5	2.331	1	210	115.5	2.378
2	0	145.5		2	330	115.5	
3	135	313.7	2.354	3	90	253.7	2.401
4	270	313.7		4	210	253.7	
5	45	221.7	2.365	5	330	131.7	2.412
6	180	221.7		6	90	131.7	
7	315	50.3	2.279	7	210	290.3	2.326
8	90	50.3		8	330	290.3	
9	225	192.0	2.489	9	90	42.0	2.536
10	0	192.0		10	210	42.0	
11	135	30.1	2.334	11	330	210.1	2.381
12	270	30.1		12	90	210.1	
13	45	262.4	2.502	13	210	52.4	2.550
14	180	262.4		14	330	52.4	
15	315	106.5	2.285	15	90	226.5	2.332
16	90	106.5		16	210	226.5	
17	225	19.9		17	330	124.9	
18	0	19.9	3.226	18	90	124.9	3.179
19	135	204.5		19	210	279.5	
20	270	204.5	3.226	20	330	279.5	3.179
21	45	83.2		21	90	128.2	
22	180	83.2	3.221	22	210	128.2	3.173
23	315	251.2		23	330	266.2	
24	90	251.2	3.243	24	90	266.2	3.196

A.4 Approximate Phasing, $PS = 90°$, CD

Since the phase shifters are mechanical they must be set by hand to maintain ideal phasing. During a run this means a cell access and about a 45 minute delay. To avoid this the ideal spectra may be approximated by leaving the phase shifters in a set position and adjusting the klystron phase. The most common setting is to have the phase shifters set for 90°, CD phasing. This means that the phase shifters on carts 1 and 2 are set to +90°, and −90° on cart 3. The settings are summarized below in Table A.3.

Table A.3: **Mechanical Phase Shifter Settings for Approximate Phasing, CD**

90° CD Settings											
Carts 1 and 2								Cart 3			
Column	1	3	5	7	9	11	13	15	18	20	22	24
PS_{pos}	3.037	3.060	3.071	2.985	3.196	3.040	3.209	2.992	2.519	2.519	2.514	2.537

The approximate spectra typically have less power in the primary peak with the loss increasing as the deviation from 90° phasing increases. For most cases of interest the losses are around 5%, which is acceptable given the amount of time required to set up ideal phasing. The losses become quite substantial above 135°. When heating is desired instead of current drive, the phase shifters should be adjusted since the peak power loss at 180° is much too great. Table A.4 includes the spectral information for the approximate phasings in the CD direction and is hyperlinked to both the klystron settings and the plots of the spectrum. The calculated power fractions are based upon Equation A.7.

Table A.4: **Approximate Phasing Current Drive Spectral Properties** $PS = 90°$, CD

ϕ_{aprox}	$n_\parallel$ CD	Power (%)	$n_\parallel$ CD	Power (%)	$n_\parallel$ CCD	Power (%)	$n_\parallel$ CCD	Power (%)
60	1.55	65.0			7.74	12.7		
67.5	1.75	65.7			7.54	14.5		
75	1.93	65.8			7.36	16.2		
82.5	2.13	65.3			7.16	18.0		
90 (ideal)	2.33	64.0			6.98	19.6		
97.5	2.51	62.1			6.78	21.2		
105	2.71	59.7			6.58	22.5		
112.5	2.89	56.8			6.40	23.8		
120	3.09	53.5			6.20	24.7		
127.5	3.29	49.9			6.00	25.4	1.31	7.4
135	3.47	46.0			5.82	25.9	1.13	10.5
142.5	3.67	42.0			5.62	26.0	0.95	14.0
150	3.87	37.7			5.44	25.7	0.75	18.1
157.5	4.05	33.5			5.24	25.1	0.57	22.3
165	4.25	29.3			5.04	24.1	0.37	26.9
172.5	4.43	25.3			4.85	22.9	0.17	31.6
180	0.01	36.5	4.63	21.4	4.65	21.3		

A.4.1 60° Approximate Phasing, $PS = 90°$, CD

WG	ϕ_{out}	ϕ_k
	60°	
1	90	145.5
2	0	145.5
3	330	283.7
4	240	283.7
5	210	161.7
6	120	161.7
7	90	320.3
8	0	320.3
9	330	72.0
10	240	72.0
11	210	240.1
12	120	240.1
13	90	82.4
14	0	82.4
15	330	256.5
16	240	256.5
17	210	4.9
18	120	4.9
19	90	159.5
20	0	159.5
21	330	8.2
22	240	8.2
23	210	146.2
24	120	146.2
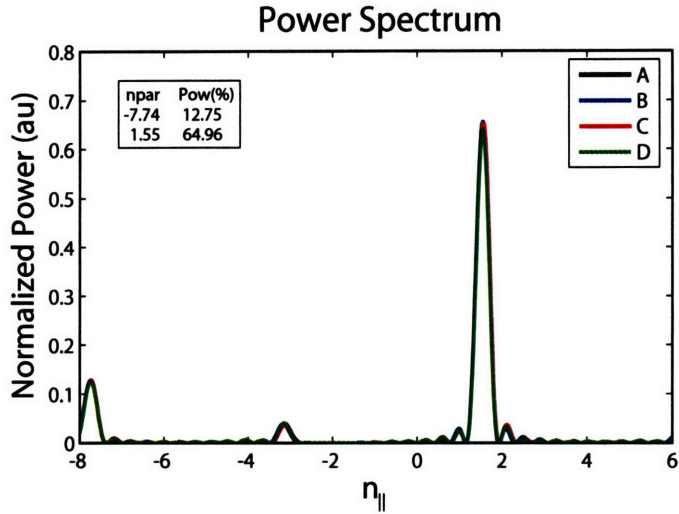
Figure A-8: Power spectrum for approximate phasing of $\phi = 60°$, which is nearly 60° ideal phasing, with about a 5% loss in peak power.

A.4.2 67.5° Approximate Phasing, $PS = 90°$, CD

WG	ϕ_{out}	ϕ_k
	67.5°	
1	90	145.5
2	0	145.5
3	315	268.7
4	225	268.7
5	180	131.7
6	90	131.7
7	45	275.3
8	315	275.3
9	270	12.0
10	180	12.0
11	135	165.1
12	45	165.1
13	0	352.4
14	270	352.4
15	225	151.5
16	135	151.5
17	90	244.9
18	0	244.9
19	315	24.5
20	225	24.5
21	180	218.2
22	90	218.2
23	45	341.2
24	315	341.2
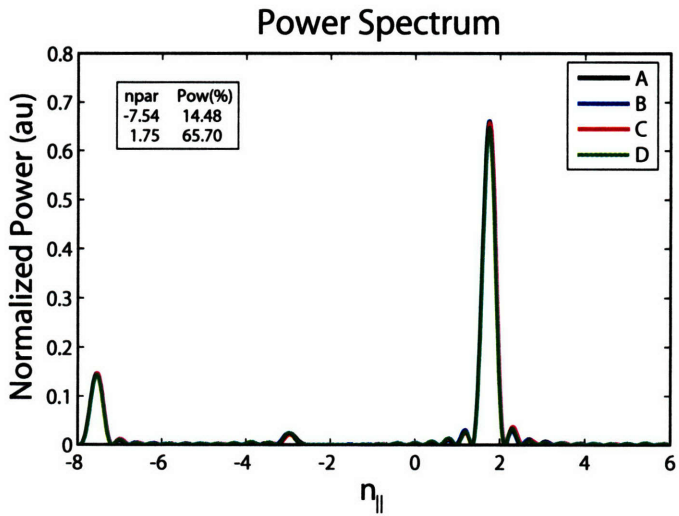
Figure A-9: Power spectrum for approximate phasing of $\phi = 67.5°$.

A.4.3   75° Approximate Phasing, $PS = 90°$, CD

75°		
WG	ϕ_{out}	ϕ_k
1	90	145.5
2	0	145.5
3	300	253.7
4	210	253.7
5	150	101.7
6	60	101.7
7	0	230.3
8	270	230.3
9	210	312.0
10	120	312.0
11	60	90.1
12	330	90.1
13	270	262.4
14	180	262.4
15	120	46.5
16	30	46.5
17	330	124.9
18	240	124.9
19	180	249.5
20	90	249.5
21	30	68.2
22	300	68.2
23	240	176.2
24	150	176.2
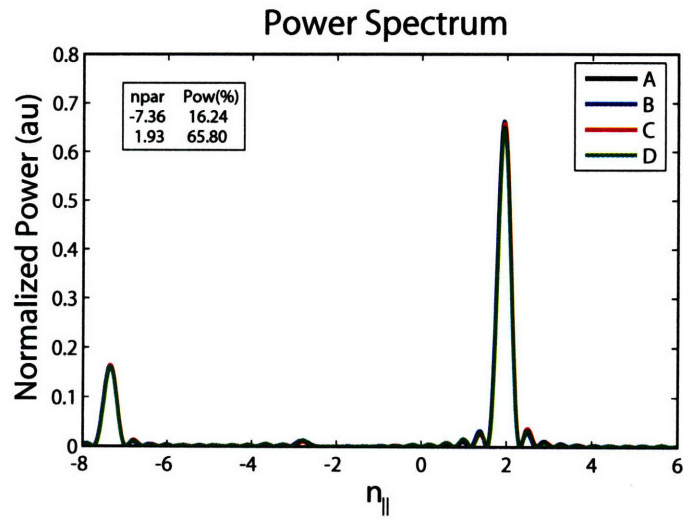
Figure A-10: Power spectrum for approximate phasing of $\phi = 75°$.

A.4.4   82.5° Approximate Phasing, $PS = 90°$, CD

82.5°		
WG	ϕ_{out}	ϕ_k
1	90	145.5
2	0	145.5
3	285	238.7
4	195	238.7
5	120	71.7
6	30	71.7
7	315	185.3
8	225	185.3
9	150	252.0
10	60	252.0
11	345	15.1
12	255	15.1
13	180	172.4
14	90	172.4
15	15	301.5
16	285	301.5
17	210	4.9
18	120	4.9
19	45	114.5
20	315	114.5
21	240	278.2
22	150	278.2
23	75	11.2
24	345	11.2
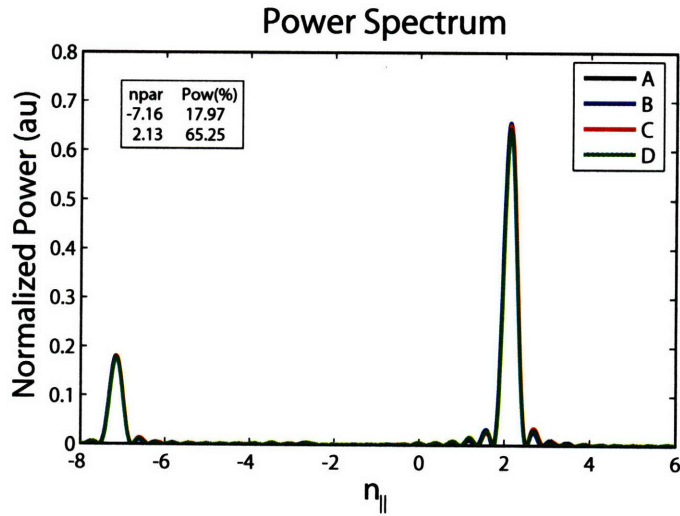
Figure A-11: Power spectrum for approximate phasing of $\phi = 82.5°$.

A.4.5   97.5° Approximate Phasing, $PS = 90°$, CD

97.5°		
WG	ϕ_{out}	ϕ_k
1	90	145.5
2	0	145.5
3	255	208.7
4	165	208.7
5	60	11.7
6	330	11.7
7	225	95.3
8	135	95.3
9	30	132.0
10	300	132.0
11	195	225.1
12	105	225.1
13	0	352.4
14	270	352.4
15	165	91.5
16	75	91.5
17	330	124.9
18	240	124.9
19	135	204.5
20	45	204.5
21	300	338.2
22	210	338.2
23	105	41.2
24	15	41.2
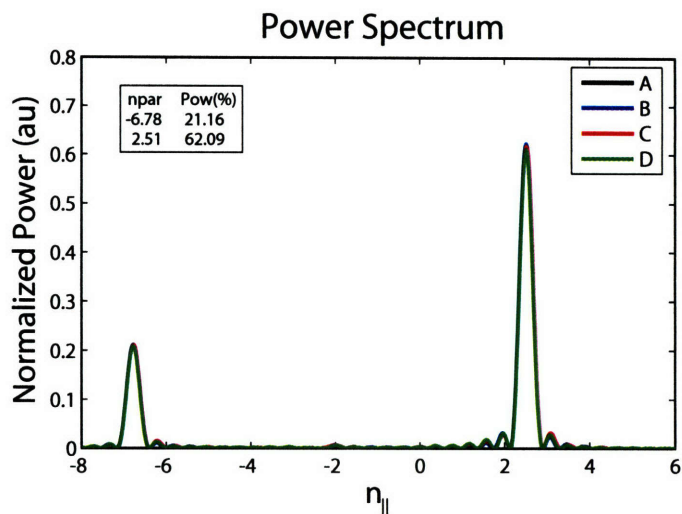
Figure A-12: Power spectrum for approximate phasing of $\phi = 97.5°$.

A.4.6   105° Approximate Phasing, $PS = 90°$, CD

105°		
WG	ϕ_{out}	ϕ_k
1	90	145.5
2	0	145.5
3	240	193.7
4	150	193.7
5	30	341.7
6	300	341.7
7	180	50.3
8	90	50.3
9	330	72.0
10	240	72.0
11	120	150.1
12	30	150.1
13	270	262.4
14	180	262.4
15	60	346.5
16	330	346.5
17	210	4.9
18	120	4.9
19	0	69.5
20	270	69.5
21	150	188.2
22	60	188.2
23	300	236.2
24	210	236.2
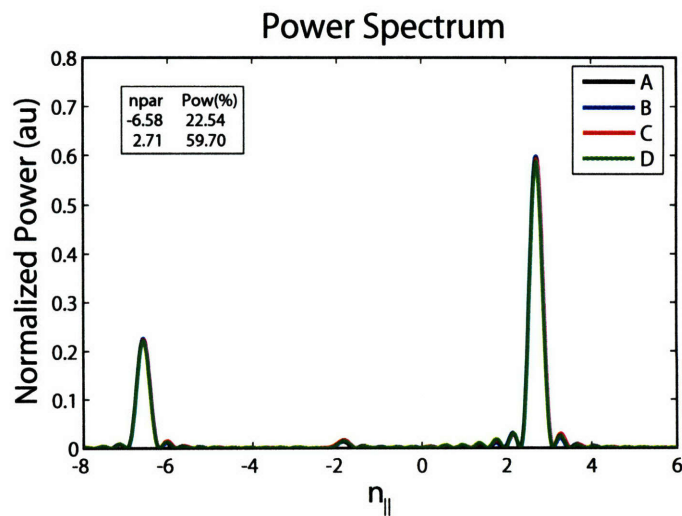
Figure A-13: Power spectrum for approximate phasing of $\phi = 105°$.

A.4.7 112.5° Approximate Phasing, $PS = 90°$, CD

112.5°		
WG	ϕ_{out}	ϕ_k
1	90	145.5
2	0	145.5
3	225	178.7
4	135	178.7
5	0	311.7
6	270	311.7
7	135	5.3
8	45	5.3
9	270	12.0
10	180	12.0
11	45	75.1
12	315	75.1
13	180	172.4
14	90	172.4
15	315	241.5
16	225	241.5
17	90	244.9
18	0	244.9
19	225	294.5
20	135	294.5
21	0	38.2
22	270	38.2
23	135	71.2
24	45	71.2
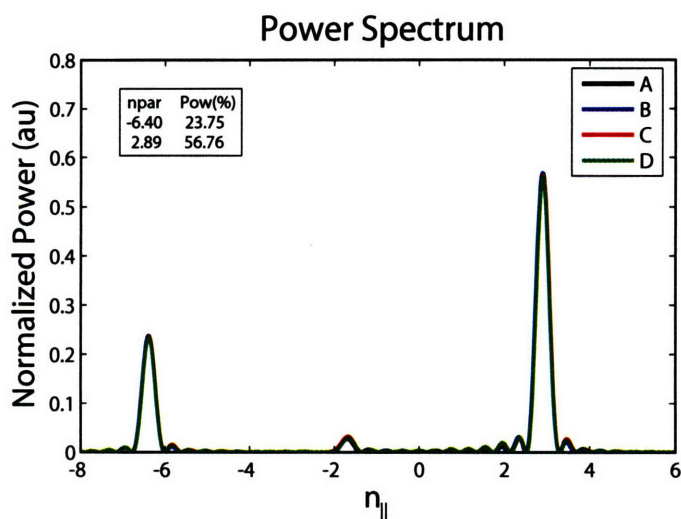
Figure A-14: Power spectrum for approximate phasing of $\phi = 112.5°$.

A.4.8 120° Approximate Phasing, $PS = 90°$, CD

120°		
WG	ϕ_{out}	ϕ_k
1	90	145.5
2	0	145.5
3	210	163.7
4	120	163.7
5	330	281.7
6	240	281.7
7	90	320.3
8	0	320.3
9	210	312.0
10	120	312.0
11	330	0.1
12	240	0.1
13	90	82.4
14	0	82.4
15	210	136.5
16	120	136.5
17	330	124.9
18	240	124.9
19	90	159.5
20	0	159.5
21	210	248.2
22	120	248.2
23	330	266.2
24	240	266.2
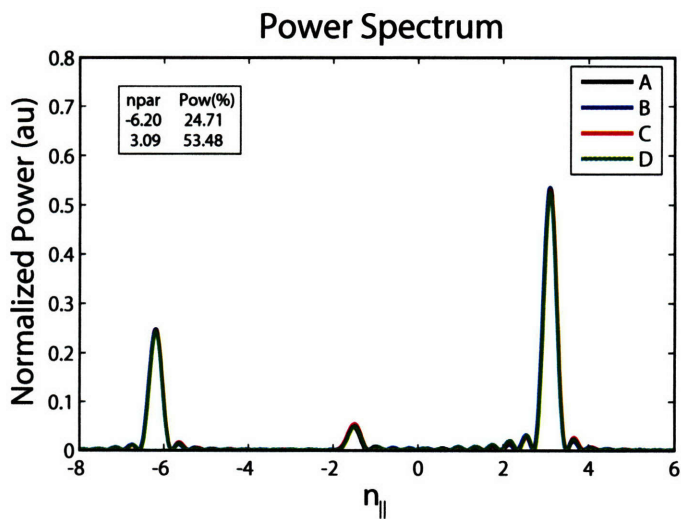
Figure A-15: Power spectrum for approximate phasing of $\phi = 120°$, which is near the ideal spectrum with a peak power loss of about 4%.

A.4.9 127.5° Approximate Phasing, $PS = 90°$, CD

127.5°		
WG	ϕ_{out}	ϕ_k
1	90	145.5
2	0	145.5
3	195	148.7
4	105	148.7
5	300	251.7
6	210	251.7
7	45	275.3
8	315	275.3
9	150	252.0
10	60	252.0
11	255	285.1
12	165	285.1
13	0	352.4
14	270	352.4
15	105	31.5
16	15	31.5
17	210	4.9
18	120	4.9
19	315	24.5
20	225	24.5
21	60	98.2
22	330	98.2
23	165	101.2
24	75	101.2
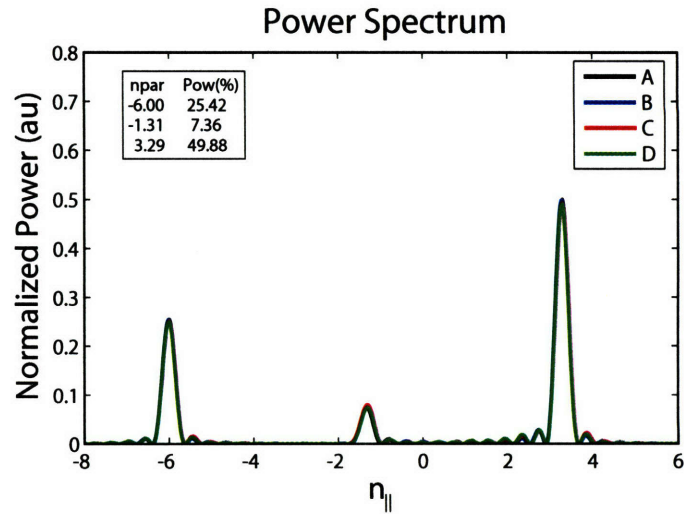
Figure A-16: Power spectrum for approximate phasing of $\phi = 127.5°$.

A.4.10 135° Approximate Phasing, $PS = 90°$, CD

135°		
WG	ϕ_{out}	ϕ_k
1	90	145.5
2	0	145.5
3	180	133.7
4	90	133.7
5	270	221.7
6	180	221.7
7	0	230.3
8	270	230.3
9	90	192.0
10	0	192.0
11	180	210.1
12	90	210.1
13	270	262.4
14	180	262.4
15	0	286.5
16	270	286.5
17	90	244.9
18	0	244.9
19	180	249.5
20	90	249.5
21	270	308.2
22	180	308.2
23	0	296.2
24	270	296.2
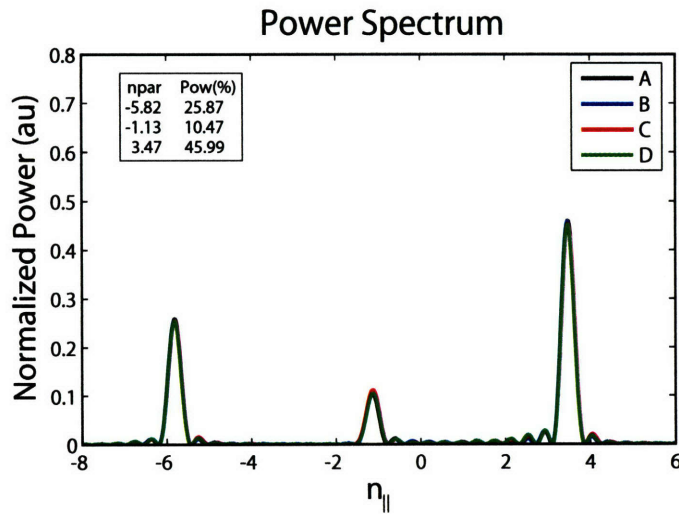
Figure A-17: Power spectrum for approximate phasing of $\phi = 135°$, which is near the ideal spectrum with a peak power loss of about 7.5%.

A.4.11   142.5° Approximate Phasing, $PS = 90°$, CD

	142.5°	
WG	ϕ_{out}	ϕ_k
1	90	145.5
2	0	145.5
3	165	118.7
4	75	118.7
5	240	191.7
6	150	191.7
7	315	185.3
8	225	185.3
9	30	132.0
10	300	132.0
11	105	135.1
12	15	135.1
13	180	172.4
14	90	172.4
15	255	181.5
16	165	181.5
17	330	124.9
18	240	124.9
19	45	114.5
20	315	114.5
21	120	158.2
22	30	158.2
23	195	131.2
24	105	131.2
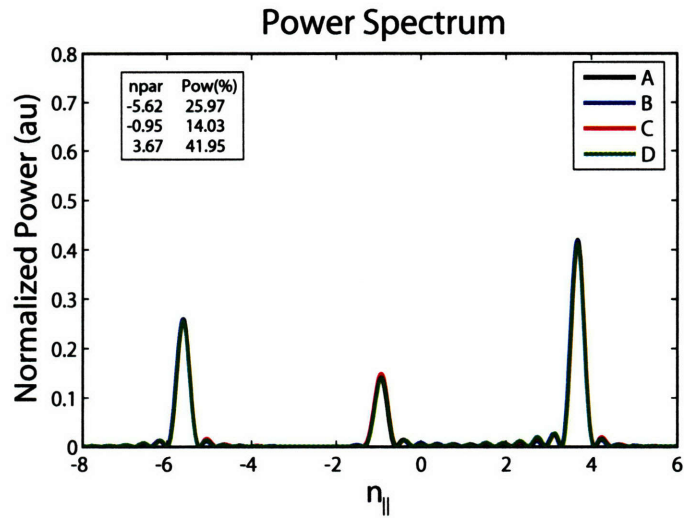
Figure A-18: Power spectrum for approximate phasing of $\phi = 142.5°$.

A.4.12   150° Approximate Phasing, $PS = 90°$, CD

	150°	
WG	ϕ_{out}	ϕ_k
1	90	145.5
2	0	145.5
3	150	103.7
4	60	103.7
5	210	161.7
6	120	161.7
7	270	140.3
8	180	140.3
9	330	72.0
10	240	72.0
11	30	60.1
12	300	60.1
13	90	82.4
14	0	82.4
15	150	76.5
16	60	76.5
17	210	4.9
18	120	4.9
19	270	339.5
20	180	339.5
21	330	8.2
22	240	8.2
23	30	326.2
24	300	326.2
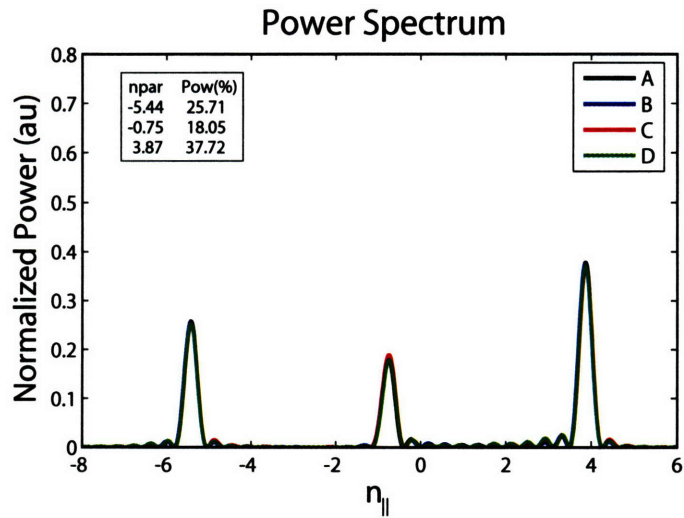
Figure A-19: Power spectrum for approximate phasing of $\phi = 150°$, which is near the ideal spectrum with a peak power loss of about 12%.

A.4.13 157.5° Approximate Phasing, $PS = 90°$, CD

WG	ϕ_{out}	ϕ_k
	157.5°	
1	90	145.5
2	0	145.5
3	135	88.7
4	45	88.7
5	180	131.7
6	90	131.7
7	225	95.3
8	135	95.3
9	270	12.0
10	180	12.0
11	315	345.1
12	225	345.1
13	0	352.4
14	270	352.4
15	45	331.5
16	315	331.5
17	90	244.9
18	0	244.9
19	135	204.5
20	45	204.5
21	180	218.2
22	90	218.2
23	225	161.2
24	135	161.2
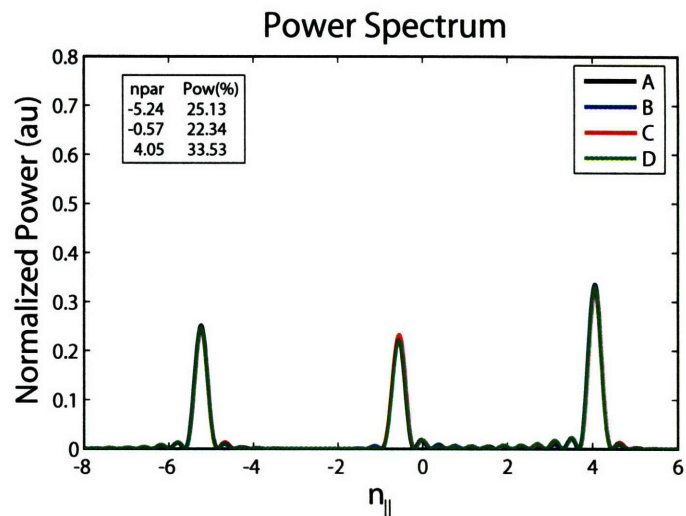
Figure A-20: Power spectrum for approximate phasing of $\phi = 157.5°$.

A.4.14 165° Approximate Phasing, $PS = 90°$, CD

WG	ϕ_{out}	ϕ_k
	165°	
1	90	145.5
2	0	145.5
3	120	73.7
4	30	73.7
5	150	101.7
6	60	101.7
7	180	50.3
8	90	50.3
9	210	312.0
10	120	312.0
11	240	270.1
12	150	270.1
13	270	262.4
14	180	262.4
15	300	226.5
16	210	226.5
17	330	124.9
18	240	124.9
19	0	69.5
20	270	69.5
21	30	68.2
22	300	68.2
23	60	356.2
24	330	356.2
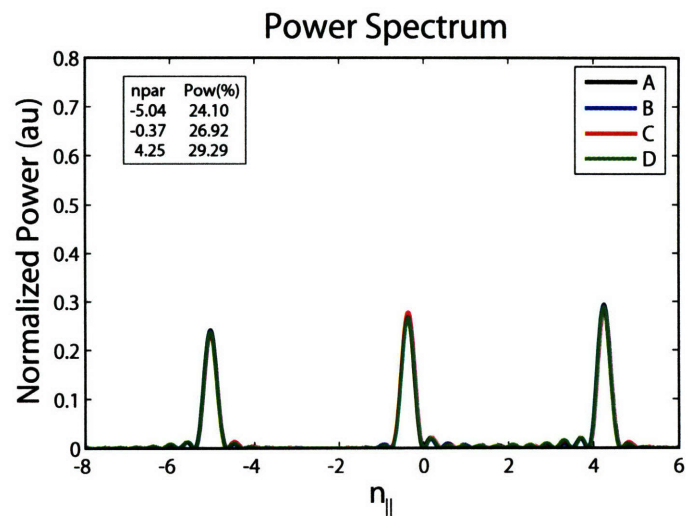
Figure A-21: Power spectrum for approximate phasing of $\phi = 165°$.

A.4.15   172.5° Approximate Phasing, $PS = 90°$, CD

172.5°		
WG	ϕ_{out}	ϕ_k
1	90	145.5
2	0	145.5
3	105	58.7
4	15	58.7
5	120	71.7
6	30	71.7
7	135	5.3
8	45	5.3
9	150	252.0
10	60	252.0
11	165	195.1
12	75	195.1
13	180	172.4
14	90	172.4
15	195	121.5
16	105	121.5
17	210	4.9
18	120	4.9
19	225	294.5
20	135	294.5
21	240	278.2
22	150	278.2
23	255	191.2
24	165	191.2
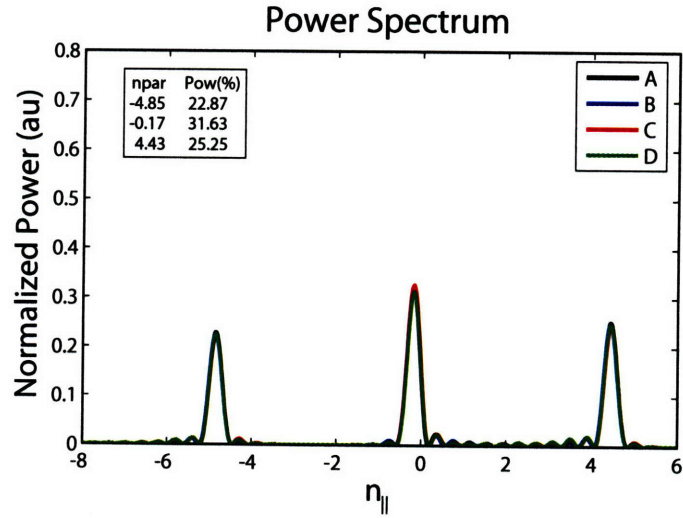
Figure A-22: Power spectrum for approximate phasing of $\phi = 172.5°$.

A.4.16   180° Approximate Phasing, $PS = 90°$, CD

180°		
WG	ϕ_{out}	ϕ_k
1	90	145.5
2	0	145.5
3	90	43.7
4	0	43.7
5	90	41.7
6	0	41.7
7	90	320.3
8	0	320.3
9	90	192.0
10	0	192.0
11	90	120.1
12	0	120.1
13	90	82.4
14	0	82.4
15	90	16.5
16	0	16.5
17	90	244.9
18	0	244.9
19	90	159.5
20	0	159.5
21	90	128.2
22	0	128.2
23	90	26.2
24	0	26.2
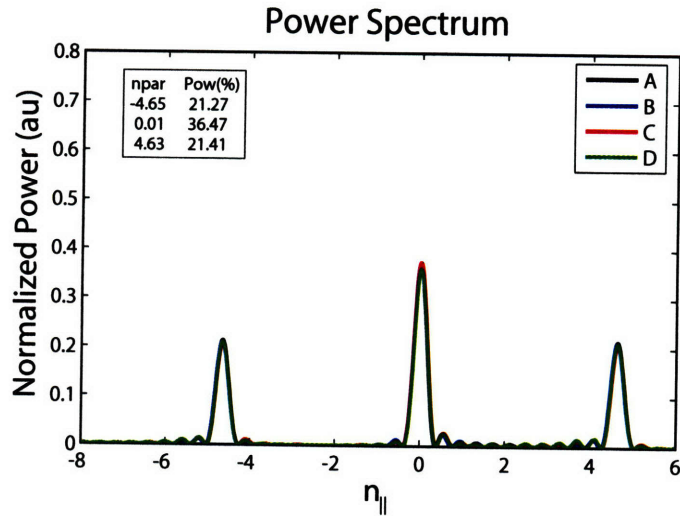
Figure A-23: Power spectrum for approximate phasing of $\phi = 180°$, about a 21% peak power loss. Change PS settings for heating.

A.5 Approximate Phasing $PS = 90°$, CCD

Approximate phasing in the CCD direction has the phase shifters set at $-90°$ on carts 1 and 2 and $+90°$ on cart 3. The settings are summarized below in Table A.5.

Table A.5: Mechanical Phase Shifter Settings for Approximate Phasing, CCD

90° CD Settings											
Carts 1 and 2								Cart 3			
Column	1	3	5	7	9	11	13	15	18	20	22	24
PS_{pos}	2.472	2.495	2.506	2.420	2.631	2.475	2.644	2.427	3.084	3.084	3.079	3.102

Sections A.5.1, A.5.2, A.5.3, and A.5.4 contain the appropriate klystron settings.

A.5.1 Approximate Phasing 60° to 82.5°, CCD

	60°			67.5°			75°			82.5°	
WG	ϕ_{out}	ϕ_k	WG	ϕ_{out}	ϕ_k	WG	ϕ_{out}	ϕ_k	WG	ϕ_{out}	ϕ_k
1	270	145.5	1	270	145.5	1	270	145.5	1	270	145.5
2	0	145.5	2	0	145.5	2	0	145.5	2	0	145.5
3	30	163.7	3	45	178.7	3	60	193.7	3	75	208.7
4	120	163.7	4	135	178.7	4	150	193.7	4	165	208.7
5	150	281.7	5	180	311.7	5	210	341.7	5	240	11.7
6	240	281.7	6	270	311.7	6	300	341.7	6	330	11.7
7	270	320.3	7	315	5.3	7	0	50.3	7	45	95.3
8	0	320.3	8	45	5.3	8	90	50.3	8	135	95.3
9	30	312.0	9	90	12.0	9	150	72.0	9	210	132.0
10	120	312.0	10	180	12.0	10	240	72.0	10	300	132.0
11	150	0.1	11	225	75.1	11	300	150.1	11	15	225.1
12	240	0.1	12	315	75.1	12	30	150.1	12	105	225.1
13	270	82.4	13	0	172.4	13	90	262.4	13	180	352.4
14	0	82.4	14	90	172.4	14	180	262.4	14	270	352.4
15	30	136.5	15	135	241.5	15	240	346.5	15	345	91.5
16	120	136.5	16	225	241.5	16	330	346.5	16	75	91.5
17	150	304.9	17	270	64.9	17	30	184.9	17	150	304.9
18	240	304.9	18	0	64.9	18	120	184.9	18	240	304.9
19	270	339.5	19	45	114.5	19	180	249.5	19	315	24.5
20	0	339.5	20	135	114.5	20	270	249.5	20	45	24.5
21	30	68.2	21	180	218.2	21	330	8.2	21	120	158.2
22	120	68.2	22	270	218.2	22	60	8.2	22	210	158.2
23	150	86.2	23	315	251.2	23	120	56.2	23	285	221.2
24	240	86.2	24	45	251.2	24	210	56.2	24	15	221.2

A.5.2 Approximate Phasing 97.5° to 120°, CCD

|	97.5°			105°			112.5°			120°	
WG	ϕ_{out}	ϕ_k	WG	ϕ_{out}	ϕ_k	WG	ϕ_{out}	ϕ_k	WG	ϕ_{out}	ϕ_k
1	270	145.5	1	270	145.5	1	270	145.5	1	270	145.5
2	0	145.5	2	0	145.5	2	0	145.5	2	0	145.5
3	105	238.7	3	120	253.7	3	135	268.7	3	150	283.7
4	195	238.7	4	210	253.7	4	225	268.7	4	240	283.7
5	300	71.7	5	330	101.7	5	0	131.7	5	30	161.7
6	30	71.7	6	60	101.7	6	90	131.7	6	120	161.7
7	135	185.3	7	180	230.3	7	225	275.3	7	270	320.3
8	225	185.3	8	270	230.3	8	315	275.3	8	0	320.3
9	330	252.0	9	30	312.0	9	90	12.0	9	150	72.0
10	60	252.0	10	120	312.0	10	180	12.0	10	240	72.0
11	165	15.1	11	240	90.1	11	315	165.1	11	30	240.1
12	255	15.1	12	330	90.1	12	45	165.1	12	120	240.1
13	0	172.4	13	90	262.4	13	180	352.4	13	270	82.4
14	90	172.4	14	180	262.4	14	270	352.4	14	0	82.4
15	195	301.5	15	300	46.5	15	45	151.5	15	150	256.5
16	285	301.5	16	30	46.5	16	135	151.5	16	240	256.5
17	30	184.9	17	150	304.9	17	270	64.9	17	30	184.9
18	120	184.9	18	240	304.9	18	0	64.9	18	120	184.9
19	225	294.5	19	0	69.5	19	135	204.5	19	270	339.5
20	315	294.5	20	90	69.5	20	225	204.5	20	0	339.5
21	60	98.2	21	210	248.2	21	0	38.2	21	150	188.2
22	150	98.2	22	300	248.2	22	90	38.2	22	240	188.2
23	255	191.2	23	60	356.2	23	225	161.2	23	30	326.2
24	345	191.2	24	150	356.2	24	315	161.2	24	120	326.2

A.5.3 Approximate Phasing 127.5° to 150°, CCD

	127.5°			135°			142.5°			150°	
WG	ϕ_{out}	ϕ_k	WG	ϕ_{out}	ϕ_k	WG	ϕ_{out}	ϕ_k	WG	ϕ_{out}	ϕ_k
1	270	145.5	1	270	145.5	1	270	145.5	1	270	145.5
2	0	145.5	2	0	145.5	2	0	145.5	2	0	145.5
3	165	298.7	3	180	313.7	3	195	328.7	3	210	343.7
4	255	298.7	4	270	313.7	4	285	328.7	4	300	343.7
5	60	191.7	5	90	221.7	5	120	251.7	5	150	281.7
6	150	191.7	6	180	221.7	6	210	251.7	6	240	281.7
7	315	5.3	7	0	50.3	7	45	95.3	7	90	140.3
8	45	5.3	8	90	50.3	8	135	95.3	8	180	140.3
9	210	132.0	9	270	192.0	9	330	252.0	9	30	312.0
10	300	132.0	10	0	192.0	10	60	252.0	10	120	312.0
11	105	315.1	11	180	30.1	11	255	105.1	11	330	180.1
12	195	315.1	12	270	30.1	12	345	105.1	12	60	180.1
13	0	172.4	13	90	262.4	13	180	352.4	13	270	82.4
14	90	172.4	14	180	262.4	14	270	352.4	14	0	82.4
15	255	1.5	15	0	106.5	15	105	211.5	15	210	316.5
16	345	1.5	16	90	106.5	16	195	211.5	16	300	316.5
17	150	304.9	17	270	64.9	17	30	184.9	17	150	304.9
18	240	304.9	18	0	64.9	18	120	184.9	18	240	304.9
19	45	114.5	19	180	249.5	19	315	24.5	19	90	159.5
20	135	114.5	20	270	249.5	20	45	24.5	20	180	159.5
21	300	338.2	21	90	128.2	21	240	278.2	21	30	68.2
22	30	338.2	22	180	128.2	22	330	278.2	22	120	68.2
23	195	131.2	23	0	296.2	23	165	101.2	23	330	266.2
24	285	131.2	24	90	296.2	24	255	101.2	24	60	266.2

A.5.4 Approximate Phasing 157.5° to 172.5°, CCD

	157.5°			165°			172.5°	
WG	ϕ_{out}	ϕ_k	WG	ϕ_{out}	ϕ_k	WG	ϕ_{out}	ϕ_k
1	270	145.5	1	270	145.5	1	270	145.5
2	0	145.5	2	0	145.5	2	0	145.5
3	225	358.7	3	240	13.7	3	255	28.7
4	315	358.7	4	330	13.7	4	345	28.7
5	180	311.7	5	210	341.7	5	240	11.7
6	270	311.7	6	300	341.7	6	330	11.7
7	135	185.3	7	180	230.3	7	225	275.3
8	225	185.3	8	270	230.3	8	315	275.3
9	90	12.0	9	150	72.0	9	210	132.0
10	180	12.0	10	240	72.0	10	300	132.0
11	45	255.1	11	120	330.1	11	195	45.1
12	135	255.1	12	210	330.1	12	285	45.1
13	0	172.4	13	90	262.4	13	180	352.4
14	90	172.4	14	180	262.4	14	270	352.4
15	315	61.5	15	60	166.5	15	165	271.5
16	45	61.5	16	150	166.5	16	255	271.5
17	270	64.9	17	30	184.9	17	150	304.9
18	0	64.9	18	120	184.9	18	240	304.9
19	225	294.5	19	0	69.5	19	135	204.5
20	315	294.5	20	90	69.5	20	225	204.5
21	180	218.2	21	330	8.2	21	120	158.2
22	270	218.2	22	60	8.2	22	210	158.2
23	135	71.2	23	300	236.2	23	105	41.2
24	225	71.2	24	30	236.2	24	195	41.2

Appendix B

Lower Hybrid Phase Control and Analysis Tools

A number of utilities were developed to both control the LH system and display the results. This appendix covers information on how to use each utility.

B.1 Controlling the Phase of the LH Antenna

A Matlab GUI interface, *ConditioningSetpointsGenerator*, or CSG, creates the set points used to control the each klystron's amplitude and phase. This file is located in */home/lha/ConditioningSetpointGenerator*. Its use is best described by going through each screen as if setting up for an actual shot. Running the program opens the main control window shown in Figure B-1. The primary settings are the shot length, duty cycle, and pulse period. The shot length is the total amount of time for the shot. The duty cycle is the percentage of each segment that the LH power is actually on, while the pulse period is the segment length. The number of segments is just the shot length divided by the pulse period. Looking at the settings shown in Figure B-1 gives four 50 ms LH pulses with a 50 ms spacing. The actual time during the plasma discharge when the LH fires is set by an IDL GUI interface called *lhcosy*, which will not be discussed here.
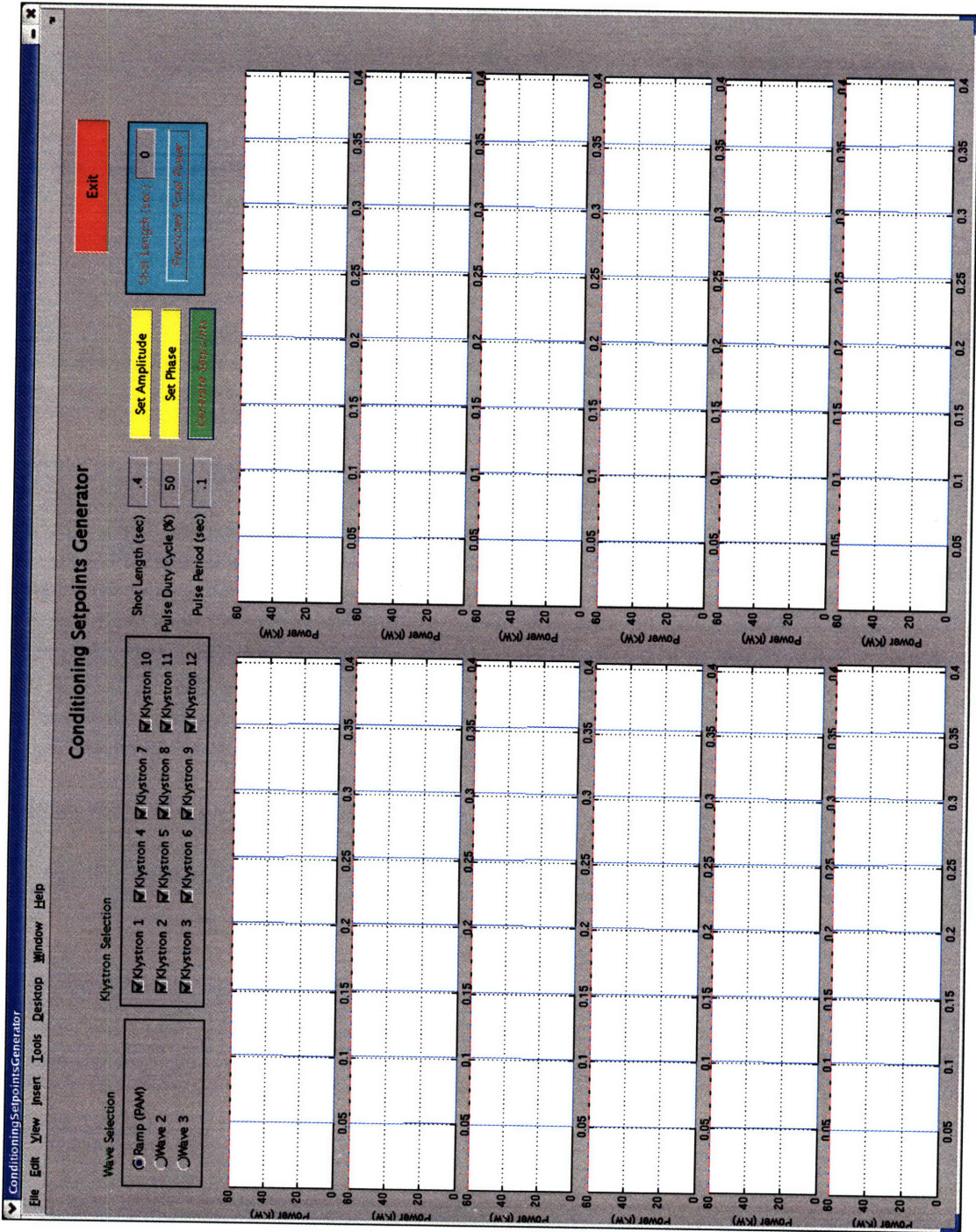
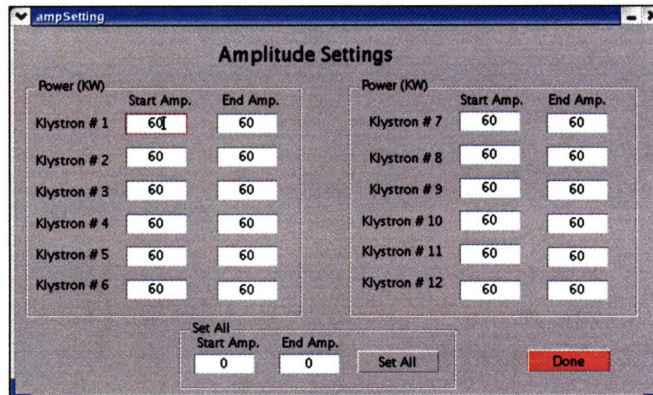Figure B-1: Screen capture from the main window of the CSG GUI.

Figure B-2: Screen capture from set amplitude window of the CSG GUI.

Clicking the *Set Amplitude* button brings up a window where the amplitudes may be set for individual klystrons as shown in Figure B-2. The power may be set as either a box function or a ramp for each klystron by specifying the starting and ending amplitudes in kW over the shot length. In this example a constant 60 kW is desired from each klystron. This power is what is asked for at the intermediate directional coupler, the power at the source will be higher due to waveguide losses. Clicking done closes the window and returns the user to the main CSG interface.

The phase for each segment is set by clicking on the *Set Phase* button, which brings up the set phase window shown in Figure B-3. Here the user selects whether the waves are to be launched in the CD or CCD direction and inputs the mechanical phase shifter setting. Here the CD direction is selected and the phase shifters are set to 90°, meaning that ideal phasing will be achieved when the klystrons are set for 90° phasing and that all other klystron phase setting will result in approximate spectra being produced. Now pushing the *Set Segments* button brings up another window which displays the number of segments available and allows the user to set the phase for each segment. Figure B-4 shows the window and that the four segments have been set to 60°, 90°, 120° and then back to 90°. Clicking done closes this window and returns the user to the set phase window. Pushing *Generate Phase* calls a Matlab script *nspectrumgui* which calculates the klystron and phase shifter settings for each segment. The results are displayed in the table and plot of the desired output spectrum. The *Plot Segment* button displays the settings and spectrum for the desired segment number from the edit box above.

Clicking done closes the set phase window and returns the user to the main CSG interface. Now selecting each klystron's check box activates the klystron and pushing *Generate Setpoints* takes the phase and amplitude inputs and makes the setpoints needed to control the klystron output at each point in time. The setpoints formed will be used until the CSG is used again to change them.

B.2   Analysis Tools

A number of analysis tools were developed to visualize the large amounts of data produced by the LH system. Three linked Matlab GUI interfaces display power and phase
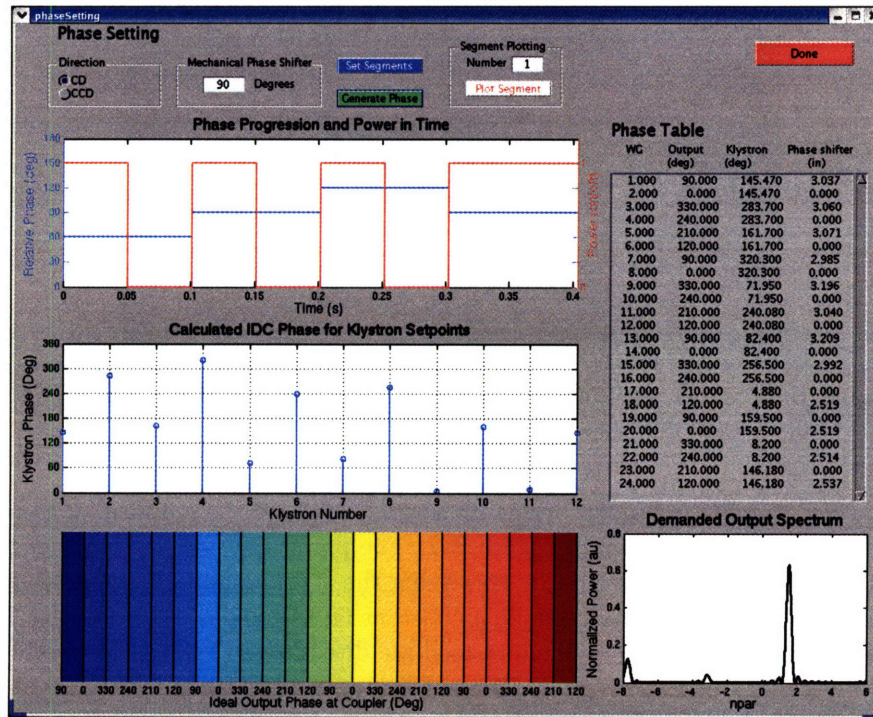
Figure B-3: Screen capture from the set phase window of the CSG GUI.
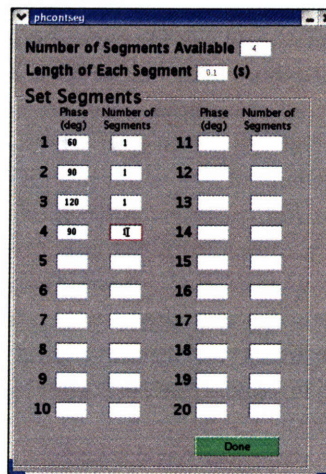
Figure B-4: Screen capture of the set segments window.

data, coupling data, and HXR results. A Matlab routine *lhpost*, gathers data, processes it and writes the results back to the LH tree. *lhpost* also generates the coupled power and reflection coefficient time traces, which may be displayed on scopes. To calculate the coupled power accurately, all signals must be accounted for, and since the LH system has hundreds of channels some may not to be working. Typically the broken channels are identified and set to an average value, and once signals are repaired they may be used again in calculations. This does, however, require current knowledge about what is and is not working and needs to be updated regularly. The GUIs are located in the */home/jliptac/matlab/lhgui* directory.

B.2.1 LH Analysis GUI

The segment phase control allows time varying quantities such as the klystron amplitude and phase to be averaged over the segment width and displayed. The *lhanalysis* GUI compares the demanded and delivered power and phase, as well as displaying the resulting spectrum and is shown in Figure B-5.
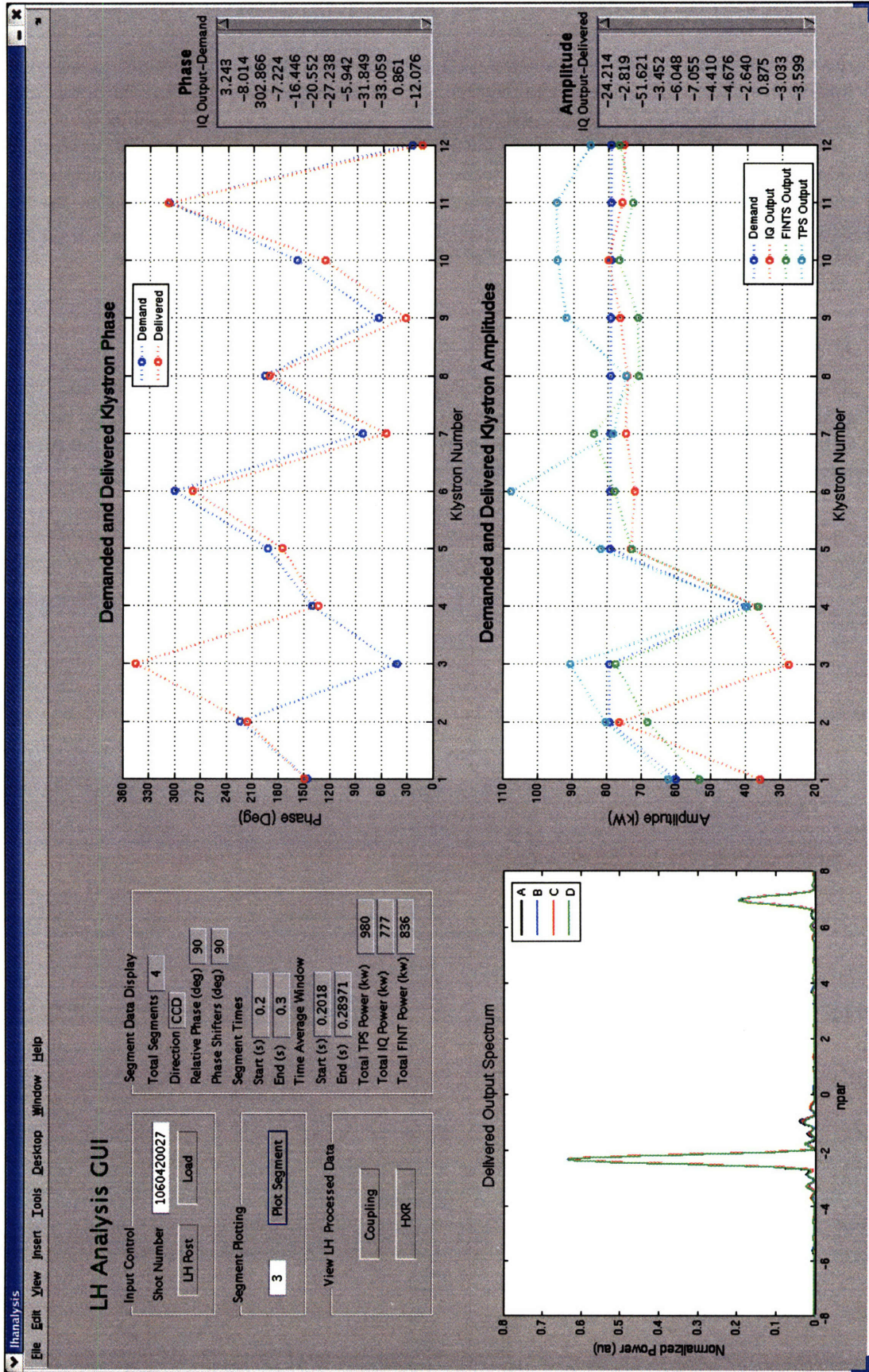
Figure B-5: Screen capture from the LH analysis GUI used to organize and display amplitude and phase data. The top right panel plots the demanded and delivered phases. The bottom left panel shows the resulting output spectrum using Equation A.7.

The segment data display panel contains a number of text boxes that summarize the main results for each segment such as the phase and direction used, number of segments, time windows used for the analysis, and total power as measured by the TPS, FINT, and IQ detectors. The data may also be plotted for each segment using the *Plot Segment* button. *lhpost* may also be run from this interface, as well as bringing up the coupling and HXR GUIs by clicking on the appropriate button.

B.2.2 Coupling GUI

With 22 columns and 4 rows there are 88 jungle gym signals and 176 probe signals, which is a tremendous amount of information to digest. A GUI interface was written to help manage, display, and understand the data in a timely manner. A screen capture from the GUI for the 90° segment of shot 1060413027 is shown in Figure B-6. Each plot panel represents a coupler row, A through D from top to bottom. All data plotted was averaged over the segment length in time. The forward and reverse directions are defined to be toward and away from the plasma.

Similar to the *lhanalysis* GUI, the panel on the left contains the most important summary information such as the calculated reflection coefficient and average probe density. Relevant total powers are displayed in the text boxes to the right of each plot for a given row.
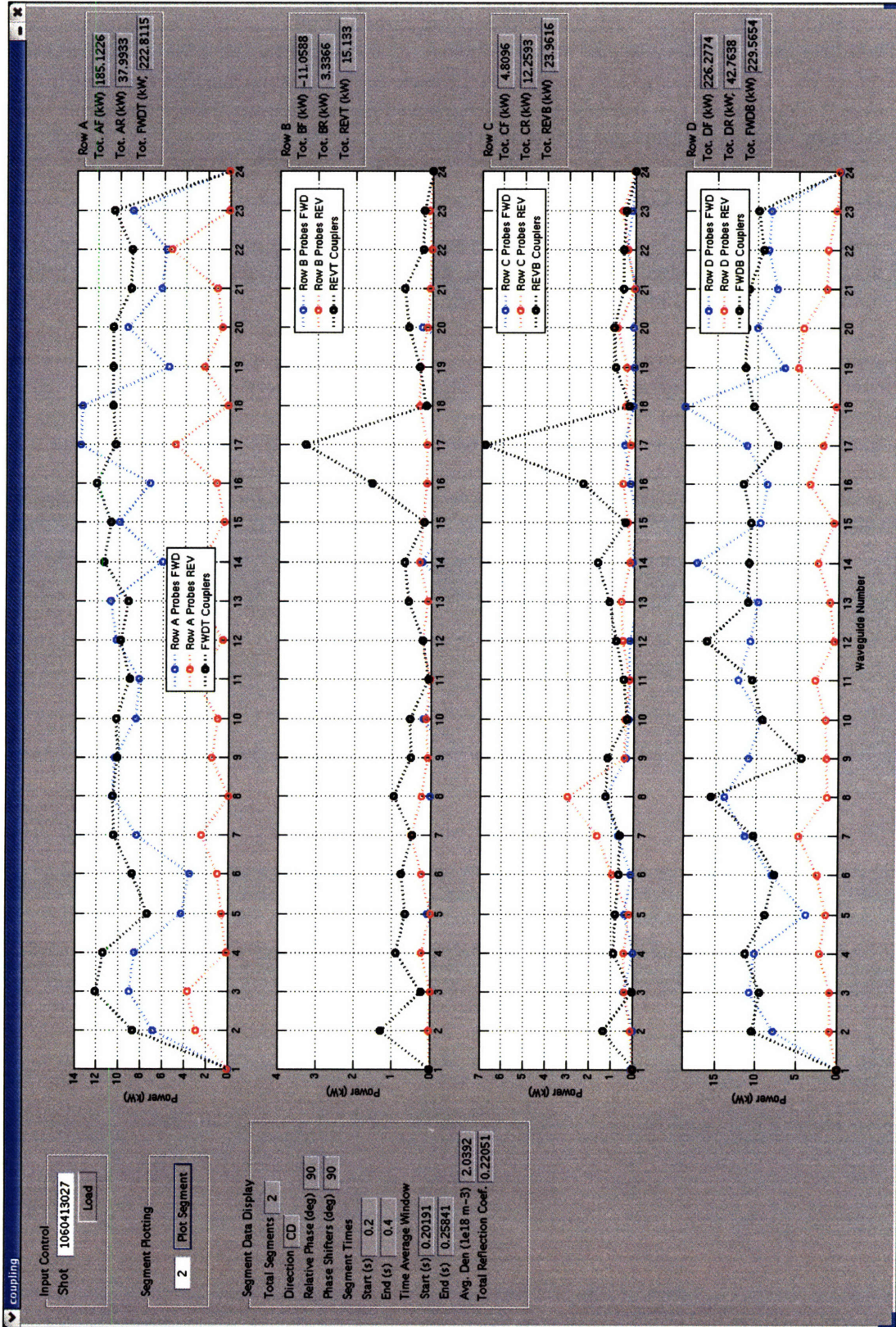
Figure B-6: Screen capture from the Coupling GUI used to organize and display forward and reflected power data. Each panel represents the measurements made for a given row of the antenna. Rows A through D are displayed in the top to bottom panels.

B.2.3 HXR GUI

A number of functions are available on the HXR GUI in addition to the ability to display data. The pulse processing and PHA processing routines may be run from the interface. Processing options for both may be input by the user for a given shot. A screen capture of the interface is shown in Figure B-7.

The top panel displays either the count rate in time or the count rate vs channel number. The bottom panel displays PHA results. The top panel display is controlled by radio buttons and the arrow buttons in the plot control panel. Selecting the radio buttons in the plot control panel switches the function of the arrow buttons, between channel number, energy bin, and time bin. Clicking a right arrow steps the quantity forward and displays the results. A left arrow steps the quantity backward.
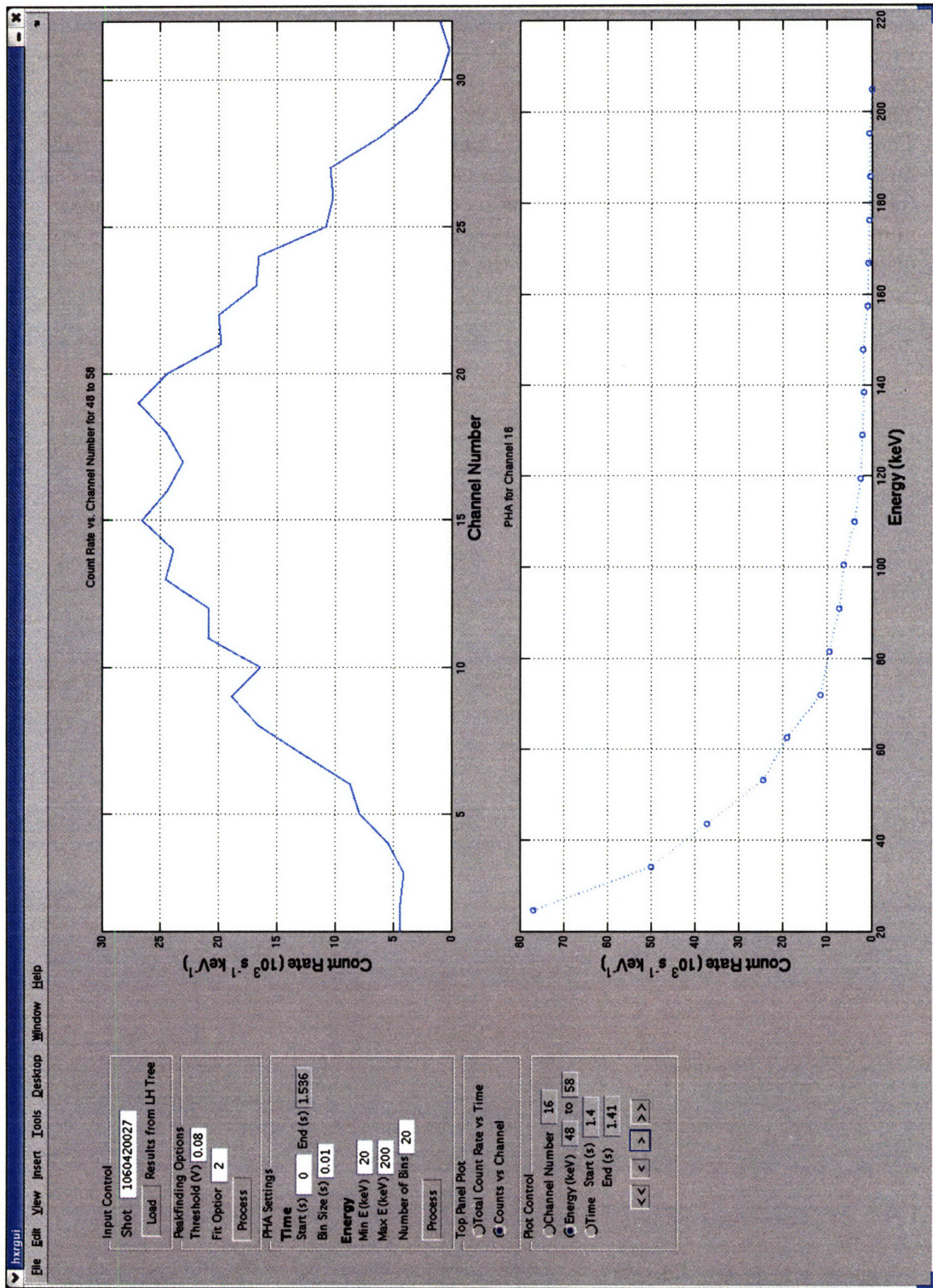
Figure B-7: Screen capture from the HXR GUI used to process and display HXR data.

Appendix C

Running FP and Coupling Codes

A number of modeling codes were used to predict and analyze experimental outcomes. Information about running DKE and the coupling code is summarized in this appendix.

C.0.4   Running DKE

Running DKE is facilitated by a number of wrapper functions which gather and prepare the required data. The primary wrapper function is *makerun*, which calls all the make files and then calls the *rundke* to start the solver. DKE uses *.mat* files, the native store format of Matlab, to save inputs for a given run. Each make file generates a single variable, a structure, containing the data. The operational flow is described pictorially in Figure C-1. *make_equil* is central to running DKE and even for running some of the other make files. EFIT data from C-Mod is used to reconstruct the flux surfaces and transform them into DKE's coordinate system. *make_equil* also takes in the electron temperature and density profiles as well as the Z_{eff} profile.

Kirill Zhorovich's IDL fitting routines are typically used to generate smooth profiles. Kirill's programs combine the density measurements from the core and edge Thomson systems and fit them into a smooth profile. The temperature is handled in a similar manner, but takes into account ECE data as well. Kirill's program also generates a Z_{eff} profile combining the Thomson data with the visible bremsstrahlung measurement. The resulting profile may or may not be useful as an input to DKE. If an unrealistic profile is produced, Z_{eff} is taken to be flat, at reasonable value.

make_equil also generates profiles for the background ions. Typically $T_i = T_e$, and the ion density is calculated from a simple model using Z_{eff} and the electron density profile assuming quasi-neutrality.

make_dkeparam creates the input parameters for the numerics of the calculation. The most important parameters are the drop tolerance and the grid size that the calculation is done on. Both parameters have a large impact on the time it takes to run the calculation. The drop tolerance, *dkeparam.param1_inv*, forces all matrix elements below the input value to zero, making the matrix more sparse and reducing the inversion time. The grid size is set by *dkeparam.nmhu_S*, *dkeparam.np_S*, and *dkeparam.pnmax_S*, which are respectively the, angular, momentum, and spatial grid sizes.

make_display controls the display options for running DKE. *make_ohm* and *make_transpfaste* contain user specified models for the ohmic electric field and the fast electron diffusion coefficient.

makerun

make_equil

equil.mat=magnetic equilibrium
n_e, T_e, and Z_{eff} profiles

make_dkeparam

dkeparam.mat=DKE run parameters:
drop tolerance, grid
size, etc

make_display

display.mat=output display options

equil.mat → make_ohm

ohm.mat=ohmic electric field model

equil.mat → make_transpfaste

transpfaste.mat=fast electron transport model

make_hxr

hxr.mat=hxr simulation parameters:
geometry, absorbers, etc

equil.mat → make_wave

wave.mat=wave parameters:
frequency, ray information
D_{ql}, velocity extent, etc

equil.mat, dkeparam.mat,
display.mat, ohm.mat,
transpfaste.mat, wave.mat → rundke → main_dke_yp

calls many functions, most importantly
dke_1_4yp, which is the main workhorse
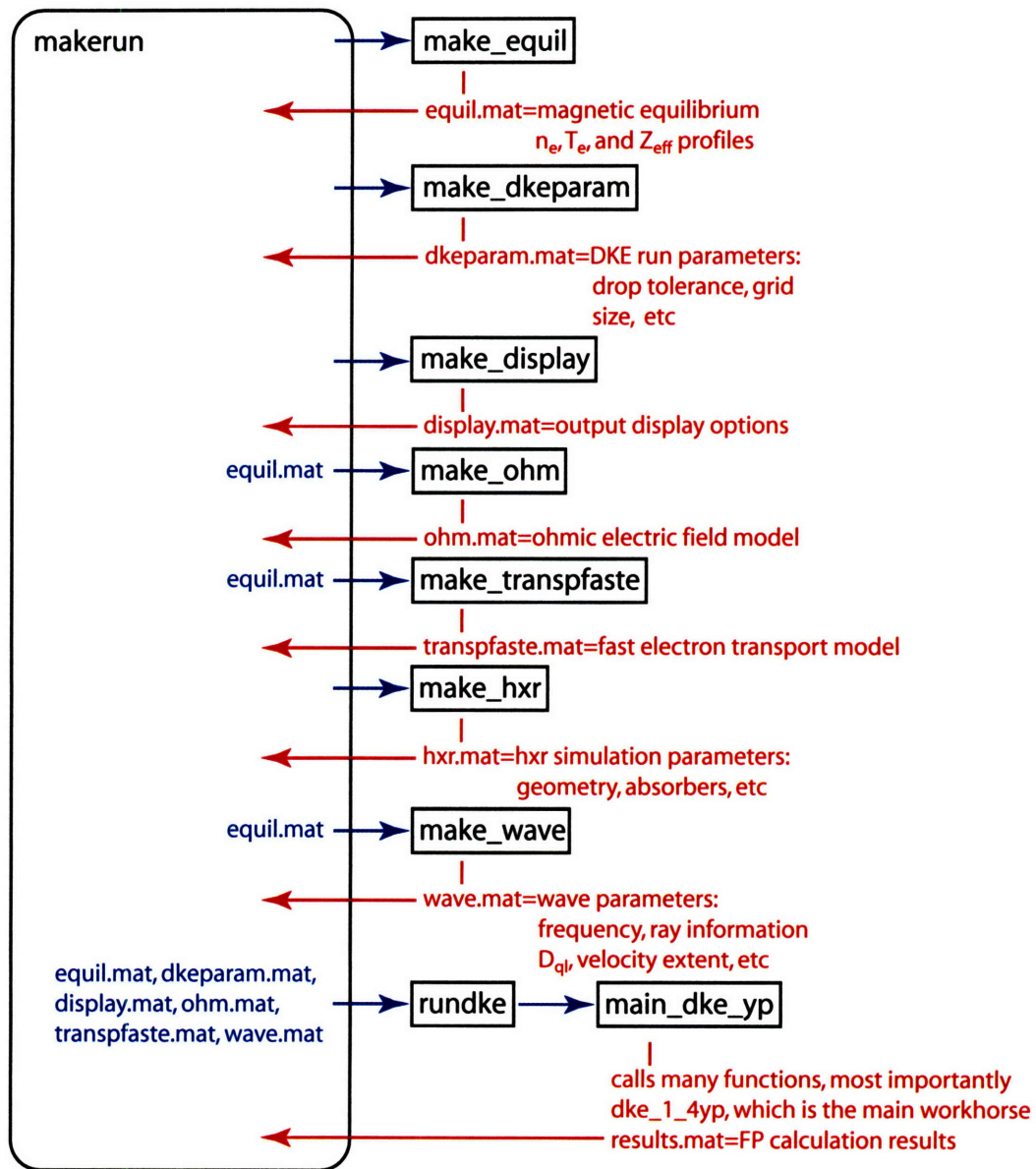results.mat=FP calculation results

Figure C-1: Operational flow for running DKE.

make_hxr contains all the information about the HXR diagnostic, such as geometry, detector type, and any absorbers used, including the vacuum window. The data is not used in the kinetic calculation, but just stored for later use in the bremsstrahlung model. *make_wave* is where all the wave information is input, whether it be for electron cyclotron waves or lower hybrid. For simple LHCD modeling a boxcar shape is entered by the user for D_{ql}, which includes the width and magnitude. The spatial extent of the wave damping is also input by the user. This produces an artificial way to control the important parameters without ray tracing. *yD0_in_c_lh* is the D_{ql} level. *ypeak_lh* and *ywidth_lh* are the peak location and width of the damping region. If DKE is coupled to a ray tracing program, this file would also contain all the ray information such as $n_\parallel$, $n_\perp$, and the power in each ray.

The actual calculation begins with a call to *dkerun*, which loads all the save files and calls *main_dke_yp*. The kernel of the code is in the file *dke_1_4yp*. All the results are also saved in a *.mat* formatted file and can be viewed easily with the program *display_dke_yp*.

C.0.5 Bremsstrahlung Emission Package

Running the simulation for HXR emission requires the kinetic results save file and the HXR system parameter make file. Once these files have been generated running the program *display_hxr_yp* guides the user through the rest of the process. The control flow for *display_hxr_yp* is shown in Figure C-2, and shows the required physics modules used. *display_hxr_yp* first loads the kinetic data and HXR parameters and then calls *bremchord_dke_yp*, which calculates the chord position in the plasma, maps to flux surfaces, interpolates, and calculates the positions where the distribution function is evaluated. *bremsstrahlung_dke_yp* takes the results from *bremchord_dke_yp* along with the equilibrium data and HXR parameters to calculate the plasma bremsstrahlung emission along each chord as well as the 4π emission. The cross sections for the calculation are generated by two functions, *bhe_dke_yp* for electron-ion emission, and *haug_dke_yp* for electron-electron emission. The cross sections are projected onto Legendre polynomials to reduce the number of integrations needed. *bhe_dke_yp* uses the Bethe-Heitler model including the Elwart factor. *haug_dke_yp* uses the Haug model and includes the Coulomb factor.

The final function, *bremdiag_dke_yp*, takes in the plasma emission results and calculates what each chord should see given the detector response function, *dresp_dke_yp*, and taking into account the absorption efficiency of the detectors including vacuum windows and other absorbers in *absx_dke_yp*. The results of *bremdiag_dke_yp* allow direct comparison of the experimental results to the model of the distribution function.

C.0.6 Running the Brambilla Code

The Brambilla code, written in Fortran, solves the system of equations described in Chapter 7 and generates $n_\parallel$ spectra and reflection coefficient information. The code input and output was modified extensively. A namelist input was developed and the output was changed to a text file that may easily be read by Matlab or IDL for analysis. The code now accepts arrays of arbitrary phase, and linearly scans parameters. Computing results for an arbitrary phase is important given that much of the time C-Mod's antenna phasing is not constant from column to column.

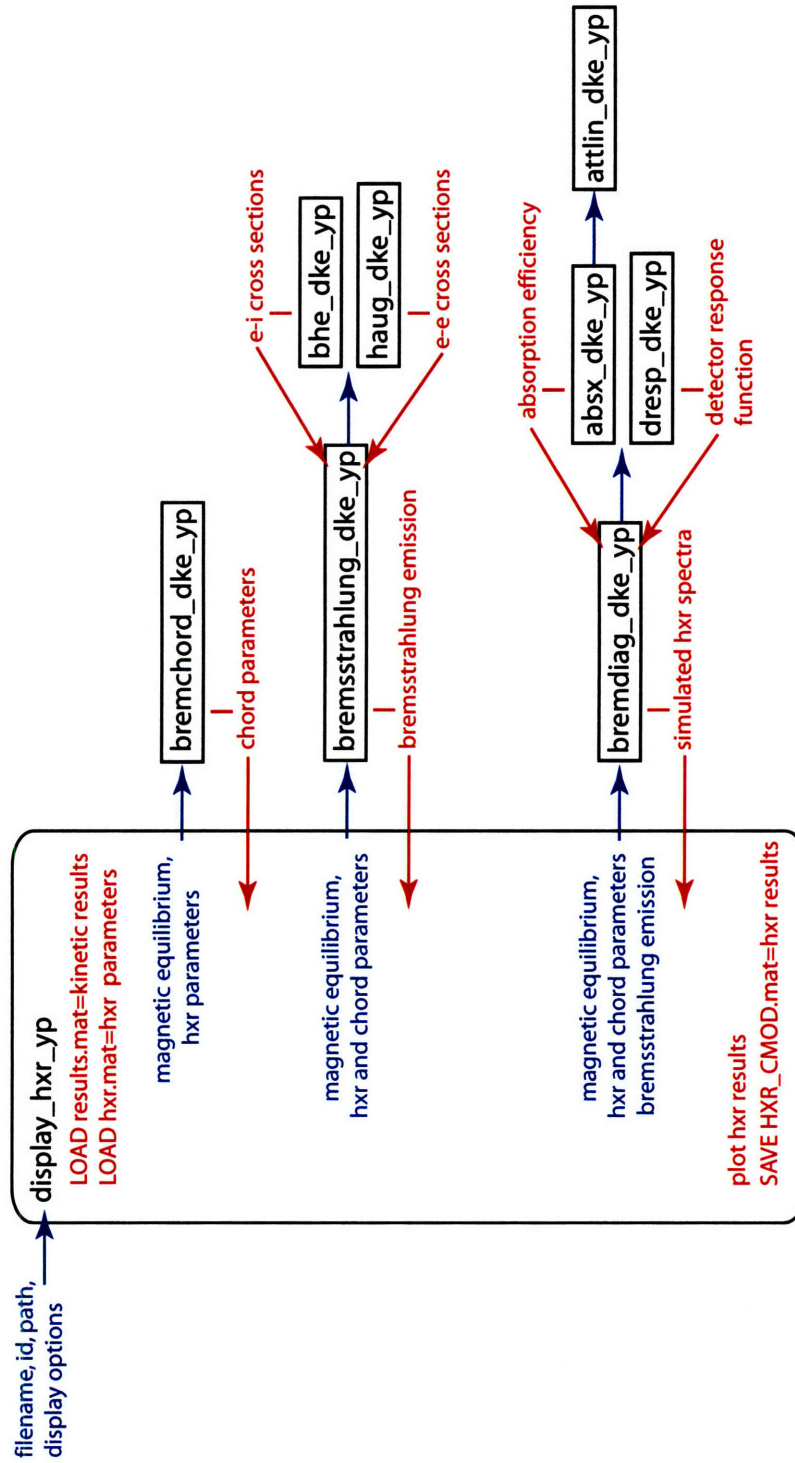The code itself exists on the *Marshall* theory cluster in directory

Figure C-2: Operational flow for HXR emission simulation. Functional list is not comprehensive, but includes all the relevant physics modules.

/u/jliptac/codes/brambilla. A compiled and compressed version also exists on the C-Mod workstations in */home/jliptac/codes/brambilla*. Each location contains the old version of the code before these changes were made as well. The code was compiled using the Lahey/Fujitsu 95 on *Marshall* producing the executable file *xbram*. The input namelist *grilnl.dat* contains all the important parameters for running the simulation: the grill geometry, plasma parameters, and arbitrary phase settings. The output file, *grill.out* is a comma delimited text file, formatted for easy machine and human reading. The file contains the reflection coefficient for each column and $n_\parallel$ spectrum for each set of parameters used. This version was used to quickly produce the sensitivity study results of Chapter 7.

A second version of the coupling code was developed for comparison with experimental data. All four rows of the grill are modeled and amplitude arrays may be input as well. The executable is *xbramc* with namelist file *bramnl.dat* and output file *bram.out*.

Bibliography

[1] John Wesson. *Tokamaks*. The International Series of Monographs on Physics, 118. Oxford University Press, third edition, January 2004.

[2] F. Najmabadi. Assessment of tokamak plasma operation modes as fusion power plants -the starlite study. Proceedings of the 16th IAEA Conference on Fusion Energy, Montreal, October 1996.

[3] I.H. Hutchinson et al. The U.S. advanced tokamak fusion science program. AT White Paper, May 1999.

[4] C. Kessel et al. Improved plasma performance in tokamaks with negative magnetic shear. *Physical Review Letters*, 72(8):1212–1215, February 1994.

[5] R.J. Goldston. Physics of the steady state advanced tokamak. *Physics of Plasmas*, 3(5):1794, May 1996.

[6] T.S. Taylor. Physics of advanced tokamaks. *Plasma Physics and Controlled Fusion*, 39:B47, 1997.

[7] A G Peeters. The bootstrap current and its consequences. *Plasma Phys. Control. Fusion*, 42(12B):B231, December 2000.

[8] M.R. Wade et al. Physics of high bootstrap fraction, high performance plasmas on the DIII-D tokamak. EPS Conference Proceedings, Madeira, Portugal Note: DIII-D uses ECCD and NBCD, June 2001.

[9] K. Ushigusa. Steady state plasma research in jt-60sc. Combined meeting of DOE/JEARI Technical Planning and IEA Large Tokamak Workshop, Februray 2001.

[10] T. Fukuda. Formation condition of internal transport barrier. EPS Conference Proceedings, Madeira, Portugal, June 2001.

[11] M. Okabayashi et al. Control of the resistive wall mode with internal coils in the diiid tokamak. *Nucl. Fusion*, 45(11):1715–1731, November 2005.

[12] S. Bernabei et al. Design of a compact lower hybrid coupler for alcator c-mod. *Fusion Science and Technology*, 43(2):145, March 2003.

[13] T.H. Stix. Radiation and absorption via mode conversion in an inhomogeneous collision-free plasma. *Phys. Rev. Lett.*, 15(23):878–882, December 1965.

[14] M. Porkolab et al. Observation of parametric instabilites in lower-hybrid radio-frequency heating of tokamaks. *Phys. Rev. Lett.*, 38(5):230–233, January 1977.

[15] J.J. Schuss et al. Lower-hybrid-wave heating in the alcator-a tokamak. *Phys. Rev. Lett.*, 43(4):274–278, July 1979.

[16] N.J. Fisch. Confining a tokamak plasma with rf-driven currents. *Physical Review Letters*, 41(13):873, September 1978.

[17] T. Yamamoto et al. Experimental observation of the rf-driven current by the lower hybrid wave in a tokamak. *Phys. Rev. Lett.*, 45(9):716–719, September 1980.

[18] S.C. Luckhardt et al. Generation of rf-driven currents by lower-hybrid-wave injection in the versator ii tokamak. *Phys. Rev. Lett.*, 48(3):152–156, January 1982.

[19] M. Porkolab et al. Observation of lower hybrid current drive at high densities in the alcator c tokamak. *Physical Review Letters*, 53(5):450–453, July 1984.

[20] S. Bernabei et al. Lower-hybrid current drive in the plt tokamak. *Phys. Rev. Lett*, 49(17):12551258, October 1982.

[21] S. Knowlton, M. Porkolab, Y. Takase, S. Texter, P. Bonoli, C. Fiore, S. McCool, F. S. McDermott, and J. L. Terry. Energy confinement of lower-hybrid-current-driven tokamak plasmas. *Phys. Rev. Lett.*, 57(5):587–590, Aug 1986.

[22] S. Texter et al. High energy x-ray measurements during lower hybrid current drive on the alcator c tokamak. *Nucl. Fusion*, 26:1279, 1986.

[23] F. Soldner. Profile control with lower hybrid waves on asdex. *Nuclear Fusion*, 34(7):985–1016, July 1994.

[24] C.D. Warrick et al. First results from lhcd in compass-d. In *Proc. 22nd EPS*, volume 19C, pages III–369–III372, 1995.

[25] J. Li et al. Quasi-steady-state high confinement at high density by lower hybrid waves in the ht-6m tokamak. *Nucl. Fusion*, 40(3Y):467–71, March 2000.

[26] G. Kuang et al. Lower hybrid current drive experiments and improved performance on the ht-7 superconducting tokamak. *Nuclear Fusion*, 39(11Y):1769–1774, November 1999.

[27] T. Imai et al. Current drive and confinement studies during lhrf experiments on jt-60. *Nucl. Fusion*, 28(8):1341–1350, August 1988.

[28] Y. Ikeda et al. Efficient lower hybrid current drive using a multijunction launcher on jt-60. *Nucl. Fusion*, 29(10):1341–1350, October 1989.

[29] R.E. Bell et al. Lower hybrid wave coupling in pbx-m. *Nucl. Fusion*, 34(2):271–275, February 1994.

[30] R. Kaita et al. Current profile modification during lower hybrid current drive on pbx-m. *Nuclear Fusion*, 36(12):1743–1750, December 1996.

[31] D. Van Hautte et al. Lower hybrid heating and current drive on petula-b. In *Heating in Toroidal Plasmas*, volume 1 of *4th International Symposium, Roma Italy*, March 1984.

[32] V.V. Alikaev et al. Lower hybrid current drive experiments in t-7 tokamak. Plasma Physics and Controlled Nuclear Fusion Research 1982 9th Conf. Proc. Baltimore, June 2001.

[33] C. Cote et al. Lower hybrid wave coupling and current drive experiments on tdev. 25th EPS Conference Proceedings, Prague, June 1998.

[34] M. Mayberry e al. Frequency scaling of the lower hybrid current drive density limit in tokamak plasmas. *Physical Review Letters*, 55(8):829–832, August 1985.

[35] C. Gormezano and D . MOREAU. Lower hybrid wave coupling in the wega tokamak. *Plasma Physics and Controlled Fusion*, 26(3):553–564, March 1984.

[36] M. Anquilini et al. The heating and current drive systems of the ftu. *Fusion Sci. Technol.*, 45(3):459–482, May 2004.

[37] A. Ekedahl et al. Long distance coupling of lower hybrid waves in jet plasmas with edge and core transport barriers. *Nucl. Fusion*, 45(4):351–359, April 2005.

[38] Y. Ikeda et al. Simple multijunction launcher with oversized waveguides for lower hybrid current drive on jt-60u. *Fusion Eng. Des.*, 24(3):287–298, June 1994.

[39] M. Seki et al. Performance of the lh antenna with carbon grill in jt-60u. *Fusion Eng. Des.*, 74(1-4):273–277, November 2005.

[40] X. Litaudon et al. Lower hybrid wave coupling in tore supra through multijunction launchers. *Nucl. Fusion*, 32(11):1883–1887, November 1992.

[41] Y. Peysson et al. High power lower hybrid current drive experiments in the tore supra tokamak. *Nucl. Fusion*, 41(11):1703–1713, November 2001.

[42] M. Sakamoto et al. Current profile control and improvement of current drive efficiency by combined lower hybrid waves in triam-1m. *Nucl. Fusion*, 40(3Y):453–459, March 2000.

[43] J.W. Conner et al. A review of internal transport barrier physics for steady-state operation of tokamaks. *Nucl. Fusion*, 44(4):R1–R49, April 2004.

[44] V. Pericoli-Ridolfini et al. High density internal transport barriers for burning plasma operation. *Plasma Phys. Control. Fusion*, 47(12):B285–B301, December 2005.

[45] B. Angelini et al. Overview of the ftu results. *Nucl. Fusion*, 45(10):S227–S238, October 2005.

[46] X. Litaudon et al. Progress towards steady-state operation and real-time control of internal transport barriers in jet. *Nucl. Fusion*, 43(6):565–572, June 2003.

[47] N. Hawkes et al. Observation of zero current density in the core of jet discharges with lower hybrid heating and current drive. *Physics Review Letters*, 87(11):115001, September 2001.

[48] A.A. Tuccillo et al. Development on jet of advanced tokamak operations for iter. *Nucl. Fusion*, 26(1):214–224, January 2006.

[49] J. Pamela et al. Overview of jet results. *Nucl. Fusion*, 43(12):1540–1554, December 2003.

[50] T. Fujita at al. Steady state operation research in jt-60u with extended pulse length. *Nucl. Fusion*, 46(1):S3–S12, January 2006.

[51] T. Fujita at al. Plasma equilibrium and confinement in a tokamak with nearly zero central current density in jt-60u. *Physics Review Letters*, 87(24):245001, December 2001.

[52] G. Giruzzi et al. Advances in the physics of steady-state plasmas by long pulse experiments on tore supra. *Nucl. Fusion*, 47(12B):B93–B105, December 2005.

[53] H. Zushi et al. Steady-state tokamak operation, itb transition and sustainment and eccd experiments in triam-1m. *Nucl. Fusion*, 45(10):S142–S156, October 2005.

[54] G.T. Hoang et al. Particle pinch with fully noninductive lower hybrid current drive in tore supra. *Phys. Rev. Lett.*, 90(15):155002–155005, April 2003.

[55] V. Pericoli-Ridolfini et al. Study of lower hybrid current drive efficiency over a wide range of ftu plasma parameters. *Nucl. Fusion*, 45(11):1386–1395, November 2005.

[56] Y. Takase et al. Observation of parametric instabilities in the lower-hybrid range of frequencies in the high-density tokamak. *Phys. Fluids*, 28(3):983–994, March 1985.

[57] N.J. Fisch. Theory of current drive in plasmas. *Reviews of Modern Physics*, 59(1):175, January 1987. Current drive review article.

[58] A. Bers. Waves and instabilities in inhomogeneous plasmas. Chapter 15 of incomplete book, 2001.

[59] P.T. Bonoli. Private communication.

[60] M.R. Spiegal. *Mathematical Handbook*. 1995. p. 124,125.

[61] P.T. Bonoli and R.C. Englade. Simulation model for lower hybrid current drive. *Physics of Fluids*, 29(9):2937, September 1986.

[62] R.W Harvey and M.G. McCoy. The cql3d fokker-planck code. Technical Report Montreal Canada, IAEA TCM Advances in Simulation and Modeling of Thermonuclear Plasmas, 1992.

[63] J. Decker and Y. Peysson. Dke: a fast numerical solver for the 3-d relativistic bounce-averaged electron drift kinetic equation. Technical Report EUR-CEA-FC-1736, EURATOM CEA-Cadarache, December 2004.

[64] D. Ignat. *Lower Hybrid Simulation Code Manual.* Princeton Plasma Physics Laboratory, November 2000.

[65] T.H. Stix. *Waves in Plasmas.* 1992.

[66] P.T. Bonoli. Linear theory of lower hybrid heating. *IEEE Transactions on Plasma Science*, PS-12(2):95, June 1984.

[67] V.L. Granatstein and P.L. Colestock. *Wave Heating and Current Drive in Plasma.* 1985. Chapter 4, Bonoli.

[68] N.J. Fisch. *Confining and Heating a Toroidal Plasma with RF Power.* PhD thesis, MIT, 1978.

[69] C.F. Karney and N.J. Fisch. Numerical studies of current generation by rf traveling waves. *Physics of Fliuds*, 22(9):1817, September 1979.

[70] M.A. Leontovich. *Reviews of Plasma Physics*, volume 1. Consultants Bureau, 1970.

[71] N.J. Fisch and A.H. Boozer. Creating an asymmetric plasma resistivity with waves. *Physical Review Letters*, 45(9):720, September 1980.

[72] J. Schachter. *Local Transport Analysis for the Alcator C-Mod Tokamak.* PhD thesis, Massachusetts Institute of Technology, June 1997.

[73] E. J. Valeo D. W. Ignat and S. C. Jardin. Dynamic modeling of lower hybrid current drive. *Nuclear Fusion*, 34(6):837–852, June 1994.

[74] P.T. Bonoli et al. Lower hybrid current drive: An overview of simulation models, benchmarking with experiment, and prediction for future devices. In C. Forest, editor, *Radio Frequency Power in Plasmas*, volume 694, pages 24–37. AIP, 2003.

[75] M Brambilla. Numerical simulation of ion cyclotron waves in tokamak plasmas. *Plasma Phys. Cont. Fusion*, 41(1):1–34, 1999.

[76] F.L. Hinton and R.D. Hazeltine. Theory of plasma transport in toroidal confinement systems. *Rev. Mod. Phys.*, 48(2):239–308, April 1976.

[77] C. Gormezano. High performance tokamak operations regimes. *Plasma Phys. Control. Fusion*, 41(12B):B367–B380, December 1999.

[78] T. Fujita et al. Internal transport barrier for electrons in jt-60u reversed shear discharges. *Phys. Rev. Lett.*, 78(12):2377–2380, March 1997.

[79] S. Ide et al. Overview of jt-60u progress towards steady-state advanced tokamak. *Plasma Phys. Control. Fusion*, 45(10):S48–S62, October 2005.

[80] V. Pericoli Ridolfini. High density internal transport barriers for burning plasma operation. *Plasma Phys. Control. Fusion*, 47(12B):B285–B301, December 2005.

[81] M. Porkolab et al. Reverse shear experiments in alcator c-mod with current ramp. In *Proc. 24th EPS*, volume 21A, pages 569–572, 1997.

[82] P. Bonoli et al. Rf current profile control studies in the alcator c-mod tokamak. In *Radio Frequency Power in Plasmas: 13th Topical Conference: Annapolis, Maryland, April 1999*, volume 341-344, 1999.

[83] S.J. Wukitch et al. Double transport barrier experiments on alcator c-mod. *Physics of Plasmas*, 9(5):2149–2155, May 2002.

[84] C. Fiore et al. Internal transport barrier production and control in alcator c-mod. *Plasma Phys. Control. Fusion*, 46(11):B281–B291, November 2004.

[85] B. Wan et al. Experimental investigation of the interaction of ibw and lhcd in the ht-7 tokamak. *Nucl. Fusion*, 44(2):400–405, February 2004.

[86] C. Karney and N. Fisch. Current in wave driven plasmas. *Physics of Fluids*, 29(1):180–192, January 1986.

[87] S. Von Goeler et al. Camera for imaging hard x rays from suprathermal electrons during lower hybrid current drive on pbx-m. *Rev. Sci. Instrum.*, 65(5):1621–1630, May 1994.

[88] D. Ignat et al. Spreading of lower hybrid wave-driven currents in pbx-m. *Nuclear Fusion*, 36(12):1733–1742, December 1996. LSC reference.

[89] Y. Peysson et al. Selfconsistent rf driven and bootstrap currents. In *IAEA 19th Fusion Energy Conference 14 - 19 October 2002, Lyon, France*, 2002.

[90] Y. Peysson et al. Advanced 3-d electron kinetic calculations for the current drive problem in magnetically confined thermonuclear plasmas. In *12th International Congress on Plasma Physics, 25-29 October 2004, Nice, France*, 2004.

[91] V. Fuchs et al. Simulations of current density profile control using lower hybrid current drive in the tdev tokamak. *Nuclear Fusion*, 15(1):1–22, January 1995.

[92] A.P. Smirnov and R.W. Harvey. The genray ray tracing code. Technical Report CompX-2000-01,Ver. 2, CompX, March 2003.

[93] Y. Peysson and F. Imbeaux. Tomography of the fast electron bremsstrahlung emission during lower hybrid current drive on tore supra. *Rev. Sci. Instrum.*, 70(10):3987–4007, October 1999.

[94] H.W. Koch and J.W. Motz. Bremsstrahlung cross-section formulas and related data. *Rev. Mod. Phys.*, 31(4):920–956, October 1959.

[95] S. Jones et. al. Calculation of an upper limit for an effective fast electron diffusion constant using the hard x-ray camera on pbx-m. *Plasma Phys. and Control. Fusion*, 35(8):1003–1017, August 1993.

[96] F. Imbeaux and Y. Peysson. Dynamics of fast electrons driven by the lower hybrid wave in giant sawtoothing plasmas. *Phy. Rev. Let.*, 84(13):2873–2876, March 2000.

[97] R. Bartiromo et. al. Fast electron conefinement during lower hybrid experiments on asdex. *Nuclear Fusion*, 33(10):1483–1492, October 1993.

[98] B. Esposito et. al. Runaway electron measurements in the jet tokamak. *Plasma Phys. and Control. Fusion*, 43(12):2035–2049, December 1996.

[99] S. Ide et. al. Enhancement of absorption of lower hybrid wave by filling the spectral gap. *Phys. Rev. Let.*, 73(17):2312–2315, October 1994.

[100] S. Texter. *Plasma x-ray spectroscopy during lower hybrid current drive on Alcator C*. PhD thesis, Massachusetts Institute of Technology, 1986.

[101] R. O'Connell et. al. Measurement of fast electron distribution using a flexible, high time resolution hard x-ray spectrometer. *Rev. Sci. Instrum.*, 74(3):2001–2003, March 2003.

[102] Y. Peysson and R. Arslanbekov. Measurement of the non-thermal bremsstrahlung emission between 30 and 200 kev with a hight time-space resolution on the tokamak tore supra. *Nuc. Inst. Meth. Phys. A*, 380(1-2):423–426, October 1996.

[103] G. Sato et. al. Characterization of cdte/cdznte detectors. *IEEE Trans. Nuc. Sci.*, 49(3):1297–1303, June 2001.

[104] G. Sato et. al. Properties of cdznte detectors in the burst alert telescope (bat) array. In L. Franks et. al., editor, *Hard x-ray and gamma-ray detector physics V*, volume 5198. SPIE, SPIE Press, January 2004.

[105] Glenn F. Knoll. *Radiation Detection and Measurement*. Wiley, third edition, December 1999.

[106] S. Ohkawa et. al. Direct synthesis of the guassian filter for nuclear pulse amplifiers. *Nuc. Ins. Meth*, 138(1):85–92, October 1976.

[107] G. De Geronimo et. al. A generation of cmos readout asics for czt detectors. *IEEE Trans. Nuc. Sci.*, 47(6):1857–1867, December 2000.

[108] M. Bolic and V. Drndarevic. Digital gamma-ray spectroscopy based on fpga technology. *Nuc. Inst. Meth. Phys. A*, 482(3):761–766, April 2002.

[109] D. Moreau et. al. Real-time control of the q-profile in jet for steady state advanced tokamak operation. *Nuclear Fusion*, 43(9):870–882, September 2003.

[110] T. Madeira et. al. Real-time signal analysis on the tcv pha diagnostic. *Rev. Sci. Instrum.*, 74(3):2004–2006, March 2004.

[111] Y. Peysson et. al. Study of radiation scattering in the hard x-ray energy range by a tokamak inner wall. *Nuclear Fusion*, 33(8), August 1993.

[112] J. Briemeister et. al. *MCNP- A General Monte Carlo N-Particle Transport Code, Version 4C*, la-13709-m edition, April 2000.

[113] C. Fiore. Alcator c-mod final safety analysis. Pfc/rr-89-8, MIT PFC, June 1989.

[114] M. Brambilla. Slow-wave launching at the lower hybrid frequency using a phased waveguide array. *Nuclear Fusion*, 16(1):47–54, January 1976.

[115] J. Stevens et al. Edge density profiles effects for lower hybrid waveguide coupling. *Nucl. Fusion*, 21(10):1259–1264, October 1981.

[116] M. Brambilla. Evaluation of the surface admittance matrix of a plasma in the finite larmor radius approximation. *Nucl. Fusion*, 35(10):1265–1280, October 1995.

[117] M. Brambilla. Waveguide launching of lower hybrid waves. *Nucl. Fusion*, 19(10):1343–1357, October 1979.

[118] A.C. England et al. Power transmission and coupling for radiofrequency heating of plasmas. *Nucl. Fusion*, 29(9):1544–1582, September 1989.

[119] F. Leuterer et al. Coupling of the 2x24 waveguide gill for lower hybrid waves in asdex. *Plasma Phys. Control. Fusion*, 33(3):169–180, 1991.